UNIVERSITÄT DUISBURG ESSEN

Open-Minded

# Effect of Synthesis Conditions on the Properties of Lead Iron Niobate Ceramics and Thin Films: Possible Candidate for Photovoltaic Devices?

Von der Fakultät für Ingenieurwissenschaften
Abteilung Bauwissenschaften,
Institut für Materialwissenschaft
der Universität Duisburg-Essen

genehmigte Dissertation zur Erlangung des akademischen Grades eines
Doktor der Ingenieurwissenschaften (Dr. -Ing.)

vorgelegt von

**M. Sc. Nicole Bartek**

Datum der mündlichen Prüfung: 22.11.2022
Hauptreferent: Prof. Dr. rer. nat. Doru C. Lupascu
Korreferent: Prof. Dr. -Ing. Kyle G. Webber


Essen 2022

**DOI:** 10.17185/duepublico/78322
**URN:** urn:nbn:de:hbz:465-20230503-142432-7

# Declaration

I declare that the contents of this dissertation are original work prepared by myself, except when a particular reference is made to the work of others, including the electronic sources. This work has not been submitted entirely or partially for any other degree or qualification in this, or any other University. This dissertation is the outcome of my original work and the work done in collaboration has been duly acknowledged.

Nicole Bartek

Essen, April 2022

# Acknowledgement

First, I would like to thank Prof. C. Lupascu very much for giving me the opportunity to do my Ph.D. at his institute. Through constant interaction, he helped me to expand and apply my knowledge and supported me throughout. I would also like to thank Prof. K. Webber for taking the time to read and evaluate my work. At the same time, I would also like to give special thanks to Dr. V. Shvartsman, who was always available with advice and his time to answer any questions and to Prof. R. Schmechel and Prof. D. Wittowsky being part of my comitee.

Special thanks goes to the German Research Foundation. Only through their funding through the project Relaxsolaire, I was given the opportunity to do my Ph.D.

Furthermore, I would like to thank the people who made samples and measurements with or for me. In the order in which it appears in this work: Thanks to the working group of the Jozef Stefan Institute in Slovenia of Dr. H. Ursic, especially to Dr. U. Prah, who made the mechanochemical-activated samples with me. This allowed me to deepen my understanding and make good ceramics myself. Further thanks go to Dr. S. Salomon, who performed the magnetic measurements and was available to answer questions during the evaluation. I owe most of the PLD coatings to H. Bouyanfif, who gave me the opportunity to make them in the laboratory of the University Jules Verne in Amiens. At the same time, I thank the working group that warmly welcomed me and especially M. A. Khaled who recorded the rocking curves for me. At the same time, I would like to thank Dr. S. Weber who allowed me to prepare additional layers in Duisburg during the pandemic period and travel restrictions. For the UPE/IPES measurements, I was allowed to send my samples to Prof. S. Olthoff who performed them. I would therefore like to thank her as well. Further thanks go to A. Schmitz, who performed the photoluminescence measurements, and to Dr. S. Sirotonskaya, who was available for the TLM measurements. At the same time, I would like to thank Prof. N. Benson, who was always ready for a discussion in the solar meetings.

Now I come to the people who imparted their spiritual knowledge to me and helped me with professional discussions. Most of all I thank D. Lewin, he helped everywhere he could and explained things to me in such a way that I could understand and internalize them. Also, I thank A. Dubey and Y. Hambal for the numerous discussions in the seminar room and Prof. Dr. U. Wiedwald, who especially supported me with his knowledge at the XRD. A special thanks also goes to M. Schmuck.

Furthermore, I would also like to thank the rest of my working group: K.- H. Menze, S. Nawrath, A. Schmidt, S. Kriegel, Dr. M. Vadala, T. Mielke, M. Escobar, Dr. J. Schell, E. Kröll, S. Mohammadi-Fathabad, G. Semugaza, A. Gierth, Y. Jin, F. Paul, A. Karabanov, T. Dang, and to the alumni Dr. A. Farooq,Dr. C. Hübner, Dr. K. Voges, Dr. D. Ganther, Dr. M. Pantaler, Dr. I. Anusca, Dr. C. Fettkenhauer, Dr. H. Trivedi, Dr. N. Ul-Haq and M. Breitkopf.

Thanks also to my family and friend for their support and help during my doctoral studies, and especially for the understanding they have shown me during this time.

# Abstract

The importance of renewable energies is increasing over time and is becoming more important to compensate for the growing high energy consumption and to counteract climate change. A central issue here is the production of solar cells. Although silicon as the market leader is highly efficient and durable, it is expensive to produce. A cheaper alternative is currently seen in organic-inorganic halide perovskites, which also have high efficiencies, however, their weak point is their longevity, as they are susceptible to humidity and UV light and thus degrade quickly.

With a view to the future, other materials should therefore be investigated for their usability as absorber cells. One group of promising materials are ferroelectrics. The open-circuit voltage is not limited by the band gap and thus the Schottky-Quisser limit could theoretically be circumvented.

This thesis deals with ferroelectric lead-iron niobate ($PbNb_{0.5}Fe_{0.5}O_3$; PFN) and first considerations to use this material as an absorber layer. In order to create a suitable layer, preliminary investigations must be carried out and the material and the manufacturing method must be properly understood. For this reason, this work also deals in detail with the production of the ceramics under various conditions. Only a very good ceramic is the basic building block for a target that can be used in pulsed laser deposition.

After the fabrication and characterization of PFN ceramics, suitable conditions for the layer growth are determined and first experiments regarding the optical properties of the material are performed. Furthermore, an alternative layer fabrication via spin coating is considered. In the end, the band gap of PFN and the possibility of using it as an absorber layer are discussed in detail.

# Zusammenfassung

Die Bedeutung von erneuerbaren Energien nimmt im Laufe der Zeit immer mehr zu und wird wichtiger um den wachsenden hohen Energiekonsum auszugleichen und dem Klimawandel entgegenzuwirken. Ein zentrales Thema dabei stellt die Produktion von Solarzellen dar. Der Marktführer Silizium besitzt zwar hohe Effizienzen und ist langlebig, jedoch teuer in der Produktion. Eine kostengünstigere Alternative wird derzeitig in organisch-anorganischen Halid Perowskiten gesehen, die zwar auch hohe Effizienzen besitzen, dennoch ihre Schwachstelle in der Langlebigkeit besitzen, da sie anfällig für Luftfeuchtigkeit und UV-Licht sind und somit schnell degradieren.

Im Hinblick auf die Zukunft sollten demnach weitere Materialen auf die Verwendbarkeit als Absorberzellen hin untersucht werden. Eine Gruppe von vielversprechenden Materialien sind Ferroelektrika. Die Leerlaufspannung ist nicht durch die Bandlücke limitiert und dadurch könnte theoretisch das Schottky-Quisser Limit umgangen werden.

Diese Arbeit handelt vom ferroelektrischen Bleieisenniobat ($PbNb_{0,5}Fe_{0,5}O_3$; PFN) und ersten Überlegungen dieses Material als Absorberschicht zu verwenden. Damit eine geeignete Schicht erzeugt werden kann, müssen Voruntersuchungen durchgeführt werden und das Material und die Herstellungsweise richtig verstanden werden. Aus diesem Grund befasst sich diese Arbeit zusätzlich noch detailliert mit der Herstellung der Keramiken unter verschiedensten Bedingungen. Nur eine sehr gute Keramik ist der Grundbaustein für ein Target, dass bei der gepulsten Laserdeposition verwendet werden kann.

Nach der Herstellung und Charakterisierung von PFN Keramiken werden geeignete Bedingungen für das Schichtwachstum ermittelt und erste Versuche hinsichtlich der optischen Eigenschaften des Materials durchgeführt. Außerdem wird eine alternative Schichtherstellung über das Spin Coating in Erwägung gezogen. Am Ende wird eingehend über die Bandlücke von PFN und über die Möglichkeit über eine Verwendung als Absorberschicht diskutiert.

# Table of Contents

# Abbreviations and Symbols

| | |
|---|---|
| $A$ | area |
| | extinction |
| AFM | atomic force microscopy |
| $B$ | constant |
| BFO | bismuth ferrite |
| Bi | bismuth |
| BSE | backscattered electrons |
| BVE | bulk photovoltaic effect |
| $C$ | curie constant |
| Cl | chloride |
| CO | combustion |
| $d$ | distance |
| | layer thickness |
| DPT | diffuse phase transition |
| $E$ | electric field |
| | energy |
| $E_C$ | coersive field |
| $E_{CB}$ | conduction band energy |
| EDX | energy dispersive X-ray specroscopy |
| $E_G$ | band gap energy |
| $E_{G,\,fund}$ | fundamental band gap energy |
| $E_U$ | Urbach energy |
| $E_{VB}$ | valence band energy |
| $f$ | frequency |
| FC | field cooled |
| Fe | iron |
| $F(R_\infty)$ | Kubelka-Munk |
| FWHF | full width half maximum |
| $g$ | effective dimension of the domain growth |
| GIXRD | grazing incidence XRD |
| GOF | goodness of fit |
| $h$ | Planck constant |
| $HBEC$ | high binding energy cutoff |
| HT | hydrothermal |
| $I$ | attenuated light |
| $I_0$ | incident light |
| ICSD | inorganic crystal structure database |
| IPES | inverse photon electron spectroscopy |
| $\vec{k}$ | crystal momentum value |
| $K$ | absorption coefficient |
| K | potassium |
| La | lanthanum |
| $m_{dry}$ | mass when sample is dried |

| | |
|---|---|
| $m_{sat,\ air}$ | mass when sample is saturated |
| $m_{sat,\ H2O}$ | mass when pores are filled with water |
| $M$ | magnetic field |
| MA | mechanochemical activation |
| MgO | magnesium oxide |
| $M_r$ | remanent magnetization |
| MS | molten salt |
| Na | sodium |
| Nb | niobium |
| NCAir | sample sintered without powder contact and air |
| NCOx | sample sintered without powder contact and oxygen |
| $P$ | polarization |
| PES | photoelectron spectroscopy |
| PL | photoluminescence |
| $P_r$ | remanent polarization |
| $P_S$ | spontaneous polarization |
| Pb | lead |
| PCAir | sample sintered in powder contact and air |
| PCOx | sample sintered in powder contact and oxygen |
| PFN | lead iron niobate |
| PFM | piezo force microscopy |
| PLD | pulsed laser deposition |
| PTO | lead titanate |
| PZT | lead zirconate |
| $P_{net}$ | net polarization |
| RHEED | reflection high-energy electron diffraction |
| $R_{wp}$ | weighted profile R-value |
| $Q$ | charge |
| $S$ | scattering coefficient |
| SE | secondary electrons |
| SEM | scanning electron microscope |
| Si | silicon |
| SRO | strontium ruthenate |
| SS | solid state |
| STO | strontium titanate |
| $T$ | temperature |
| $T_B$ | burns temperatur |
| $T_C$ | Curie temperature |
| $T_{Cal}$ | calcination temperature |
| $T_d$ | depolarization temperature |
| Ti | titanium |
| $T_{Max}$ | maximum temperature |
| $T_N$ | Néel temperature |
| tan$\theta$ | dielectric loss factor |
| $T_s$ | sintering temperature |

| | |
|---|---|
| UPS | ultraviolet photon spectroscopy |
| UV | ultraviolet |
| $V_{in}$ | input voltage |
| vis | visible |
| $V_{out}$ | output voltage |
| VSM | vibrating sample magnetometer |
| XRD | X-ray diffraction |
| XRR | reflectometry |
| YSZ | yttrium stabulized zirconium oxide |
| ZFC | zero field cooled |
| Zr | zirconium |
| $x$ | distance |
| $\alpha$ | absotption coefficient |
| $\alpha_E$ | magneto-eletric coefficient |
| $\gamma$ | diffuseness coefficient |
| $\varepsilon$ | dielectric permittivity |
| $\varepsilon_0$ | permittivity of free space |
| $\varepsilon_{max}$ | dielectric permittivity at $T_{Max}$ |
| $\varepsilon_r$ | relative permittivity |
| $\theta$ | Curie Weiss temperature |
| | Incident angle |
| | position of satellite maximum |
| $\theta_C$ | critical angle of reflecticity |
| $\kappa$ | different value for direct or indirect band gap |
| $\lambda$ | wavelength |
| $\rho$ | density |
| $\rho_{abs}$ | absolute density |
| $\rho_{H2O}$ | density of water |
| $X_e$ | electric susceptibility |
| $\phi_{material}$ | work function of the material |
| $\phi_{spectrometer}$ | work function of the spectrometer |
| $\varphi$ | azimuth angle |
| $\psi$ | tilted angle |

# 1. Introduction and Foundations

## 1.1. Introduction

Renewable energies have been an important topic for the last decades. In the beginning, it was mainly about the scarcity of fossil fuels. In recent years, however, climate change has increasingly come into focus, as its effects can already be felt all over the world. To counteract this, research is being carried out in all different directions. Several energy sectors are currently experiencing a turnaround, such as for example the automotive industry with the switch to electric cars: New registrations for electric cars worldwide increased by 38 % in 2020 alone [1]. This is not the only reason why energy consumption will increase in the next years [2], as also the world population, the industrialization and the field of digitization are growing. The main policies in Europe and all over the world are to transfer to renewable energy sources and replace fossil fuel sources as fast as possible [3]. A large field is the generation of electricity by wind [4]. For wind turbines, there are difficult requirements for the locations and the space is limited [5]. Therefore, great hope is placed in solar energy which has so far accounted for a smaller proportion of energy production [4], although the benefits of placement are obvious as the solar panels can be spread all over the roofs in a city and no special space is needed. Another advantage is that they do not produce any noise. Silicon solar cells have a high efficiency and are already commercially available, nevertheless, the production and equipment are expensive and not affordable for everyone.

For this reason, research is already being done on other materials that promise good results. These materials must fulfill several requirements to gain high efficiency like a suitable band gap, high charge carrier mobility and lifetime, and an appropriate work function. Organic-inorganic halide perovskites fulfill these requirements [6]. However, the longevity of the materials must be high as well for an effective use which is not given for this material class so far. Inorganic perovskites on the other hand do not suffer from the degrading influences like humidity or UV-light. Some of them which have ferroelectric properties have already been considered as alternative photovoltaic materials [7–11] and have already achieved a power conversion efficiency of up to 8.1 % in a multilayer system [8].

Normally classical ferroelectrics exhibit a large band gap of usually 2.5 – 4.5 eV (~ 2.98 eV for $Ba(Zr_{0.25}Ti_{0.75})O_2$ [12], ~ 3.1 eV for $PbZn_{1/3}Nb_{2/3}O_3$-$PbTiO_3$ [13], 3.6 eV for $PbTiO_3$ [14–16], and $Pb(Zr_xTi_{1-x})O_3$ [17–19], and a larger band gap than 3.35 eV for $Pb(Zr_xTi_{1-x})O_3$ [20,21]). Lead iron niobate (PFN) which is proposed to have a band gap of ~ 0.43 eV according to DFT

calculations [22] which makes it a promising material for an absorber layer in photovoltaic devices. This thesis deals with the properties of PFN ceramics in relation to the synthesis conditions and the initial investigation of PFN thin films in the direction of photovoltaic devices.

## 1.2. Ferroelectrics

Information about ferroelectrics were taken from [23–25] if not denoted otherwise.

### 1.2.1. What is a ferroelectric?

Ferroelectrics have a spontaneous electrical polarization $P_S$ that can be reversed when a corresponding external electrical field (coercive field $E_C$) is applied. This spontaneous polarization is due to the displacement of ions in the crystal, which either can be located up or down as seen on the left side of Figure 1.1 a. This requires an absence of a center of symmetry. In addition, a unique polar axis is necessary for pyroelectrics, which makes ferroelectrics a subgroup of pyroelectrics, which is a subgroup of piezoelectrics and in turn a subgroup of dielectrics. This makes all ferroelectrics pyro-, piezo-, and dielectric.

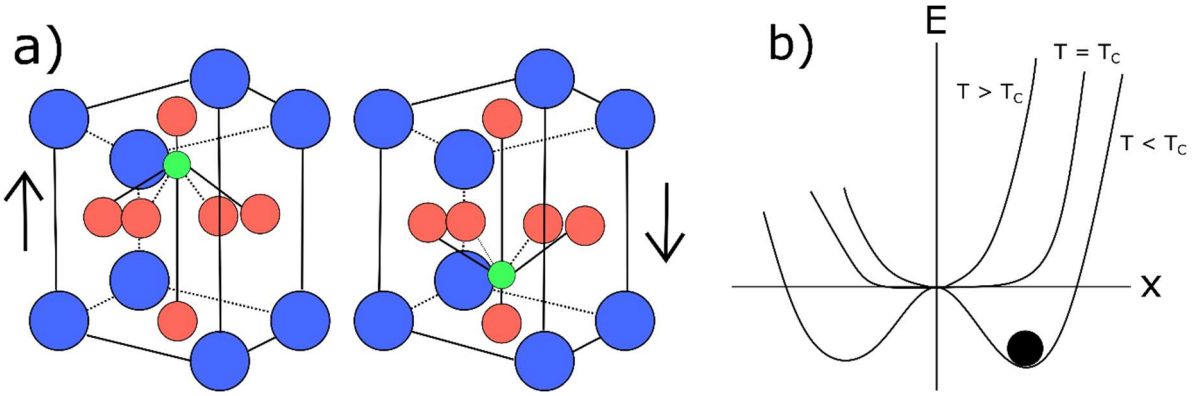


*Figure 1.1 a) Displacement of ions in the crystal. b) Model of the double-well potential for polarization.*

When increasing the temperature, ferroelectrics tend to loose their ferroelectric properties after they have reached a temperature $T_C$ due to the change of the crystal lattice to a higher symmetry. $T_C$ is the transition temperature and is called the Curie temperature. With the model of the double-well potential in Figure 1.1 b the procedure of the phase transition can be explained. At temperatures smaller than $T_C$ the ion either sits on one side of the double-well potential or the other which denotes the polarizations up or down. When the temperature is increased the barrier of the potential will decrease. The movement of the ions is inhibited until the temperature is above $T_C$. The ions stay in the middle of the crystal which means a paraelectric phase is reached.

Another possibility to overcome the potential barrier at low temperatures is to apply an external electric field (Figure 1.2). At very small fields there is a linear dependency of the polarization on the field due to electronic, ionic and sometimes dipolar contribution like in every dielectric material. In ferroelectrics another extrinsic contribution related to the reversible displacement of the domain walls is added. However, if the field is increased, the polarization increases faster, and the linearity is no longer given: the domains grow irreversibly. When a sufficiently large field is generated, a single domain structure (B) is reached and it comes to saturation. If the field will be increased further, the polarization also increases owing to the induced polarization. When the field is then subsequently reduced, the domains begin to recede, but since the displacement of the domain walls is irreversible, the polarization stays higher than for A, why A is also called the initial curve. Arriving at point D, the residual polarization has remained due to the irreversible domain wall displacement, which is reported as remanent polarization $P_r$. To reverse the domain wall displacement, an opposing field must be created which is large enough to reverse the process. This field is called the coercive field $E_C$ (F). If the negative field is increased further, the saturation range is reached again, and the process can be repeated which leads to a hysteresis loop.

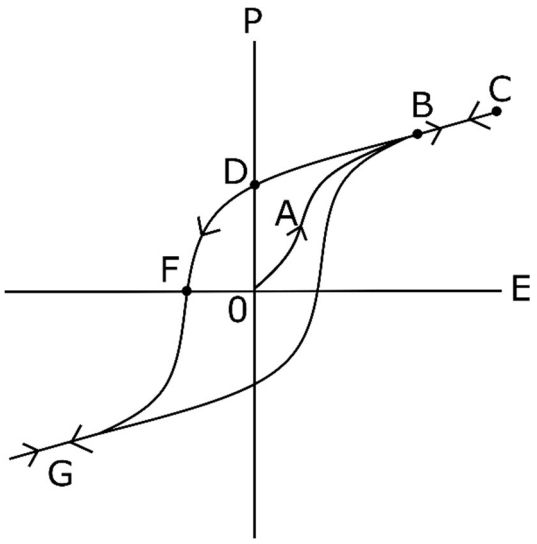


*Figure 1.2 Typical polarization hysteresis loop with its stages: A is the initial curve, B is the saturation polarization, D is the remanent polarization, F is the coercive field, and G again the saturation polarization.*

Another characteristic of a ferroelectric is the non-linearity of the dielectric permittivity $\varepsilon$. Normally the permittivity is also high at temperatures not close to the transition temperature, but when the temperature is near $T_C$, $\varepsilon$ reaches very high values. This dependence of $\varepsilon$, especially above the Curie temperature, can be described by the Curie-Weiss law:

$$\varepsilon = \frac{C}{T - \theta} \qquad \text{Eq. 1.1}$$

$C$ is the Curie constant and $\theta$ the Curie-Weiss temperature.

### 1.2.2. Relaxor ferroelectrics

Unlike normal ferroelectrics, which have a sharp peak, the permittivity in relaxors increases slower, reaching the maximum value of permittivity at the temperature $T_{Max}$. Thereafter, the permittivity decreases slowly towards higher temperatures as well, making the peak broader than in normal ferroelectrics. Furthermore, the peak position shifts when the permittivity is plotted as a function of temperature to other frequencies with a strong frequency dispersion of the dielectric permittivity around and below $T_{Max}$ [26–28].

This difference can be explained by the fact that the two B-cations do not arrange themselves homogeneously, so that fluctuations exist within the material in the cation ratio. This yields fluctuations in the Curie temperature. Because of this, there are ferroelectric and paraelectric regions over a wide temperature range, which become more and more paraelectric with increasing temperature [26]. An additional theory is the presence of polar micro- or nanoregions. In order to compensate charge differences due to the nonhomogeneous balance of the cations, regions with a short range order are formed [26], as also seen in other materials like $Pb(Mg_{1/3}Nb_{2/3})O_3$ [29]. However, there are three different polar states: Above the Burns temperature $T_B$, relaxor ferroelectrics are in the paraelectric phase, in which the dielectric properties follow the Curie-Weiss law (state 1). When the temperature decreases below $T_B$ polar regions start to gradually emerge. At this point, the nano-polar regions are highly dynamic, that they are easily switchable within the matrix. Near $T_B$, the relaxation frequencies of the nano-polar regions are higher than $10^7$ Hz, so the frequency dispersion of permittivity cannot be detected in typical 10 MHz measurements. With further cooling, the motions of the nano-polar regions become slower and the frequency dispersion can be seen at frequencies below 10 MHz as well. From the temperature at which dielectric dispersion can be clearly seen to the depolarisation temperature $T_d$, the relaxor is in state 2. When the temperature is further decreasing below $T_d$, state 3 is reached, at which relaxors can achieve a dipolar glass state or a mixed glass-ferroelectric state [28,30].

### 1.2.3. Diffuseness coefficient

In relaxor ferroelectric materials the temperature dependencies cannot be described by the Curie-Weiss law (Eq. 1.1), because their behaviour is deviating. The higher the frequency of the applied field, the higher the deviation [27]. For this reason a modified Curie-Weiss law is used as follows [31,32]:

$$\frac{1}{\varepsilon_m} - \frac{1}{\varepsilon_{Max}} = \left(\frac{T - T_{Max}}{C}\right)^{\gamma} \qquad \text{Eq. 1.2}$$

Where $C$ is a constant and $\varepsilon_m$ and $T$ are the relative permittivity and temperature above $T_{Max}$, respectively. The 'diffuseness' of the dielectric peak can be represented by the diffuseness exponent $\gamma$.

Clarke and Burfoot [31] related the diffuseness of the dielectric peak to stoichiometry, $\gamma = 1$ corresponds to the stoichiometric case, while $\gamma = 2$ stands for an extreme, non-stoichiometric composition. Raymond et al. [33] explain the diffuseness of the dielectric maximum for PFN by the presence of polar nano- or microregions with different Curie temperatures, meaning the iron and niobium ions are randomly distributed and form areas, where they are accumulated or evenly distributed. Therefore, this gives information about the phase transition, weather it is a "normal" ferroelectric transition ($\gamma = 1$) or a completely diffuse phase transition (DPT) ($\gamma = 2$). With a value in between it shows an incomplete DPT with a specific degree of diffuseness [34].

### 1.2.1. Frequency dependence of the coercive field

The phenomenological theory based on the Landau-type thermodynamic potential for spatially uniform systems describes the origin of the typical hysteresis curve [35]. However, the critical field from the theory is usually one to two orders of magnitude higher than the experimental coercive field. This discrepancy is due to the fact that the theory considers that the polarization reversal is occurring homogenously in the entire volume of the sample. On the contrary, in real materials, the polarization switching usually occurs through the nucleation and growth of domains [35]. This is a dynamic process, so the coercive field depends on the frequency of the applied field. The hysteresis loops can be described theoretically by two different approaches. One of them is based on the simulations in the presence of a sinusoidal field [36–39]. The second one, which is simpler, is derived from the Avrami model [40–42], which assumes that the velocity of the domain walls is only dependent of the field strength. On this basis, Orihara

et al. [35] and Hashimoto et al. [43] derived a simplified formula with which the frequency dependence of the coercive field $E_C$ can be described as follows [43]:

$$E_C \propto f^{\frac{g}{\alpha}} \qquad \text{Eq. 1.3}$$

Where $g$ is the effective dimension of the domain growth and $\alpha$ is a constant with the value 5.7.

### 1.2.2. Ferroelectric materials and multiferroics

Ferroelectrics have been investigated since J. Valasek [44] discovered the ferroelectric properties in Rochelle salt in 1921. He measured a hysteresis in $P$ which was analogous to the ferromagnetic hysteresis. After this, research on ferroelectrics started prospering after 1944. Wul [45] and von Hippel et al. [46] found ferroelectricity in $BaTiO_3$ independently. $BaTiO_3$ has a perovskite structure in the typical chemical formula of $ABO_3$ form. On the A and B sites, there are usually two different cations while the A site cation is 12-coordinated and the B site cation is 6-coordinated forming an octahedron. They can be differently charged and form many combinations of how the charge is distributed on the A and B sites so that more complex structures such as AB'B''$O_3$ also can be formed. Normally the ideal structure is cubic, but many oxides exhibit lower symmetry, because they are slightly distorted. Later, many ferroelectrics were discovered in the perovskite group also including multiferroics. Multiferroics are materials in which at least two ferroic orders can exist at the same temperature, such as electric, elastic or magnetic [47,48]. However, not only the coexistence is fascinating in these materials, the fact, that the ferroic orders can be coupled offers new scientific and technological possibilities [49]. Important for this work is the combination of the magnetic and electric orders, which can include any ordering types like ferro-, antiferro-, ferri-, para- and superpara- ordering. The magneto-electric effect enables a change between the energies stored in electric and magnetic fields. On the one hand, an applied external magnetic field can change the polarization and vice versa the external electric field changes the net magnetization. This coupling is mathematically described through the magneto-electric coupling coefficient $\alpha_E$ and the derivative of the magetic ($M$) and elctric ($E$) field [49]:

$$\alpha_E = \frac{\partial M}{\partial E} \qquad \text{Eq. 1.4}$$

Multiferroics can be used as field sensors, resonators, memories, for thermal energy harvestors and as many other devices [49].

By now, many multiferroic materials and systems have been discovered wherefore Khomskii [50] categorized them into two groups: In type-I multiferroics, the magnetic and ferroelectric transition temperatures can be well above room temperature, nevertheless, the coupling of magnetic and ferroelectric properties is rather weak. They have typically good ferroelectric properties. Type-I multiferroics can be divided in different subgroups depending on their mechanisms of ferroelectricity e.g. lone pairs ferroelectricity which occurs in many Pb-containing ferroelectrics. These ions have *s* electrons which are not participating in chemical bonds. They have a high polarizability and therefore order in one direction. Another one is e. g. the charge ordering where inequivalent sites (long or short bonds) with different charges lead to ferroelectricity. The type-II multiferroics are also called magnetic multiferroics since the ferroelectricity occurs only in a magnetically ordered state. Here, it can be distinguished between a specific type of magnetic spiral and the appearance of ferroelectricity even for collinear magnetic structures.

## 1.3. Magnetism

Different magnetic orderings can occur in a material. The best known is the ferromagnetism, which has analogous properties to the ferroelectricity. The neighbouring magnetic moments of a domain are oriented in one direction (Figure 1.3, left). When an external magnetic field is applied, the individual domains grow to a single-domain structure and the typical hysteresis occurs [51].

In addition, there are also ferri- or antiferromagnetics. In ferrimagnetics, the magnetic moments align antiparallel, their magnitudes being unequal (Figure 1.3, middle), and the magnetism is partially compensated. The magnetic susceptibility is significantly lower than in ferromagnetics. Antiferromagnetics are similar to ferrimagnetics: The neighboring magnetic moments are oriented antiparallel as well, however, their magnitudes are equal (Figure 1.3, right), so that the magnetic moments compensate each other [51].

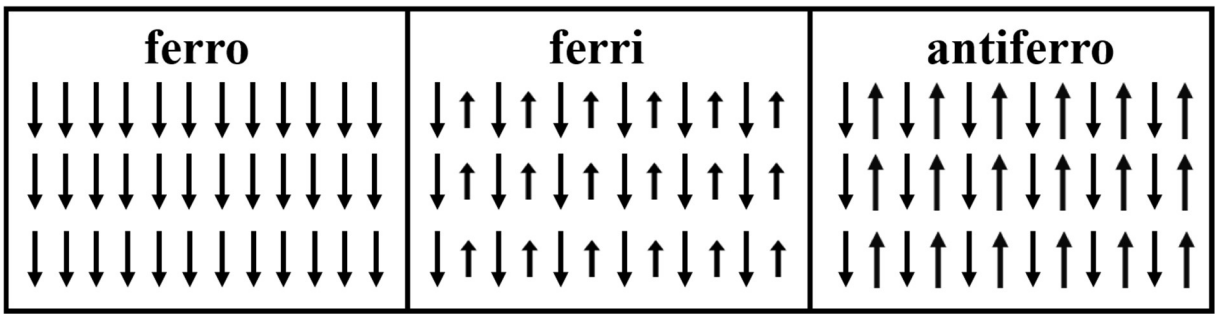


*Figure 1.3 Schematic ordering of magnetic moments for ferro-, ferri-, and antiferromagnetics.*

Figure 1.3 shows only a simplified view of the spin orientation. In the case of layered antiferromagnetics, a distinction is made between A-, C-, and G-types, which differ in their combination of spin orientations (Figure 1.4). In A-types, the single layer is ordered ferromagnetically and the next layer has opposite spins; in C-types, the single layer is antiferromagnetic, but the next layer is ferromagnetic to the first layer; and in G-types, all spins are antiferromagnetic to each other. This means, that the neighbor spins are antiparallel, however, the next neighbor spins are parallel [52,53].

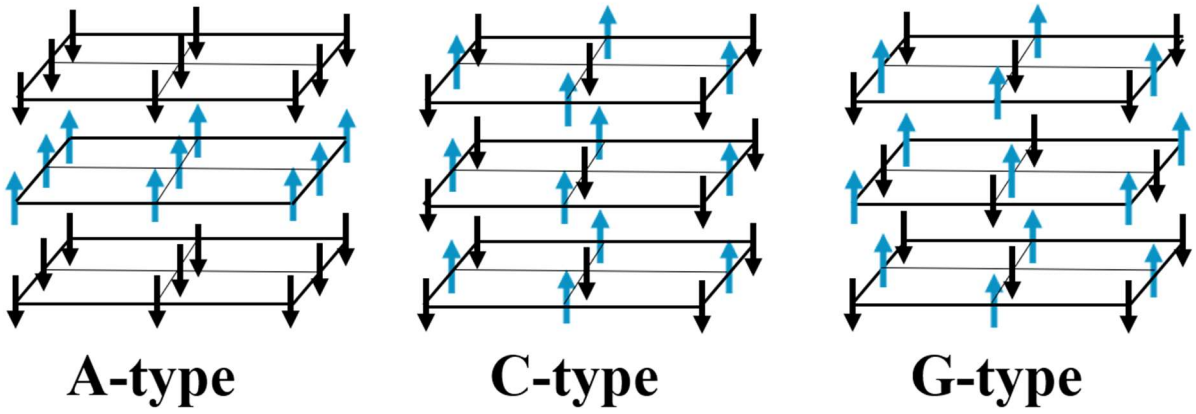


*Figure 1.4 Different antiferromagnetic types depending on their spin orientations.*

## 1.4. Lead iron niobate

### 1.4.1. PFN bulk and ceramics

Lead iron niobate, $Pb(Fe_{1/2}Nb_{1/2})O_3$ (PFN), was discovered by the group of Smolenskii et al. [54] in 1958 and declared as a ferroelectric. In 1962 Bokov et al. [55] proved that PFN has antiferromagnetic behaviour as well, so PFN can be classified as a multiferroic, in particular as a type-I multiferroic after Khomskii [50]. PFN is a lead-based perovskite with the general formula $A(B'_xB''_{1-x})O_3$, where $Pb^{2+}$ is on the A-site while $Nb^{5+}$ and $Fe^{3+}$ are sharing the B-site position equally, but randomly ordered. The $Pb^{2+}$ cations have a lone electron pair and drive an off-centering displacement. Due to the cooperative displacement of lead and niobium a spontaneous polarization occurs which leads to a ferroelectric to paraelectric phase transition with the Curie temperature $T_C$ in the range of 370-390 K [55–59]. It shows a broad dielectric maximum and, different from relaxor ferroelectrics, no shift with frequency of the *ac* electric field [32,33,56,60]. Since the dielectric constant is high, PFN can be used for many electrical devices like e. g. resonators, multilayer capacitors, micropositioner applications, and inductors [58,61–63]. Due to the magnetic ordering of the iron on the B-site, which stems from

the superexchange interaction through the $Fe^{3+}$-$O^{2-}$-$Fe^{3+}$ [64,65] and $Fe^{3+}$-$Pb^{2+}$-$Fe^{3+}$ paths [66,67], PFN shows an antiferromagnetic to paramagnetic phase transition at a Néel temperature of $T_N$ = 143 K [55]. In particular it orders as G-type where all spins are antiparallel to each other [57,68]. At a much lower temperature of 10 K a spin glass transition occurs [69–71]. A spin glass in general is a magnetic state that is disordered with respect to its spin structure and the position of the spins, with a disordered geometric frustration. This is a quantifiable measure of the inability of the system to reach a simple spin state of lowest energy [72]. In PFN the spin states result from the coexistence of two magnetic phases. The first is due to a large number of finite-sized $Fe^{3+}$-clusters which make up a spin cluster glass. The second is a phase of exchange coupled $Fe^{3+}$ ions following the percolation theory. While the phase transition at $T_N$ is allowed on the latter magnetic phase, the non percolating clusters undergo super antiferromagnetic blocking beneath 10 K [73]. It also shows a non-linear magnetoelectric (electrobimagnetic) effect. It is maximal around 20 K and significantly decreases around the Neel temperature [70], up to the Curie temperature [74] it is still observed, but the effect is rather small which makes it less attractive for applications.

Nowadays, PFN is a well-known material and has been intensively studied in all forms as single crystals, ceramics, and layers [56,75]. There is not the one ideal way to synthesize PFN as many methods can be used [76]. The most common and reliable method is the solid state method which is mostly preferred [56,58,60,77–80]. However, other methods e. g. mechanochemical activation [81,82], the columbite route [57,83,84] or the sol-gel route [85,86] are also often represented. Nevertheless, the synthesis conditions differ not only in the different methods but also in one method itself depending on many factors like e. g. precursors and homogenization. However, the highest impact on the results has the calcination/sintering temperature and time. The main problem in synthesizing a pure PFN phase is the competition between the pyrochlore ($A_2B_2O_7$) and the perovskite phases. The pyrochlore phase has a cubic structure and a lower density than the perovskite phase, and it inhibits the ferroelectric properties [87]. The formation of pyrochlore is favoured at low calcination and sintering temperatures, but it can also be the dominant phase with short calcination and sintering times. PFN forms only at higher temperatures or can be favoured with a longer sintering time. This makes the synthesis even more difficult, since lead is volatile, especially at temperatures above 700 °C. With increasing the calcination/sintering temperature and time, the possibility of lead evaporation will increase and the stoichiometry is no longer given. This reduces the ferroelectric effect and reduces the dielectric constant as shown by Raevski et al. [88]. Another disadvantage that comes with the

lead loss is the compensation of the charge difference by forming oxygen vacancies which make the sample conductive. To avoid these difficulties and to obtain dense, electrically loss free ceramics with good ferroelectric parameters such as high permittivity and polarization higher calcination/sintering temperatures are necessary. The lead loss can be compensated by adding more lead in the precursor powders. Not only do the above-mentioned parameters need to be considered, but also the atmosphere in which the PFN is sintered. By using an oxygen atmosphere the reduction of iron from $Fe^{3+}$ to $Fe^{2+}$ can be avoided, which negatively affects the ferroelectricity in PFN as well [79].

### 1.4.2. PFN thin films

PFN thin films have already been prepared by spin coating [63,89,90], dip coating [91], and RF sputtering [92] but the most investigated method is the layer deposition via pulsed laser deposition (PLD) [56,93–101]. The first experiments synthesizing a PFN layer were done by Quek and Yan [63] in 1987. They successfully spin-coated a PFN film on a Si substrate with the maximum relative dielectric constant of 81 at room temperature. Liu et al. [89] enhanced the dielectric properties of a film spin-coated on a STO (001) substrate to a value of more than 315 for different frequencies at room temperature.

The properties of PFN deposited via PLD strongly depend on the substrate which is used. First attempts were made on Si (001) by Gao et al. [56]. They achieved a pure perovskite phase with an average grain size of 80 nm. The remanent polarization $P_r$ (7.4 µC/cm²) was half of the bulk material, but the coercive field $E_C$ (10.5 kV/cm) was larger. This was rationalized by the loss of PbO and size effects. Also, the dielectric constant $\varepsilon$ (458, 10 Hz) and loss factor $\tan\theta$ (0.21, 10 Hz) were found smaller than in the bulk. Although the Curie temperature could not be identified, the sample showed a broad maximum in the curve of the dissipation factor at 360 K. Later Yan et al. [93–95,102] investigated the properties of PFN on $SrTiO_3$ (001), (110), and (111) substrates. The deposited phase structure changed with the different substrate orientations from tetragonal, to orthorhombic and rhombohedral, respectively, due to different lattice mismatch stresses. Through the change in the slope of the lattice constants, they found the Curie temperature to be around 400 K. They could enhance $P_r$ to 18 µC/cm² and $E_C$ to 16 kV/mm for the film on the STO (001) substrate. For the other orientations, $P_r$ had a lower value, but $E_C$ stayed the same. The $\varepsilon$ (1000, 300 K) was also increased and the $\tan\theta$ (0.1 - 0.3, 300 K) decreased in comparison to Gao et al. [56]. Their work showed that the use of STO (001) gives films with the tetragonal structure and the best ferroelectric properties.

Peng et al. [97] found $T_N$ at 200 K which is much higher than for bulk (145 K). They excluded strain effects and explained the high value of the Néel temperature with an increase in high-spin $Fe^{3+}$ cation content leading to a possible nonstoichiometry in the Nb-Fe ratio, which could occur during film growth. Beneath $T_N$ the layer showed an antiferromagnetic behaviour with a weak ferromagnetism since the remanent magnetization $M_r$ was nonzero. When depositing PFN on MgO (001) [96], the lattice mismatch is higher than for STO (001) resulting in a rhombohedral structure. $T_C$ between 337 and 380 K for different frequencies and $T_N$ at around 170 K was found to be. Magnetoelectric coupling was identified due to an anomaly in the dielectric constant in the vicinity of $T_N$. The magnetic measurements show a weak ferromagnetic behaviour at room temperature and a spin glas like behaviour below $T_N$. Mostly these studies are about structural, ferroelectrical and magnetic properties. Only a few publications involve other measurements like Raman [99,101]. The comparison of the Raman spectra from thin films on STO(001) to ceramics [101] revealed a shift of 20 $cm^{-1}$ to higher frequencies for the 250 $cm^{-1}$ and 700 $cm^{-1}$ bands corresponding to the Fe-O bonds vibrational modes. These bonds get strengthened in the nanoscale regions, because the Fe ions settle into chemical clusters, this will cause a disorder resulting in an increase of $T_N$ and is in agreement with [56,96,97]. The temperature dependence of the Raman spectra [99] of PFN on MgO (001) showes changes in the phonon positions, the intensities, the linewidths, and the kink in the Raman shift of the $A_{1g}$ doublet at around 650 K.

## 1.5. Photovoltaic effect in ferroelectrics

### 1.5.1. Band gap structure

An important criterion for checking whether a material is suitable as an absorber layer for a solar cell is its band gap $E_G$. The band gap is the energy difference between the conduction band minimun $E_{CB}$ (first unoccupied state) and the valence band maximum $E_{VB}$ (last occupied state).

$$E_G = E_{CB} - E_{VB} \qquad \text{Eq. 1.5}$$

A distinction is made between direct and indirect band gaps. In the case of a direct band gap, the valence band maximum and the conduction band minimum are located at the same value of the electron momentum $\vec{k}$. If the material with a direct band gap is irradiated with a photon $hv$ of energy higher than $E_G$, an electron can be transferred from the valence band to the conduction band and an electron-hole pair is generated (Figure 1.5 a). In the case of an indirect band gap,

however, the valence band maximum and the conduction band minimum are not at the same $k$ value. To lift an electron into the conduction band needs either a higher photon energy or an intermediate state must be generated. This intermediate state can be generated by the motion in the lattice. If the phonon energy is large enough, a photon with the energy of the band gap can lift an electron into the conduction band by overcoming the momentum difference $\Delta\vec{k}$.

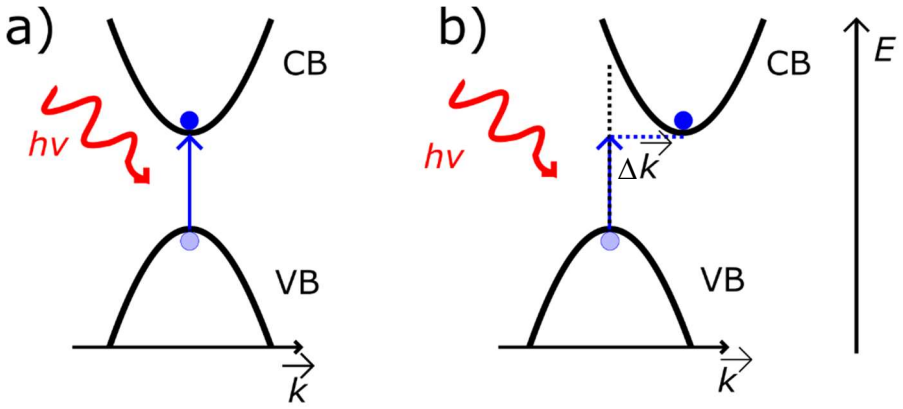


*Figure 1.5 Energy vs. electron momentum for a direct (a) and an indirect (b) band gap.*

At low temperatures there are less phonons and the possibility that a photon and a phonon are absorbed at the same time to produce a direct transition is smaller for the indirect band gap. Due to this fact, the absorption spectrum of an indirect band gap is more dependent on temperature than that of a direct band gap.

#### 1.5.1.1. Band gap determination through Tauc plots

The easiest way to estimate the band gap is a spectrum obtained from a UV-Vis measurement, converted into a Tauc plot. With fitting straight lines to these plots one can obtain the material band gap as explained by Makuła et al. [103] either from absorption or diffuse reflection data. For the absorption measurement the following correlation is used:

$$(\alpha \cdot h\nu)^{\frac{1}{\kappa}} = B\,(h\nu - E_G) \qquad \text{Eq. 1.6}$$

where $E_G$ is the band gap, $\alpha$ is the absorption coefficient, $h$ is the Planck constant, $\nu$ the photon frequency, and $B$ is a constant. Depending on the band gap nature, the parameter $\kappa$ takes the value ½ for the direct band gap or 2 for the indirect band gap. Plotted and fitted Tauc plots for both cases are represented in Figure 1.6 b and c estimating two possible band gaps. If diffuse reflectance spectra are measured, the absorption coefficient is replaced by the Kubelka-Munk function:

$$F(R_\infty) = \frac{K}{S} = \frac{(1-R_\infty)^2}{2R_\infty} \qquad \text{Eq. 1.7}$$

With $$R_\infty = \frac{R_{Sample}}{R_{Standard}} \qquad \text{Eq. 1.8}$$

$K$ and $S$ are absorption and scattering coefficients, respectively, and $R_\infty$ is the reflectance of an infinitely thick specimen. Equation Eq. 1.6 takes the form

$$(F(R_\infty) \cdot h\nu)^{\frac{1}{\kappa}} = B\,(h\nu - E_G). \qquad \text{Eq. 1.9}$$

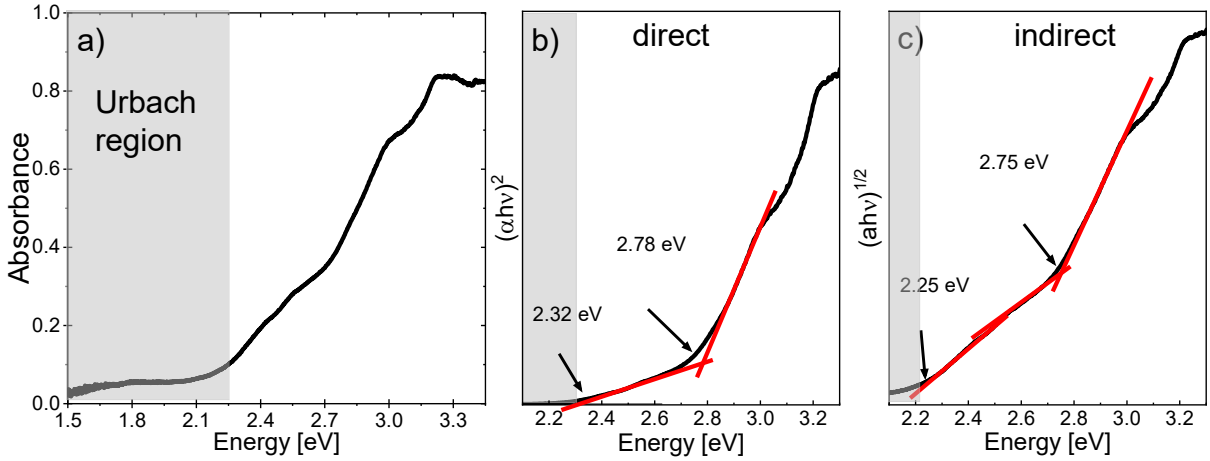


*Figure 1.6 Absorbance spectra for the PFN layer from UV-Vis absorption measurements (a). Tauc plots for direct (b) and indirect (c) band gaps. The gray box represents the Urbach region.*

#### 1.5.1.2. Urbach tail

A closer look at the absorption spectrum in Figure 1.6 a) reveals a weak absorption at lower photon energies in the grey marked part of the spectrum. This absorption is caused by defects and impurities and is known as the Urbach region named the Urbach tail [104] after F. Urbach [105], who found out that the fundamental absorption decays exponentially with the decrease of photon energy. A relation between the photon energy $h\nu$ and the absorption coefficient $\alpha$ in this range is given by the empirical Urbach rule [104,106,107]:

$$\alpha = \alpha_0\, e^{\frac{h\nu}{E_U}} \qquad \text{Eq. 1.10}$$

$\alpha_0$ is a constant and $E_U$ is the width of localized tail states in the band gap or the Urbach energy, respectively. A small $E_U$ indicates a high structural quality of the measured material [107] and can be calculated from a straight line fit of $ln(\alpha)$ versus $hv$ with the inverse of the slope as in Figure 1.7 [104,106]. As the absorbance is temperature dependent, also the Urbach tail and therefore the Urbach energy are shifting with temperature as well [107–109].

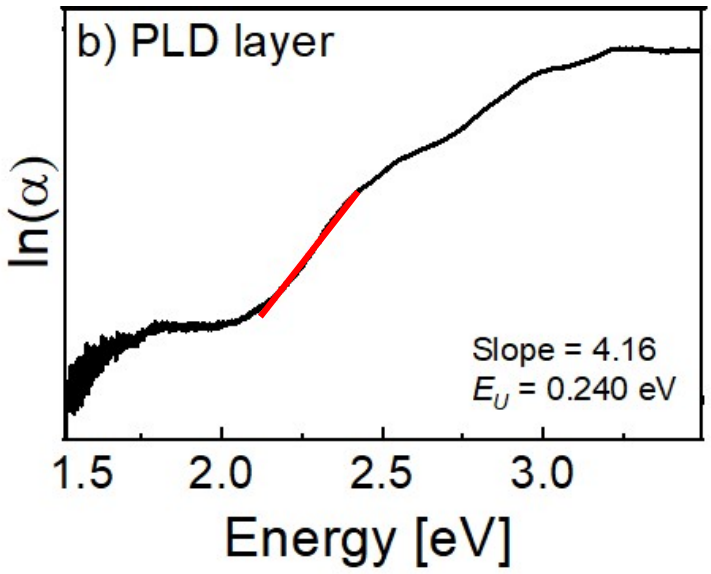


*Figure 1.7 Linear fit for ln(α) versus energy to calculate the Urbach energy $E_U$.*

### 1.5.2. The photovoltaic effect in semiconductors

The photovoltaic effect was discovered by the French physicist Edmond Alexandre Becquerel in 1839 [110]. The effect describes the direct conversion of sunlight into electric current through the interaction of photons with an absorber material. If the energy of a photon is higher than the band gap of the material, it will be absorbed and excites an electron from the valence band to the conduction band as explained in 1.5.1 creating an electron-hole pair. If there is a sufficiently strong electric field, such as exists e. g. in a p-n junction of a semiconductor, the electrons and holes drift in opposite directions, the electrons migrate to the n-layer and the holes to the p- layer. The charge shift creates photocurrent when the two layers are connected via an external circuit, producing electrical energy from light. Devices based on doped silicon (Si) involving a p-n junction are currently the market leader due to their high efficiency and long life stability. Nethertheless, the production of Si photovoltaic devices is expensive. For this, researchers are investigating other materials like hybrid halide perovskites, which show a good efficiency as well and are cheap in production. However, their lifetime is limited due do degredation through UV-light, temperature, and humidity [111–113]. These materials are limited by the Shockley-Queisser-limit which allows for a maximal efficiency of the material in dependency

of their band gap [114]. For this reason, ferroelectrics have gained a high interest since it is known, that the open-circuit voltage in these materials is not limited by their band gap and voltages several times higher can be achieved [11,115–117]. However, the disadvantage of a low photocurrent in bulk materials still exists due to the scattering of photoinduced charge carriers on defect sites.

### 1.5.3. Different working mechanisms in ferroelectrics

There are different theories on how the working mechanisms of a ferroelectric and a ferroelectric photovoltaic device can be explained. These will be described in the following:

#### 1.5.3.1. Bulk photovoltaic effect

The bulk photovoltaic effect (BVE) has been known since 1956, when Chynoweth [118] investigated the surface space-charge layers in barium titanate. The BVE can only be seen in non-centrosymmetric crystals and depends on the ferroelectric polarization [119,120]. Three models are proposed for the generation of charge carriers for the bulk photovoltaic effect [120–122]: (a) the asymmetric carrier scattering center (Figure 1.8 a), (b) the divided conduction bands in the reciprocal space, relativistic spin-orbit coupling (Figure 1.8 b), and (c) the asymmetric potential well at the center of the carrier generation (Figure 1.8 c).

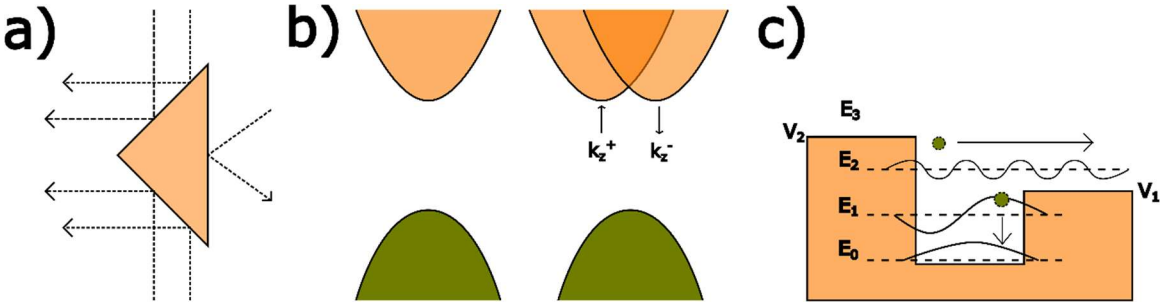


*Figure 1.8 Different models for the bulk photovoltaic effect: a) the asymmetric carrier scattering center. b) the divided conduction bands in the reciprocal space relativistic spin-orbit coupling and c) the asymmetric potential well at the center of the charge carrier generation [123].*

(a) The material exists of asymmetric scattering centers which are randomly distributed. In absence of an external field these centers scatter charge carriers in any direction leading to random diffusion and drift of these carriers. When the scattering centers are now aligned with one orientation the diffusion and drift can eventually set up to a net current. Nevertheless, the current is local and due to the entropy increase limitation it cannot be persistent (Figure 1.8 a) [120–123].

(b) The second model considers spin-orbit coupling in ferroelectrics. When it is weak the electrons will be equally excited when enough photons are absorbed. However, when the spin-orbit coupling is strong, e. g. under Dresselhaus or Rashba spin-orbit coupling [124], the conduction bands divide, and the spin affects the momentum of the photo-induced carriers. This means that the net current will change with differently polarized light (Figure 1.8 b) [120,123].

(c) The last model deals with the asymmetric electrostatic potential in the material which is most likely formed due to the electrical polarization. Photons excite the electrons from $E_0$ to either $E_1$, $E_2$ or $E_3$. The carriers from $E_1$ will be trapped in the potential well and the carriers at $E_3$ can leave in any direction so that the net current becomes zero. However, if the carriers are excited to $E_2$, they can leave the potential well all in the same direction and contribute to the net current (Figure 1.8 c) [120,122,123].

#### 1.5.3.2. Domain wall theory

Yang et al. [125] measured the photocurrent of $BiFeO_3$. Their material consisted of parallel oriented ferroelectric domains as seen schematically in Figure 1.9. They placed two different sets of electrodes on the material: one parallel (Figure 1.9 a) and one perpendicular (Figure 1.9 b) to the net polarization $P_{net}$. They found out that the set-up a) generated more photocurrent than the set-up b). Due to the component of the polarization perpendicular to the walls and the resulting electric field the domain walls develop built-in potential steps. When the sample is now illuminated, a net voltage can be measured across the entire sample due to the higher charge carrier generation and the better separation at the domain walls. The photovoltage of a device is affected by the amount of domain walls, on the orientation of the electrodes, as well as on the electric polarization intensity and the thickness of the sample [123].

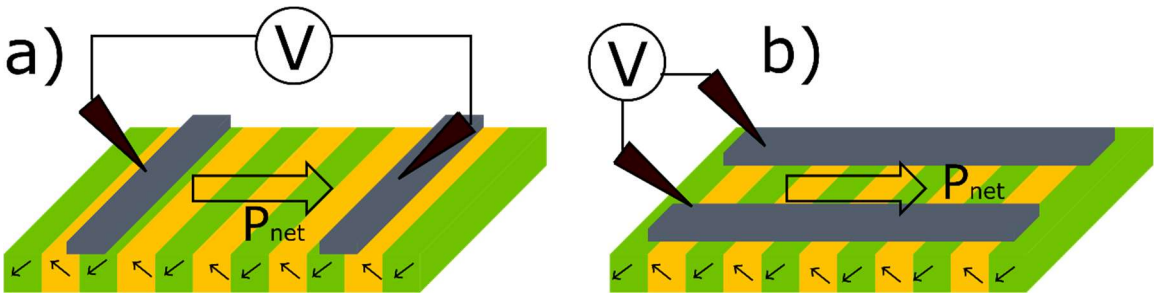


*Figure 1.9 Schematic structure of the net polarization ($P_{net}$) a) perpendicular and b) parallel to the electrodes. The small arrows indicate the different components of the polarization and the large arrow the net polarization direction [125].*

#### 1.5.3.3. Schottky Junction Theory

If a complete device is built, the contact between the ferroelectric and the electrode is also important for the yield. Depending on the material, a Schottky barrier can be formed and band bending happens. The built-in electric field can help separating the electron-hole pairs. The intensity of the photocurrent therefore depends on the height of the barrier and the depletion layer. Nevertheless, the Schottky junction photovoltaic current is restricted to the materials band gap. However, a photovoltaic enhancement can be seen at a vertical device structure due to their mostly different top and bottom electrodes, and therefore different Schottky barrier junctions. The photovoltage and current generated by both junctions do not cancel each other resulting in a net current [123].

#### 1.5.3.4. Depolarization field effect

When a ferroelectric thin film device is polarized, high density polarization charges are located at the surface of the ferroelectric material. They create a depolarization field directed against polarization. When the material is in contact with a metal, the free charge carriers can screen the depolarization field, but typically the screening is not complete. Under certain circumstances, when the depolarization field is high enough, charge carriers can be separated and contribute to the photovoltaic effect. Since the depolarization field depends on the spontaneous polarization and dielectric constant of the material, as well as on the thickness and the electrodes, the photovoltaic effect can be influenced: when the depolarization field is high, the photovoltaic effect is increased. As most systems are well screened, this contribution is typically small [123].

### 1.5.4. Thin films

Since the photocurrent in a bulk material is rather small, researchers have investigated the effect of the thickness of the material and concluded that the photovoltaic efficiency can be increased with decreasing layer thickness [11,115,126]. Many studies have been carried out on lead based ferroelectric materials, which are the focus of this Chapter due to the similarity to PFN. These materials are e. g., $PbTiO_3$ (PTO) [9] $Pb(Zr,Ti)O_3$ (PZT) [10,17,18,127,128], and $(Pb,La)(Zr,TiO)_3$ (PLZT) [11,115]. Although the BPE exists in these materials, the photovoltaic efficiency strongly depends on the band gap due to the absorbance of the photons. The above mentioned materials have band gaps of approximately 3.6 eV for PTO [14–16], and PZT [17–19], and a band gap larger than 3.35 eV for PLZT [20,21]. The photon absorption in these

materials is thus limited to the ultraviolet spectrum and only around 8 % of the solar spectrum can be used efficiently [14]. For this reason, these materials themselves have only reached a photovoltaic efficiency of 0.05% for PTO [9], 0.75% for PZT [10,129], and ~0.28% for PLZT [11]. However, their high absorption in the ultraviolet spectral range, makes them a possible candidate in tandem solar cells.

The well-known multiferroic $BiFeO_3$ (BFO) needs to be mentioned here as well, since recently it has gained significant attention due to its smaller band gap of 2.2–2.7 eV [130–132]. However, the efficiency is still < 1 % [133].

## 1.6. Motivation and Scope of This Work

To combat climate change and drive progress for renewable energy, more and more materials are being tested for suitability as absorber layers for solar cells. Ferroelectric materials have already been considered here, as they are not limited by the Schottky-Quiesser limit and the open circuit voltage can become significantly higher than the band gap.

Lead-containing known ferroelectrics have also been investigated so far, however, no one has considered PFN yet. One reason for this could be that the material has been known since the 1950s and science has mainly focused on its multiferroic properties. As a result, no one has really thought about the optical properties of this material, let alone researched in this direction. For this reason, the potential of this material has not been recognised yet.

There are several ways to produce layers of this material. The most common is the pulsed laser deposition. However, since PFN is not a conventional material for a ceramic target, the targets have to be produced by the scientists.

Ceramic PFN has already been investigated by many scientists and the material is generally understood. Nevertheless, the properties vary enormously depending on the manufacturing methods and parameters [33,78,79,134]. This study deals with the fabrication of a suitable target in detail. Studies are conducted to obtain the best possible properties based on different sintering athmospheres, synthesis methods and calcination and sintering temperatures. It becomes clear that all these parameters have a great influence on the material. The best possible manufacturing variant is thus filtered out and the target is manufactured on the basis of this. After all, the quality of the target determines the quality of the layers. The layer production is also characterised by various parameters, so that these must first be determined.

The optical properties of the material are then examined to determine whether this material is suitable for absorber coatings. In particular, the band gap, which determines the absorption of photons, is measured. The width of the band gap is determined by various methods. The question arises whether this material has a direct or indirect band gap and various hypotheses are discussed that lead to an answer.

A brief introduction into ferroelectrics is given in **Chapter 1** dealing with the basics of ferroelectricity, informing about the state of the art in the PFN ceramics and thin films literature and discussing the photovoltaic effect in ferroelectrics and the different working mechanisms. The analytical techniques and experimental details of this work are then described in **Chapter 2.** The main part of this thesis opens with **Chapter 3** investigating the PFN ceramics and their properties by changing the synthesis conditions. Starting with the difference in the sintering atmosphere improving the properties from sintering in air to oxygen, followed by different synthesis methods and dealing with the challenge of lead volatility. In conclusion to the previous work the solid-state method was selected to investigate the influence of the calcination and sintering temperatures. In **Chapter 4** PFN thin films deposited by pulsed laser deposition and spin coating are tested with respect to their structure and optical properties especially with a focus on the band gap.

# 2. Analytical Techniques

This Chapter describes the principles and the parameters of the used techniques.

## 2.1. Diffraction techniques

### 2.1.1. X-ray diffractometry (XRD)

X-ray diffractometry (XRD) is one of the most commonly and widely used methods for studying the phase structure and purity in crystalline materials. This Chapter explains the XRD principle and the various measurement methods.

#### 2.1.1.1. Principle

The wavelength $\lambda$ of X-rays has the same order of magnitude as the atomic distances in the lattice. When a sample is irradiated with X-rays, they will be scattered on the atoms, which leads to interference. When specific diffraction angles are matched, the interference becomes constructive as seen in Figure 2.1 and a pattern will be detected. With the help of Bragg´s equation (Eq. 2.1) and the diffraction angles, at which constructive interference occurs, the lattice plane distance $d$ can be calculated.

$$n\lambda = 2d\ sin\theta \qquad \text{Eq. 2.1}$$

The formula can be derived geometrically from Figure 2.1. Here, $\theta$ is the incident angle and $\lambda$ is the wavelength of the incident X-rays. Constructive interference can only occur when the optical way difference for the interfering rays is a multiple of $\lambda$, i.e., $n$ takes integer values ($n$ = 1, 2, 3, etc.) to fulfill Bragg´s equation. This is valid for any lattice structure. The Bragg equation determines the position of the peaks. However, the intensity of the diffraction peaks depend on the scattering factors of the different atoms.

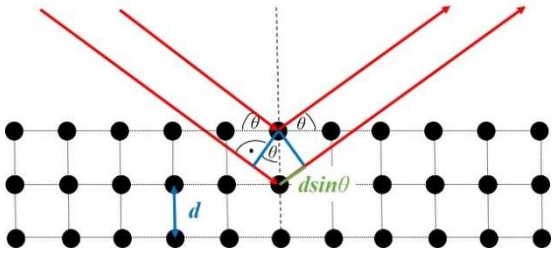


*Figure 2.1 Schematic of the geometric derivation of Bragg´s equation.*

### 2.1.1.2. Instrument

A schematic setup (left) and the real instrument (Empyrean, PANalytical) (right) can be seen in Figure 2.2. It consists of an X-ray source (1) from which the incident X-rays are coming, a detector (3) that captures the diffracted X-rays and a sample table (2). The sample table can be tilted in the angle $\psi$ or rotated with the azimuth angle $\varphi$. For an optimal alignment of the sample, the angle $\theta$ of the table can also be adjusted. These angles play a special role, especially with layer samples, which will be discussed in more detail later.

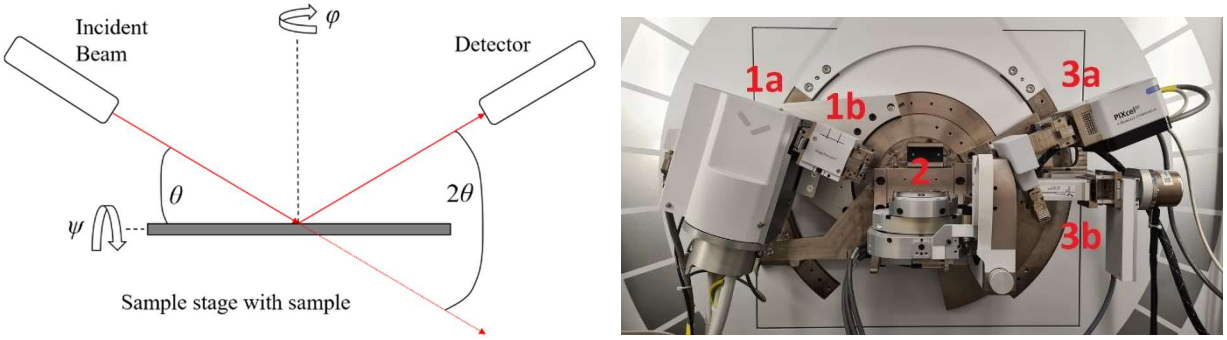


*Figure 2.2 The schematic setup of an X-ray diffractometer with individual components and different setting angles (left). The diffractometer used in this work (right). 1: Incident beam optics with the CuKα$_1$ source (1a) and the Bragg-Brentano optics (1b). 2: The sample stage (Euler cradle). 3: the detectors PIXcel$^{3D}$ (3a) and collimator (3b).*

### 2.1.1.3. Different measurement methods

Aside of the basic principle presented in 2.1.1.1 the characterization of the samples investigated in this work requires advanced measurement methods presented here. Information that follows in this Chapter was mainly taken from the textbook by Mario Birkholz [135].

**Powder diffractometry *θ/2θ***

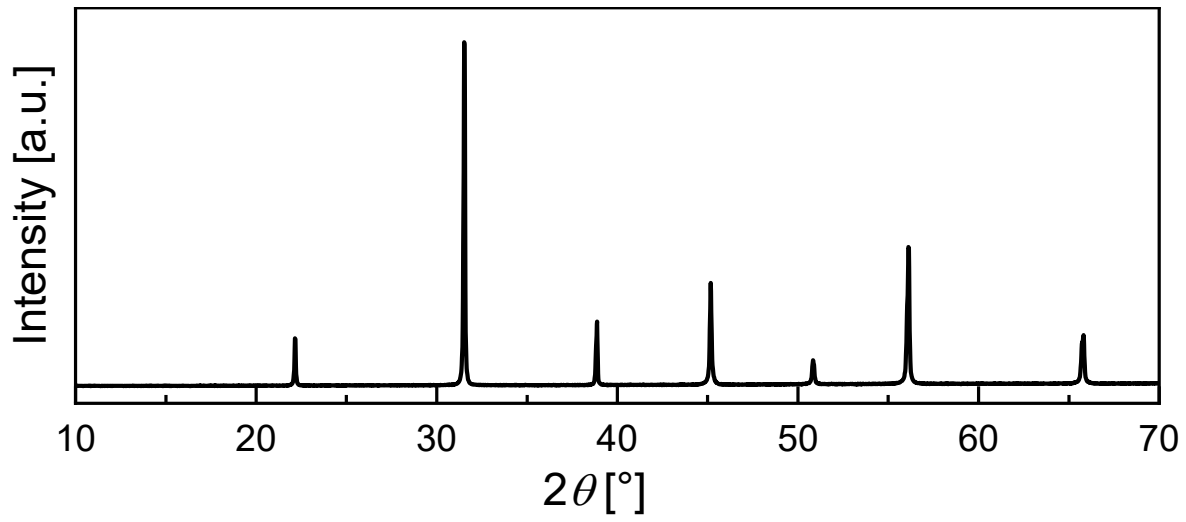


*Figure 2.3 Powder diffractometry pattern of a polycrystalline material.*

This method is mostly used for polycrystalline powders. Thick layers can also be examined with it. During the scan, the angle is always considered with respect to the surface plane of the sample. The incident beam is directed onto the sample by the parafocusing Bragg-Brentano optics, which gives the best combination of peak intensity, shape and angular resolution, and covers the complete range of incidence angle $\theta$. The detector moves symmetrically to the source and the outcoming beam can be considered as a prolongation of the incident beam, that is why this geometry is also called $\theta$-$2\theta$. The pattern that follows from this measurement is represented by the intensity of X-rays diffracted to the detector as a function of the angle $2\theta$ as shown in Figure 2.3.

**Grazing incidence X-ray diffractometry (GIXRD)**

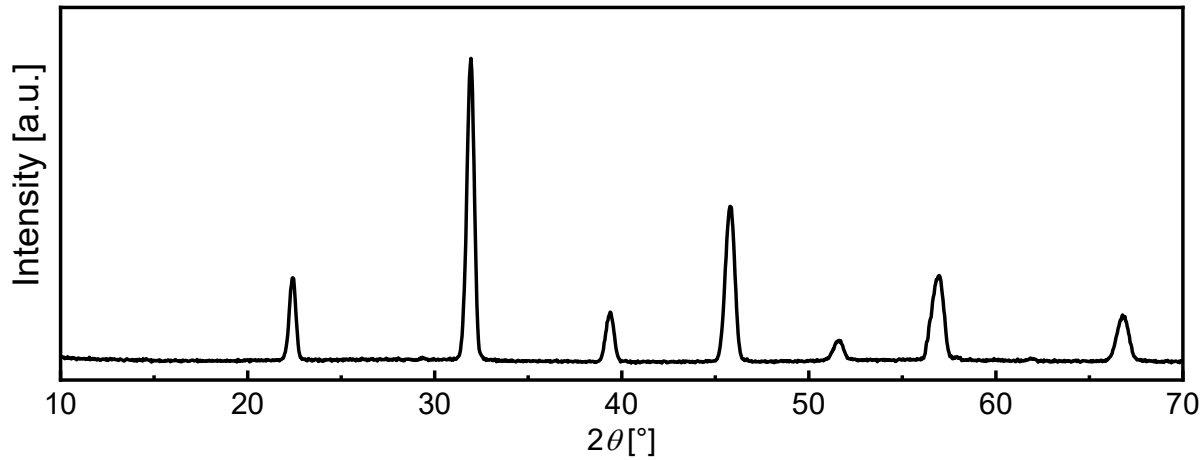


*Figure 2.4 GIXRD pattern of a polycrystalline thin film material.*

In thin films where the layer is thinner than the penetration depth (10 - 100 μm) of the X-rays, not only the diffraction peaks of the layer, but also the XRD peaks corresponding to the substrate will be detected in a $\theta$-$2\theta$ measurement. The intensity of the substrate peaks can be so high that the layer peaks are superimposed or have a low intensity compared to the substrate that they can no longer be perceived.

For this reason, grazing incidence X-ray diffractometry (GIXRD) can be used, in which the incidence angle is kept very small so that the path of the X-rays in the sample layer is significantly elongated. To get a grazing incidence, the parafocusing geometry of the Bragg Brentano optics is no longer sufficient because the divergence of the beam is too high, and a special parallel beam mirror optics must be installed that especially shapes the beam for this application.

The incident angle $\alpha$ is kept constant throughout the whole measurement, while the detector is moving along $2\theta$, which is the angle between the outgoing beam and the incoming beam. It needs to be considered, that the lower limit of the incident angle $\alpha$ is the critical angle $\alpha_c$, below which total reflection occurs. The resulting pattern is, again, intensity vs. $2\theta$ (Figure 2.4), it does practically not differ from the powder diffraction pattern (see Figure 2.3)

**Reflectometry (XRR)**

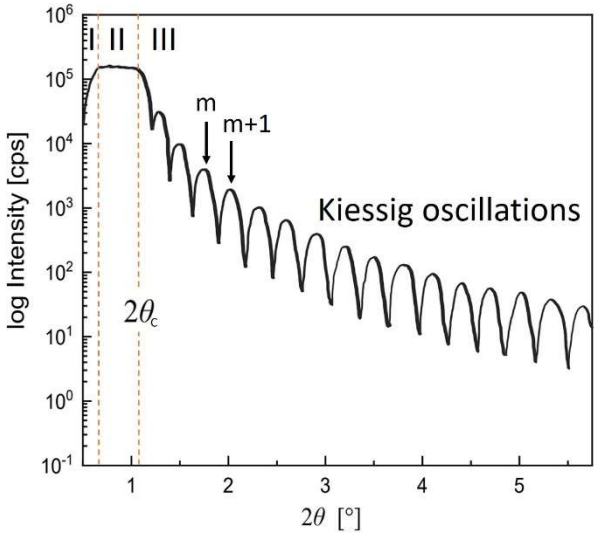


*Figure 2.5 A schematic XRR spectrum with Kiessig oscillations [135].*

Using X-ray reflectometry (XRR), the layer thickness $d$ of a sample can be determined. The diffraction of the X-ray beams is not important here, but the reflection and refraction, as in optical ellipsometry. The device is operated in $\theta$-$2\theta$ mode, though the incident angle is significantly smaller here, so that the parallel beam optics must be used. In this way, conclusions can be made not only about the thickness of the sample, but also about the quality of the surface and its roughness. The XRR spectrum is represented by a logarithmic intensity depending on $\theta$ or $2\theta$, as displayed in Figure 2.5. First, the intensity increases (I), after reaching a plateau (II) it gradually decreases again (III). Region II is caused by total reflection from the primary beam and is the border to region III. Region III manifests the so-called Kiessig oscillations, from which, using the distance between the maxima, one can infer the thickness of the layer using the following equation:

$$\theta^2 - \theta_c^2 = m^2\left(\frac{\lambda}{2d}\right)^2 \qquad \text{Eq. 2.2}$$

where $\theta$ is the position of the satellite maximum, $\theta_c$ is the critical angle of reflectivity, $m$ is the order of reflection, and $\lambda$ is the X-ray wavelength. The layer thickness $d$ can be extracted from the slope of the linear fit in the plot of the maxima $\theta^2$ versus the reflection order $m^2$.

**Pole figures**

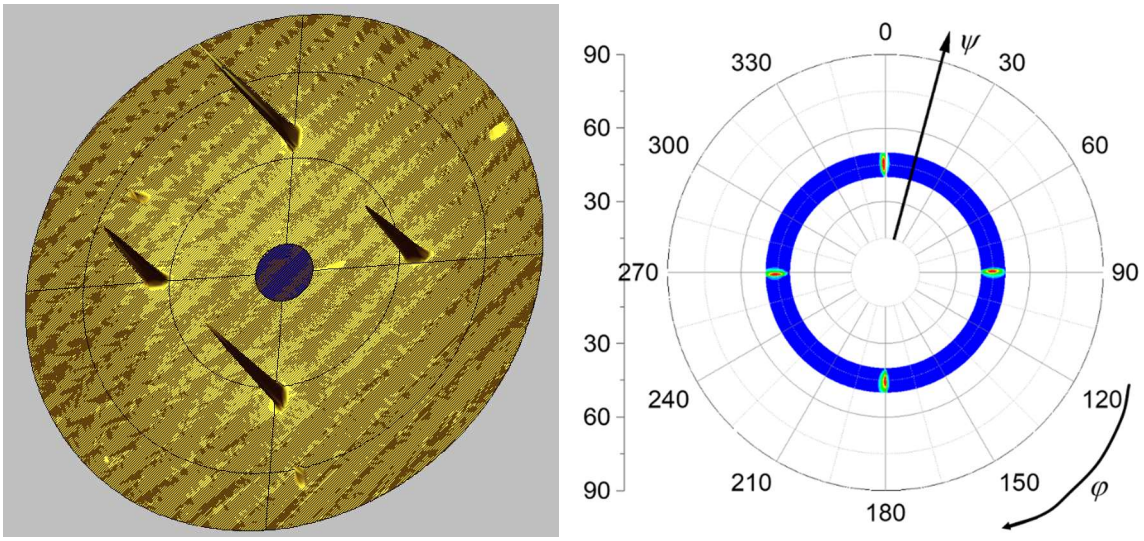


*Figure 2.6 left: 3D image of a pole figure. Right: the 2D representation of the (φ, ψ) plane with a constant Δψ projection and epitaxial growth.*

Pole figures are a helpful tool to estimate the orientation of a film in the plane. Typically, a preferred orientation exists in thin films, so when measuring the film, only those lattice planes are detected that are oriented parallel to the film surface. Nevertheless, the film may be highly oriented out-of-plane, but not have a preferred in-plane orientation, and the grains may be randomly rotated. To check the in-plane texture, the sample is tilted so that the planes inclined to the surface can be measured. The pole figures represent XRD intensity as a function of the tilt angle, $\psi$, and the azimuthal angle, $\varphi$. If a layer has grown epitaxially, peaks are recognized in the pole figures, unlike in the non-epitaxial case, where a ring appears. Figure 2.6 shows the representation of a pole figure of an epitaxial film in a 3D image (left) and in a constant $\Delta\psi$ projection (right).

If there is a strong orientation and the diffraction pattern only has a few free-standing reflections, the rocking curve technique can yield further statements about the crystallinity. The detector is fixed on a certain peak, and the sample is then tilted at an angle $\theta$ ("rocked"). In this case, the incident beam angle $\theta$ is decoupled from the detector angle $2\theta$ and is therefore usually referred to as $\omega$. The more crystalline the sample, the narrower the peak. The full width at half maximum (FWHM) is used for the evaluation. With this method, a partial statement about

crystallinity can be made, yet for a really precise determination a single crystal reference sample of the material with the same thickness needs to be compared.

#### 2.1.1.4. Instrument settings

All diffraction patterns excluding the XRR measurements were recorded using an Empyrean diffractometer (PANalytical) with a CuK$\alpha_1$ source. For $\theta$-$2\theta$-measurements the Bragg-Brentano optics and a PIXcel$^{3D}$ detector were used. The measurements were performed with a step size of 0.013 ° in the $2\theta$-range of 10-90° (except the results described in Chapter 3.2, where the $2\theta$-range was 10 – 70 °). The scanning time was 100 s per step. When measuring films grown on a single crystal substrate, the peak intensity of the substrate was so high, that the $\beta$-peaks were also displayed, as shown in Figure 2.7. To prevent this, a Ni-$\beta$-filter was used.

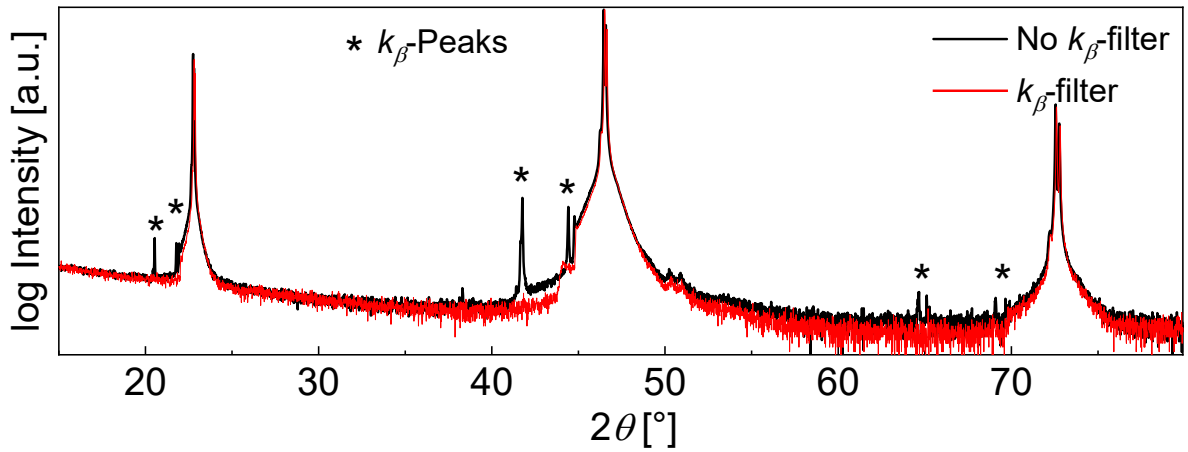


*Figure 2.7 XRD pattern of the STO substrate with (red) and without (black) $k_\beta$-filter. The stars mark the $k_\beta$ -peaks.*

GIXRD were performed with parallel beam mirror optics and a collimator as a detector. The scanning range was 10 - 90° with a step size of 0.4° and a scanning time of 30 s. The incident angle was 3° for "thick" films (layer thickness more than 1 µm) and varied from 0.25 – 1° for thinner films.

The pole figures were operated using Bragg-Brentano optics and PIXcel$^{3D}$ as the detector. The measurements were taken at different incident angles of 22.15 °, 31.5 °, 38.8 °, 45.18 °, 56.7 °, 65.82 °, 70.37 ° and 74.81°. These correspond to the XRD peak positions for polycrystalline PFN and not all these measurements will be shown in this thesis. The tilting angles were scanned from 1° to 90 ° (a step size of 1°), while the azimuthal angle $\varphi$ was rotated from 0 to 360° in steps of 1° and a time of 1 s per step.

For phase analysis the HighScore Plus software (PANalytical) was used. Different patterns from the inorganic crystal structure database (ICSD) were used for fitting depending on the sample measured. The most important properties can be found in the appendix 6.3. Refinement was initially started with the automated process that fits the scaling factor, the background, and the sample height. It also fits the lattice constants as well as the Cagliotti parameter *W*. In order to obtain a better refinement, the Cagliotti parameters *U* and *V*, and the peak shape were also adjusted. At the end, all parameters were fine-tuned individually to generate the best possible result. The parameters which will be displayed for comparisons are the weighted profile *R*-value, $R_{WP}$, Goodness of fit, *GOF,* and the lattice constants.

### 2.1.2. Reflection high-energy electron diffraction (RHEED)

Reflection high-energy electron diffraction (RHEED) is a physical technique with which surfaces can be examined by electron diffraction. In Figure 2.8 a schematic set-up is shown. An electron gun generates an electron beam (energy between 20 and 50 keV) which is directed onto the sample at a small angle of incidence (< 2 °). The electrons are diffracted at the atoms on the surface and create a diffraction pattern on the screen. The shape of this pattern is dictated by the Laue law and the geometry of the Ewald sphere, so that the image shows a representation of the crystalline structure in reciprocal space. A volume material has a periodicity in three dimensions (3D) and the image on the Ewald sphere results in spots, as can be seen in Figure 2.8 d. However, since the electron beam only grazes the surface, the third-dimension is perpendicular to the sample surface and thus the third diffraction condition is missing. As a result, the reciprocal lattice of the crystal surface appears as a series of infinite rods (Figure 2.8 b and c) [136].

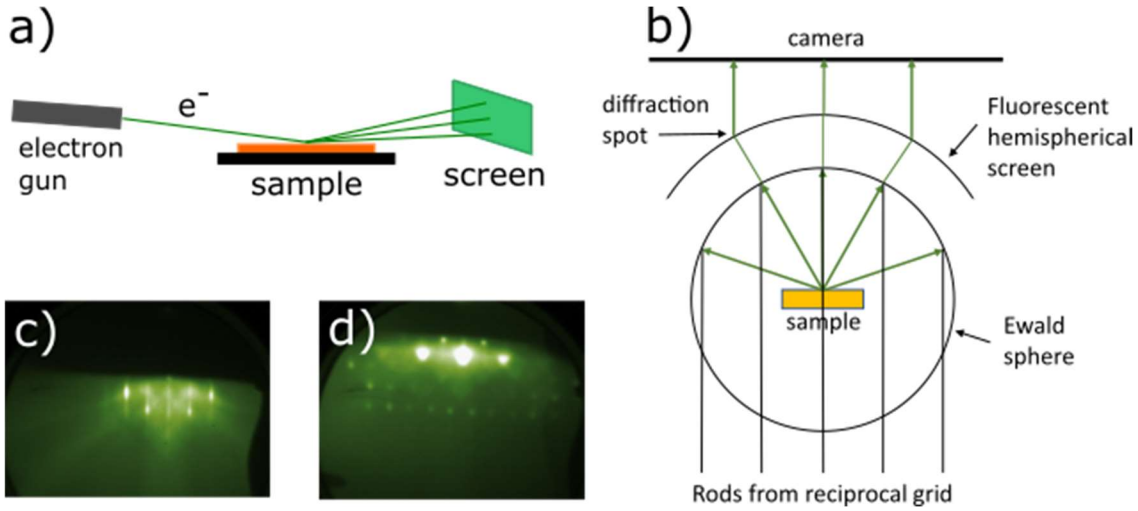


*Figure 2.8 a) Schematic set-up of an RHEED. b) Ewald construction for a 2D structure in reciprocal space. c) 2D structure as seen on the screen. d) 3D structure as seen on the screen*

#### 2.1.2.1. Kikuchi lines

The Kikuchi lines – which can be seen in Figure 2.8 c - are artefacts that appear in RHEED images as a result of multiple scattering, which is mainly caused by thermal lattice vibrations. The electrons are initially scattered inelastically and can then be elastically scattered at the next lattice plane, whereupon the Bragg condition is fulfilled. The sum of the elastically scattered electrons then forms the Kikuchi line which is linked to the family of planes and the diffraction itself. Another electron can be inelastically scattered in another direction respecting the Bragg condition as well and leading to another parallel Kikuchi line. However, the Kikuchi lines appear with a certain width instead of parallel lines since the scattering processes are more complicated [136].

## 2.2. Imaging techniques

### 2.2.1. Scanning electron microscope

Scanning electron microscopy (SEM) is a very important tool for analyzing a sample surface through the interaction of the electrons with the material. Electrons are emitted thermally or by field emission from a cathode and are accelerated to the anode by a variable voltage of approximately 500 V to 30 kV. A subsequent electromagnetic lens system – consisting of two or three lenses – focuses the electron probe on the sample surface. A schematic set-up is shown in Figure 2.9. The emitted interaction products used for imaging mainly are the secondary electrons (SE) or the backscattered electrons (BSE), which are detected with a suitable detector. When the electron probe is directed over the sample with the help of scanning coils, a raster image is created point by point.

Many SEM devices have an integrated possibility for energy dispersive X-ray spectroscopy (EDX). Here the atoms in the sample are excited by an electron beam of a certain energy. The incident beam may eject an electron from an inner atomic shell, creating an electron hole there. An electron from the outer shell fills the vacant state and the difference in energy between the higher-energy outer shell and the lower energy inner shell is released in the form of an X-ray. The emitted X-rays have a specific energy for the respective element. This radiation spectrum provides information about the elemental composition of the sample.

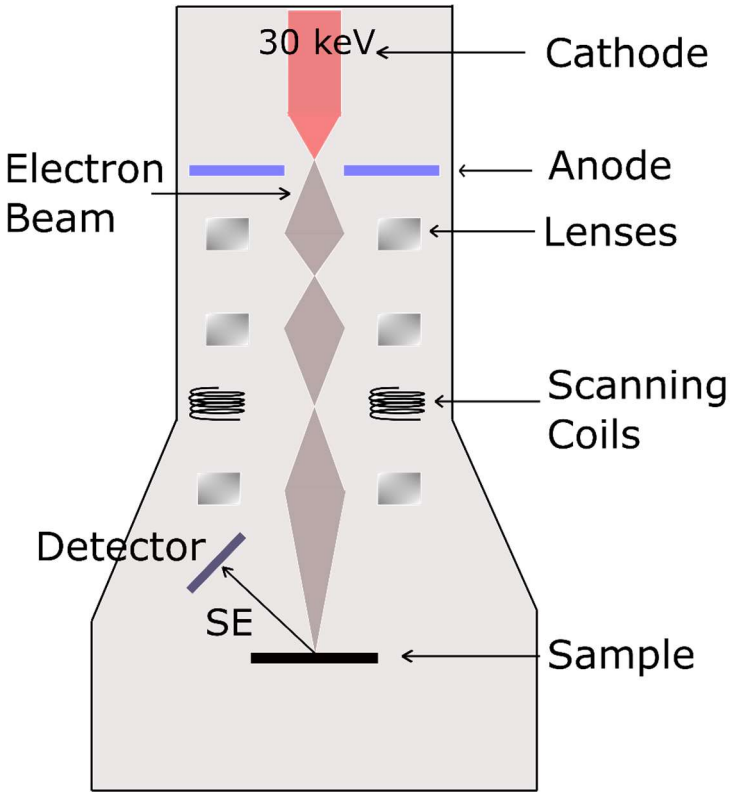


*Figure 2.9 Schematic build-up of a scanning electron microscope.*

### 2.2.2. Atomic force microscopy

Atomic force microscopy (AFM) is a frequently used method in surface physic and chemistry. The setup in its simplest way consists of a laser, a cantilever and a detector. The laser beam is directed to the top of the cantilever, where it is reflected to the detector. A needle (tip) on the underside of the cantilever is either attracted or repelled from the sample by the atomic forces at a very small distance. In the non-contact mode, the cantilever oscillates at its resonance frequency driven by a piezoelectric actuator. The feedback loop maintains a constant oscillation amplitude by adjusting the distance between the tip and the surface during scanning. The feedback-loop information then yields the profile of the surface. Another mode is the contact mode when a quasi-static deflection of the cantilever due to the repulsive force between the surface and the tip is monitored as a feedback loop parameter. These two methods are the most common ways to use the AFM to represent the topography of a sample.

#### 2.2.2.1. Piezoresponse force microscopy

A more advanced AFM mode is the piezoresponse force microscopy (PFM), which was developed to image ferroelectric domains and measure nanoscale piezoelectric properties of ferroelectric materials [137]. To obtain the PFM signal, a special cantilever with a sharp and conductive tip is used. To measure the ferroelectric domains, the tip is placed in contact with a

ferroelectric sample and an AC-bias is applied. Through the converse piezoelectric effect, local sample deformations are exited, which can be detected by deflection of the cantilever and demodulated using a lock-in amplifier. The amplitude of the deflection is proportional to the local piezoelectric coefficient, and its phase depends on the polarization orientation. For domains with the opposite directions of polarization, the phase is shifted by 180 °. This method also offers the opportunity to locally switch the polarization by applying a DC bias to the tip, so domain formation can be investigated.

## 2.3. Density measurements

To estimate the density, $\rho_{abs}$, of the samples the Archimedes method is used. The sample is weighed in three different ways. First, it is stored in DI-water under vacuum conditions for 2 h. The vacuum pulls the air out of the pores and refills them with water ($m_{sat,\,H2O}$). In the second step, the sample is dried on the surface so that the pores are still filled with water ($m_{sat,air}$). In the last step, the sample is stored in a furnace at 130 °C for 12 hours so that the water can evaporate ($m_{dry}$). With Eq. 2.3 and the density of the water $\rho_{H2O}$ in which it was measured in step one the density of the sample can be calculated.

$$\rho_{abs} = \frac{m_{dry}}{m_{sat,air} - m_{sat,H_2O}} \times \rho_{H_2O} \qquad \text{Eq. 2.3}$$

Usually, the literature reports the relative density value, which is the ratio of the measured density, $\rho_{abs}$, to the theoretical density of 8.47 g/cm³, as specified in the PFN dataset ICSD 98-008-8358. The density values in this work are the relative density values unless noted otherwise.

## 2.4. Electrical Characterization Methods

To measure the electrical properties, like the polarization hysteresis loops and the dielectric constant, the Sawyer-Tower-circuit, which is shown in Figure 2.10, is used as a basic method. The ferroelectric sample itself is a capacitor with two metallic electrodes. It is connected with a capacitor with a known value in series. A requirement is that the capacitance *C* of the reference capacitor needs to have a much higher capacitance value than the capacitance of the ferroelectric sample *FE*, which is normally in the nF range. Otherwise the voltage across the *FE* decreases if the voltage at *C* increases (back voltage effect). The measurement capacitor *C*

must be a linear capacitor. In this case, the voltage drop at the reference capacitor can be neglected and the voltage measured at the ferroelectric is nearly the same as the voltage from the source. Knowing the input voltage $V_{in}$ and the thickness of the ferroelectric $d$, the applied electric field $E$ can be calculated through Eq. 2.4

$$E = \frac{V_{in}}{d} \qquad \text{Eq. 2.4}$$

To generate the polarization hysteresis, the polarization $P$ can be calculated with Eq. 2.5 where $A$ is the area of the electrodes and $Q$ is the charge. To determine $Q$ from Eq. 2.6., only the voltage $V_{out}$ across $C$ needs to be measured as the capacitance $C_C$ from the reference is already known [23,138].

$$P = \frac{Q}{A} \qquad \text{Eq. 2.5}$$

$$Q = \frac{V_{out}}{C_C} \qquad \text{Eq. 2.6}$$

However, this method is mostly used up to high speeds and restricted by parasitic effects e. g. cabling capacitances. These cable capacitances add up to the fact, that the reference capacitance needs to have a several percent tolerance (e. g. the voltage drop is around 1 %, if the reference capacitor is 100 times larger) [139,140].

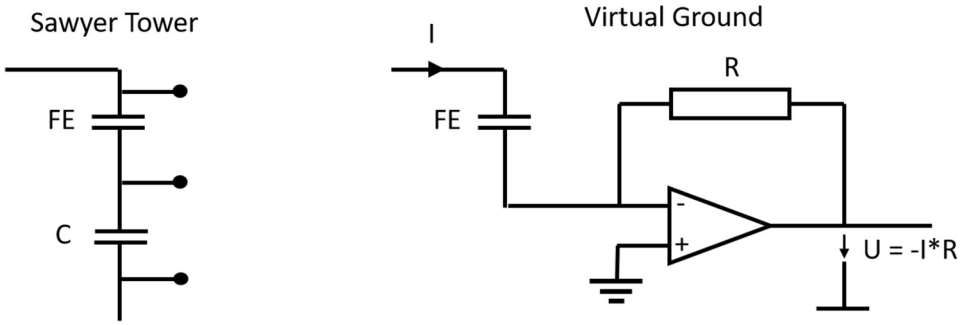


*Figure 2.10 Left: Sawyer-Tower-circuit with the ferroelectric sample (FE) and a reference capacitor (C) which may have a capacitance of e. g. 100 µF.Right: Virtual Ground method with the ferroelectric sample (FE), a feedback resistance R and the amplifier [139,140].*

To avoid the measurement difficulties of the Sawyer Tower method the Virtual Ground method (see Figure 2.10, right) can be used. It uses a current to voltage converter based on a current

measurement with an operational amplifier and a feedback resistance *R*. The non-inverting input of the operational amplifier is connected to the ground, while the inverting input is connected to the output of the current to voltage converter. Ideally, the voltage difference between the inputs of the amplifier is zero. However, in reality it is a few microvolts, means that the inverting input is essentially on ground level. Due to this, the cable capacitances are there, nevertheless, they are electrically ineffective as a result of, that the electrodes of the capacitor are kept at the same potential. Also, there is no back voltage since the full excitation voltage is always applied on the sample. This method leads to the highest precision for ferroelectric measurements like polarization hysteresis loops [139,140].

### 2.4.1. Polarization hysteresis loops

For measuring the polarization-electric field (*P*-*E*) hysteresis loops in this work the TF analyzer 3000 (aixACCT) is used which uses the principle of the Virtual Ground method. In this device usually, a triangular excitation signal is generated. The measurements consist of one pre-poling pulse and three bipolar excitation signals. After each signal, a relaxation time of 1 s follows. Figure 2.11 describes the measurement procedure and the corresponding generated signal. The detected value is the average of the three bipolar measurements [140].

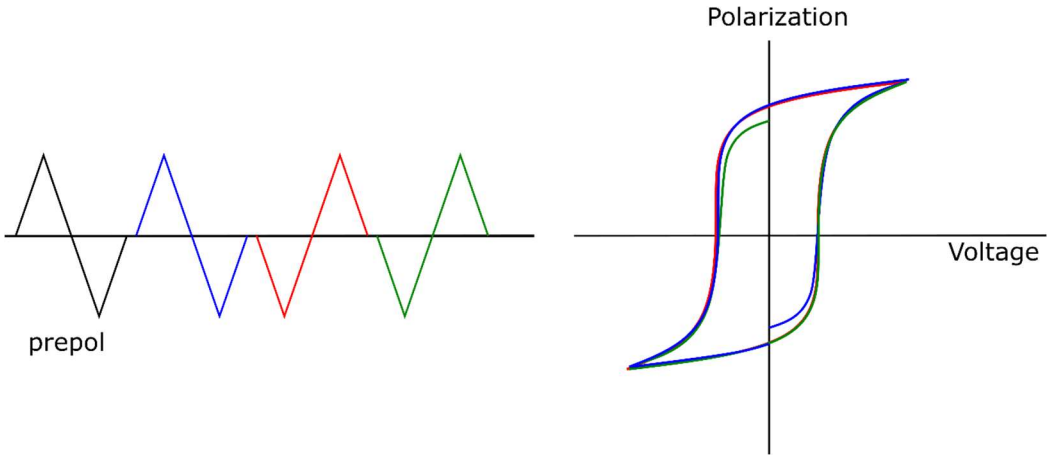


*Figure 2.11 Measurement procedure of a dynamic hysteresis measurement with one pre-poling pulse and three bipolar excitation signals [140].*

#### 2.4.1.1. Leakage compensation

Another useful option, while measuring with the aixACCT device, is the possibility of leakage compensation, especially for highly conductive samples. In such samples, the charge related to the leakage current superimposes the ferroelectric polarization and both contributions cannot be clearly distinguished. To estimate the leakage current contribution, a staircase waveform like in Figure 2.12 is applied and the response is analyzed. The current is monitored during each

voltage step and averaged in the region of 70 to 90 % of the step time to exclude the charging current of the ferroelectric material which occurs directly after increasing the voltage, so that the leakage current can be extracted [140].

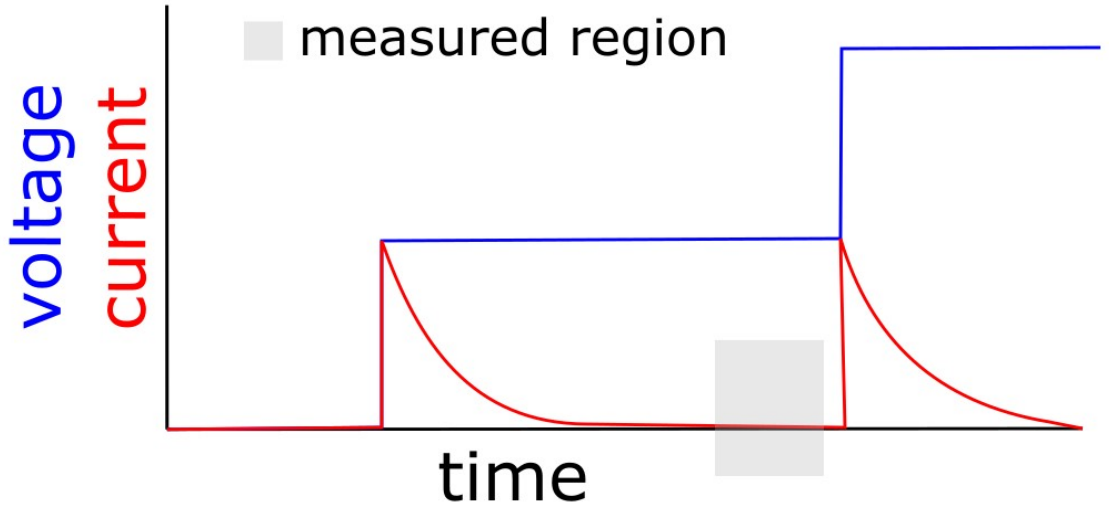


*Figure 2.12 Measurement procedure of the leakage current measurement [140].*

The polarization-electric filed hysteresis loops were measured by a TF analyzer 3000 (aixACCT) at room temperature using a sine wave signal with different frequencies between 1 and 100 Hz. The electric fields were applied up to 30 kV/cm. The aixACCT device enables the possibility for leakage current compensation simultaneously with the hysteresis measurement.

### 2.4.2. Dielectric measurements

The dielectric response is an important characteristic of ferroelectrics. The measurement of the dielectric permittivity provides valuable information on phase transitions and the mechanisms of polarization of ferroelectrics. The dielectric permittivity $\varepsilon$ of the material describes its response to an applied electric field $E$ which can vary with the frequency $f$. While applying the electric field, the material will be polarized and depending on the frequency different polarization mechanisms e. g. electronic, ionic, and orientation polarization can occur. The relation between the polarization $P$ and the electric field is as follows:

$$P = \chi_e \varepsilon_0 E \qquad \text{Eq. 2.7}$$

where $\varepsilon_0$ ($8.854 \cdot 10^{-12}$ As/Vm) is the permittivity of free space, and $\chi_e$ is the electric susceptibility. $\chi_e$ is a second rank tensor, however, this work deals with polycrystalline materials

and the simplified scalar form is used here, as it is common for isotropic materials. $\chi_e$ is frequency dependent and a material property that indicates the ability to polarize in an applied electric field. It is related to the relative dielectric permittivity $\varepsilon_r$ as

$$\chi_e = \varepsilon_r - 1 \qquad \text{Eq. 2.8}$$

Polarization does not instantly follow an applied electric field. Therefore, at a finite frequency there is a phase shift between the polarization and an AC electric field. Correspondingly, both the electric susceptibility and the relative dielectric permittivity are complex quantities.

$$\varepsilon_r = \varepsilon'_r - i\varepsilon''_r \qquad \text{Eq. 2.9}$$

With the relation in Eq. 2.10 the loss factor can be described.

$$tan\delta = \frac{\varepsilon''_r}{\varepsilon'_r} \qquad \text{Eq. 2.10}$$

The complex relative dielectric permittivity, $\varepsilon_r$, was measured using a Solartron 1260 impedance analyser with a dielectric interface 1296. The measurements were performed on cooling from 430 to 310 K and investigated in detail for different frequencies. The data points were collected every 1 K and no DC-offset voltage was used.

### 2.4.3. Transmission line measurements

Transmission line measurements are normally used for determining the sheet and contact resistance of a device. To do this, an electrical voltage is applied to the electrodes and the obtained current is measured. To then determine the resistances, electrodes must be present at different distances from one another. This can be used to create a plot of the resistances as a function of the distance between the electrodes.

In this work, this method was used to examine whether a photocurrent is generated in the sample and how it changes with different electrode distances. To do so, electrodes in distances of 110, 200, 400 and 800 µm were evaporated onto the sample. The voltage was swept from -10 to

10 V and vice versa in a 0.01 V step. Measurements were done in dark and under illumination of the sample.

## 2.5. Magnetic Characterization Methods

To characterize the magnetic properties, the magnetization of the samples was measured in two different ways: on the one hand, versus temperature at a constant magnetic field and, on the other hand, versus magnetic field at a constant temperature. The vibrating sample magnetometer (VSM) option of a Quantum Design PPMS DynaCool was used in both methods on crushed ceramic pellets.

Figure 2.13 shows a schematic build-up of a VSM. The sample is positioned in a sample holder which itself should generate a minimal magnetic response. A static magnetic field is then generated by a superconducting electromagnet. An actuator or piezoelectric element causes the sample holder to vibrate in a set of pickup coils. The periodic oscillation of the magnetic sample leads to a local change in the magnetic flux which generates a periodic current with the known frequency of the oscillations in the pickup coils shown in light blue in the picture. This signal can then be demodulated using a lock-in amplifier and its magnitude reflects a magnetization value.

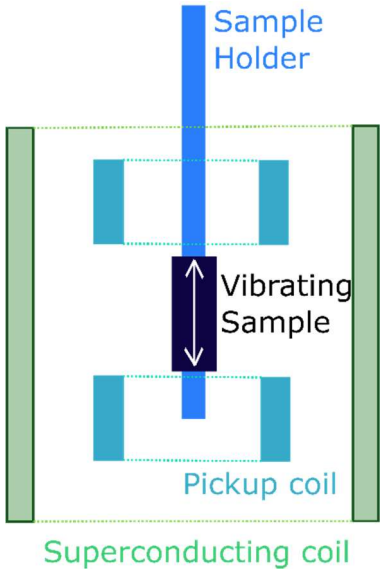


*Figure 2.13 Schematic build-up of the sample chamber of a vibrating sample magnetometer.*

### 2.5.1. Zero Field Cooling – Field Cooling

Zeri-field cooling: The sample is cooled down from room temperature to 5 K without an applied external magnetic field. While this cooling, the spins, which were in an arbitrary orientation, freeze into a quasi-random state. Then the measurement takes place during a heating phase up to 320 K where a constant magnetic field of 0.1 T was applied, representing the ZFC branch. Here the spins start aligning due to the outer magnetic field. This leads to an increase in the magnetic moment of the sample. This is followed by a magnetization measurement in which the sample is cooled down to 5 K again, but with an applied external magnetic field of 0.1 T (field-cooled measurement, FC). The apparent magnetization is monitored at all rising and decreasing temperatures.

### 2.5.2. Magnetic hysteresis loops

The field dependent magnetization measurements were recorded up to a maximum magnetic field of 9 T. They were performed at different temperatures. Since PFN is an antiferromagnet a S-shaped line was expected.

## 2.6. Optical Characterization Methods

### 2.6.1. UV-Vis spectroscopy

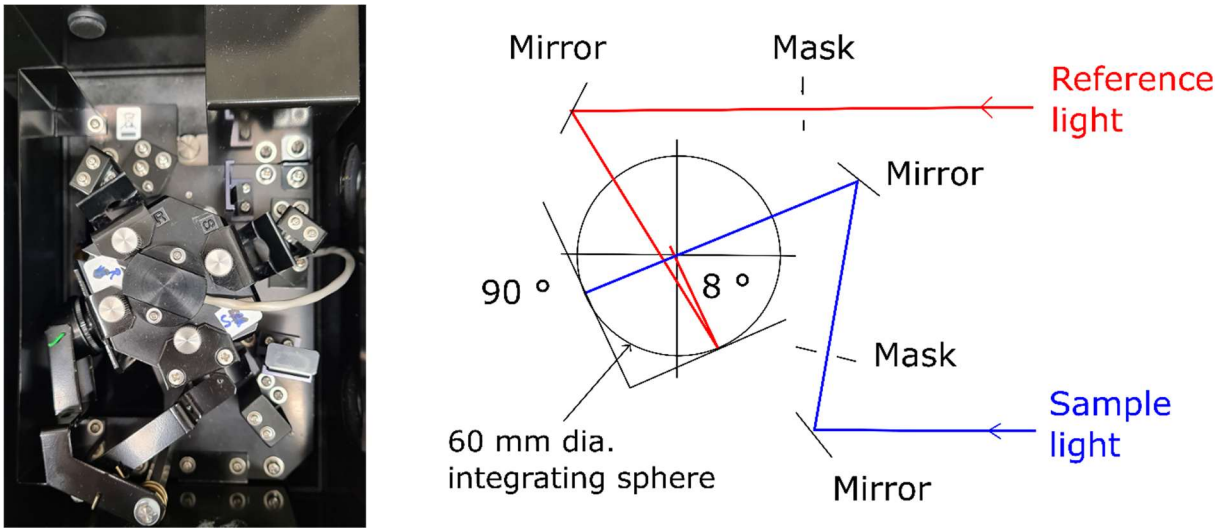


*Figure 2.14 a) UV2600 integrating sphere attachment. b) Light path [141]*

UV-Vis spectroscopy is a method widely used to measure the absorption of a material and works as one of the fundamental analysis techniques in optical measurements. The sample is illuminated with monochromatic light with a wavelength in the range of 185 – 900 nm (ultraviolet (UV) to visible (Vis)). It is placed in an integrating sphere attachment (Figure

2.14 a) either in the transmission configuration or in the absorption configuration. Depending on the material, the incident radiation is partially absorbed. The intensity of the transmitted light is detected in dependence on the wavelength. The measured UV-Vis spectrum is also known as the absorption spectrum. The intensity of the incident light $I_0$ is attenuated ($I$) according to the Lambert-Beers law and is related to the extinction $A(\lambda)$ as follows:

$$A(\lambda) = \log\left(\frac{I_0}{I}\right) \qquad \text{E. 2.11}$$

From the UV-spectrum an estimation of the band gap value can be derived by plotting a Tauc plot as explained in Chapter 1.5.1.1.

To define the band gap two different UV-Vis spectrometers were used. Transmission spectra for the PFN layers were recorded with a Shimadzu UV2550 (Shimadzu, Duisburg) double-beam spectrometer. For the diffuse reflectance measurements of powders and layers, a Shimadzu UV2600 (Shimadzu, Duisburg) was used. In both cases the investigated wavelength range was from 300 nm to 850 nm and an integrating sphere was used to reduce scattering.

### 2.6.2. Photoluminescence (PL) Spectroscopy

Photoluminescence (PL) spectroscopy is a non-destructive method to investigate the emission of photons in a material. The sample is excited with a fixed wavelength where the absorbed photons cause electrons to move to a higher energy level. This is followed by the relaxation of these electrons generating emission of light or luminescence which is called photoluminescence. The energy of the emission is then recorded using an emission monochromator.

The PL-device used here was a Horiba Spectrum-1 CCD coupled to a Horiba iHR550 grating monochromator. The PL-spectra of the PFN film were measured with different excitation lasers with wavelengths of 325, 405, and 532 nm in a confocal setup.

#### 2.6.2.1. Time Resolved Photoluminescence

With time resolved photoluminescence the spectral and temporal change of the emission from a sample can be measured. Electron-hole pairs can be generated in the sample with a short laser pulse. These decay to lower energy levels and then recombine emitting light. The emitted light consists of a set of wavelengths that can be assigned to the transition energies of the electronic

states. By measuring the optical spectrum as a function of time, it is possible to measure the electronic transition energies and thus their lifetimes.

The time resolved photoluminescence was measured in a Horiba Fluorolog-3 system with a 375 nm diode laser at a ~90 nJ/pulse.

### 2.6.3. Photoelectron spectroscopy

Occupied electronic states in a material can be examined with photoelectron spectroscopy (PES) which is based on the external photo effect. Photoelectrons with the kinetic energy $E_{kin}$ are released from the solid by electromagnetic radiation. $E_{kin}$ is related to the incident excitation energy $h\nu$ ($h$ is the Planck constant and $\nu$ the frequency of the incident light), the binding energy $E_B$ and the work function $\phi_{spectrometer}$ of the spectrometer as in equation Eq. 2.12. If the photon energy is known, statements about the $E_B$ in the examined material can be made with the help of the measured electron energy.

$$E_{kin} = h\nu - E_B - \phi_{spectrometer} \qquad \text{Eq. 2.12}$$

Various measurement methods are used to determine the band edges of the valence ($E_{VB}$, maximum value) and conduction ($E_{CB}$, minimum value) bands. Ultraviolet photoelectron spectroscopy (UPS) is used for the former and inverse photoemission spectroscopy (IPES) for the latter. Once the two band edges have been determined, the fundamental band gap $E_{G,fund}$ [142] can be deduced, which is calculated as follows:

$$E_{G,fund} = I_E - E_A = E_{CB} - E_{VB} \qquad \text{Eq. 2.13}$$

with
$$I_E = h\nu - (HBEC - E_{VB}) \qquad \text{Eq. 2.14}$$

and
$$E_A = E_{vac} - E_{CB} \qquad \text{Eq. 2.15}$$

$I_E$ stands for the Ionization energy, $HBEC$ for the high binding energy cutoff, $E_A$ for the electron affinity and $E_{vac}$ for the vacuum level. The $HBEC$ also can be used to calculate the work function $\phi_{material}$ of the material.

$$\phi_{material} = h\nu - HBEC \qquad \text{Eq. 2.16}$$

All PES measurements were performed under ultra-high vacuum in a custom-built multi-chambers set-up.

#### 2.6.3.1. Ultraviolet Photoemission Spectroscopy

To determine the valence band structure, ultraviolet light is used, because it carries enough energy to release valence electrons to the vacuum level (Figure 2.15 a). The kinetic energy of the released photoelectrons is measured with an electrostatic analyzer.

A monochromatic helium plasma source (VUV 5 k, Scienta Omicron, Germany) was used at an excitation energy of 21.22 eV. A hemispherical electron analyzer (Phoibos 100, Specs, Germany) was used with an electron pass energy of 2 eV. To observe the high energy cutoff a sample bias of 8 V was applied during the measurements.

#### 2.6.3.2. Inverse Photoelectron Spectroscopy

In order to determine the conduction band structure, electrons of known energy are accelerated to the kinetic energy relative to the equilibrated Fermi level of the gun/sample system which are in electrical contact. The accelerated electrons bombard the material under the emission of photons which got detected (Figure 2.15 a).

To perform the measurements a low energy gun (ELG-2, Kimball physics, USA) was used at a 2 µA emission current in combination with a bandpass photon detector ($SrF_2$/NaCl bandpass, IPES 2000, Omnivac, Germany).

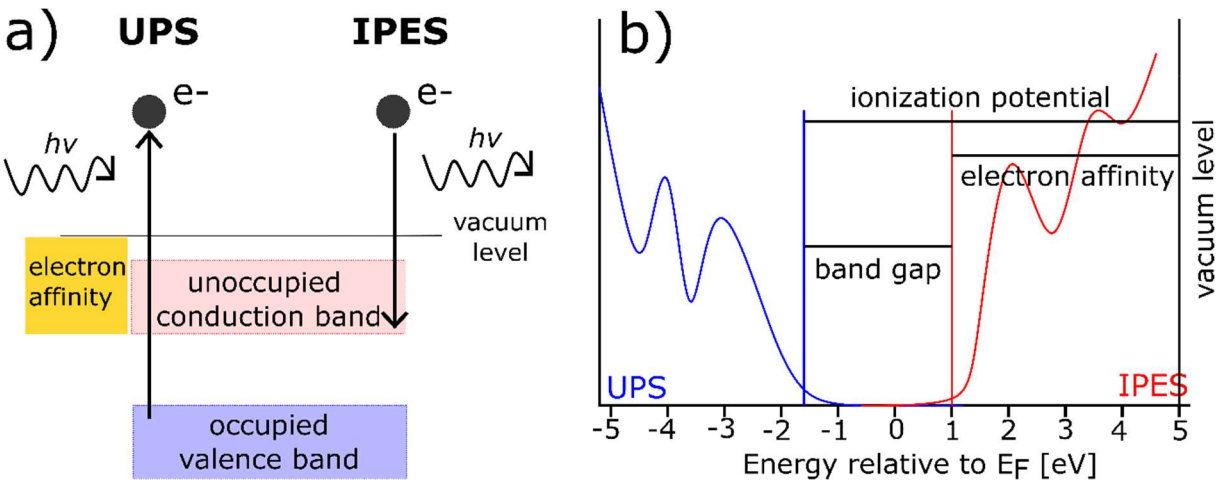


*Figure 2.15 The energy diagram a) and a schematic spectra of an UPS/IPES [143].*

The schematic spectra of the UPS/IPES measurements are shown in Figure 2.15 b. From this the band gap, the ionization potential and electron affinity can be estimated. For more accurate numbers the equations from above need to be solved.

# 3. PFN Ceramics

The PLD target plays a major role in the manufacture of layers deposited by PLD. In order to obtain a target with the best possible properties for the layers, the ceramic manufacturing process must first be completely understood. In the literature many different methods are used to synthesize PFN. These differ not only in their methodology [56,58,78,144,145] of powder production, but also in the individual synthesis parameters. In order to gain an understanding of the material and the changes in the various methods and parameters, various experiments were carried out. The effect of synthesis conditions on structure, dielectric, magnetic and optical properties of PFN ceramics is addressed in this Chapter.

The first Chapter 3.1 shortly describes the effect of pre-milling of iron oxide which enhances the reactivity for the oxide routes. Since the sintering atmosphere is a critical point, Chapter 3.2 deals with the mechanochemical activation of PFN and changes in its properties due to the sintering atmosphere: air or oxygen. Additionally, it discusses the changes due to the embedded powder/crucible-construction while sintering. To point out the differences in the synthesis methods, Chapter 3.3 deals with the properties of five different synthesis methods to produce PFN, such as solid-state, hydrothermal, molten salt, combustion and mechanochemically assisted under the same synthesis conditions (means calcination/sintering temperatures, times and atmosphere). The most practical and easiest method is the solid-state method. In the Chapter 3.4 the focus is placed on this method and the influence of various synthesis temperatures is examined.

## 3.1. Premilling $Fe_2O_3$

Due to the reason that iron oxide ($Fe_2O_3$) has a lower reactivity than lead (PbO) and niobium ($Nb_2O_5$) oxides, an inhomogeneous phase distribution of the resulting product can occur [134]. By premilling the $Fe_2O_3$, the particle size is decreased and the surface area increases which enhances the reactivity. The premilled iron oxide was used for all oxide synthesis routes.

$Fe_2O_3$ (99.9 %, Alfa Aesar) was premilled in ethanol by planetary ball milling for 6 h at 200 rpm using yttrium stabilized zirconium oxide (YSZ) balls. The particle size distributions in Figure 3.1 show the effect of premilling. While the commercial particle size (0 h) is around 1 µm, it decreases to 0.78 µm after 2 h of milling already. By further premilling (4 h), agglomerates bigger that 100 µm are forming, but the overall particle size is still decreasing. After 6 h of premilling, the big agglomerates still exist, but they do not add up. Focusing on the smaller particles, it can be seen that the particle size was reduced a lot. To get rid of the big agglomerated the premilled iron oxide was sieved through a sieve with a mesh size of 40 µm.

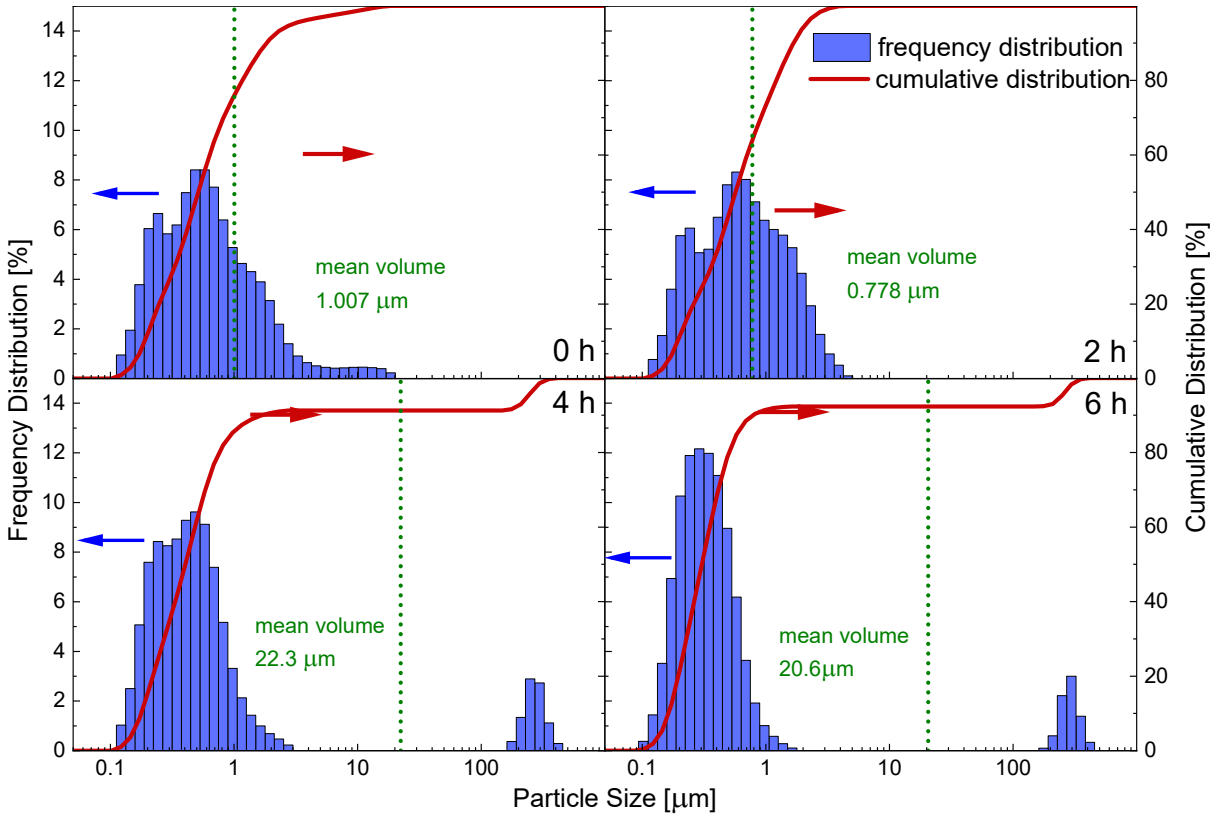


*Figure 3.1 Change in frequency and cumulative distributions of the particle size of $Fe_2O_3$ at the beginning (0 h), after 2 h, 4 h, and after 6 h (c) of premilling.*

## 3.2. Mechanochemical activation with different sintering conditions

The following subsection presents the differences between the various sintering atmospheres for samples that have been produced with the mechanochemical activation and the help of Dr. U. Prah at the Jozef Stefan institute in Slovenia. This method was the best-known method in the slovenian working group at this time and helped to gain a basic understanding of the material and the ceramic processes. The mechanochemical activation process had been optimized so the focus of this study was put on the sintering atmosphere. Sintering was carried out under four different sets of conditions and the resulting structure, electric, and dielectric properties of PFN are discussed.

### 3.2.1. Experimental

For mechanochemical activation synthesis stoichiometric amounts of PbO (99.99 %, Alfa Aesar), premilled $Fe_2O_3$ (Chapter 3.1) and $Nb_2O_5$ (99.9 %, Alfa Aesar) were mixed in ethanol by planetary ball milling for 4 h at 200 rpm using yttrium stabilized zirconium oxide (YSZ) balls. Milling is necessary in order to obtain a homogeneous particle size distribution. Furthermore, a smaller particle size is thus achieved, which gives a higher reactive area for mechanochemical activation [146]. As shown in Figure 3.2, the mean volume distribution decreased from 2.37 µm to 0.95 µm after 2 h. After milling the powder for two more hours, the size of the particles is only slightly reduced to an average of0.8 µm.

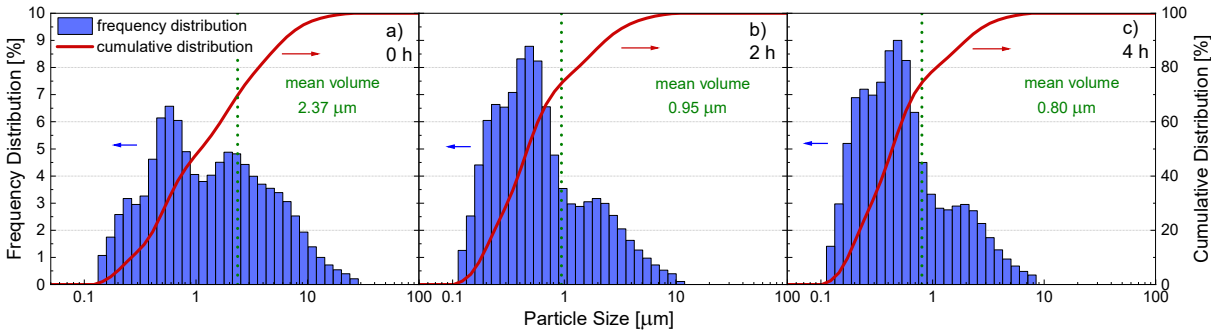


*Figure 3.2 Change in frequency and cumulative distributions of the particle size at the beginning (a), after 2 h (b) and after 4 h (c) of homogenization.*

Thereafter, the powder appeared in a reddish color (Figure 3.3 a) and was dried. For the mechanochemical activation a tungsten carbide milling jar and six tungsten carbide milling balls were used The powder was mechanically activated in the planetary mill for 6 h and 362 rpm. After activation, the synthesized powder changed from the reddish to a more orange color (Figure 3.3 b) which confirms the reaction, also the particle size increased to 3.54 µm (Figure 3.4 a). The powder was then milled again using a planetary ball mill in ethanol for 4 h and 200 rpm using YSZ balls, which reduces the particle size via an intermediate step of agglomeration, where the size was 43 µm (2 h), to 0.59 µm (4 h) (Figure 3.4 b and c). As the perovskite phase is already formed during the high energy milling, no additional calcination step is needed.


*Figure 3.3 Change in color from reddish (a, after homogenization) to orange (b, after mechanochemical activation.*

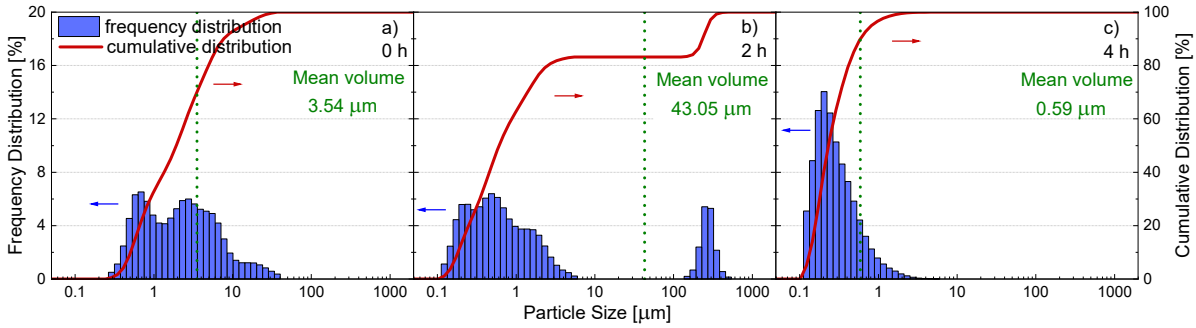


*Figure 3.4 Reduction of particle size from 3.54 µm (0 h, a) to 0.59 µm (4 h, c) via an intermediate step of agglomeration (b)*

In order to find out the best sintering conditions, a sintering curve with a heating rate of 5 K/min was recorded with an optical dilatometer (Leitz Version 1A, Leitz) (Figure 3.5, left). On the right, the images of the pellet for temperatures of 850, 900, 950 and 1000 °C are displayed. The relative shrinkage increases slightly starting from 800 °C and then sharply from 850 to 1000 °C, where the maximum shrinkage is reached. The pellet does not shrink evenly, but significantly more in the middle, so that a curved side is created. Thus, the densification is the strongest in the middle of the pellet. The sintering temperature was then set to 50 °C below the temperature where maximum shrinkage was achieved (1000 °C), so the densification is the highest possible, but the pellet does not start to melt. Therefore, sintering was conducted at 950 °C for 2 h.

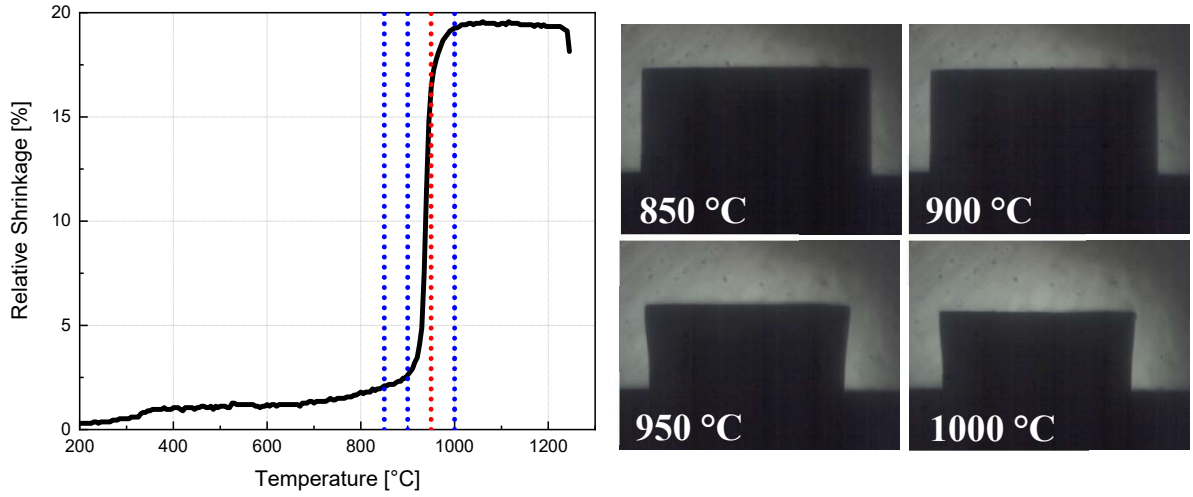


*Figure 3.5 The sintering curve for the powder synthesized by mechanochemical activation (left) and corresponding images of the pellet at temperatures of 850, 900, 950, and 1000 °C (right)*

After defining the sintering temperature for subsequent samples, the powder was pressed with a uniaxial pressure of 50 MPa followed by an isostatic pressure of 300 MPa. Sintering was conducted in either air (Air) or oxygen (Ox). Additionally, the green body was either fully embedded into the powder (powder contact, PC) of the same material or segregated from it (no contact, NC) as shown in the images to the right of Table 3-1. A total of four different sintering conditions as used, named PCAir, PCOx, NCAir and NCOx.

*Table 3-1 Sintering conditions and the absolute and relative densities for the sintered pellets. The images on the right sketch the construction of the crucible und how the pellets and the embedding powder were positioned.*

| Sample | Construction | Atmosphere | Density |
|---|---|---|---|
| **PCAir** | one crucible, contact | air | 8.21 g/cm³ 97.05 % |
| **PCOx** | one crucible, contact | oxygen | 8.34 g/cm³ 98.53 % |
| **NCAir** | double crucible, no contact | air | 8.07 g/cm³ 95.58 % |
| **NCOx** | double crucible, no contact | oxygen | 8.31 g/cm³ 98.27 % |

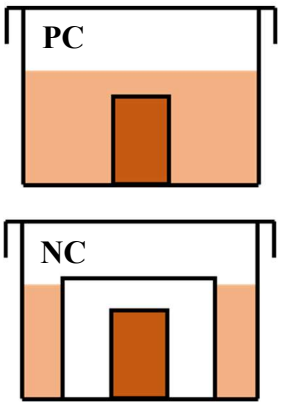


The density measurements were done with a He-pycnometer (AccuPyc II 1349, Micromeritics). All samples have a higher density value than 8 g/cm³ which results in a relative density of more than 95 % for all samples. It can be seen, that the samples sintered in oxygen have a higher density than those sintered in air. Rahaman [147] discusses the possible reasons, which could lead to these differences. One reason can be that diffusion for smaller particles is more

favourable than for bigger ones. Since $O_2$ (r = 152 pm) has nearly the same size as $N_2$ (r = 155 pm) no difference would be seen. Because of this the only conclusion is, that oxygen needs to have a higher solubility in PFN than air (nitrogen). If the solubility is high enough the gas which is trapped in the pores will diffuse rapidly through the lattice or the grain boundaries. For a low solubility the gas will be compressed, and the gas pressure will increase until it becomes equal to the compressive pressure of the driving force for sintering. The gas in the pores is trapped. Supplementary, the oxygen vacancies can be filled up with the higher oxygen partial pressure.

The samples which are sintered in contact with the embedded powder have a slightly higher density than the samples without contact. Since lead is volatile at high temperatures, it is already known that embedded powder counteracts this [148]. One assumption here is that if the sample is separated from the embedded powder by a second crucible, the lead partial pressure in the inner crucible must first be established, probably with the lead from the sample. The powder in the outer crucible helps keeping the lead from escaping from the inner crucible. However, if the sample is brought in the direct contact with the sample, lead from the powder can diffuse directly back into the sample, so that less lead vacancies are created.

### 3.2.2. Crystalline structure and phase composition

In Figure 3.6 the XRD patterns of the powder before sintering (left) and of the pellets after sintering (right) are shown. Before sintering the pattern is not a pure perovskite. Rietveld refinement analysis shows that the amount of a secondary phase is around 10 % but cannot be clearly identified also due to the presence of amorphous phase which has been also observed by other authors [149,150]. After sintering the secondary phase disappears and the pure perovskite phase is left. Rietveld refinement analysis was done with only monoclinic (ISCD 98-008-8358, space group $C1m1$) and monoclinic and rhombohedral (ISCD 98-009-0491, space group $R3m$) phases. The results show that if the XRD pattern is fitted by a combination of both phases, the amount of the rhombohedral phase is less than 5 %. However, if the fit is done with only the monoclinic phase, the comparative values $R_{wp}$ and GOF remain nearly the same, which leads to the conclusion that the mechanochemical activation with subsequent sintering at 950 °C for 2 h results in the almost monoclinic phase.

The peak positions do not shift with the different sintering conditions, consequently the lattice parameters are almost the same for the samples sintered in air and in oxygen as is also proven by the Rietveld refinement. The peak form is sharp with a small broadening and do not differ

in the patterns of the different samples. This is in disagreement with Font et al. [79] who investigated the difference between oxygen and air atmospheres in solid state synthesis. They obtained a rhombohedral structure for both atmospheres. Nevertheless, they recognized a shift in the peak positions from the in-air-sintered sample to higher $2\theta$ angles for the oxygen-sintered sample, and also a peak broadening, as a result of a larger lattice constant and a smaller crystallite size. In our case, the mechanochemical activation and probably also the milling steps lead to nearly the same lattice constants and small crystallite sizes.

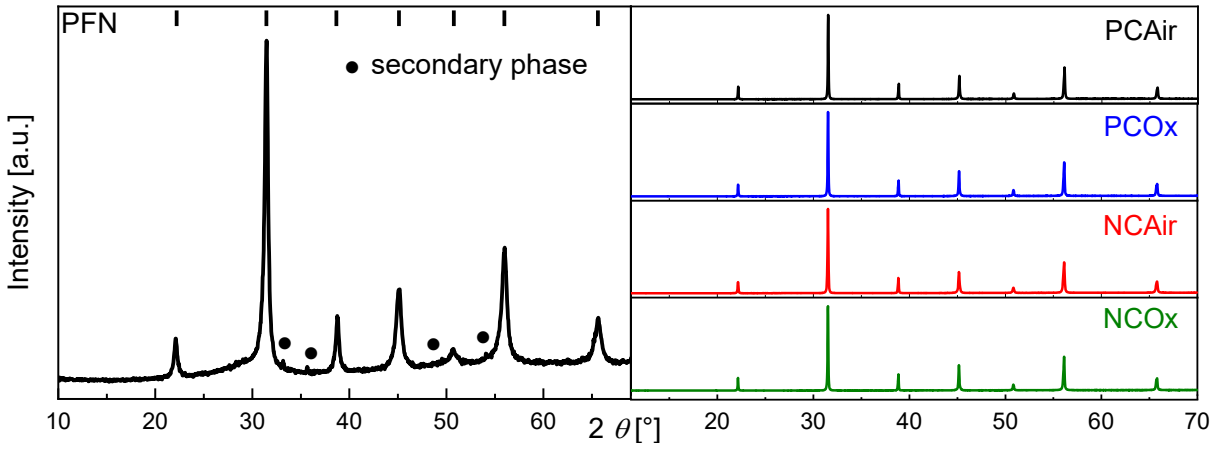


*Figure 3.6 On the left side is the XRD pattern of the mechanochemically activated sample – the lines indicate the positions of the PFN peaks and the points the position of secondary peaks. The patterns after sintering (right) do not show any secondary peaks anymore.*

*Table 3-2 Comparison of Rietveld analysis values for the different samples for the fits with monoclinic/rhombohedral and only monoclinic phases.*

| Sample | Monoclinic/ Rhombohedral [%] | Monoclinic/ Rhombohedral $R_{wp}$ | Monoclinic $R_{wp}$ | Monoclinic/ Rhombohedral *GOF* | Monoclinic *GOF* |
|---|---|---|---|---|---|
| **PCAir** | 95<br>5 | 10.87 | 10.98 | 2.35 | 2.37 |
| **PCOx** | 97.2<br>2.8 | 10.42 | 10.43 | 2.21 | 2.21 |
| **NCAir** | 98.2<br>1.8 | 11.18 | 11.19 | 2.43 | 2.44 |
| **NCOx** | 96.5<br>3.5 | 8.26 | 8.25 | 2.08 | 2.08 |

In Figure 3.7 the microstructures of the different sintered pellets are shown. NCOx, PCOx, and PCAir have visibly the same grain size, with NCAir appearing coarse-grained on the fractured samples. However, in the sample NCAir some larger grains appear occasionally in the structure.

This can be proven with the histogram of Figure 3.8, in which at least 450 grains were taken into account. The average diameter value of the grains for NCAir is 1.4 µm, with individual grains larger than 3 µm. For NCOx it has only a slightly smaller value of 1.2 µm. The fractured samples (Figure 3.7 d, g and h) only have intergranular fractures, except for the NCAir sample (Figure 3.7 a) where transgranular fracture also appears in the big grains. For NCAir and NCOx, both the polished samples and the thermally etched samples were examined further, since the pores in the fractured samples cannot be clearly seen. NCAir has more pores than NCOx, which was already explained in the density section (3.2.1) and confirms the results in Table 3-1. A difference in the grain size between NCOx and PCOx cannot be seen here. This is again in disagreement with Font et al. [79] who could detect a significant difference. Their samples sintered in oxygen had an average grain size of 2.7 µm against 2 µm for samples sintered in air. The only congruence is that the number of intragranular cracks increases with the grain size. Gao et al. [134] synthesized PFN also via mechanochemical activation for 30 h with subsequent sintering at different temperatures. The parameters they used were not efficient enough in our case, because after activation for 30 h, a pure PFN ceramic could only be achieved by sintering at 1000 °C. The corresponding SEM images show a highly porous ceramic with a density of only 85 % which leads to bad electrical properties, so these will not be compared further. However, it should be note, that with the same parameters, but with previous calcination of $Fe_2O_3$ and $Nb_2O_5$ to $FeNbO_4$, Gao et al. achieved significantly better results [134]. Pure PFN was already formed above 400 °C with a density starting from 88 % at 950 °C and increasing with higher sintering temperature. They explained these differences by the fact that $Fe_2O_3$ is the most inert material, long distance diffusion is therefore affected and not every iron molecule will participate in the reaction. In order to prevent this, the $Fe_2O_3$ was milled beforehand as described in Chapter 3.1 in order to increase its reactivity.

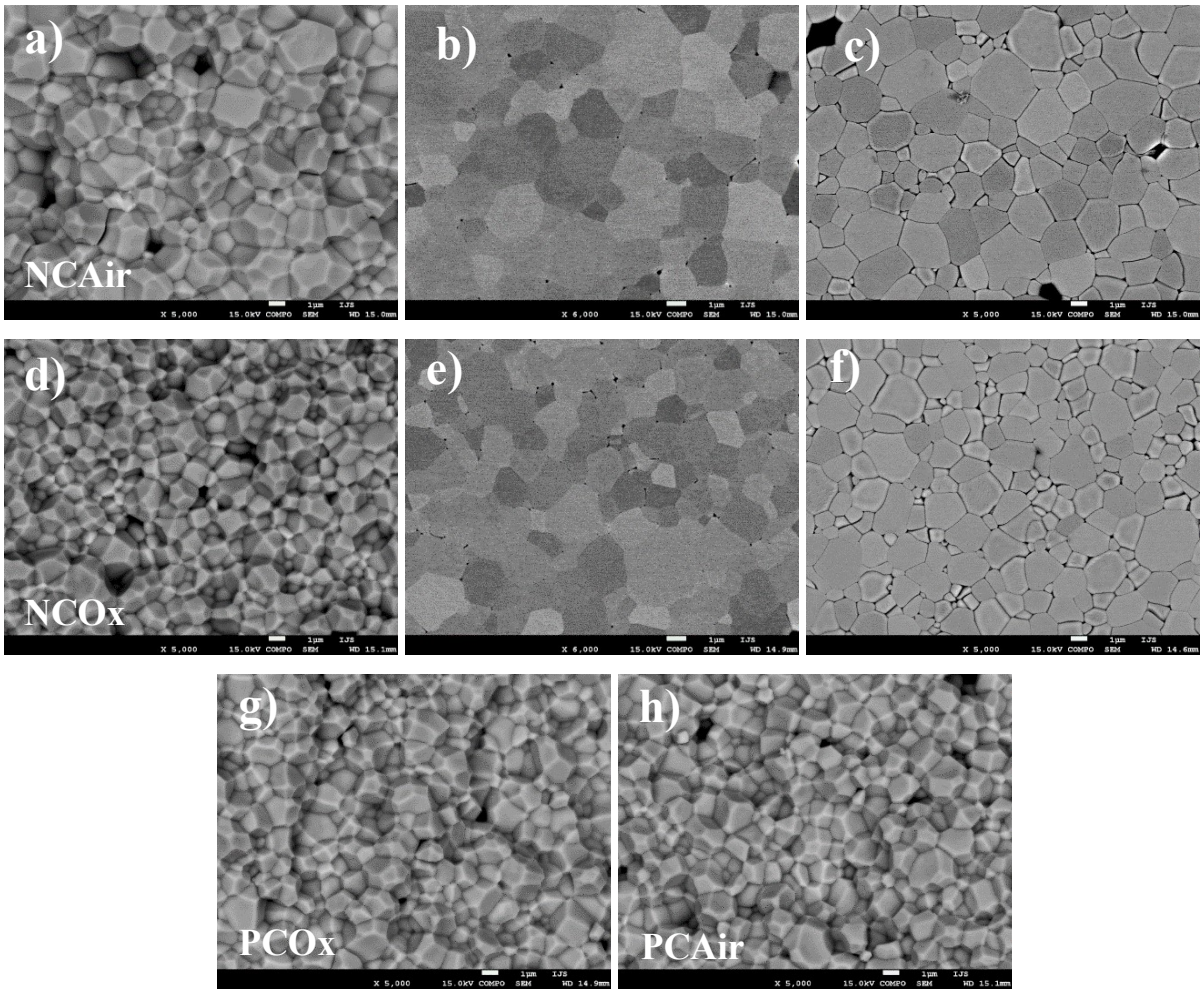


*Figure 3.7 SEM images of the different pellets. For NCAir and NCOx, the fractured, polished and thermally etched samples are shown and for PCOx and PCAir only the fractured samples*

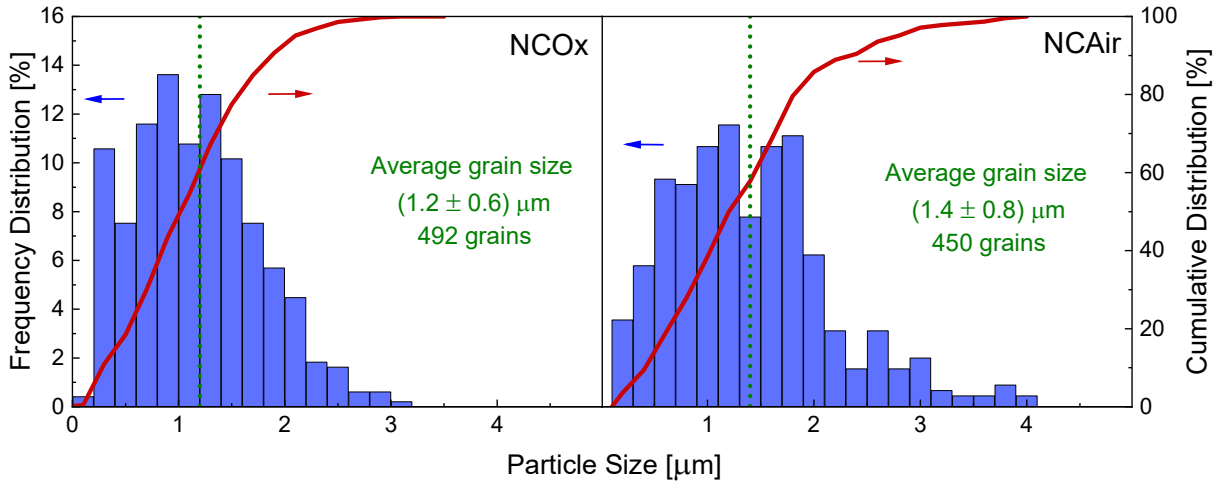


*Figure 3.8 Grain size distribution for NCOx and NCAir*

### 3.2.3. Dielectric and ferroelectric characterisation

The I-V characteristics for the four different samples are shown in Figure 3.9. A closer look at the scale points out that the samples sintered in air have more than three orders of magnitude

higher conductivity (mA) than the samples sintered in oxygen (nA). The values of conductivity for an electric field of 0.5 kV/cm are 0.03 and 0.02 nA/cm² for PCOx and NCOx and 0.09 and 2.34 mA/cm² for PCAir and NCAir, respectively. This can be explained by the lack of oxygen in the lattice. As a result, in the lattice two electrons are missing for each oxygen atom, and two holes are created for each oxygen vacancy. These are partially compensated by a reduction of iron from $Fe^{3+}$ to $Fe^{2+}$ and, probably, by the formation of lead vacancies. Not all charge differences can be balanced out. Possible conductivity mechanism can be either an oxygen vacancy drift, hole conduction, electron hopping from $Fe^{3+}$ to $Fe^{2+}$, or a combination of all of them. While the difference in current density between NCOx and PCOx is rather insignificant, the difference between PCAir and NCAir is more noticeable. It can be rationalized by the formation of a smaller number of lead vacancies in PCAir, so that the electrical balance is better.

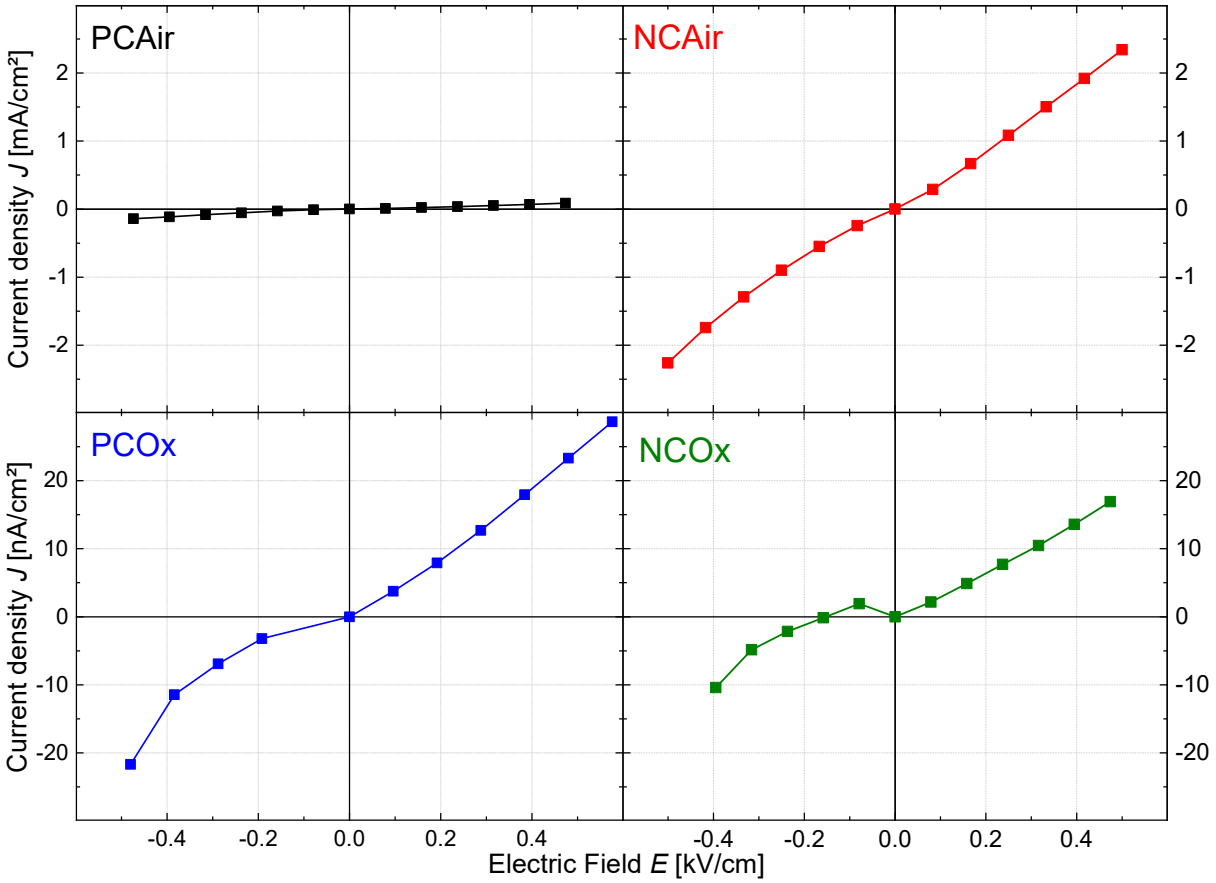


*Figure 3.9 I-V curves for the four different samples. To better display the results, the current density has different scales.*

The polarization hysteresis loops in Figure 3.10 correlate with the trend observed for the I-V-curves. The pellets that were sintered in oxygen show typical, but relatively narrow, ferroelectric hysteresis loops with $P_{max}$ higher than 30 µC/cm², $P_S$ more than 26 µC/cm² and $P_r$ around 19 µC/cm² at 30 kV/cm at 1 Hz. However, the polarization curves of the pellets that

were sintered in air have a large contribution of leakage current, so $P_{Max}$ and $P_S$ cannot be read out anymore. For PCAir, the hysteresis form of the curve can still be recognized, while for NCAir the conductivity contribution dominates and overrules the ferroelectric contribution. Correspondingly, the polarization curve loses its hysteresis shape. Ferroelectricity in PFN is mainly related to correlated off-center displacements of lead ions. Therefore, the suppressed ferroelectric contribution for the sample sintered in the non-contact mode may indicate formation of more lead vacancies than in sample sintered in the contact mode. The hysteresis loops measured at different frequencies are compared in Figure 3.11 and the corresponding parameters are listed in Table 3-3.

The parameters of the polarization curves for PCAir and NCAir were taken from measurements with leakage compensation (Appendix Figure 6.1). Due to the high amount of oxygen vacancies the samples are highly conductive. This can influence the ferroelectric phase. However, this influence is quite small and the intrinsic polarization, which is coupled with the ferroelectric phase, stays the same. This is the reason why the values from measurements with leakage compensation can be used for comparison. Only at 1 Hz the conductivity leads to an elliptic shape of the curves, while at higher frequencies, where the contribution from conductivity loss is smaller, the hysteresis loops could be measured without leakage compensation. The values for $P_S$ and $P_r$ only change by a small amount of 1 or 2 µC/cm² for all samples, which could also be in the error range of fitting, while the change in $P_{Max}$ for the samples sintered in air drops from 32.4 µC/cm² at 1 Hz to 25.5 µC/cm² at 100 Hz caused by conductivity. The coercive electric field, $E_C$, increases at higher frequencies for all samples, as it is expected from equation Eq. 1.3.

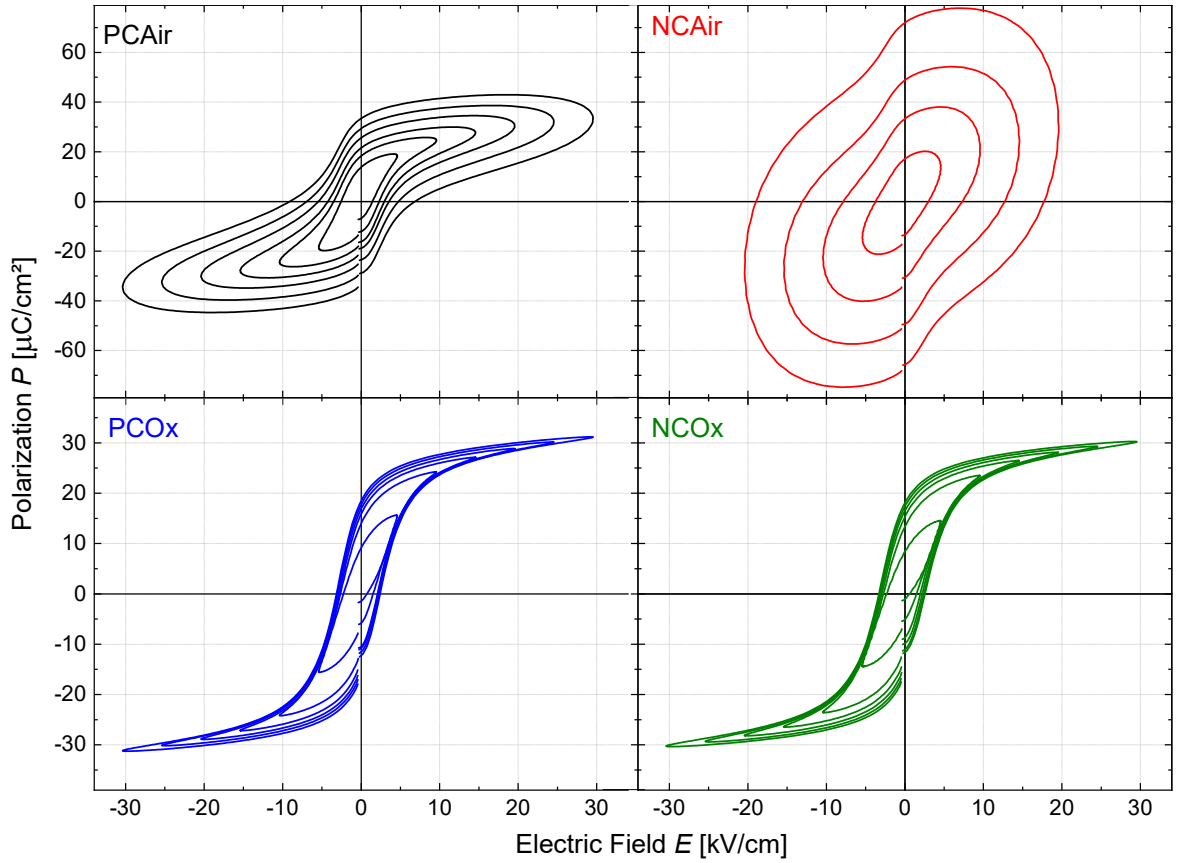


*Figure 3.10 Polarization hysteresis loops of the four different samples at room temperature and 1 Hz.*

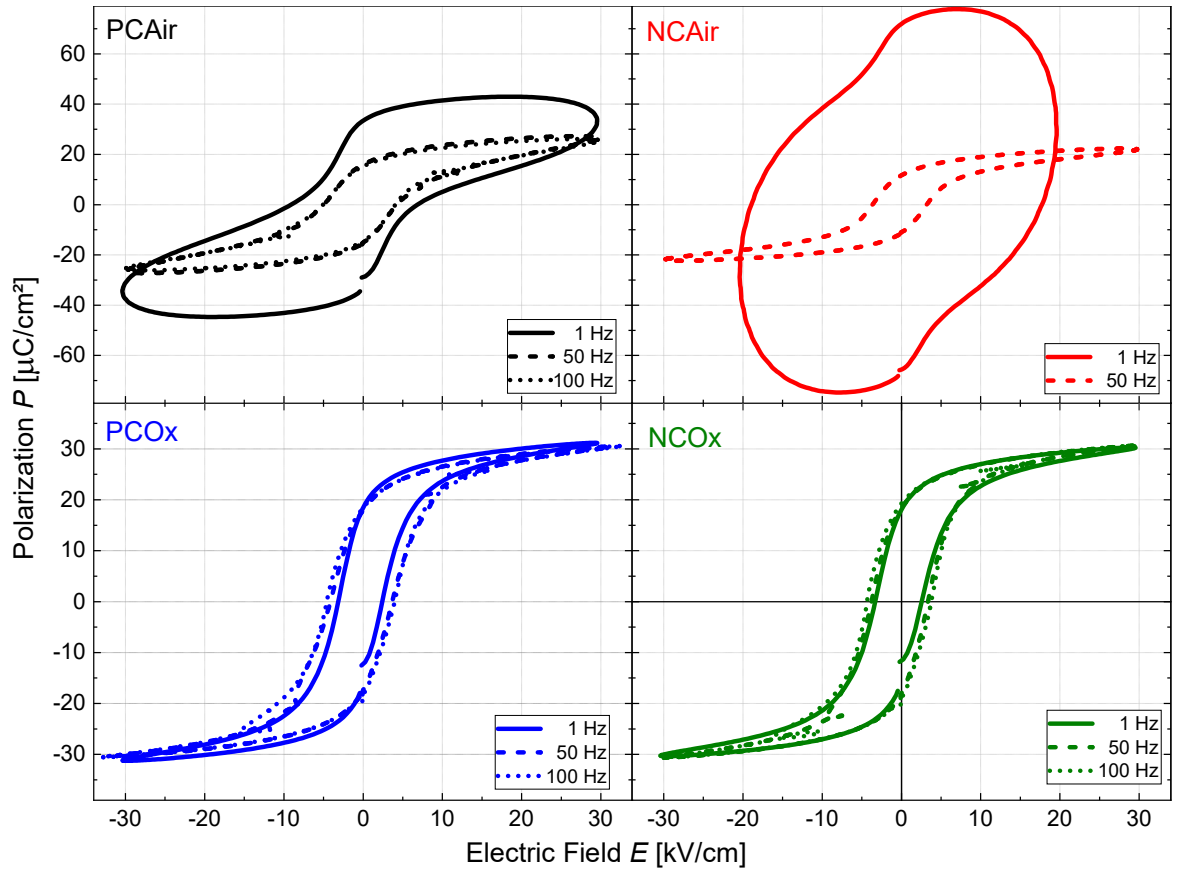


*Figure 3.11 Polarization hysteresis loops of the four different samples at room temperature and 30 kV/cm for 1, 50 and 100 Hz. The NCAir sample could not withstand 100 Hz and was broken at around 10 kV/cm.*

The comparison of the polarization hysteresis loops measured with and without the leakage compensation and at different frequencies shows that the ferroelectric properties are influenced not only by the sintering atmosphere, as $P_S$ is decreasing from $P_S$ = 27.5 µC/cm² for the samples sintered in oxygen to 23.5 µC/cm² for the samples sintered in air, but also by the way of the sample contact with the embedding powder, as $P_S$ further decreases to only 18.2 µC/cm² for the sample sintered in air and without embedded powder contact. It means that the higher amount of vacancies and defects not only counteract with the ferroelectric state, but it also increases the conductivity, which makes the use of oxygen inevitable to achieve the best ferroelectric properties.

*Table 3-3 Polarization and electric field parameters of the polarization curved dependent on the frequency. NCAir broke at 10 kV/cm at 100 Hz so no values could be detected.*

| **Sample** | ***PCAir*** | | | ***NCAir*** | | | ***PCOx*** | | | ***NCOx*** | | |
|---|---|---|---|---|---|---|---|---|---|---|---|---|
| **Frequency [Hz]** | ***1*** | ***50*** | ***100*** | ***1*** | ***50*** | ***100*** | ***1*** | ***50*** | ***100*** | ***1*** | ***50*** | ***100*** |
| $P_{Max}$ **[µC/cm²]** | 32.4 | 29.7 | 25.5 | 24.1 | 22.0 | - | 31.2 | 30.1 | 30.0 | 30.2 | 30.6 | 30.1 |
| $P_r$ **[µC/cm²]** | 17.4 | 16.0 | 15.2 | 11.2 | 11.4 | - | 18.3 | 17.9 | 18.6 | 18.2 | 18.3 | 19.2 |
| $E_C$ **[kV/cm]** | 3.9 | 5.0 | 5.2 | 3.1 | 3.6 | - | 3.3 | 4.1 | 4.6 | 3.2 | 3.7 | 4.3 |
| $P_S$ **[µC/cm²]** | 23.5 | 23.5 | 23 | 18.2 | 19 | - | 27.5 | 26.5 | 26 | 26 | 26.5 | 26.5 |

The temperature dependences of dielectric permittivity in Figure 3.12 show a broad maximum, corresponding to the phase transition from paraelectric to ferroelectric phase in all samples. For the samples sintered in oxygen, the width of the dielectric peak does not depend on frequency, but for the samples sintered in air, it broadens at smaller frequencies. The phase transition temperature is between 373 K and 375 K, which agrees well with the values reported in literature [56,151]. The peak position is independent of frequency, which points out a non-relaxor behavior of PFN, contrary to some claims in literature [70,152,153]. All samples have $\varepsilon'_{max}$ values greater than 20 000 (for 100 kHz), with the pellets sintered in oxygen having higher values, as shown in Table 3-4. It can be seen that the pellets sintered in contact with the powder have higher $\varepsilon'_{max}$ values than the pellets without contact.

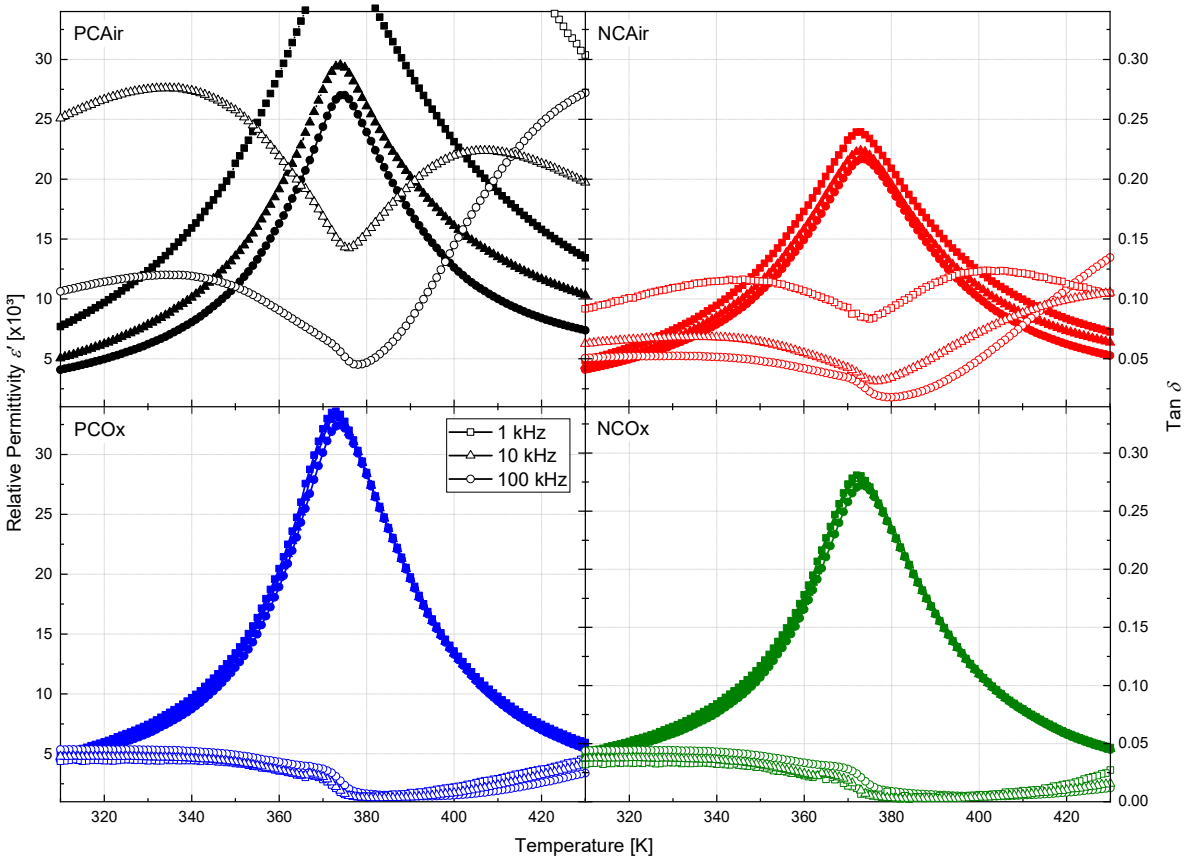


*Figure 3.12 Temperature dependences of the relative dielectric permittivity, ε′r, and dielectric loss tangent, tanδ, for the different samples measured at 100 kHz. 10 kHz, and 1 kHz.*

The dielectric loss tangent does not exceed 0.3 (at 100 kHz) for all samples. It remains stable for the oxygen-sintered samples but increases to lower frequencies for the air-sintered samples. For the PCAir and NCAir samples, the loss factor does not change much with different frequencies.

In contrast to Font et al. [79], in our case the phase transition temperature drops by only 1 K for the contact samples and remains the same for the non-contact samples. Like for the lattice constant and the grain size, this may be due to the homogeneity of the sample, which is improved by milling. Nevertheless, there is a clear difference in the diffuseness coefficient $\gamma$. The samples sintered in air have a higher diffuseness coefficient and a lower density than the samples sintered in oxygen. The pores do not contribute to the change of the Curie point. Nonetheless, the number of lead vacancies has a higher impact since the values for the samples not sintered in the embedding powder ($\gamma$ = 1.64 and 1.61) are higher than for the samples in the embedding powder ($\gamma$ = 1.37 and 1.25), which results in bigger sample volumes not contributing to the Curie point.

*Table 3-4 Comparison of the values for dielectric permittivity*

| Sample | $\varepsilon'_{RT}$ | $T_C$ [K] | $\varepsilon'_{max}$ | $\gamma$ |
|---|---|---|---|---|
| **PCAir** | 3 422 | 375 | 27 013 | 1.37 |
| **PCOx** | 3 718 | 374 | 32 436 | 1.25 |
| **NCAir** | 3 435 | 373 | 21 675 | 1.64 |
| **NCOx** | 3 218 | 373 | 27 226 | 1.61 |

### 3.2.4. Magnetic characterization

Temperature dependences of magnetization measured upon FC and ZFC for all four samples are shown in Figure 3.13. They show the typical trend for PFN [70,154,155]: The magnetization increases upon lowering temperature and has a cusp at around 154 K, which corresponds to the Néel temperature $T_N$, i. e. the paraelectric-antiferroelectric phase transition. $T_N$ is almost the same for all four samples. Upon further decrease in temperature, the slope of $M(T)$ is increasing until the magnetization reaches a maximum at around 10 K, which corresponds to a transition to the spin glass state [70,156]. The FC and ZFC curves for the samples sintered in oxygen (Figure 3.13, right) overlap well, while the FC and ZFC curves for the samples sintered in air diverge beneath $T_N$. One of the possible reasons could be a difference in the amount of $Fe^{2+}$ and $Fe^{3+}$ ions. Font et. al [79] already proved that the sintering in oxygen can prevent the formation of $Fe^{2+}$ in the material. The magnetic hysteresis loops (Figure 3.14) look very similar for all samples as well, without an opening until 10 K. Only the hysteresis loops measured at 5 K show a small opening with a magnetic coercive field of around 20 mT. With increasing temperature, the s-shaped loops are straightened and become linear above 160 K.

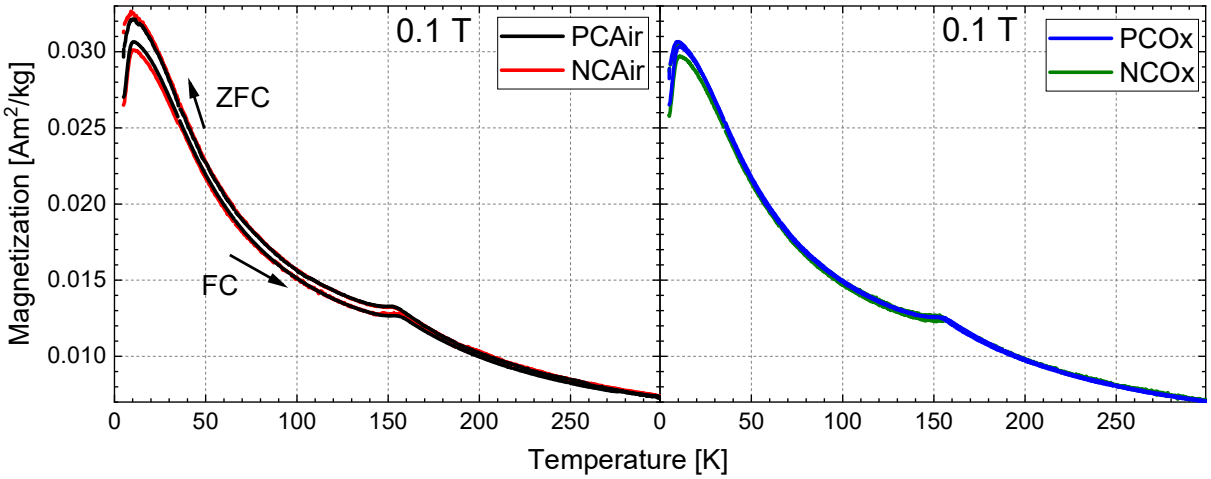


*Figure 3.13 FC-ZFC magnetization measurements at a magnetic field of 0.1 T for the samples sintered in air (left) and sintered in oxygen (right).*

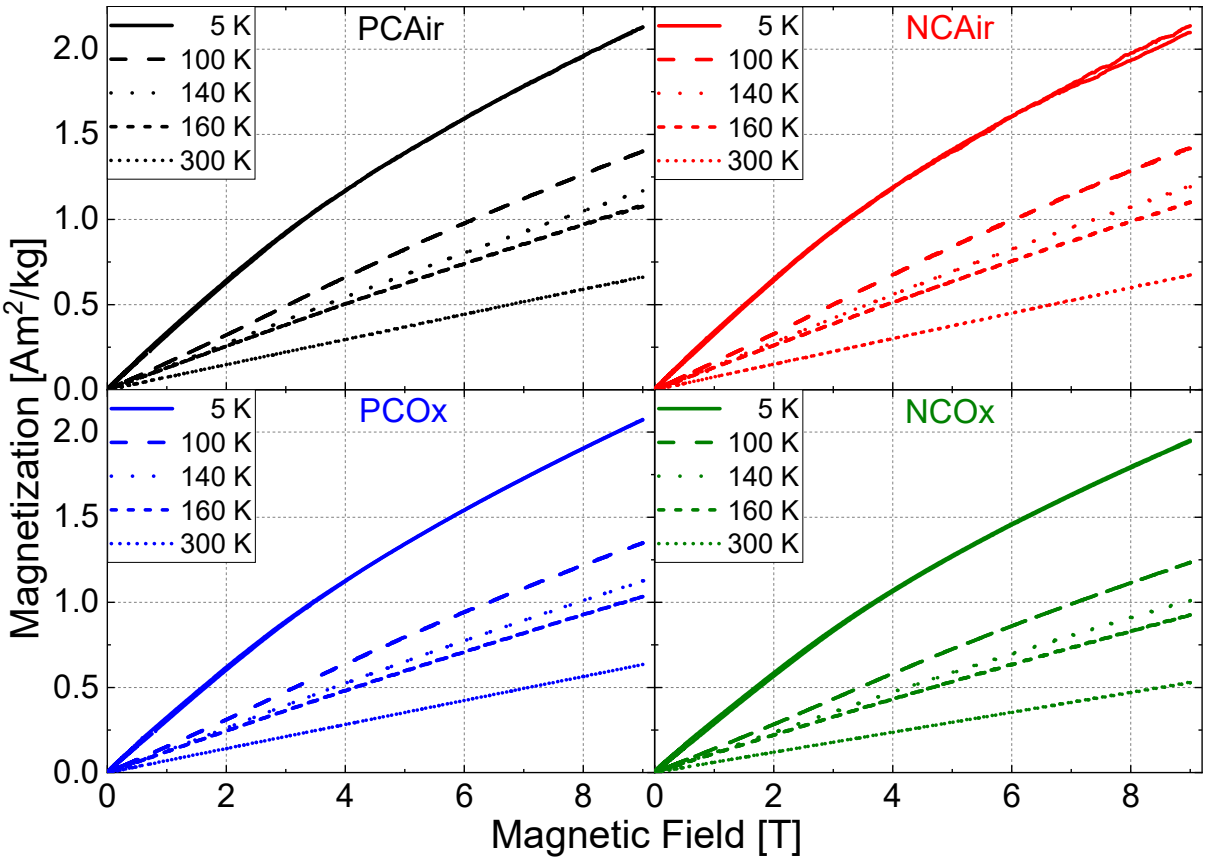


*Figure 3.14 Magnetization at temperatures 5, 100, 140, 160 and 300 K. The measurements were done also at negative magnetic fields (Appendix Figure 6.2), but for better visibility only the part corresponding to positive magnetic fields is shown.*

### 3.2.5. Summary

In this Chapter various sintering methods for powders obtained with mechanochemical synthesis were described and discussed. Sintering was carried out in oxygen and air atmosphere and the green bodies were either in direct contact with an embedding powder or separated from it by a second crucible during sintering.

It was observed that the atmosphere plays a major role in sintering of mechanochemically synthesized powders with regard to the ferroelectric and electrical properties of the obtained ceramics. It was shown that the ceramics sintered in oxygen had better ferroelectric and dielectric properties than the ceramics sintered in air. The former method minimized the number of oxygen vacancies and prevented the formation of $Fe^{2+}$, both a responsible for increasing the conductivity of the samples.

There is also a slight difference between the samples sintered by the contact and non-contact methods. The samples sintered in oxygen atmosphere in contact with the sacrificial powder showed slightly improved properties, however, the difference was more noticeable for the samples sintered in air. The ferroelectric properties of PFN were strongly affected by the volatility of lead. In the contact mode, the sacrificial powder ensured a more lead-rich environment in comparison to the non-contact mode. This prevents rapid lead diffusion out of the lattice and the formation of lead vacancies. As a result, the spontaneous polarization is greater for the samples sintered in contact.

FC-ZFC measurements shows the same trend for all samples with the difference in a bifurcation for the samples sintered in air. These bifurcations come from the formation of $Fe^{2+}$ during sintering influencing the magnetic behavior like shown. However, the magnetic hysteresis loops shows no difference in shape for the samples sintered in oxygen or air.

A comparison to the work of Font et al. [79] shows that not only the sintering atmosphere (oxygen or air), but also the synthesis method with all intermediate steps has influence on the final properties of the ceramic.

## 3.3. Influence of powder synthesis routes

As a significant difference in sample quality was achieved only due to the change in sintering atmosphere and the sintering conditions, a systematic study of different powder synthesis routes with focus on the precursor composition was performed, because the properties of PFN might change. This is explained and summarized in this Chapter.

### 3.3.1. Synthesis routes

The different synthesis routes used for the comparison are the solid state (SS), the molten salt (MS), the combustion (CO), the hydrothermal (HT), and the mechanochemical activation (MA) methods. A schematic overview of the synthesis steps is illustrated in Figure 3.15.

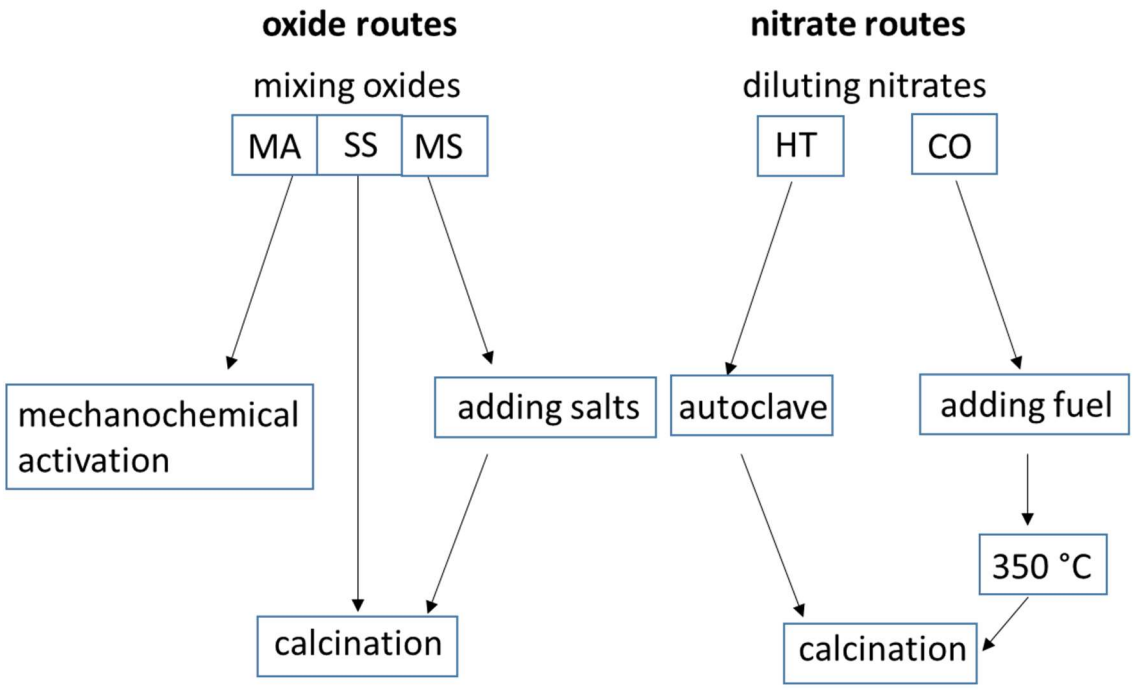


*Figure 3.15 Schematic representation of the different synthesis routes of PFN powder preparation (MA: mechanochemical activation, SS: solid state, MS: molten salt, HT: hydrothermal, CO: combustion). © 2019 IEEE. Reprinted, with permission, from Ref. [76]*

#### 3.3.1.1. Solid state (SS) and molten salt (MS)

For SS and MS synthesis, stoichiometric amounts of PbO (99.99 %, Alfa Aesar), premilled $Fe_2O_3$ (Chapter 3.1), and $Nb_2O_5$ (99.9 %, Alfa Aesar) were mixed. For the MS synthesis, NaCl (99.8 %, Riedel de Haën) and KCl (≥ 99 %, Fluka) salts were added. The powder to salt ratio was 1:1 wt. % and the NaCl to KCl salt molar ratio was 1:1 [145]. The powders were mixed in a planetary ball mill for 4 h, so that a homogeneous mixing ratio was created.

#### 3.3.1.2. Hydrothermal (HT) and combustion (CO)

For both the HT and CO synthesis routes, the stoichiometric amounts of $Pb(NO_3)_2$ (≥ 99 %, Sigma Aldrich), $Fe(NO_3)_3 \cdot 9H_2O$ (98+ %, Alfa Aesar), and $(NH_4)NbO(C_2O_4)_2 \cdot xH_2O$ (99.99 %, Sigma Aldrich) were dissolved in water separately and poured together. For the CO synthesis, an additional fuel containing $NH_4NO_3$ (99+ %, Acros organics) and urea $CO(NH_2)_2$ (> 99 %, Fluka) was added to the solution in a molar ratio 1:5 (fuel:Nb), as in [144]. Both solutions were then dried while stirring. The HT synthesis was carried out in an autoclave for 2 h at a temperature of 140 °C and a pressure of 7 bar. The CO synthesis was performed by heat treatment of the mixture at 350 °C for 1 h, afterwards the powder changed its bright yellowish color to brownish.

For all four methods, the obtained powders were then calcined at 850 °C for 1 h in oxygen atmosphere. To reduce the particle size, the calcined powders were ground again in a planetary ball mill for 4 h.

#### 3.3.1.3. Mechanochemical activation (MA)

The mechanochemical activation is already described in detail in Chapter 3.2.1. The powder used here was prepared under oxygen atmosphere without sacrificial powder (the NCOx sample). In order to make the comparison with the other methods easier, it is called MA in the following.

Finally, the powders obtained from all the methods were pressed into pellets and sintered at 1000 °C (950 °C for the MA synthesized powder) for 2 h in an oxygen atmosphere, as this gives the best properties, was shown in Chapter 3.2.

Before the MS powder was pressed into green bodies, the NaCl and KCl residues were removed in several steps of washing with distilled water. In order to minimize the PbO losses during the heat treatment, sintering was carried out in the presence of PFN sacrificial powder. The obtained ceramic samples were cut and polished for further investigation.

### 3.3.2. Crystalline structure and phase composition

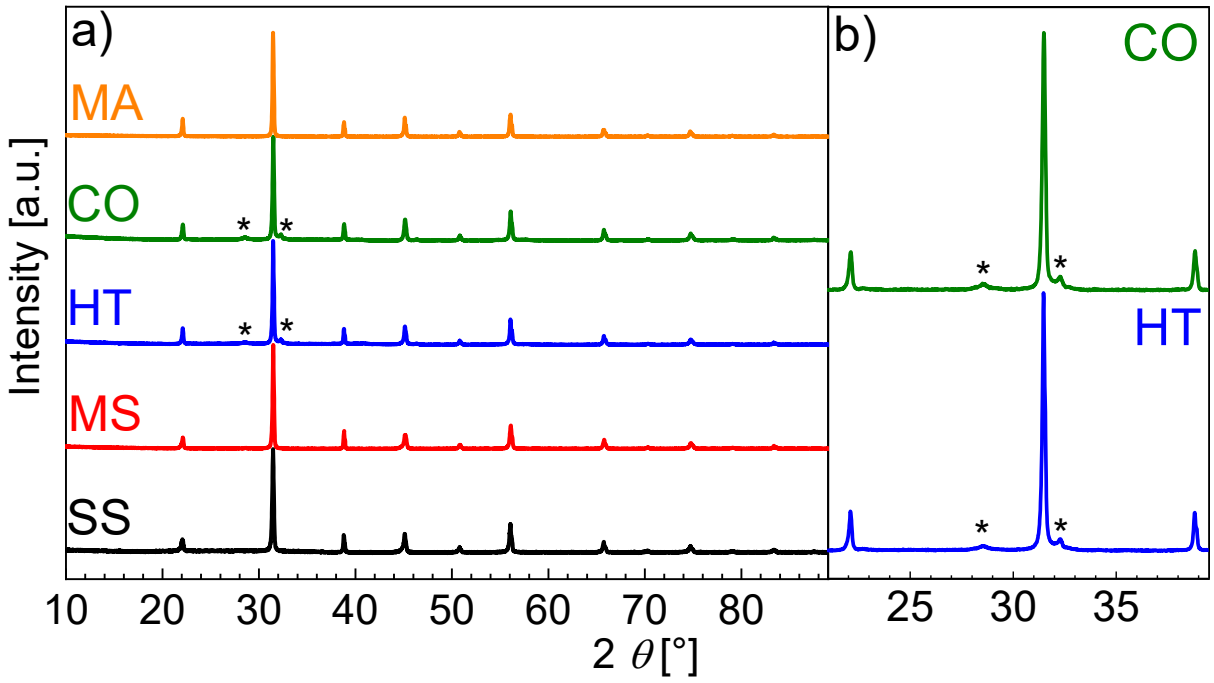


*Figure 3.16 a) XRD patterns of PFN ceramics prepared by different synthesis methods. B) Close up of the secondary peaks for CO and HT. The peaks of the secondary PbO phase are marked by asterisk symbols.*

Figure 3.16 a shows the diffraction patterns of all ceramic samples. The oxide routes result in a pure single-phase, while the samples prepared by the nitrate routes show XRD peaks - marked with an asterisk - that do not correspond to the perovskite phase (see also zoomed in image in Figure 3.16 b). According to the standard Rietveld refinement, this secondary phase is identified as additional PbO (ICSD 98-006-2842). The amount of PbO is 2.6 % and 1.8 % for the CO and HT syntheses, respectively. The PbO secondary phase was only detected in the samples prepared by the nitrate routes. A reason for that can be the use of the nitrate precursors, which involves additional steps in the synthesis, like dissolving, mixing, and drying. The possibility of contamination is higher, because nitrates form hydrates, in which water and/or $CO_2$ from the atmosphere can be adsorbed. Despite heating up to 1000 °C, some residuals may remain, which will lead to a change in stoichiometry of the final composition. In addition, the transition of the nitrates into the PbO could be favored in contrast to the transition into the Perovskite due to different binding enthalpies.

A detailed refinement of the XRD pattern allowed to determine the PFN structure in all of these samples as a mixture of monoclinic (ICSD 98-008-8358, *C1m1*) and rhombohedral (ICSD 98-009-0491, *R3m*) phases, with the monoclinic being the main phase (Table 3-5).

*Table 3-5 The Rietveld refinement analysis data and relative density of the PFN ceramics obtained by different synthesis methods.*

| **Synthesis Method** | **Oxide Routes** | | | **Nitrate Routes** | |
|---|---|---|---|---|---|
| | **SS** | **MS** | **MA** | **CO** | **HT** |
| **Monoclinic [%]** | 81.7 | 91.1 | 96.5 | 80.2 | 86.5 |
| **Rhombohedral [%]** | 18.3 | 8.9 | 3.5 | 17.2 | 11.8 |
| **PbO [%]** | - | - | - | 2.6 | 1.8 |
| $R_{wp}$ | 14.96 | 12.53 | 8.26 | 8.05 | 7.87 |
| **Relative density [%]** | 94 | 93 | 99 | 67 | 81 |

The lattice parameters for the different methods obtained by Rietveld refinement are listed in Table 3-6. The lattice parameters of the *R3m* phase in the hexagonal presentation, show no change in the different methods except for the CO method. There, the lengths for *a* and *b* are slightly larger and *c* is slightly compressed. For the monoclinic phase, however, differences in the lattice parameters can be seen, but they do not seem to show a trend.

The values of the relative density are shown in Table 3-5. The densification of the ceramics prepared by the oxide routes (SS, MS and MA) is quite high and amounts to ≥ 93 % of the theoretical density. The MA ceramic has the highest relative density value of 99 %, followed by SS (94 %). This is different for the nitrate routes, which show densities of 81 % and 67 % of the theoretical density for the HT and CO synthesis routes, respectively. These values are much lower, the possible reasons for the differences will be discussed more in detail in the following paragraph.

*Table 3-6 The Rietveld refinement analysis data: lattice constants for the monoclinic (mono) and hexagonal (hexa) phase obtained by different synthesis methods.*

| **Synthesis Method** | **Oxide Routes** | | | | | | **Nitrate Routes** | | | |
|---|---|---|---|---|---|---|---|---|---|---|
| | **SS** | | **MS** | | **MA** | | **CO** | | **HT** | |
| | **mono** | **hexa** | **mono** | **hexa** | **mono** | **hexa** | **mono** | **hexa** | **mono** | **hexa** |
| ***a*** | 5.674 | 5.665 | 5.669 | 5.665 | 5.677 | 5.665 | 5.674 | **5.667** | 5.673 | 5.665 |
| ***b*** | 5.670 | 5.665 | 5.669 | 5.665 | 5.671 | 5.665 | 5.669 | **5.667** | 5.669 | 5.665 |
| ***c*** | 4.023 | 6.959 | 4.020 | 6.959 | 4.019 | 6.959 | 4.021 | **6.951** | 4.02 | 6.959 |
| ***α*** | 90 | 90 | 90 | 90 | 90 | 90 | 90 | 90 | 90 | 90 |
| ***β*** | 90.16 | 90 | 90.13 | 90 | 90.13 | 90 | 90.14 | 90 | 90.13 | 90 |
| ***γ*** | 90 | 120 | 90 | 120 | 90 | 120 | 90 | 120 | 90 | 120 |

The SEM images of the fractured surfaces are shown in Figure 3.17. The nitrate routes tend to produce smaller, rounder grains with a grain size of 1.14 and 0.58 µm for CO and HT, respectively. For the precursors dissolved in a solution the particles are smaller before calcination and sintering than in the case of the oxide methods. Also, the images show a high porosity, confirmed by the low density of the nitrate routes, so grains of spherical shape can be formed. The grains of the ceramics prepared by the SS and MA methods have sizes of 3.45 and 2.28 µm, respectively, and differ only slightly in shape. The ceramics prepared by these methods have less pores and more faceted grains than the ceramics synthesized by the nitrate routes. In the publication by Chiu et al. [145] the powders synthesized by the SS and MA methods, calcined at 800 and 900 °C, are compared. The difference in grain size of the powders prepared by the MS methods compared to the conventional SS method is visible in their work. The grains for the MS method after calcination at 800 °C are already bigger than for the SS method and are even further increasing at a calcination temperature of 900 °C. This is in agreement with the results of this work where the MS method results in the ceramics with the largest grain size of 8.24 µm.

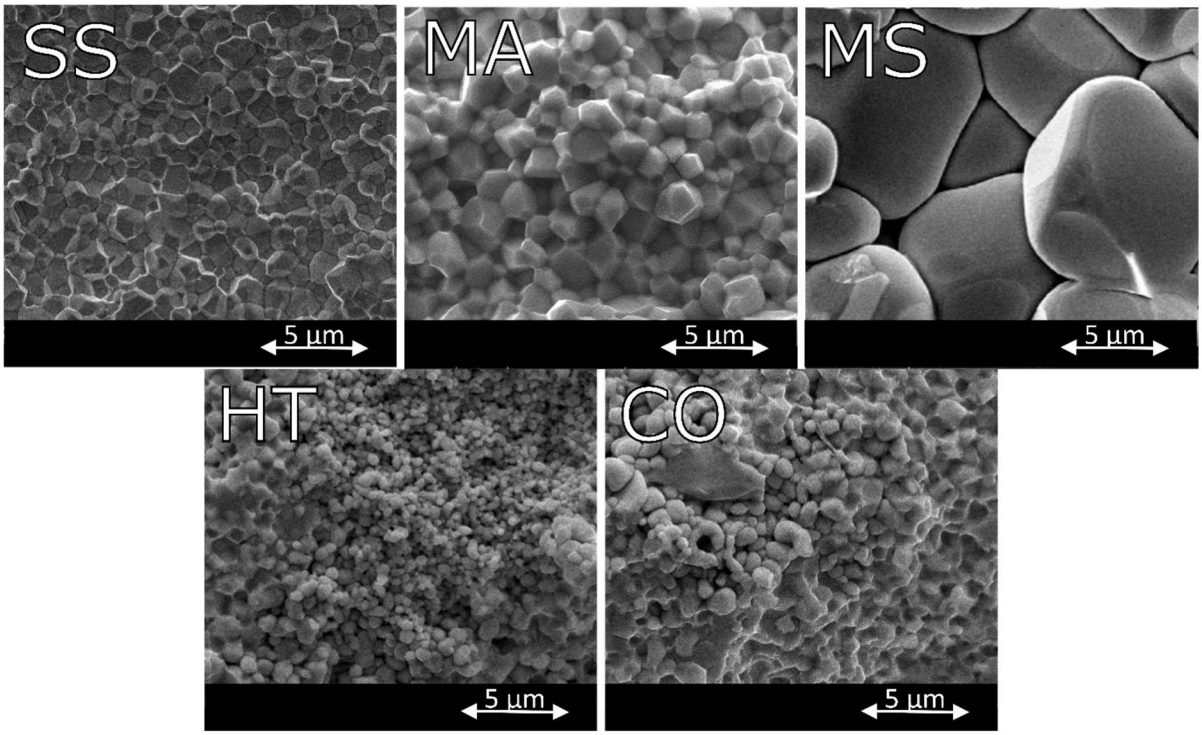


*Figure 3.17 Fractured SEM images for the ceramics prepared by the different synthesis methods.*

### 3.3.3. Dielectric and ferroelectric response

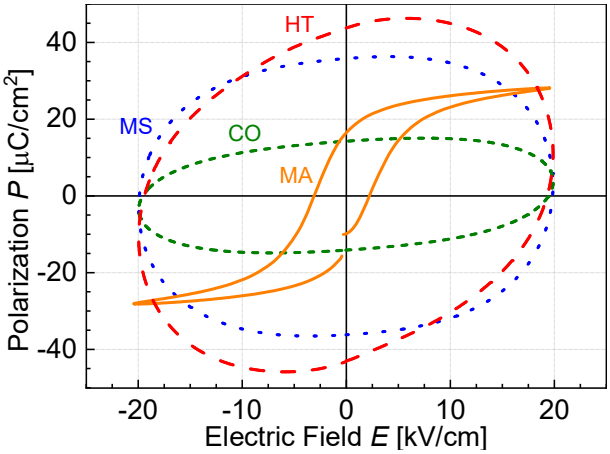


*Figure 3.18 The polarization hysteresis loops of the ceramics synthesized by the different synthesis routes measured at room temperature and at a frequency of 50 Hz. Due to the high electrical conductivity, the P–E loop of the SS synthesized sample is not shown. © 2019 IEEE. Reprinted, with permission, from Ref. [76].*

The polarization hysteresis loops for all samples are shown in Figure 3.18. Only the sample from the MA synthesis route has a typical ferroelectric hysteresis loop with the saturated polarization at room temperature, while for the others the polarization is superimposed by a large conductivity contribution resulting in a round-shaped hysteresis. The values for $P_S$, $P_r$ and $E_C$ of the MA sample are 28.1 µC/cm$^2$, 16.7 µC/cm$^2$ and 3.1 kV/cm, respectively, which agrees with literature [79,157]. While the MA synthesis is the only method which produces PFN

samples that are not highly conductive, this leads to the conclusion that the additional calcination step for the samples prepared by SS, MS, CO and HT is associated with a higher conductivity. As already mentioned, the volatility of PbO above 700 °C results in the formation of Pb vacancies, which adversely affect the dielectric and ferroelectric properties of lead-contained ceramics. In Chapter 3.2.3 it is already discussed, which influence Pb vacancies have on the ferroelectric properties and on the appearance of the polarization hysteresis loops. A higher amount of Pb vacancies leads to a more rounded shape of the polarization hysteresis loops, as shown in Figure 3.10 for the PFN samples sintered in air. Although the samples discussed in this Chapter are sintered in oxygen, the loss of Pb by the SS, MS, CO and HT methods is much higher due to the extra calcination step. Thus, the stoichiometry of the material is strongly influenced, and not only elliptic polarization hysteresis loops are seen, but rounded-oval ones.

The temperature dependency of the real permittivity ($\varepsilon'$) and the dielectric loss (tan $\delta$) at a frequency of 1 kHz are presented in Figure 3.19 a and b, respectively. In the samples prepared by the oxide routes the dielectric response shows a broad maximum with a peak position of $\varepsilon'$ at temperatures of 391 K and 372 K for SS and MA, respectively. This maximum corresponds to the paraelectric-ferroelectric phase transition, and its position (the Curie temperature, $T_C$) is in agreement with the literature data for SS [79,148] and MA [157] synthesized ceramics. However, the value for $\varepsilon'$ at $T_C$ for SS (> 60 000) is three times higher than for the MA samples (> 25 000). A reason for that is the higher electrical conductivity as already discussed in the paragraph before. It is also confirmed by the dielectric losses in Figure 3.19 (right) where significantly higher tan $\delta$ values are obtained for the SS synthesized sample. For the ceramics synthesized by the MS, CO, and HT routes, the dielectric permittivity increases continuously upon heating and no maximum can be detected. In these samples the conductivity contribution becomes very large already around 370 and 380 K and overlaps the peak of dielectric permittivity at $T_C$. The MA sample has the lowest dielectric loss tan $\delta \leq 0.1$ in contrast to the other methods where tan $\delta$ rapidly increases with higher temperatures.

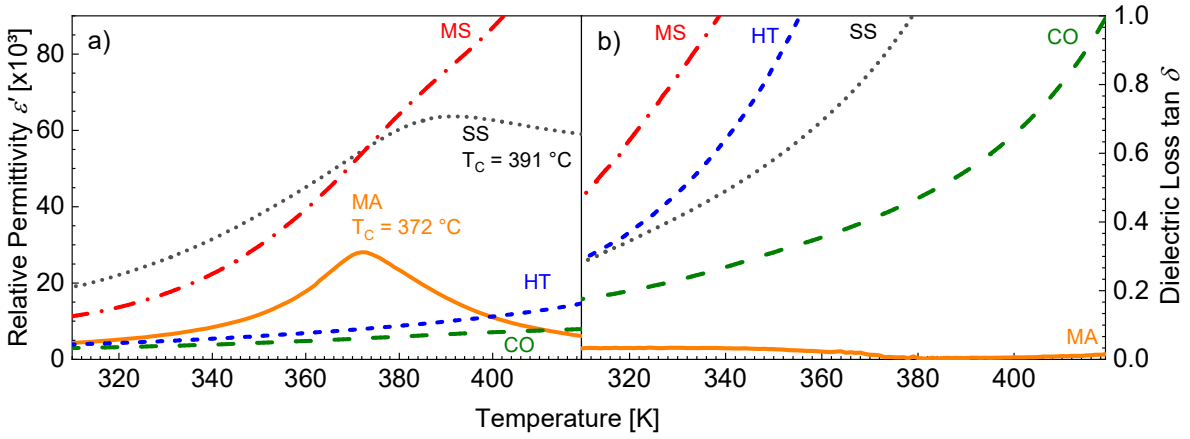


*Figure 3.19 The temperature dependences of (a) the real relative permittivity and (b) dielectric loss tangent of the samples prepared by the different synthesis methods measured at 1 kHz. © 2019 IEEE. Reprinted, with permission, from Ref. [76].*

### 3.3.4. Optical measurements

Bharti et al. [22] proposed that PFN has a direct band gap of 0.43 eV by calculation of the density of states. To estimate the band gap experimentally, measurements of the reflectance of PFN ceramics at room temperature were performed. Figure 3.20 shows the Tauc plots plotted from the Kubelka-Munk function assuming a direct band gap for the PFN ceramics prepared by the various synthesis methods. It can be seen that the experimental data significantly differ from the theoretical calculations in Ref. [22]. The measured band gap values vary from 2.17 eV to 2.55 eV. The MA synthesis provides the material with the largest band gap of 2.55 eV followed by the MS (2.3 eV) and SS (2.28 eV) methods. The smallest band gap has the ceramics prepared by the HT method (2.17 eV) and slightly higher the CO method (2.21 eV). The differences in the methods could lead to an increase in the number of defects, which reduce the measured effective band gap value due to the formation of defect-related trap states in the band gap. PFN can be compared with other perovskite oxide materials, like $BiFeO_3$ or PZT. Therefore, it is reasonable to expect that the band gap of PFN is higher than at least 2.0 eV. Moreover, it is likely that the true band gap value lies in the range obtained for the MA method (~ 2.5 eV), which provides the samples with the lowest amount of defects. Indeed, the MA synthesized ceramics have the highest density, low electrical conductivity and no secondary phases.

For completeness, the Tauc plots assuming an indirect band gap were also analyzed. They are shown in Appendix Figure 6.3. Also, in this case, the band gaps are higher than 2.0 eV. When discussing the band structure of PFN, it has to been taken into account that UV-Vis

spectroscopy only gives the energy of optical transitions and not the fundamental band gap (see Chapter 2.6.3). Because the fundamental band gap is larger than the optical band gap, the band gap of the PFN ceramics is definitely larger than 2.17 eV.

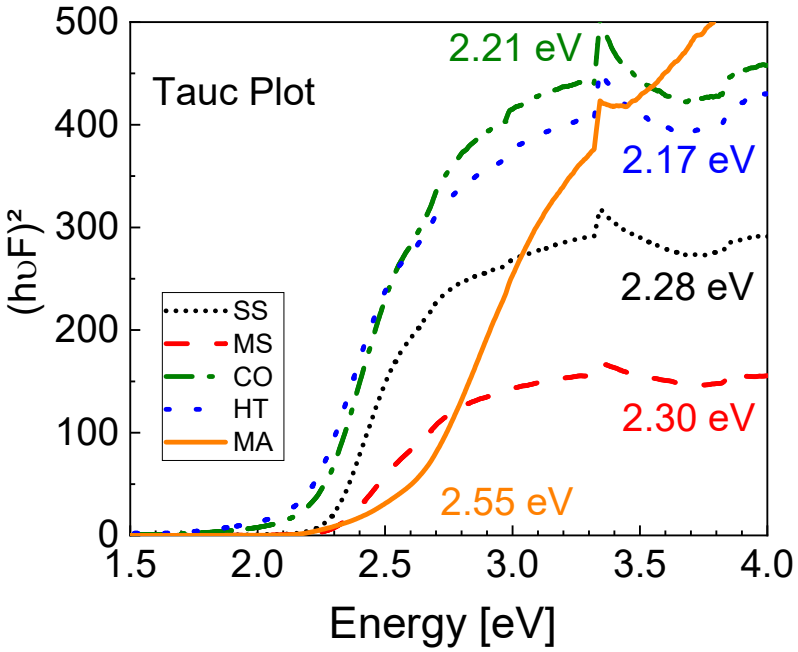


*Figure 3.20 The Tauc plots of the Kubelka-Munk function for PFN ceramics prepared by different synthesis routes. A direct band gap is assumed. © 2019 IEEE. Reprinted, with permission, from Ref. [76].*

### 3.3.5. Summary and conclusions

Different methods were used for the synthesis of PFN ceramics using on the one hand oxide precursors and on the other hand nitrate precursors. All samples were treated the same way as the calcination and sintering temperatures were the same, except for the MA synthesis, where no calcination step was needed. The oxide routes show a pure perovskite structure with mainly a monoclinic and a small amount of a rhombohedral phases, while the nitrate routes have a small amount of PbO left.

The samples prepared by the oxide precursors have a higher relative density of ≥ 93 % in comparison to the nitrate routes which only achieved 67 – 81 % of the theoretical density. Fractured SEM images show the reason for this. The “nitrate” ceramics have smaller rounded particles with a grain size of 0.58 (HT method) to 1.14 µm (CO method) with more pores than the ceramics prepared by the oxide routes with a grain sizes of 2.28 (SS method) and 4.45 µm (MA method). The MS method stands out here with a grain size of 8.24 µm.

PFN Ceramics

The sample with the best electrical properties is the MA ceramic, which shows a typical ferroelectric loop with saturated polarization at room temperature, a well-defined maximum of the dielectric permittivity at the paraelectric-ferroelectric phase transition, and low dielectric losses, $\tan \delta \leq 0.1$. The other samples, synthesized both by the nitrate and oxid routes, have large electrical conductivity, so their ferroelectric properties cannot be resolved by macroscopic measurements. The reason for that is mostly related to the high loss of Pb at the additional calcination step, which leads to Pb vacancies and related defects.

All these properties affect the optical properties as well, as the different defects form trap states within the band gap. Different from the literature the band gap is altering from 2.17 to 2.55 eV with the MA synthesized sample having the largest band gap due to less defects.

These results show that the choice of the synthesis route has a strong influence on all properties of the PFN. Each method requires to find its own optimum conditions for achieving the best results, with lead and oxygen compensation during the heating stages being fundamental.

## 3.4. Temperature variation for the solid-state route

As not only the method and sintering atmosphere can change the properties, this Chapter deals with the solid-state method putting the focus on the impact of the calcination and sintering temperatures. The solid-state method was chosen since the mechanochemical activation process - which had the best results in the last Chapter - could not be performed at the university in Essen. For this reason, the solid state method has been chosen as it promised the best results due to its easier synthesis steps and fewer precursors. Besides the change in sintering atmosphere the variation in calcination and sintering temperature promised to have the biggest influence on the properties. These parameters were changed while looking for the optimal combination of phase purity, density, dielectric, ferroelectric, and magnetic parameters. It was found out that there is a temperature regime that allows to obtain ceramics with large polarization and low dielectric losses. The influence of the sintering temperature on the diffuseness of the ferroelectric phase transition and the Néel temperature is discussed as well. Information that follows in this Chapter is mainly taken from [87].

### 3.4.1. Preparation

The ceramics described in this Chapter were prepared using the conventional solid-state method. Stoichiometric amounts of PbO (99.99 %, Alfa Aesar), premilled $Fe_2O_3$ (Chapter 3.1), and $Nb_2O_5$ (99.9 %, Alfa Aesar) were mixed by a planetary ball mill for 4 h. As previously discussed, lead loss compensation plays a major role for achieving good final properties, so preventively 2 wt. % excess of lead oxide were added for compensation. To obtain the best properties, the milled powders were calcined at three different calcination temperatures $T_{Cal}$ of 750 °C (C1), 800 °C (C2), and 850 °C (C3) for 1 h. For each $T_{Cal}$, three green bodies, around 5 mm thick, were uniaxially pressed at 250 MPa and sintered at three different sintering temperatures $T_s$ of 1000 °C (S1), 1050 °C (S2), and 1100 °C (S3) for 2 h. Both calcination and sintering steps were curried our in an oxygen atmosphere. The heating/cooling ramp was 2 K/min. In total, samples were prepared according to nine different routes (Table 3-7) and cut into multiple thin pellets with a thickness of 200 - 300 µm each. For all further experiments at least four of these thin pellets were measured.

*Table 3-7 Overview of sample naming.*

| **Sintering temperature $T_S$** | **Calcination temperature $T_{Cal}$** | | |
|---|---|---|---|
| | **750 °C** | **800 °C** | **850 °C** |
| **1000 °C** | C1 S1 | C2 S1 | C3 S1 |
| **1050 °C** | C1 S2 | C2 S2 | C3 S2 |
| **1100 °C** | C1 S3 | C2 S3 | C3 S3 |

### 3.4.2. Crystalline structure and phase composition

From literature [62,76,78,84] it is well known, that the perovskite phase is not easily formed in the case of PFN, because it competes with the pyrochlore phase in almost all synthesis methods. On this basis it is not possible to obtain a pure perovskite phase at low calcination and sintering temperatures. When only the calcination step is used, not only perovskite is formed, but also pyrochlore, and, depending on the calcination temperature, other phases as well, as shown in Figure 3.21. The ratio of the different phases compared to the pure perovskite (ICSD 98-008-8358) depends on the calcination temperature. Other phases, as the precursor oxides, disappear at higher temperatures: their amount decreases from 18 % at 750 °C, to 1.8 % at 800 °C, and vanishes completely at 850 °C. The pyrochlore phase is more persistent and only reduces from 46.7 % (750 °C) to 38.2 % (800 °C). Even at higher $T_{cal}$, 3.3 % of pyrochlore is left meaning that no pure perovskite could be achieved after calcination. This contradicts the work of Jenhi et al. [78], in which they calcined PFN at 850 °C without lead excess and got a pure perovskite phase. However, they only focused on phase formation and did not investigate other properties or the influence of lead vacancies on the further properties.

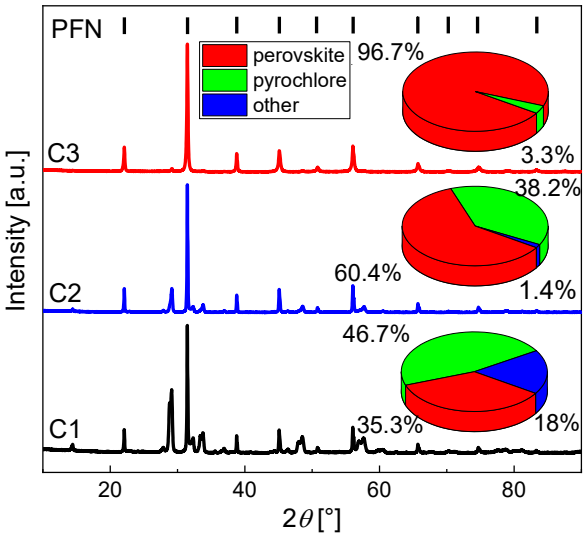


*Figure 3.21. XRD patterns of PFN powders synthesized at different calcination temperatures: C1, black (750 °C); C2, blue (800 °C); C3, red (850 °C), in comparison to the pure perovskite phase for bulk PFN (lines on top). The pie charts show the relative amounts of the perovskite, pyrochlore, and other phases in the powders. © 2021 Elsevier Ltd and Techna Group S.r.l.. Reprinted, with permission, from Ref. [87].*

To achieve a highly dense dielectric ceramic with a pure perovskite phase, a sintering step is necessary which can change the phase content strongly, as it can be seen in Table 3-8. No precursor oxides are left anymore and the higher both the calcination and the sintering temperatures, the less pyrochlore phase remains as well. For C1 a sintering temperature of 1100 °C is necessary for a pure perovskite, while at C2 1050 °C is sufficient. C3 needs the same sintering temperatures as C2, but with the difference that the amount of pyrochlore in S1 is halved. The pyrochlore phase is less than 1 % in all samples, however, a sintering temperature of 1050 °C is necessary for a pure phase independent of the initial calcination temperature.

*Table 3-8. The relative amount of the pyrochlore phase in the PFN ceramics for the different calcination and sintering temperatures.*

| **Sintering temperature** $T_S$ | **Calcination temperature $T_{Cal}$** | | |
|---|---|---|---|
| | 750 °C | 800 °C | 850 °C |
| 1000 °C | 0.97 ± 0.31 % | 0.73 ± 0.53 % | 0.24 ± 0.29 % |
| 1050 °C | 0.98 ± 0.10 % | 0.00 ± 0.00 % | 0.00 ± 0.00 % |
| 1100 °C | 0.00 ± 0.00 % | 0.00 ± 0.00 % | 0.00 ± 0.00 % |

According to literature, the crystalline phase of PFN is either monoclinic [158,159] or rhombohedral [57,83,160]. However, as already discussed in the previous Chapters, Rietveld refinement gives the best fit when considering a mixture of monoclinic (ICSD 98-008-8358, space group $C1m1$) and rhombohedral (ICSD 98-009-0491, space group $R3m$) phases. The ratio of monoclinic to rhombohedral phases varies with the calcination/sintering temperature, as can be seen in Figure 3.22, but the main phase always remains monoclinic with a content of more than 68 mol. %. What is also striking here is, that the amount of the rhombohedral phase increases with the higher synthesis temperatures. As an explanation for this we suggest that the rhombohedral phase might be energetically more preferable at higher temperatures.

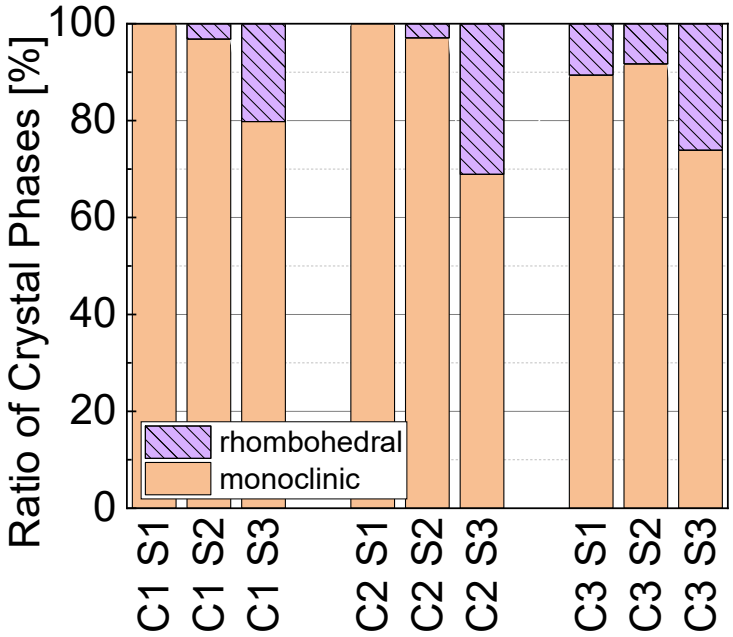


*Figure 3.22. Ratio of the rhombohedral and monoclinic phases in the sintered PFN ceramics, in percent. The pyrochlore phase was excluded here from the analysis for all samples © 2021 Elsevier Ltd and Techna Group S.r.l.. Reprinted, with permission, from Ref. [87].*

The values for the Archimedes density in relation to the theoretical density for all temperature combinations are displayed in Figure 3.23. With increasing either calcination or sintering temperature, the density becomes higher. The density of the perovskite phase (ISCD 98-008-8358, $\rho = 8.47$ g/cm³) is higher than for the pyrochlore phase (ISCD 98-001-7038, $\rho = 6.78$ g/cm³). When comparing S1, the density step from C1 to C2 is not remarkable high, due to the fact that after calcination, the amount of pyrochlore is only decreasing by around 10 %, so after sintering the density changes from 79 to 81 %. However, when the pyrochlore content is small after calcination like in C3, the density increases rapidly up to 93 %. The change in the density at S3 is much smaller: More heat energy is given to the system, so the perovskite phase can form much faster. When focussing on the same calcination

temperature and increasing the sintering temperature, the relative density is increasing as well. Diffusion processes are faster and easier at higher temperatures so that also at C3, where only 3.3 % pyrochlore is left, densification is still higher with the higher sintering temperature.

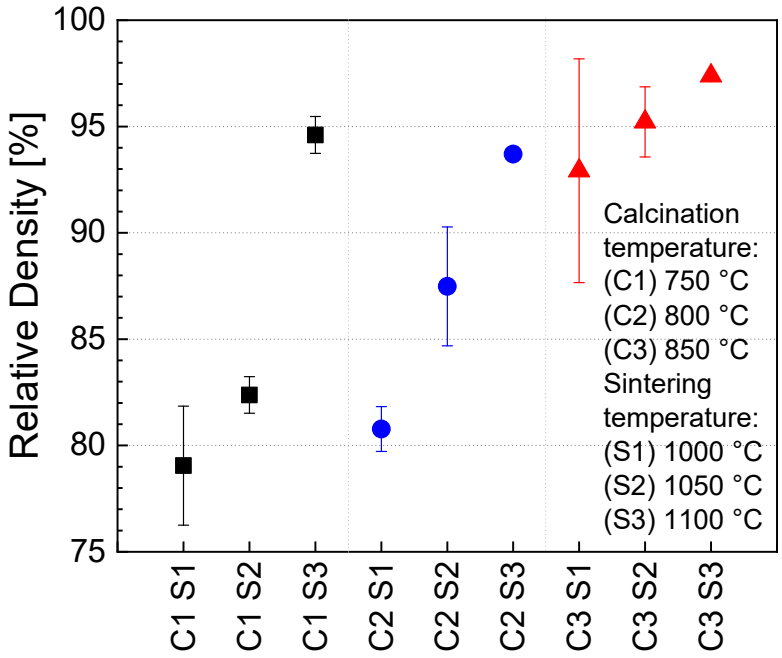


*Figure 3.23. The relative Archimedes density is shown for different calcination temperatures (C1-C3) and different sintering temperatures (S1-S3), respectively. Acronyms are shown in the right bottom corner © 2021 Elsevier Ltd and Techna Group S.r.l.. Reprinted, with permission, from Ref. [87].*

*Table 3-9. The grain size values of the PFN ceramics for the different temperature combinations measured on the fractured samples.*

| **Sintering temperature** $T_S$ | **Calcination temperature $T_{Cal}$** | | |
|---|---|---|---|
| | **750 °C** | **800 °C** | **850 °C** |
| **1000 °C** | 2.3 ± 0.7 µm | 1.6 ± 0.5 µm | 2.9 ± 1.1 µm |
| **1050 °C** | 1.6 ± 0.5 µm | 1.5 ± 0.5 µm | 1.6 ± 0.5 µm |
| **1100 °C** | 10.9 ± 3.2 µm | 20.9 ± 7.5 µm | 15.8 ± 4.6 µm |

For further investigations, SEM images were taken for both the powders (after calcination) and the ceramics (fractured and thermally etched), which are shown in Figure 3.24. All calcinated powders (Figure 3.24 (a - c)) have a small particle size but differ in shape. The C1 powders

(Figure 3.24 a) have random particle shapes with sharp edges and additionally some elongated particles. For the higher calcination temperature C2 (Figure 3.24 b), the particles seem to have softer edges and are more rounded. They are partially sintered and agglomerated. For the highest calcination temperature C3 (Figure 3.24 c), the particles start to form some sintering necks. The calcination temperature influences not only the formation of the perovskite phase, but also the particle shape. When the temperature is high enough, the particles even start to partially sinter. With further increasing the calcination temperature the risk of formation of hard sintered agglomerates is growing. These are difficult do densify at the sintering step, since the pores will be too big. The fractured images of the sintered ceramics (Figure 3.24 (d - l)) display a uniform distribution of grains and well-defined grain boundaries. In Table 3-9 the corresponding grain sizes for all nine samples are listed. The grain size is around 2 µm for a sintering temperature of 1000 °C and only intergranular fracture is observable. When the sintering temperature is increased to 1050 °C (S2) the grain size does not change notably. At the calcination temperatures of 800 and 850 °C transgranular fracture appears. When the sintering temperature increases further to 1100 °C, all samples show transgranular fracture. Due to the heat impact, the grain boundaries are strengthened and the bigger grains seem to break inside more easily than along the grain boundaries. What is noticeable in particular is that at a sintering temperature of 1100 °C, the grain size increases rapidly to 10 µm - 20 µm. The calcination temperature influences the resulting grain size as well, as the grain size increases with higher calcination temperature too.

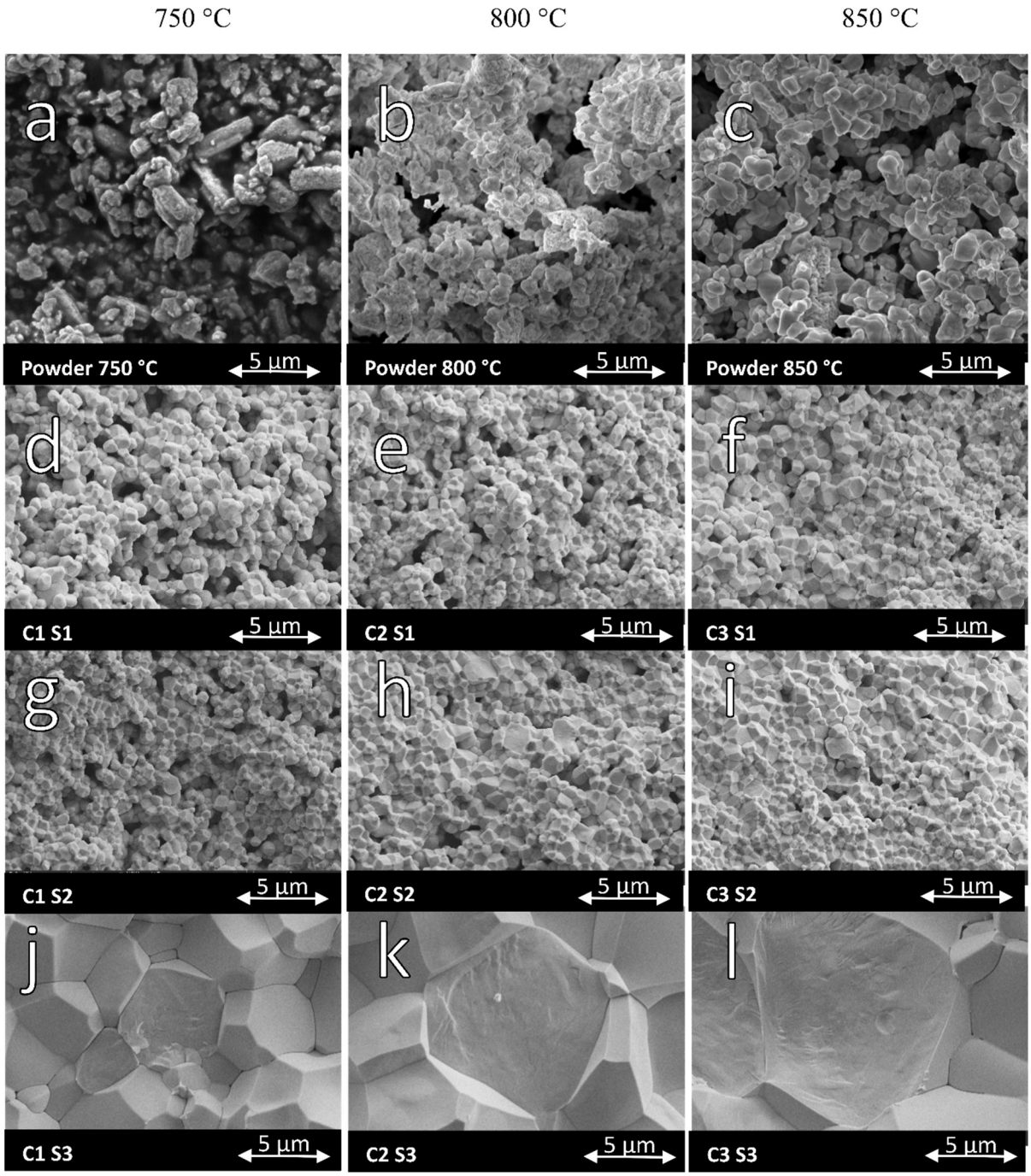


*Figure 3.24. SEM-images of the PFN calcined powder (a-c) and fractured ceramics (d-l) for different calcination and sintering temperatures. The powder at calcination temperature of 750 °C (a), 800 °C (b), 850 °C (c), and fractured ceramics for 1000 °C (d-f), 1050 °C (g-h) and 1100 °C (j-k) © 2021 Elsevier Ltd and Techna Group S.r.l.. Reprinted, with permission, from Ref. [87].*

By increasing both the calcination and the sintering temperatures the number of pores gets reduced as this can be seen in Figure 3.25 which shows the SEM images of the thermally etched samples for all temperature combinations. These results are in reasonable agreement with the relative density data in Figure 3.23.

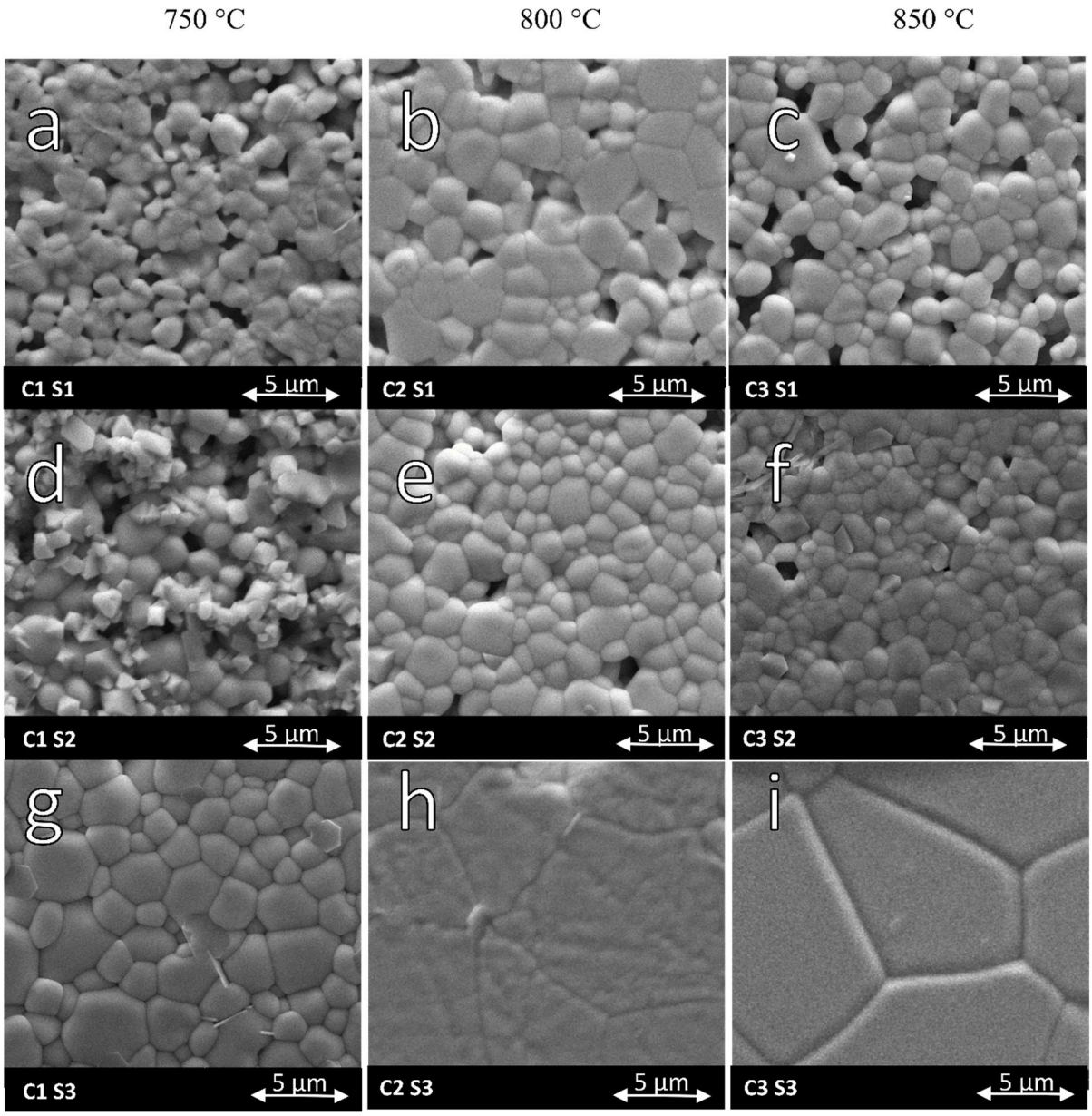


*Figure 3.25 SEM-images of the thermally etched PFN ceramics for different calcination and sintering temperatures. For the sintering temperature of 1000 °C (a-c), 1050 °C (d-f) and 1100 °C (g-i).*

### 3.4.3. Electrical Characterization

The representative polarization hysteresis loops at room temperature for the different ceramics are shown in Figure 3.26. The leakage current contribution is weak in all samples and a tendency to polarization saturation at high field is clearly apparent. The same applies even to the ceramics sintered at lower temperatures, which reveal good ferroelectric properties. The coercive field $E_C$, which is around 2.2 kV/cm, does not differ much for the different sintering temperatures when the same calcination temperature is used. Figure 3.27 shows the comparison of the polarization hysteresis loops for all processing temperatures. The change in values for both the spontaneous ($P_S$, open symbols) and maximal ($P_{Max}$, solid symbols) polarization is represented in Figure 3.27 a. $P_{Max}$ depends on the maximal electric field, however it is plotted

for comparison, since it is common practice in literature. The remanent polarization $P_r$ is shown in Figure 3.27 b. The spontaneous and remanent polarizations do not vary a lot for the different sintering temperatures after calcination at 750 °C and are around 10 µC/cm² and 4 µC/cm², respectively. In these samples, around 1 % residual pyrochlore remains, which is not ferroelectric. This amount probably affects the properties of the material through pinning the polarization direction or domain walls and/or defects considerably, resulting in lower values of $P_S$ and $P_{Max}$. For the higher calcination temperature of 800 °C, $P_r$ and $P_S$ increase with the sintering temperature from 4 to 16 µC/cm² and from 11 to 23 µC/cm², respectively. In C2 S1, the amount of pyrochlore is the same as in the C1 samples, resulting in the same polarization values for the same reasons. Bochenek et al. [58] prepared ceramics calcined at 800 °C with a higher sintering temperature of 1125 °C with 3 h sintering time and only achieved a $P_{Max}$ of about 20 µC/cm² without saturation at the field of 20 kV/cm, which is lower than for the C2 S3 sample (28 µC/cm²). At the calcination temperature of 800 °C the remanent polarization is growing constantly when increasing the sintering temperature, while the maximal and spontaneous polarizations increase from S1 to S2, but then are reduced slightly for S3. This could originate from the lead loss causing lead vacancies which adversely affect the ferroelectric properties. Nevertheless, the values for the maximal polarization are higher than those recorded by Gao et al. [56] at the same processing temperatures (C3 S2) and higher fields ($P_{Max} \approx 15$ µC/cm²). The difference in this work is that the samples here were sintered in oxygen and, therefore, have fewer oxygen vacancies which is the reason, that the leakage current contribution is less than in [56]. However, the remanent polarization for the C3 S2 sample is lower than reported by Gao (11.5 µC/cm²), which could also be due to the extrinsic contribution of the leakage in the latter case. The highest polarization was achieved for the C2 S3 ceramic with $T_{cal} = 800$ °C and $T_s = 1100$ °C.

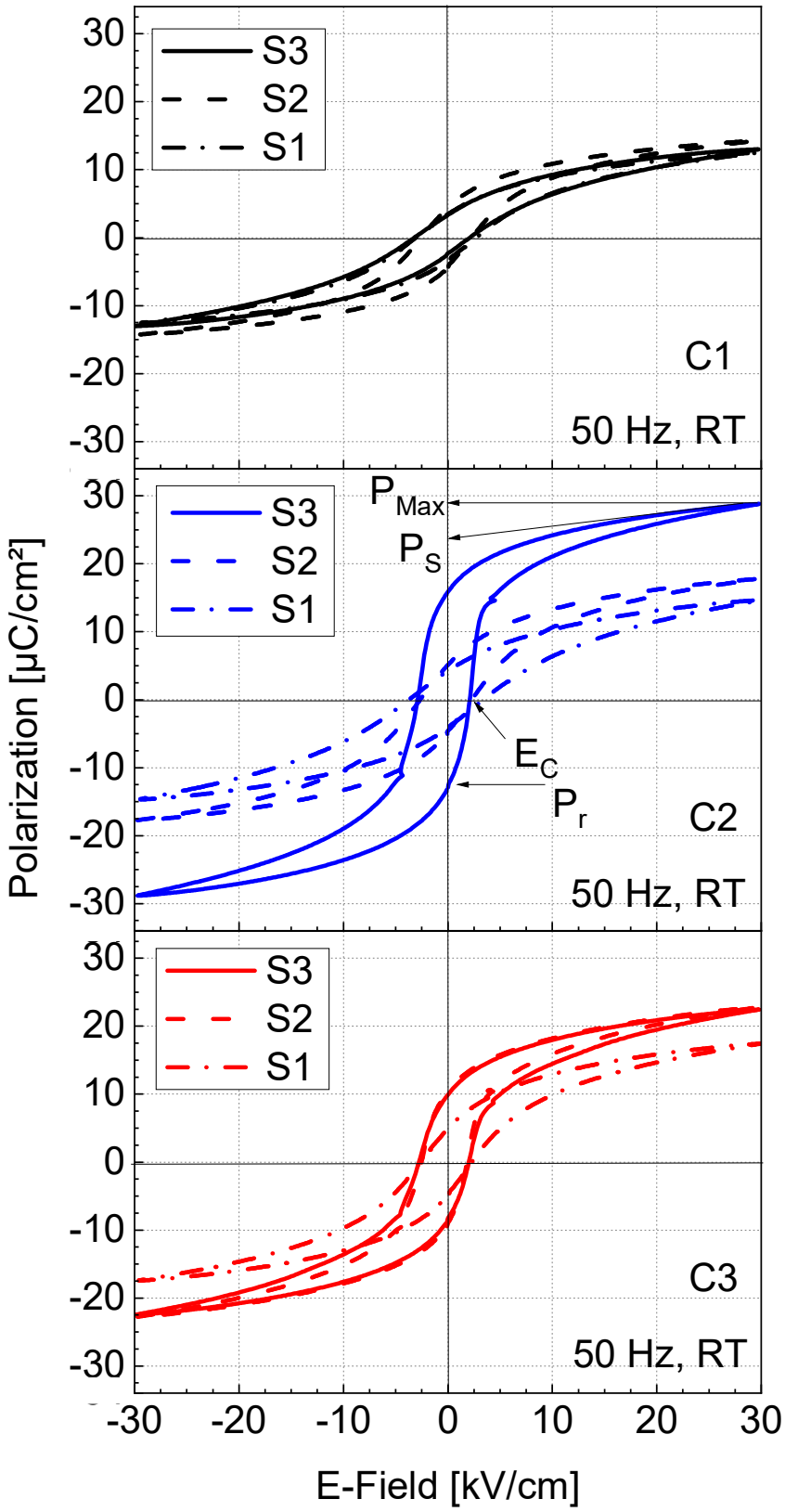


*Figure 3.26. Polarization hysteresis loops measured at room temperature for each calcination and sintering temperature © 2021 Elsevier Ltd and Techna Group S.r.l.. Reprinted, with permission, from Ref. [87].*

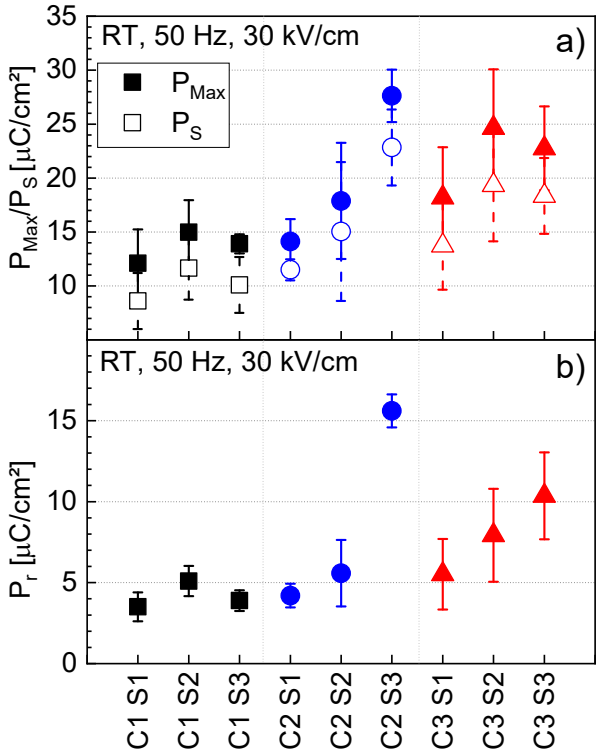


*Figure 3.27. Mean values of the maximal, $P_{Max}$ (solid symbols), spontaneous, $P_S$ (open symbols), (a) and remanent, $P_r$, (b) polarizations with standard deviation for all measured pellets © 2021 Elsevier Ltd and Techna Group S.r.l.. Reprinted, with permission, from Ref. [87].*

The different calcination and sintering temperatures do not only influence the polarization, but the dielectric permittivity as well. The relative dielectric permittivity $\varepsilon$ and loss tangent $tan\ \delta$ for the different samples measured at 100 kHz are shown in Figure 3.28 in dependence on temperature. All samples show a broad maximum of the dielectric permittivity, which is characteristic for a diffuse phase transition (DPT) [56]. This dielectric maximum lies between 377 K and 390 K. The dielectric loss is less than 0.04 at temperatures below 400 K for all samples. The variation of the maximal dielectric permittivity $\varepsilon_{Max}$ for the different samples is shown in Figure 3.29 a. The values of $\varepsilon_{Max}$ for C1 are quite low, as it was for the polarization data as well. When increasing the sintering temperature, the $\varepsilon_{Max}$ value increases from 8 000 to 13 000. A higher calcination temperature only gives better permittivity values for the highest sintering temperature of 1100 °C. The highest permittivity was achieved for C2 S3 and reaches an $\varepsilon_{Max}$ of ~ 55 000. The same trend as for the polarization is also seen here for the calcination temperature of 850 °C. S1 reaches $\varepsilon_{Max}$ = 13 000, but S3 only achieves an $\varepsilon_{Max}$ of 42 000. The explanation for this does not differ from the explanation for polarization reduction. The sample is affected by the lead loss which decreases the dielectric permittivity and probably is the main reason for the decrease. Though, microstructure can here play a role as well, because the permittivity also depends on the grain size with C3 S3 having the biggest grains.

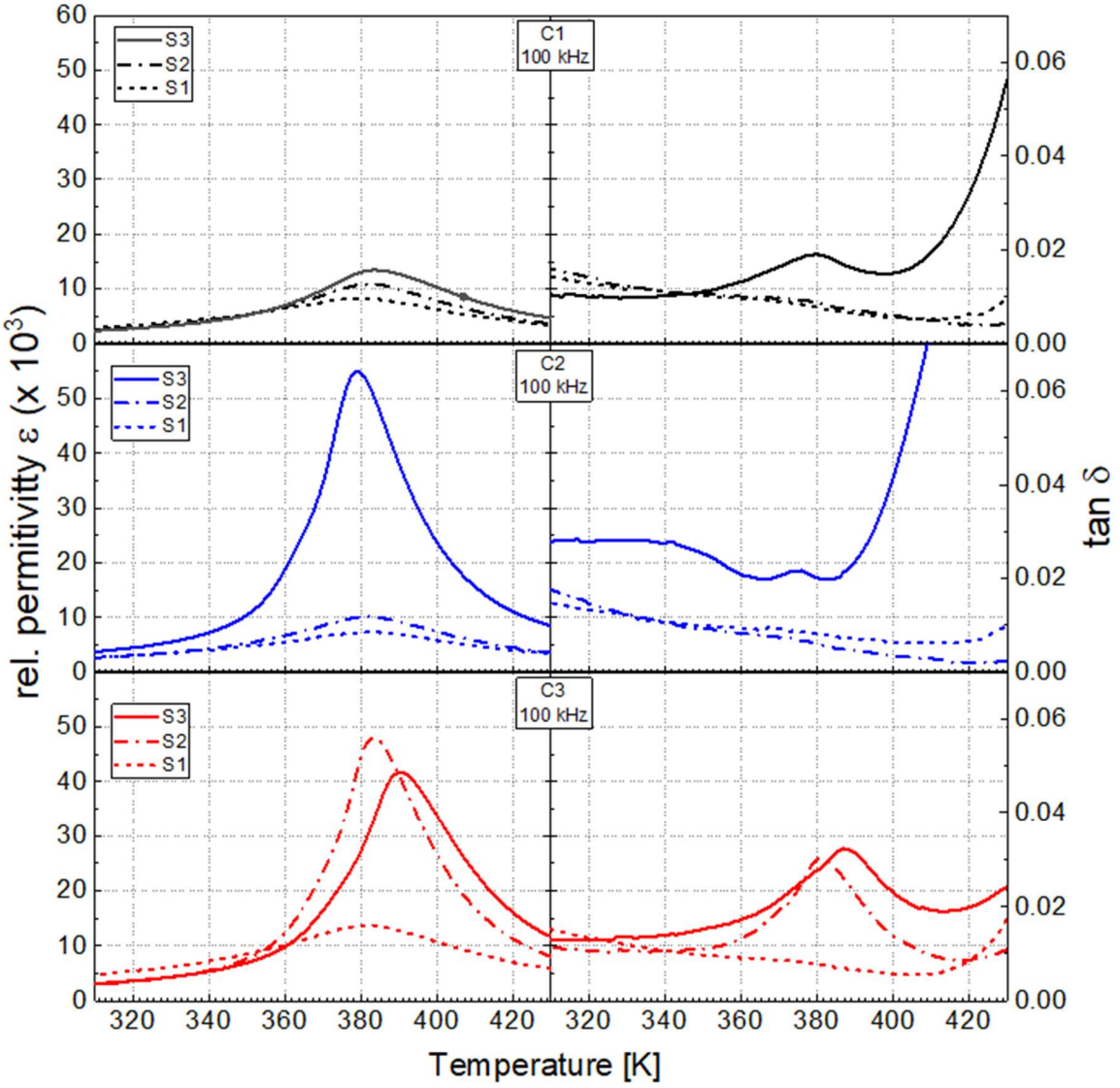


*Figure 3.28. Temperature dependences of the relative permittivity and dielectric loss tangent measured on cooling for one respective sample for each calcination and sintering temperature © 2021 Elsevier Ltd and Techna Group S.r.l.. Reprinted, with permission, from Ref. [64].*

The synthesis conditions affect both the position and the width of the dielectric maximum as it can be seen in Figure 3.29 a where $T_{Max}$ moderately shifts up with increasing sintering temperature.

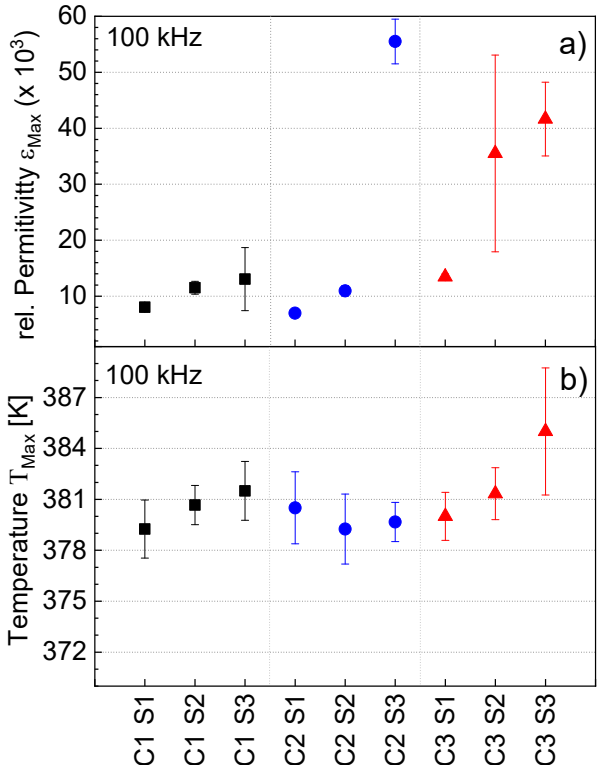


*Figure 3.29. Mean values of the relative permittivity $\varepsilon_{Max}$ (a) and temperature $T_{Max}$ of the maximum $\varepsilon_r$ -value(b) measured at 100 kHz for the PFN ceramics obtained for different calcination and sintering temperatures © 2021 Elsevier Ltd and Techna Group S.r.l.. Reprinted, with permission, from Ref. [87].*

In Figure 3.30 a an example of the modified Curie-Weiss law fit (Eq. 1.2 in Chapter 1.2.3) of the $\varepsilon(T)$ dependence for the C1 S3 sample is shown. The best fit values of the diffuseness exponent $\gamma$ for the different ceramics are presented in Figure 3.30 b. For the increasing sintering temperature, the mean value of $\gamma$ is decreases from 1.78 to 1.69 for C1, from 1.81 to 1.75 for C2 and from 1.76 to 1.72 for C3. Kirillov and Isupov [161] proposed a model to explain the diffuse phase transition (DPT) behaviour. The broadening of the phase transition is believed to originate from composition fluctuations. These result in the formation of microregions, which have different local Curie points. The maximum of the dielectric permittivity corresponds to a mean Curie temperature. It is possible that composition fluctuations related to the disordered distribution of the B-site cations affect the local ferroelectric ordering here as well. The more ordered the system, the less fluctuations in Curie point occur.

The diffuseness coefficient slightly decreases with increasing sintering temperature. It is possible that a higher sintering temperature promotes the local ordering of $Fe^{3+}$ and $Nb^{5+}$ cations.

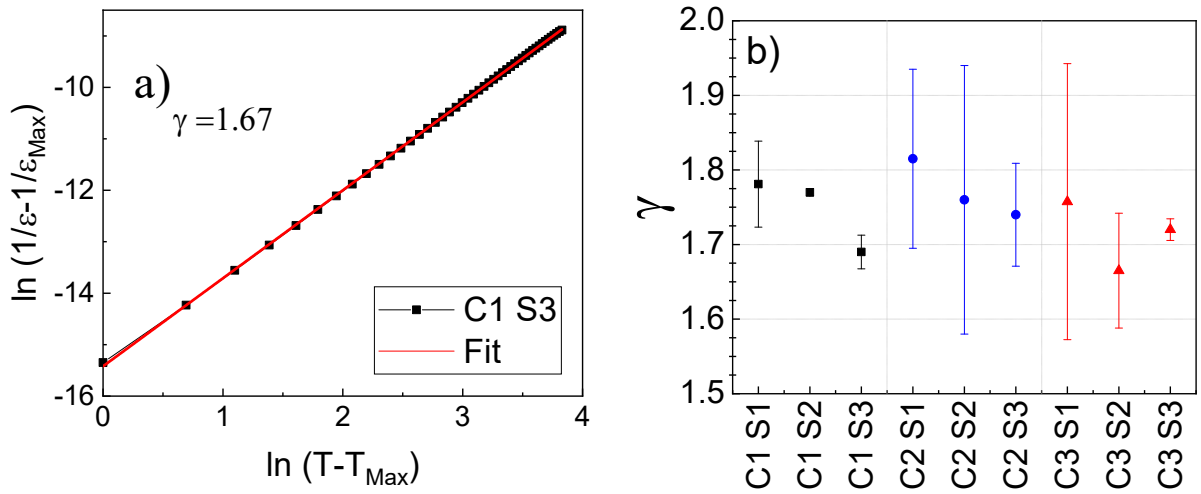


*Figure 3.30 An example of the fit of curve ε(T) by the modified Curie-Weiss law. The C1 S3 sample was taken as a representative. b) Mean value of the diffuseness parameter, γ, for the samples obtained at different calcination and sintering temperatures © 2021 Elsevier Ltd and Techna Group S.r.l.. Reprinted, with permission, from Ref. [87].*

### 3.4.4. Magnetic characterization

The influence of the synthesis conditions on the magnetic properties of the ceramics was also investigated. ZFC-FC measurements (Figure 3.31) show an increasing magnetization with decreasing temperature. On both ZFC and FC curves a maximum at a temperature of 10 K and a hump at around 150 K are visible, which are related to the transition to a spin glass state [69] and the paramagnetic-antiferromagnetic phase transition [55], respectively. As indicated in Table 3-10, $T_N$ shifts from 162 K (C1 S1) to 150 K (all C3 and all S3) with increasing calcination and sintering temperatures, but for a calcination temperature of 850 °C it remains the same. This shift is illustrated for the calcination temperature of 800 °C in the inset of Figure 3.31. The change of the antiferromagnetic transition temperature in relation to the distribution of the B-site ions was discussed by Smolenskii et al. [162]. When a completely ordered state is present, $T_N$ would shift to 0 K due to the unavailable magnetic interaction. Iron needs at least two magnetic neighbours for magnetic ordering as determined by Goodenough et al. [163] and Gilleo et al. [164]. In the other case of a completely disordered state, the iron ions in PFN would be all connected and promote the magnetic ordering which would shift $T_N$ to 300 K. These are two extrema and it is more realistic, that PFN implies a partial ordering of B-cations. The magnetic state of PFN relies on a partial chemical ordering as DFT calculations confirmed [8]. Besides the conventional $Fe^{3+}$-$O^{2-}$-$Fe^{3+}$ superexchange, the superexchange interaction of the $Fe^{3+}$-$Pb^{2+}$-$Fe^{3+}$ pathway plays a substantial role here [66,67]. Therefore, we can assume that the lower $T_N$ for the samples sintered at the higher temperatures can be attributed to the lead

losses. However, this contradicts the results for the C3 series, where the paramagnetic-antiferromagnetic phase transition temperature does not change, although the lead loss is proven by the electrical data.

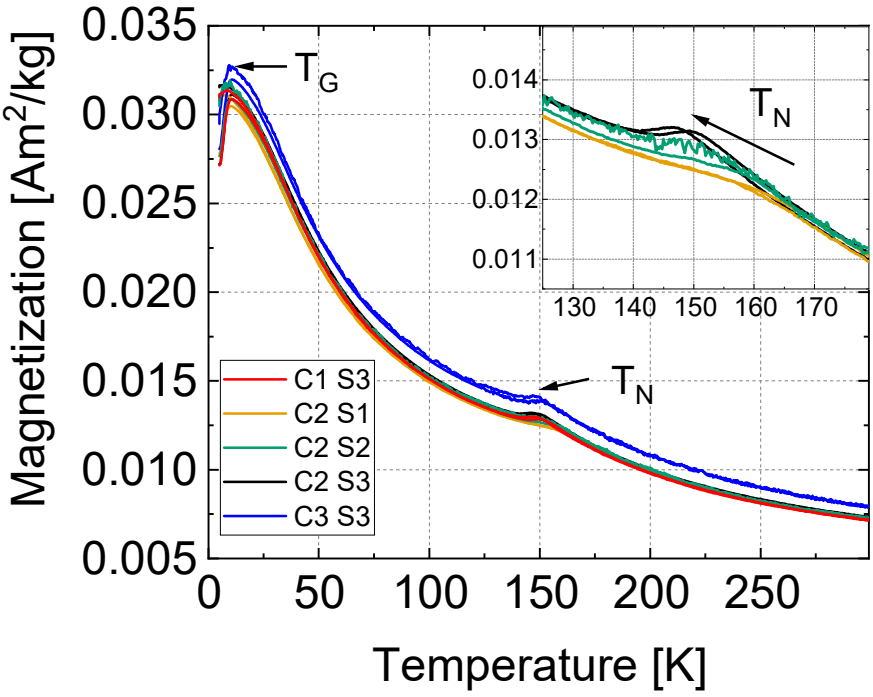


*Figure 3.31 ZFC-FC magnetization curves for the PFN ceramics prepared at the same calcination (C2) or the same sintering (S3) temperatures: The main figure gives the full measurement range, spin glass transition temperature Tg and Néel temperature $T_N$ are indicated © 2021 Elsevier Ltd and Techna Group S.r.l.. Reprinted, with permission, from Ref. [87].*

Raevskaya et al. [165] evaluated the atomic order-disorder phase transition temperature for PFN at approximately 1000 °C. This is the lowest sintering temperature used here. They also mentioned that a ceramic which is cooled slowly has a higher ordering and therefor a lower Néel temperature than ceramics or crystals with a faster cooling rate. From the results of this work it can be concluded that a more ordered state develops for the higher sintering temperature and the slow cooling process with 2 K/min, which is consistent with the dielectric data shown before.

In Figure 3.32 the magnetic hysteresis loops are plotted for different temperatures. They do not show any major change for the different samples and are linear above 160 K. This is characteristic for paramagnetic behaviour. For lower measurement temperatures they become more S-shaped, as reported by many authors [62,166,167]. Below the spin glass temperature $T_G$ (at 5 K) a hysteresis appears for all samples with a magnetic coercive field from 9 mT to 43 mT. C2 S3 shows the representative opening of the hysteresis in the inset of Figure 3.32.

*Table 3-10 The Neél temperature $T_N$ (in Kelvin) of the PFN ceramics under study for the different calcination and sintering temperatures.*

| **Sintering temperature $T_S$** | **Calcination temperature $T_{Cal}$** | | |
|---|---|---|---|
| | **750 °C** | **800 °C** | **850 °C** |
| **1000 °C** | 162 | 160 | 150 |
| **1050 °C** | 158 | 156 | 150 |
| **1100 °C** | 150 | 148 | 150 |

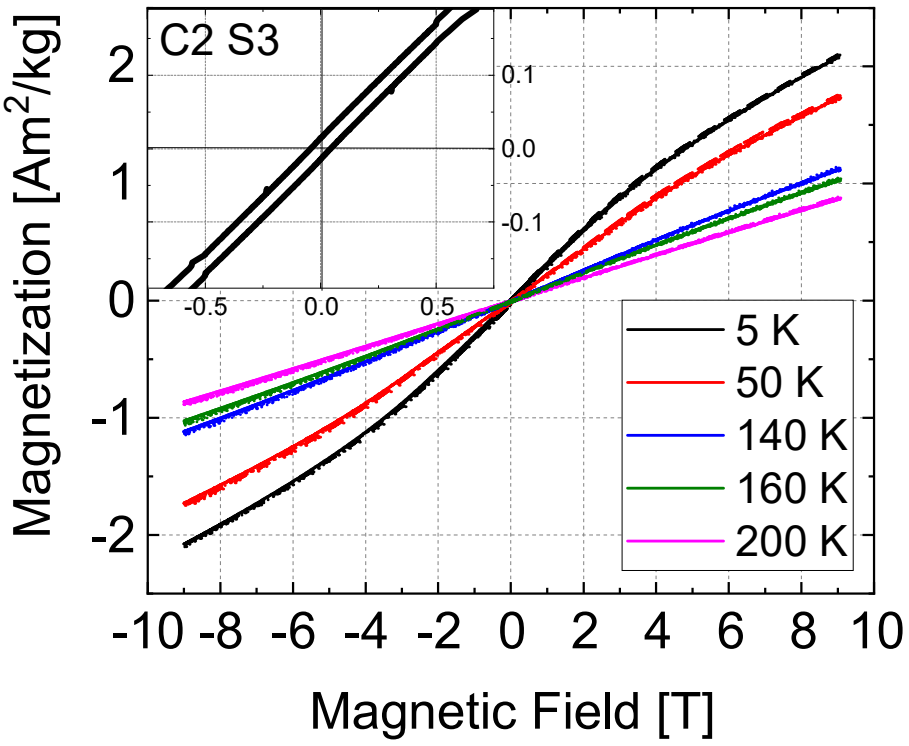


*Figure 3.32. Magnetization vs. magnetic field dependences for C1 S3, C2 S1, C2 S2, C2 S3, and C3 S3 samples at different temperatures. The inset gives a closer look at the hysteresis at 5 K for C2 S3 © 2021 Elsevier Ltd and Techna Group S.r.l.. Reprinted, with permission, from Ref. [64].*

### 3.4.5. Summary and conclusions

This Chapter shows the influence of the calcination and sintering temperatures on the properties of PFN. The ceramics were calcined at three different temperatures and sintered at three different sintering temperatures. At lower sinterin/calcination temperatures, the parasitic pyrochlore phase was detected. Increasing only the calcination temperature was not enough to achieve a pure phase which was only obtained at sintering temperatures above 1050 °C. The synthesized PFN is a mixture of the monoclinic $C1m1$ and rhombohedral $R3m$ phases. With increasing sintering temperature, the density of the ceramics could be improved, but also the grain size enlarged by one order of magnitude. However, also the lead losses increased at the highest sintering temperature which was harmful for the dielectric properties of the ceramics. The best dielectric and ferroelectric parameters were achieved for the ceramic prepared at $T_C$ = 800 °C and $T_S$ = 1100 °C, where a compromise between enough energy for the perovskite forming is given and the lead loss is not disadvantageous for the properties. Nevertheless, all synthesized samples show saturated polarization hysteresis loops with a negligible leakage contribution.

The distribution of the B-site cations can be varied in a small range by changing the sintering temperature as demonstrated by the analysis of the dielectric and magnetic data. Both the "diffuseness" exponent $\gamma$ of the ferroelectric phase transition and the Néel temperature decrease with the increase of the sintering temperature. This suggests a higher local ordering of the B-site cations for the ceramics sintered at higher temperatures. It is a small effect, limited by the fact that the driving force for chemical ordering is too weak, since the ionic radii of $Fe^{3+}$ (78.5 pm) and $Nb^{5+}$ (78 pm) are very close to each other.

# 4. PFN Thin Films

Thin films in general can be prepared by many different techniques e. g. dip coating, doctor blade, drop casting, pulsed laser deposition, and spin coating. Not every technique is usable for every material. In the next Chapter PFN thin film preparation will be introduced. The most promising technique for epitaxial growth is the pulsed laser deposition. On the other hand, this technique is quite laborious, since only one sample can be prepared at once and adjusting the deposition conditions takes time. Whereas spin coating was tried as well with the advantage of faster and thicker film grow, but also the disadvantage of non-plane parallel layers with local differences in thickness. In this Chapter the principles of pulsed laser deposition and spin coating as well as the synthesis of PFN films deposited on STO substrates prepared by these methods are presented. Optical properties of the synthesized layers will be discussed and compared.

## 4.1. Pulsed Laser Deposition

The description of the pulsed laser deposition method is based on Ref. [168] if not denoted otherwise.

### 4.1.1. Principle

Pulsed laser deposition (PLD) is a common method to prepare thin films and multilayer structures. The quality of these films is comparable to films from molecular beam epitaxy (MBE), but it is 10 times cheaper to produce. In general, the useful wavelength range of the laser lies between 200 nm and 400 nm and the most commonly used lasers are excimer lasers. However, a poor beam quality can result in nonstoichiometric films as well as undesirable droplet formation. Between the laser output port and the input port of the deposition chamber, optical elements like lenses and apertures; mirrors and beam splitters, are placed to steer and focus the beam on the target to increase the beam quality. The basic elements of a PLD deposition system are shown in Figure 4.1. The substrate is glued with a heat conductive glue to the substrate holder which can be heated to provide the required deposition temperature. A target is placed on a rotator: this enables the target to be used evenly and reduces local overheating and hole formation. Deposition is carried out either in vacuum or in a gas atmosphere, which are provided with the help of a pump or a gas flow system, respectively.

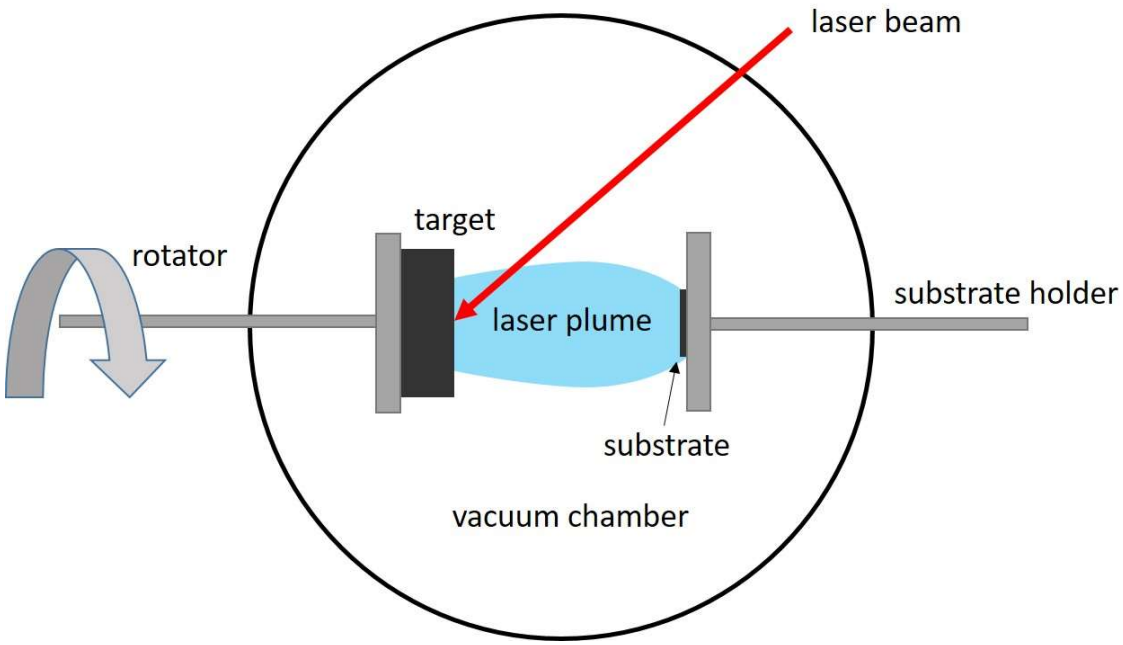


*Figure 4.1 Schematic of a PLD deposition system with its elements*

The PLD process can be divided into three steps. The first step involves the interaction between the laser and the target: After the target is bombarded with a laser pulse, thermal, electronic, and macroscopic sputtering processes can occur depending on the target material and the laser photons (wavelength and pulse duration). These processes lead to particle emission, also commonly termed ablation or desorption. Afterwards, the second step occurs which is the formation of the laser plume. In vacuum, a hot bubble-shaped plasma is formed at a distance of several microns from the target surface. As soon as it is formed, the plasma particles interact with each other and lose their "memory" of the previous ablation process. Gas molecules scatter, attenuate, and thermalize the plasma. This changes the film growth parameters such as the deposition rate, spatial distribution and the kinetic energy distribution of the gas molecules. Furthermore, the plasma particles can chemically react with the particles present in the gas. The background pressure influences all of the above-mentioned processes as well. The last step is film formation. The incoming particles are adsorbed on the substrate surface. Depending on the ambient conditions, these diffuse to the respective location where they react with each other and nucleate to clusters on the surface. Depending on the conditions on the substrate, the structure and morphology of the growing film can be changed.

### 4.1.2. Substrates

The most common substrate used for PFN in literature is cubic STO (001) [98,100–102]. It has a lattice constant of around 3.928 Å which is the closest to ~4.01 Å for PFN found in commercial substrates. However, in-plane strain can affect the stable phase, ferroelectric response and other properties as Yan et al. have investigated in Ref [102]. STO (110) and STO (111) can be used as substrates as well, but films grown on STO (001) manifest the best ferroelectric properties. For this reason, it is used by most authors either for PLD [93,98,100,101] or even for sol-gel deposition [63,89–91].

The XRD pattern of a STO (001) substrate is shown in Figure 4.2. In the range of $2\theta$ from 5 to 90 ° only the (00*l*) peaks are detected including the (001), (002), and the (003) peak. Because STO is not conductive, a conductive layer of $SrRuO_3$ (SRO) (typically with a thickness of around 50 nm) on top of STO can help with any kind of measurements that require a bottom electrode. SRO has the same orientation and therefore shows the same (00l) peaks as the STO only shifted to lower angles (Figure 4.2, bottom).

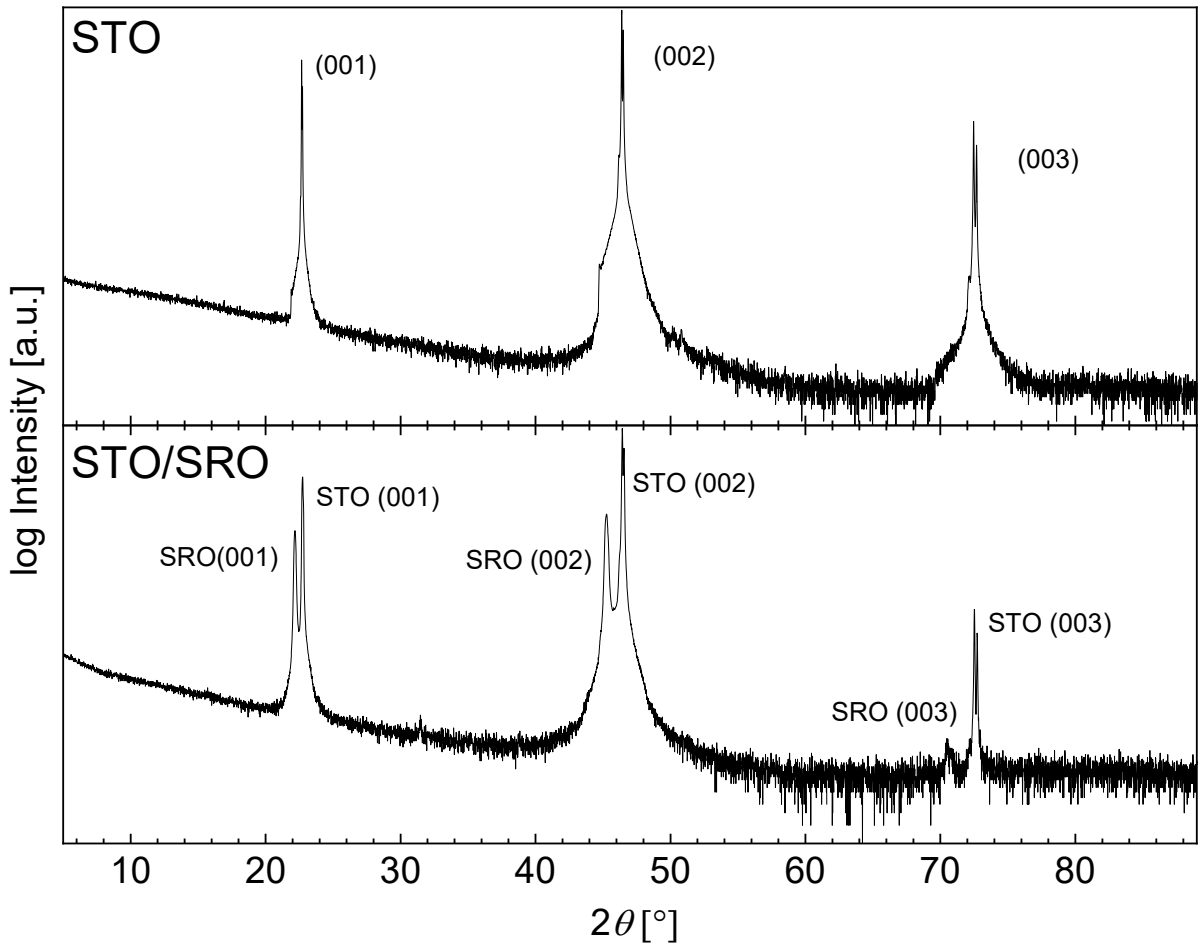


*Figure 4.2 XRD pattern for a pure STO (001) substrate (top) and STO (001) substrate with a SRO film on top (bottom).*

## 4.2. PFN thin films by PLD

### 4.2.1. Target Preparation

PFN is not a common target material which can be easily bought. The best way to get one is to make it by yourself. As already discussed in Chapter 3, the lead in PFN is volatile at high temperatures, and, with each heating step, the material loses more lead. Chapter 3.4 explained that an excess of 2 wt. % lead can prevent the stoichiometry change in PFN ceramics due to lead loss when two heating processes (calcination and sintering) are applied. When using PLD, a third heating process is induced by the laser at the actual deposition, and also the substrate is heated to the critical temperature for lead loss (around 700 °C). This requires the starting material to contain more excess lead then in other experiments. As a result of this, we decided to use a PFN target with 10 wt. % lead excess.

For preparing the target, the solid-state method and the same materials as in Chapter 3.4.1 were used. The only difference was a 10 wt. % instead of 2 wt. % lead excess. The calcination and sintering parameters were adjusted according to the results reported in Chapter 4.4 ($T_C$ = 850 °C, 2 h; $T_S$ = 1050 °C, 2 h). 25 g of the calcined PFN powder was pressed under a pressure of about 20 MPa into a pellet with a diameter of 2.5 cm. The orange green body (Figure 4.3 a) shrunk after sintering to a diameter of 2 cm and appeared well densified (Figure 4.3 b) while changing colour to blackish. Afterwards, the pellet was ground with 1200 and 2400 grinding papers for a smooth surface. The geometric density was calculated to be 8.31 g/cm³, which corresponds to a relative density of 98.24 % to the ideal crystal thus reflecting a very low porosity of the sample.

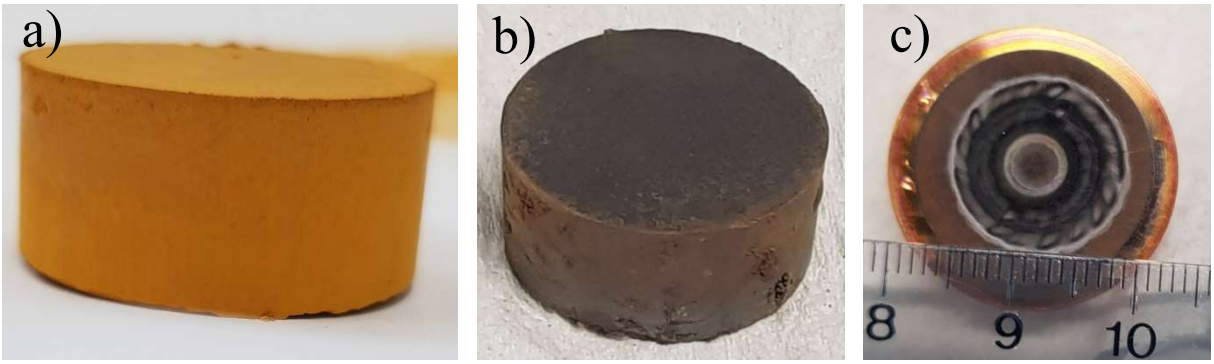


*Figure 4.3 Different stages of the PLD target. a) is the green body pellet. b) is the sintered pellet and c) is the surface of the pellet after PLD.*

The XRD patterns for the calcined powder and the sintered target can be seen in Figure 4.4 a and b, respectively, with the corresponding Rietveld refinement values in Table 4-1. The main phase is the perovskite PFN with an amount of ≥ 98.5 % for both patterns marked by a star. It

is a mixture of the monoclinic (ICSD 98-008-8358, *C1m1*) and the rhombohedral (ICSD 98-009-0491, *R3m*) phases in agreement with the results presented in Chapter 3.

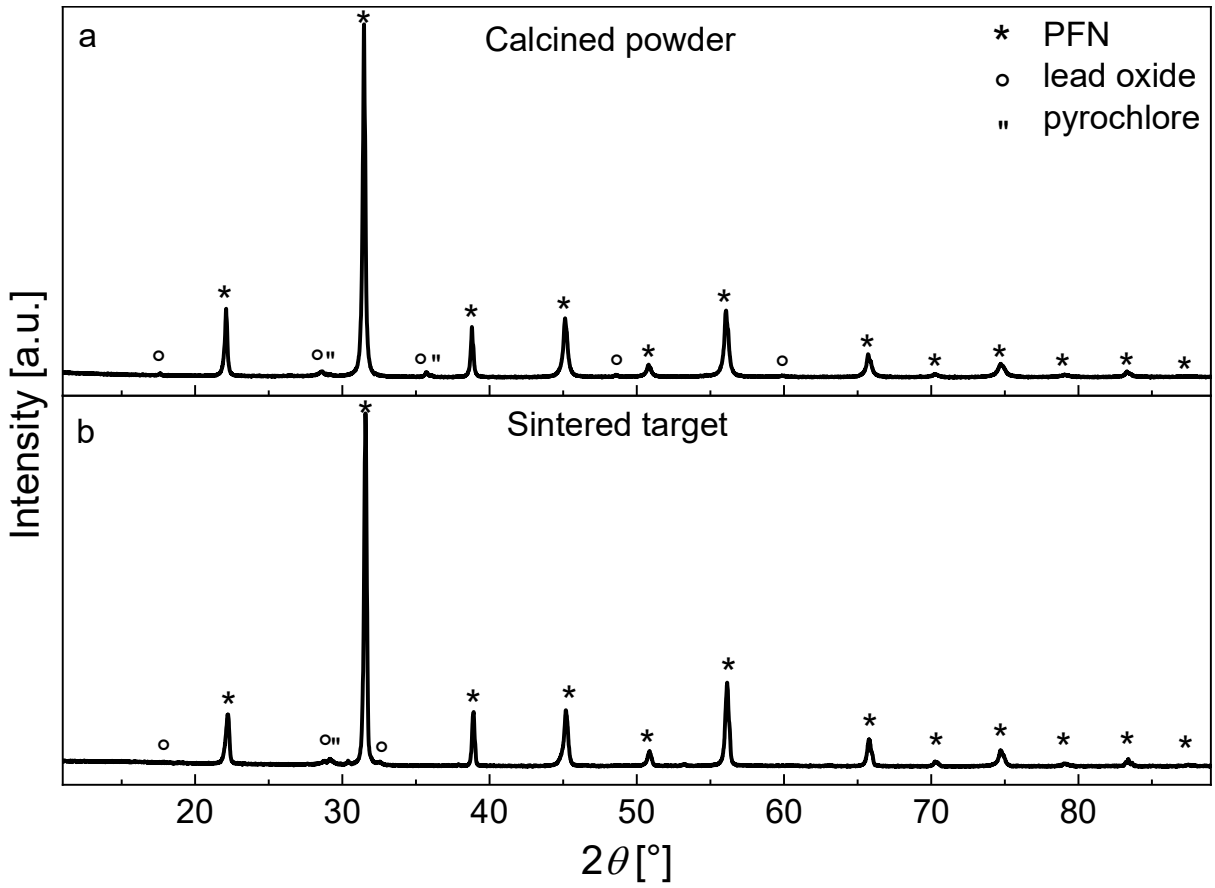


*Figure 4.4 XRD pattern for the calcined powder (a) and the sintered pellet (b). The PFN phase is marked by the star (*), the lead oxide by a circle (°) and the pyrochlore by two lines (").*

The secondary phase appears to be mostly PbO (ICSD 98-006-2849). In the calcined powder, means after the first heating step, the amount of PbO is 1.1 %. After sintering, this value decreases to 0.4 % due to the second heating step. There is still enough PbO left for the third heating step during the deposition. Therefore, the residual pyrochlore increases, nevertheless its amount is ≤ 0.6 % which is acceptable for this purpose.

*Table 4-1 Rietveld refinement values for the calcined powder and the sintered pellet.*

| Sample | Monoclinic/ Rhombohedral [%] | PbO [%] | Pyrochlore [%] | $R_{WP}$ | GOF |
|---|---|---|---|---|---|
| **Calcined powder** | 75.7<br>22.8 | 1.1 | 0.4 | 9.15 | 2.68 |
| **Sintered target** | 52.2<br>46.7 | 0.4 | 0.6 | 10.49 | 2.66 |

After grinding, the target is glued to the target holder and installed into the PLD system. After an iteration of deposition, the top layer of the target must be removed through polishing/grinding paper to avoid non-stoichiometry in the following experiments.

### 4.2.2. Parameter Variation

All PLD layers mentioned in this work were prepared at the laboratories of the university Jules Verne in Amiens with the help of H. Bouyanfif. To achieve an epitaxial layer without secondary phases the optimal parameters for the deposition needed to be found. There are many parameters that can be changed in a PLD process, in general, starting from the substrate, the substrate temperature, over chamber pressure, to laser energy. As already mentioned, STO (001) substrates (PLD targets, UK) are used here. The most critical parameter for PFN deposition is the substrate temperature. Literature gives values between 600 °C [96] and 720 °C [56].

*Figure 4.5 A PFN film deposited on STO (001) by PLD.*

This study starts from 640 °C and increases the temperature to 720 °C in 20 °C increments. The other parameters are fixed: oxygen pressure is 0.2 mbar [56,98,100]; the distance from target to the substrate is 5.5 cm, and a laser fluence of around 2 J/cm² (laser energy 60 mJ, laser spot area 3 mm²). The number of laser shots is 5000 at a frequency of 3 Hz. The samples are compared for purity, crystallinity and roughness. A summary of the results is given in Table 4-2. After deposition, the films appear in an orange-yellowish colour (Figure 4.5).

Figure 4.6 shows $\theta$-$2\theta$ XRD patterns for films deposited at the different substrate temperatures. The STO and PFN diffraction peaks are clearly visible for all samples. At the temperature of 640 °C many secondary phase peaks - apart from the $k_\beta$-peaks - at $2\theta$ values of 19, 26, 41, 65, 77 and 81° are found in the pattern, which are marked with asterisks. When the temperature is increased up to 680 °C, most of the secondary phase peaks disappear and only the one at 42° remains. At 700 °C no other peaks than the substrate and PFN peaks are left. When the temperature increases to 720 °C, the secondary phase peaks appear again. Thus, only the substrate temperature of 700 °C gives a layer with the pure perovskite PFN phase.

*Table 4-2 Overview of the results of the different measurement for comparison of the different deposition temperatures*

| Sample | 720 °C | 700 °C | 680 °C | 660 °C | 640 °C |
|---|---|---|---|---|---|
| **pure phase** | No | Yes | No | No | No |
| **Rocking curve (FWHM, $C_{RC}$)** | - | 0.385°<br>1.53 | 0.581°<br>1.32 | 0.567<br>1.39 | 0.716°<br>2 |
| **Pole figures** | In plane orientation, epitaxial, four-fold structure | In plane orientation, epitaxial, four-fold structure | In plane orientation, epitaxial, four-fold structure | In plane orientation, epitaxial, four-fold structure | In plane orientation, epitaxial, four-fold structure |
| **RHEED** | 3 D structure<br>points | smooth<br>Laue circle rods<br>Kikuchi lines | smooth<br>Laue circle rods<br>Kikuchi lines | rough<br>Laue circle rods | rough<br>Laue circle rods |

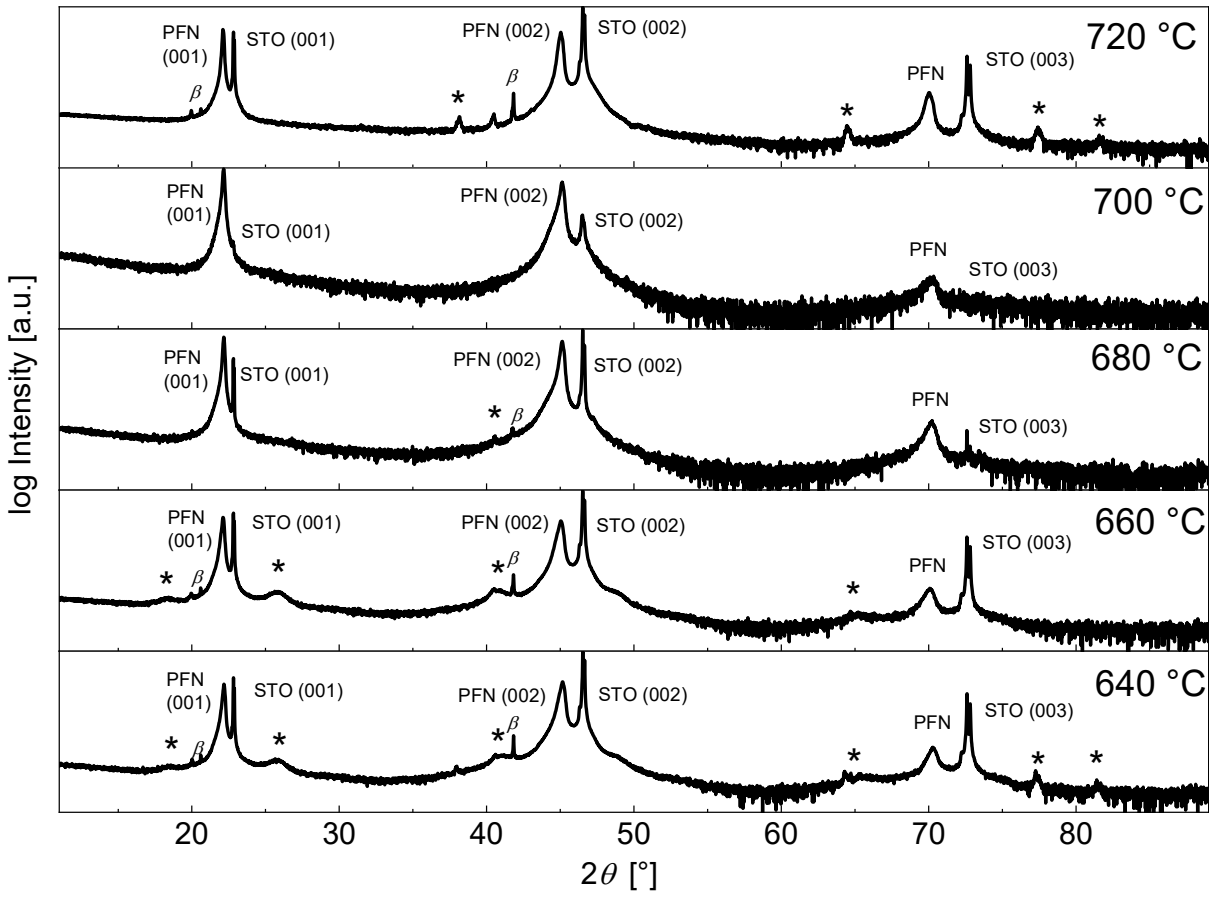


*Figure 4.6 θ-2θ XRD pattern for the different substrate temperatures while deposition without $k_\beta$-filter. The secondary phase peaks are marked with the asterisks.*

PFN Thin Films

To evaluate the crystallinity of the films deposited at the different substrate temperatures, rocking curves were measured. As already mentioned in Chapter 2.1.1.3 (XRR), a single-crystal reference sample with the same layer thickness is required for the proper analysis of rocking curves to arrive at a precise statement about the crystallinity. Since there has not been such a sample previously, only the relationship between the individual samples can be considered. The rocking curves shown in Figure 4.7 and Figure 4.8 were measured with an old diffractometer from Siemens (D 500), so that the instrumental peak broadening from the device is bigger in comparison to all other measurements in this work. The FWHM of the PFN diffraction peaks decreases from 0.716° at 640 °C to 0.387° at 700 °C, respectively, as it can be seen in Figure 4.8. It can be concluded, that the crystallinity improves with the higher deposition temperature, which is in agreement with the results of $\theta$-$2\theta$ measurements showing that only in the film deposited at 700 °C the pure perovskite phase is achieved. Figure 4.8 shows the different rocking curves in one graph, so the differences in FWHM are presented in a clearer way. Nevertheless, this statement should still be carefully questioned, as also the alignment in the device cannot be carried out to the 2$^{nd}$ or 3$^{rd}$ decimal place, as modern XRD devices can do. Therefore, also the associated STO peaks need to be considered. We introduce a parameter $C_{RC}$ that indicates normalization of the FWHM of the PFN peak with the associated FWHM of the STO peaks. It seems that the crystallinity for the films deposited at 680 °C and 660 °C that have values $C_{RC}$ of 1.32 and 1.39, respectively, is better than for the film at 700 °C where $C_{RC}$ is 1.53. What can be concluded, however, is that the sample obtained at 640 °C has the lowest crystallinity, since its $C_{RC}$ is 2.

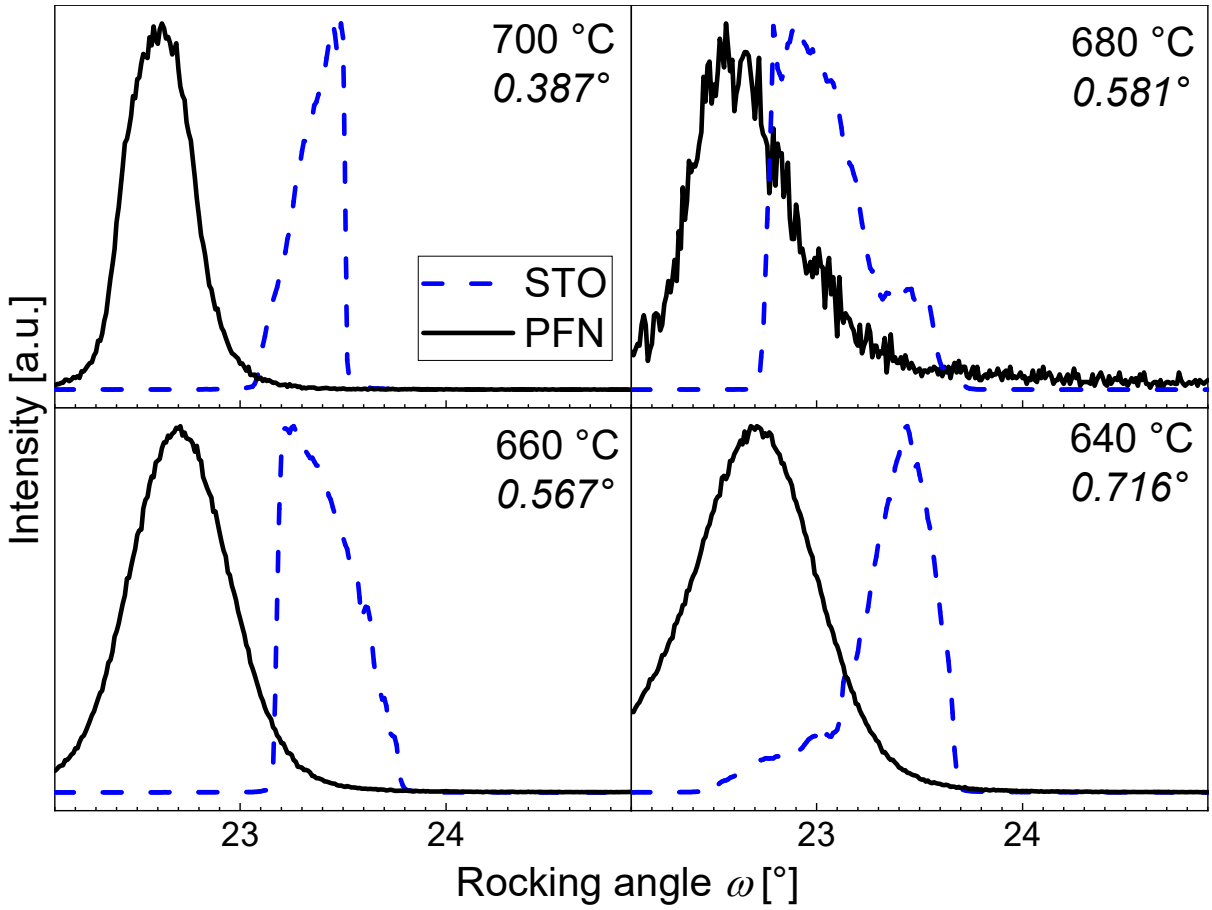


*Figure 4.7 Rocking curves for the PFN layer (black line) and STO substrate (blue dashed line) for the substrate temperatures of 640 to 700 °C.*

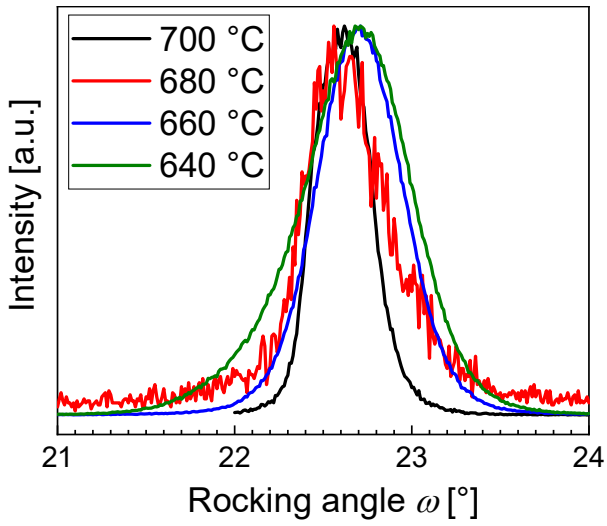


*Figure 4.8 Comparison of the FWHM of the rocking curves for the PFN layer for the substrate temperatures of 640 to 700 °C.*

As the rocking curve measurements can only give an estimate about the crystallinity, additional pole figure measurements were made. In Figure 4.9 a representative pole figure of the sample deposited at 700 °C is shown (the pole figures for the other samples can be found in Appendix 6.5.). All of them have four distinct peaks in the $\psi$ range of 40 to 50 °. This means that all five samples have the same in-plane orientation and no rotation of individual grains is seen. Since

four peaks are visible, the PFN phase needs to have a fourfold structure symmetry either cubic, or tetragonal. Bulk PFN forms mostly in a monoclinic structure like shown in the previous Chapters. However, mechanical misfit stress may be a reason that another structure stabilizes in epitaxial thin films. Yan et al. [102] investigated the structure of the PFN films deposited on a STO (001) substrate and found out, that the *a* and *b* sides of the unit cell are compressed equally and the *c* side is expanded due to the lattice mismatch, resulting in a tetragonal structure.

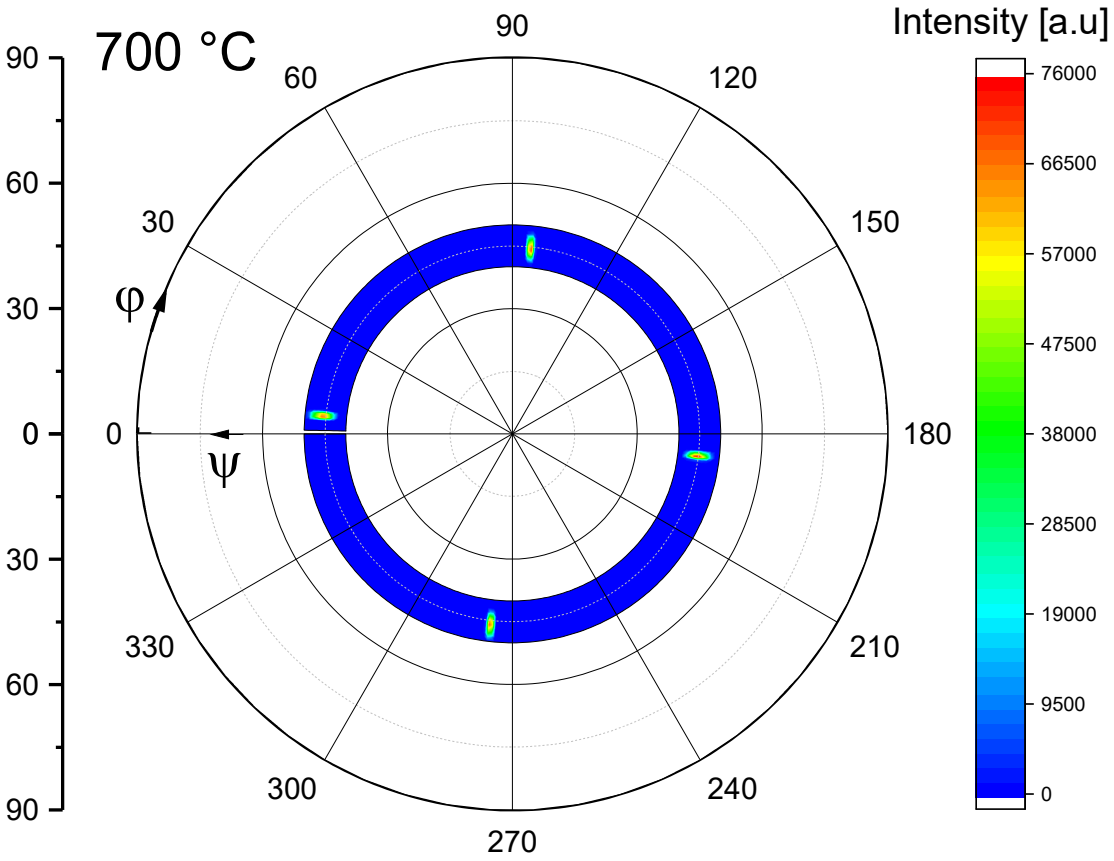


*Figure 4.9 A representative pole figure measurement of the PFN layer deposited at 700 °C in the ψ range of 40 to 50 °.*

Not only the phase or the crystallographic orientation are important factors for the quality of a layer, but also the surface roughness. For this reason, RHEED measurements of the surface were carried out after the deposition. The images in Figure 4.10 show the results. The surface of the sample deposited at 720 °C is already a 3D structure which means that the surface is very rough. Therefore, the RHEED beam is not grazing the sample anymore, instead it is going through the material. This can be seen in the point structure and the quadratic area of the pattern in the image. This is different at 700 °C where no points but rods are visible. Also, in comparison to 720 °C the Laue circle is formed in the RHEED image for the film deposited at 700 °C and a clear appearance of the Kikuchi lines [136] is observed. This all indicates a smooth surface. For the films deposited at the lower temperatures, the Laue circles and the rods are still

present, however, from 680 °C to 660 °C the Kikuchi lines attenuate and vanish at 640 °C. This means that the surface is getting rougher with decreasing deposition temperature. Due to less energy from heating, the velocity of the arrangement of the molecules on the structure decreases, while the same number of new molecules will be transported to the substrate. This decreases the time for each molecule to diffuse to the right spot to form a smooth surface [169].

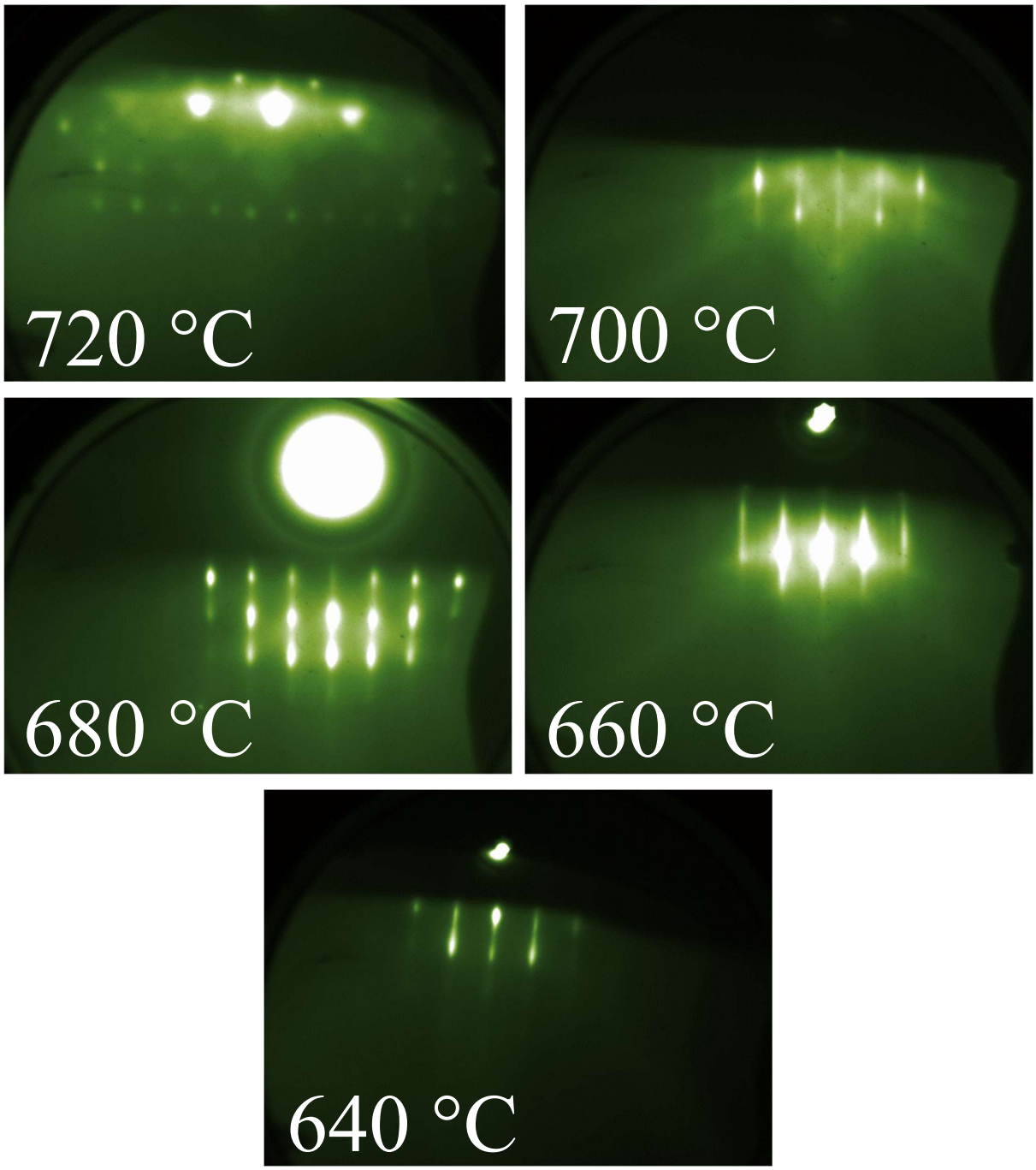


*Figure 4.10 RHEED images for the films deposited at the different substrate temperatures indicating the roughness of a sample.*

All these investigations show that a substrate temperature of 700 °C results in films with the best properties. The sample has a pure PFN phase that is grown epitaxially, and the roughness of the surface is low as well. At this point in time, other parameters are no longer adjusted, as this is very time-consuming and the quality of the layer is already high.

### 4.2.3. Layer thickness

To estimate the layer thickness and the deposition rate, reflectivity measurements were done. As the only parameter for the given laser deposition setup which can be changed is the number of laser pulses, the deposition rate can be calculated and scaled by that number. To confirm the deposition rate and to check whether the deposition rate is changing with thicker layer, two different samples were prepared at a temperature of 700 °C, one with 1500 and another with 5000 shots. A reflectivity program calculates the layer thickness throughout equation Eq. 2.2 and the Kiessig oscillations in Figure 4.11. For the layer generated from 1500 shots a thickness of 31.2 nm and for 5000 shots a layer thickness of 95.5 nm is calculated which gives a deposition rate of $\frac{10.4\ nm}{500\ shots}$ and $\frac{9.5\ nm}{500\ shots}$, respectively. These values do not differ a lot from each other. This leads to the conclusion that the deposition rate does not change significantly when the layer grows in this range.

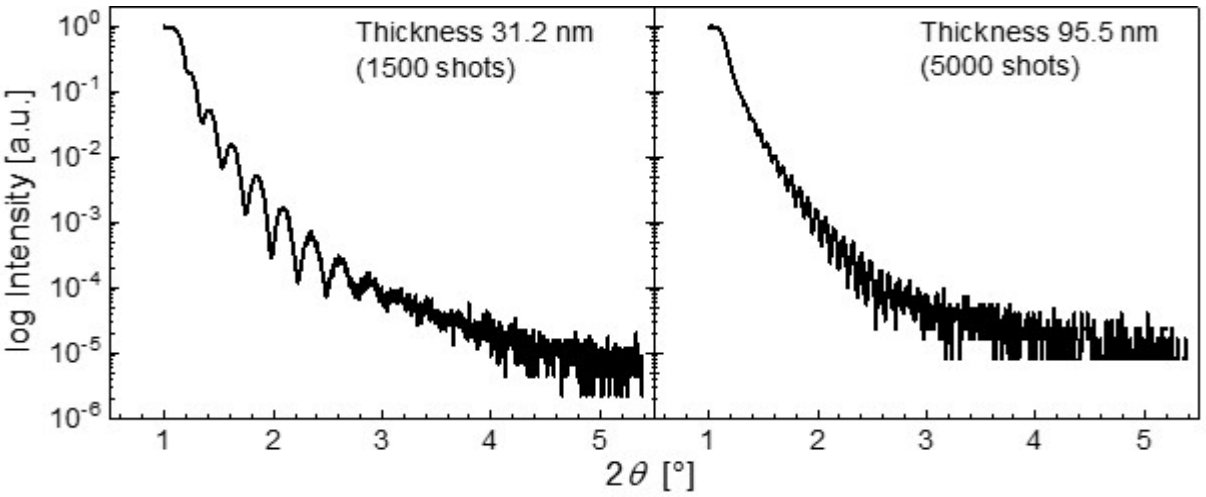


*Figure 4.11 reflectivity measurements with Kiessig oscillations for a layer deposited with 1500 laser shots (left) and 5000 laser shots (right).*

Since size effects can occur in structures in the lower nanometer thickness range, the minimum layer thickness of the sample, as it is the case in the previous experiments, is set to at least 100 nm. To check if a thicker film might be beneficial, another sample with twice the layer thickness was produced and both are compared with each other. RHEED measurements reveal that the roughness of the layer increases with the longer deposition time (10000 shots). Figure 4.12 b again shows the already mentioned smooth surface of the layer after 5000 shots with the

Laue circles and the Kikuchi lines. In comparison, the layer with twice the deposition time shows points in the RHEED image (Figure 4.12 a), which means a rougher surface.

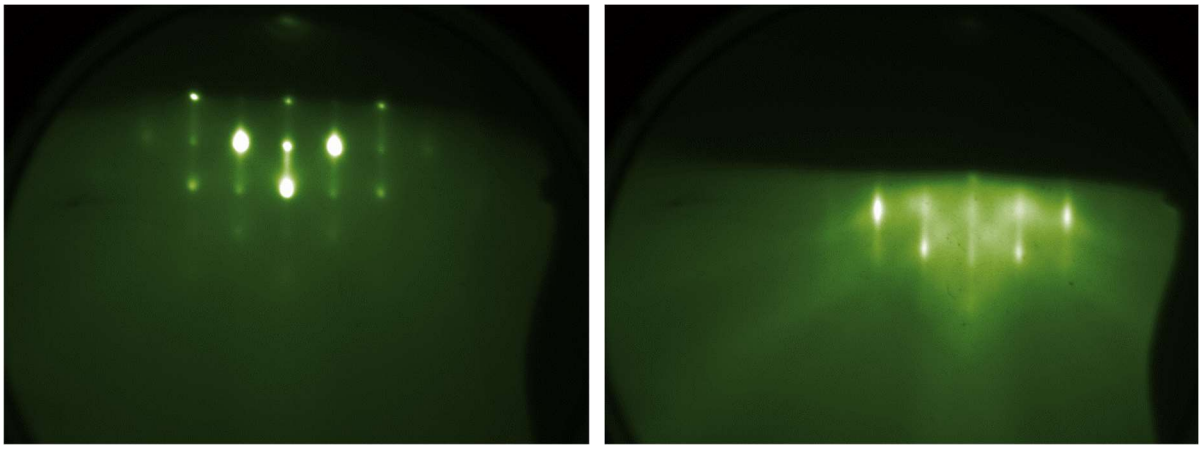

*Figure 4.12 RHEED images from the sample prepared with 10000 shots (a) and 5000 shots (b).*

The topography of the surface measured with the AFM confirms that the roughness of the films increases from 2.95 nm at 5000 shots (Figure 4.13 a and b) to almost the double of 5.46 nm at 10000 shots (Figure 4.13 d and e). There can be several reasons for this. On the one hand, larger molecules or particles could have been released from the target by the ongoing bombardment. Another reason could be the increased number of particles in the laser plume, which are more likely to hit the substrate and hinder diffusion to the favorable location through nucleation and growth due to oversaturation [168]. The AFM images also show that the grains are round and of the same size for one deposition time. However, the grain size for the samples with the different thickness is different. The 5000-shot sample has a grain size of 75 ± 15 nm, whereas the sample with 10000 shots has a grain size of 114 ± 18 nm. In the latter case, due to the longer heating time of the substrate at 700 °C the grains grow as well.

In Figure 4.13 c and f vertical PFM images are shown where the dark and the bright quadratic area were polarized in different directions. The polarization was done by scanning these are under a positive or negative bias (±10 V) applied to the AFM tip. In the non-polarized area a good correlation between the topography and the PFM image is visible. Nevertheless, it is difficult to infer the domains from this measurement since the bright and dark spots in the grains are always in the same place. This leads to the assumption, since the layer can be polarized, that the domains within one grain are too small to be differentiated from each other. It is however possible to prove the ferroelectric state of the PFN films through polarizing different areas of the layer in different directions as seen in Figure 4.13 c and f.

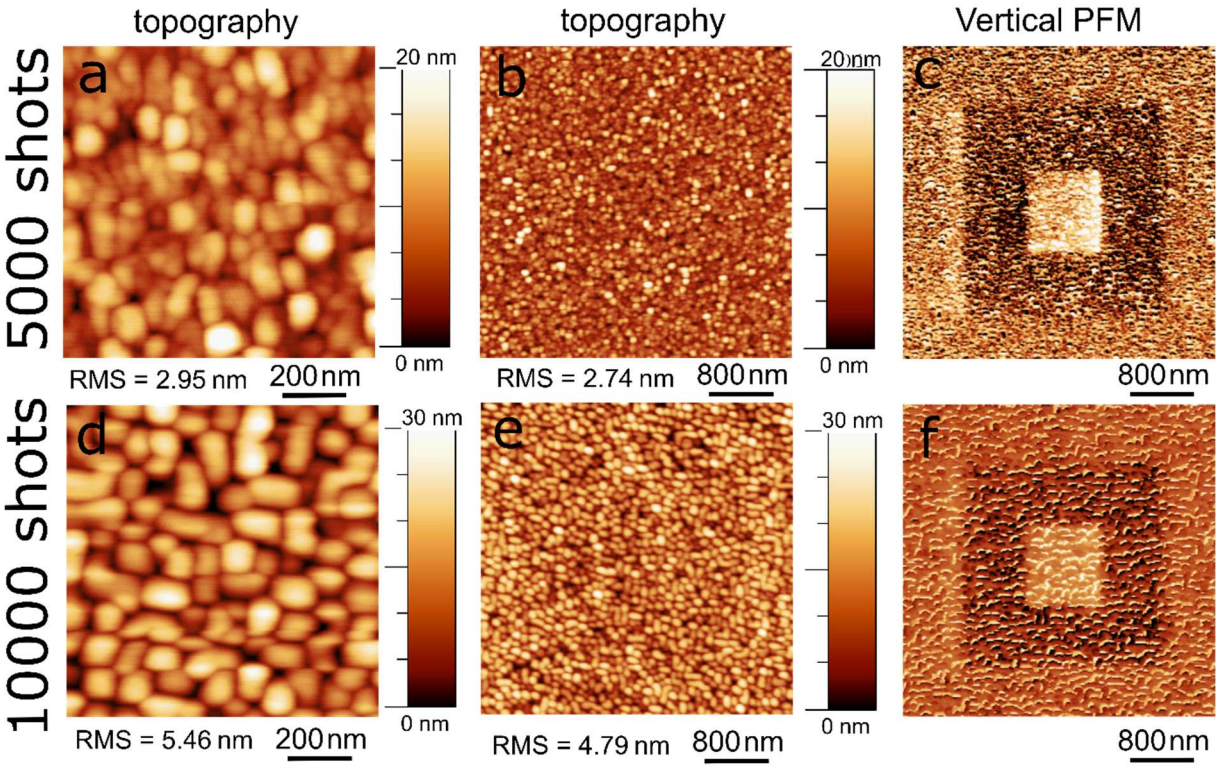


*Figure 4.13 Topography images of PFN layer deposited with 5000 (a, b) and 10000 shots (d, e). C (5000 shots) and f (10000 shots) show a polarized pattern on the surface.*

To give further proof of ferroelectricity, local piezo response hysteresis loops were measured. An example is shown in Figure 5.15. The amplitude PFM signal (Figure 4.14a) is similar to macroscopic strain measurements. The PFM phase changes by approximately 180°, which confirms that polarisation switching occurs (Figure 4.14 b).

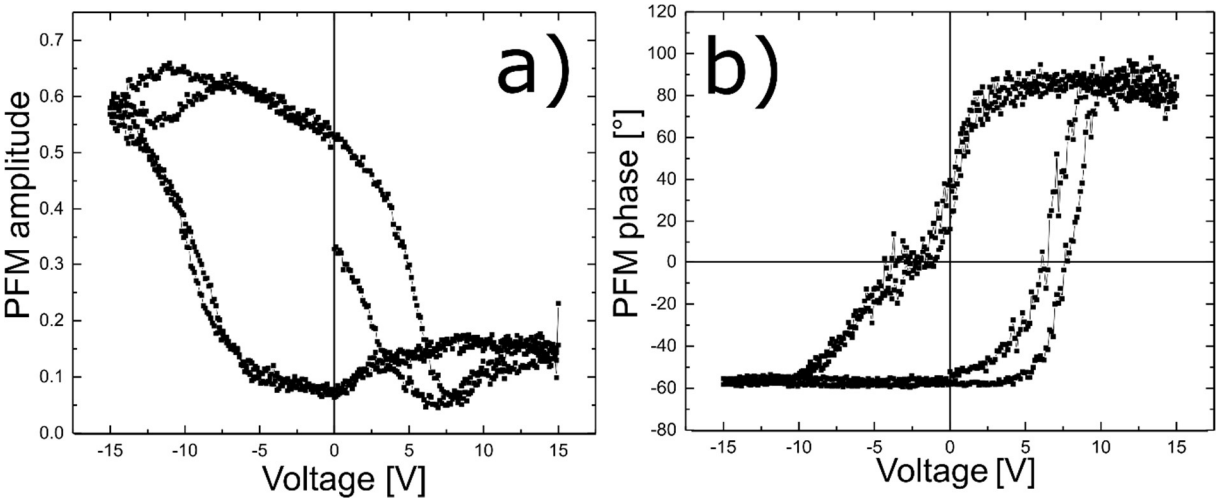


*Figure 4.14 The local piezo response hysteresis loops: amplitude (a) and phase (b), of a PFN layer.*

### 4.2.4. Optical Properties

No experimental study of the band gap of PFN films has been reported in literature so far. The theoretical calculations of Bharti et al. [22] claim that PFN has a direct band gap of 0.43 eV, which is appealing for photovoltaic applications. However, the experimental UV-Vis reflectivity measurements of PFN powders discussed in Chapter 3.3.4 have shown that the band gap for the bulk material is at least 2.17 eV.

Here we discuss the optical properties of PFN thin films. Since the layers are grown epitaxially and are well oriented, the grain boundaries and related trap states should be minimized. The easiest way to do a first estimation of the band gap to study the absorbance spectra from UV-Vis spectroscopy (Figure 4.15 a). The spectra show several absorption edges between ~2.3 eV and 3.2 eV. The resulting Tauc plots after Eq. 1.6 for both direct and indirect band gap are shown in Figure 4.15 b and c, respectively. By fitting the straight segments of the plot corresponding to the direct band gaps (Figure 4.15 b), two possible energies could be considered as the band gap at 2.32 eV and 2.78 eV. The first energy of 2.32 eV agrees with the data for the PFN powders (Chapter 3.3.4) for which values lie in between 2.17 and 2.55 eV depending on the synthesis conditions. The values of 2.78 eV is relatively large, but it can be compared with the value of 2.55 eV, obtained for the powder synthesized by the MA method, which has the lowest number of defects. Fitting the Tauc plot for the indirect band gap (Figure 4.15 c) also resulted in two options for the band gap width, either 2.25 or 2.75 eV, which are relatively close to the values estimated under the assumption for the direct band gap. The indirect band gap Tauc plots for the powders (Appendix Figure 6.3) show the similar trend [170].

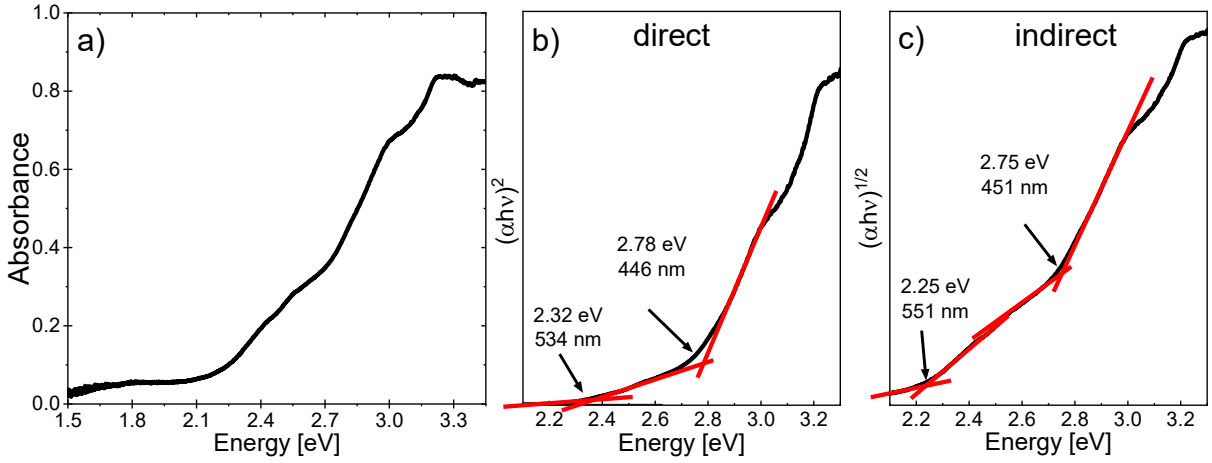


*Figure 4.15 Absorbance spectra for the PFN layer from UV-Vis absorption measurements (**a**). Tauc plots for direct (**b**) and indirect (**c**) band gap [170].*

It is hard to conclude about the fundamental band gap of PFN just from the results of the UV-Vis spectroscopy. For that, additional UPS/IPES measurements were done displayed in Figure 4.16. Before discussing these results, some things should be noted. These measurements were done using a STO/SRO sample with a size of 0.5 x 0.5 cm². Since the sample was so small, some of the signals might originate from the surrounding substrate holder. It also needs to be considered that the sample studied in this experiment was deposited in oxygen and there is some contamination on the surface. Therefore, the calculated values for the work function $W_f$, the ionization energy $I_E$, and the electron affinity $E_A$ might differ by some 100 meV from the real values, because of the high surface sensitivity of the method. Keeping all this in mind, the conduction band $E_C$ lies at -0.8 eV and the valence band $E_V$ at 1.95 eV with respect to the Fermi level, which forms a band gap of 2.75 eV (see equation Eq. 2.13). This result is in good agreement with the higher value obtained from the UV-Vis spectroscopy data discussed before, for both the direct and indirect band gap [170]. The fundamental band gap must be bigger than the optical band gaps. However, the UPS/IPES data show a slightly smaller band gap than the direct UV-Vis measurement. Most probably it is related to measurement and fitting errors. The real band gap value might be slightly different from the values reported here. Nevertheless, the error should lie within the range of 0.1 eV.

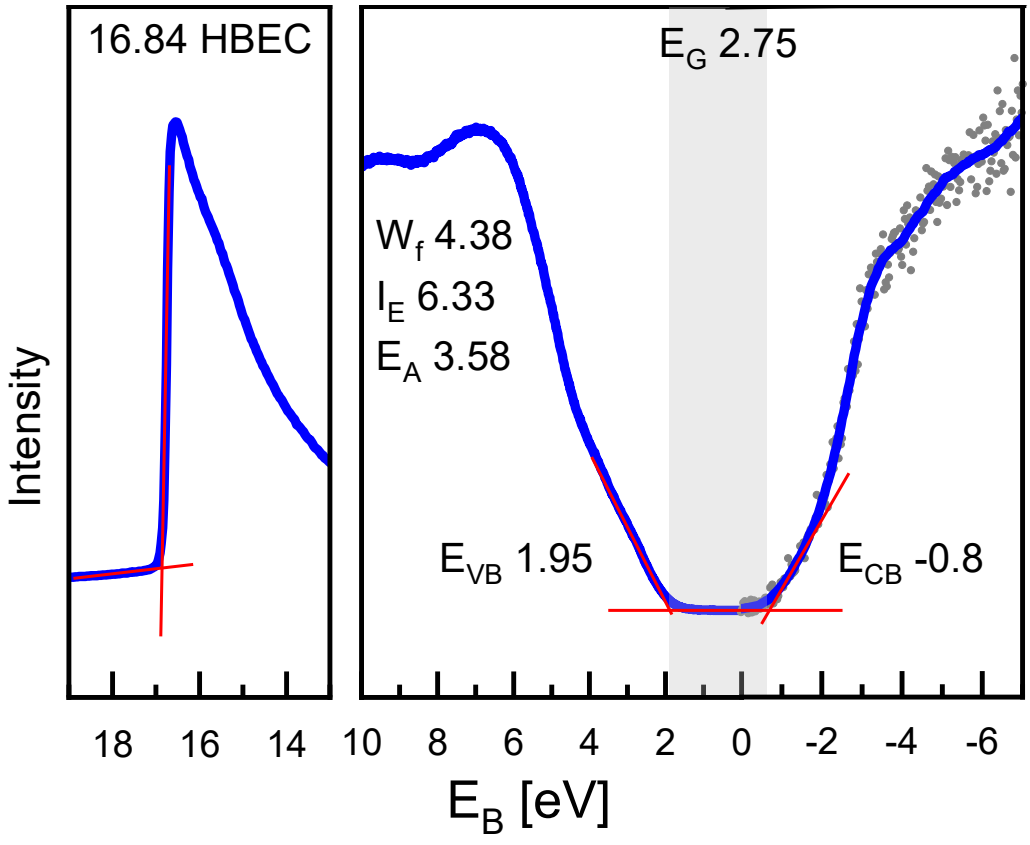


*Figure 4.16 Combined IPES/UPS measurements of the PFN layer deposited on STO/SRO. The band onset, the position of the high binding energy cut-off (HBEC), and the extracted energy values are indicated in the graph [170].*

In order to understand how the smaller band gap of 2.3 eV occurs, photoluminescence (PL) measurements were carried out at the Chair of Materials in Electrical Engineering by A. Schmitz. PL spectra of the PFN thin film were measured with different excitation lasers in a confocal setup shown in Figure 4.17. They exibit sharp peaks close to the cut-off of the excitation laser filters at ~2.3 eV and ~3 eV for 532 and 405 nm lasers, respectively. The excitation from a 405 nm diode laser is the most reliable one and tends to generate the real PL signal, as the excitation energy (~ 3.06 eV) is higher than the band gap value deduced from the UV-Vis spectroscopy and IPES-UPS measurements. A broad emmision is centered in the green spectral region around ~2.3 eV, close to the absorption onset. The fundamental band gap at around 2.7 eV PFN seems to have many states within. Strong absorption related to the transition between the conduction/valence band and defect states in the band gap are observed. The presence of the defect states cannot be controlled, however, the contribution is strong in materials with many defects e. g. prepared by the combustion or hydrothermal methods. This is indicating that the luminescence originates from an optical band gap which is related to defect levels within the fundamental band gap. In the further course of this thesis, the term defect related transitions will therefore be used. While exciting in the UV-range ($\lambda$ = 325 nm) another additional blue feature appears around 2.6 – 2.8 eV, which is similar to the green emission and stems from the fundamental band gap.

Different authors [171–173] have observed a similar broad maximum in their $ABO_X$ materials. It is mentioned that the PL emission in these materials originates mainly from the degree of structural order-disorder in the lattice of ceramic materials in the $ABO_X$ structure which can be influenced by the processing of the material. The more ordered the structure the less near band edge intermediary energy levels occur [171,172]. Longo et al. [173] obtained in their PZT samples three different components through deconvolution, which they described as blue, green, and red. Each of these deconvolutions is linked to different types of electronic transitions located in the band gap of the material. Different structural defects like oxygen or lead vacancies and bond distortions generate energy levels [174] in the band gap. Hu et al. [175] have investigated $PbTiO_3$ nanowires and concluded that the blue light emission ($\lambda$ = 453.5, 471.4, and 489.3 nm) can be attributed to the oxygen vacancy ($V_O^{\cdot\cdot}$) and lead-oxygen vacancy centers ($V_{Pb}^X$ and $V_O^X$). The oxygen and lead vacancies are known defects in PFN which can occur very easily during synthesis. The previously in UV-Vis measurements shown defect related transitions at around ~2.3 eV can therefore be a result of the band gap states which are formed by the vacancies as it is in good agreement with literature and the reported PL emission spectra.

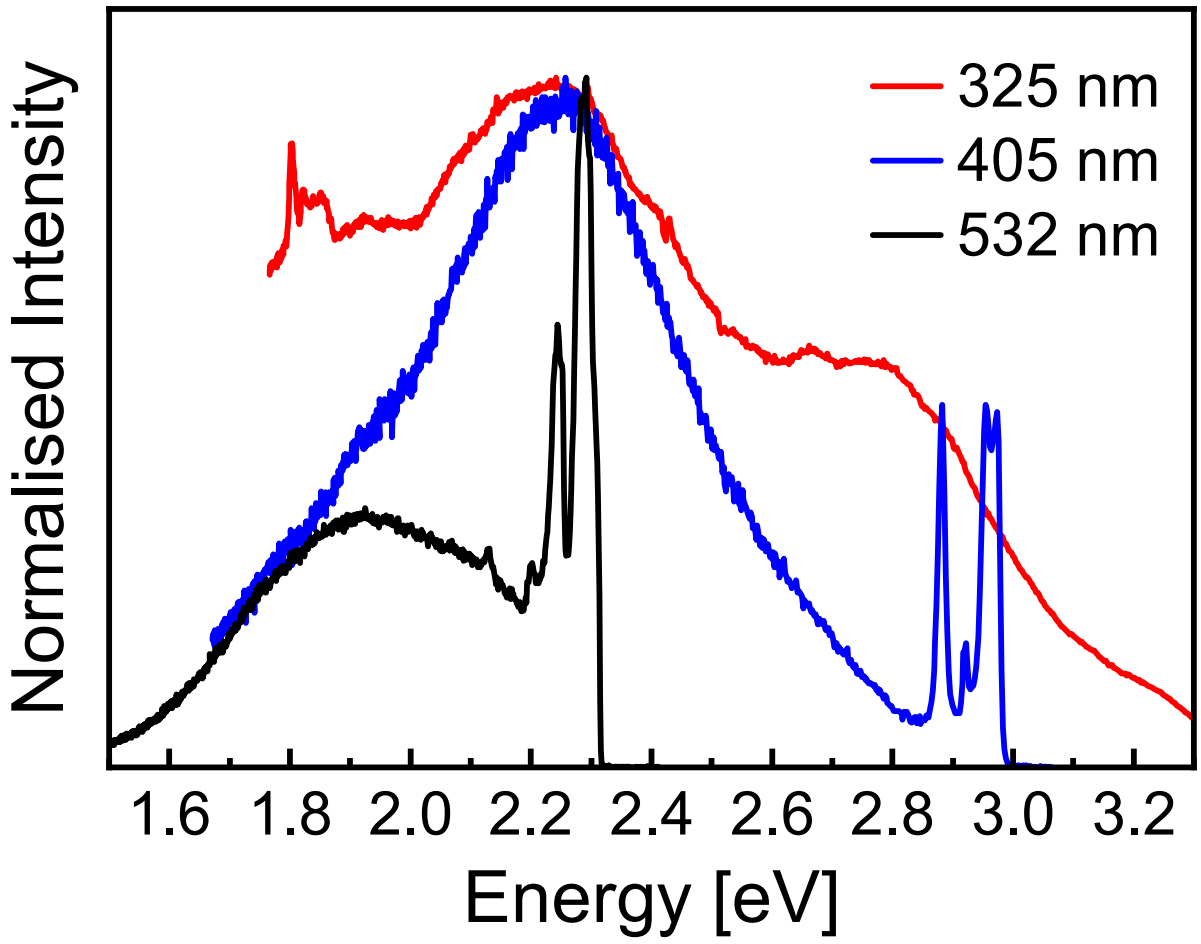


*Figure 4.17 Photoluminescence spectra of the PFN thin film with different excitation lasers.*

#### 4.2.4.1. Transition Line Measurement

The band gap of PFN is smaller than that for PZT (3.6 eV [10,17,18,127,128]) and the photovoltaic effect for other lead-based materials have already been proven. In conclusion, it can be considered, that PFN would lead to a higher device efficiency than other lead-based materials (see Chapter 1.5.4) since the absorbance spectrum is extended from the ultraviolet to the visible spectrum up to 450 nm. With a smaller band gap, generally more photons can be absorbed, and more charge carriers can be generated. However, viewing the solar spectrum, it is also evident that the solar output peaks at about 500 nm. The number of incident photons is the highest in this energy range, decreasing sharply in the UV range. First measurements arecarried out to see if a photocurrent will be generated when the film is illuminated.

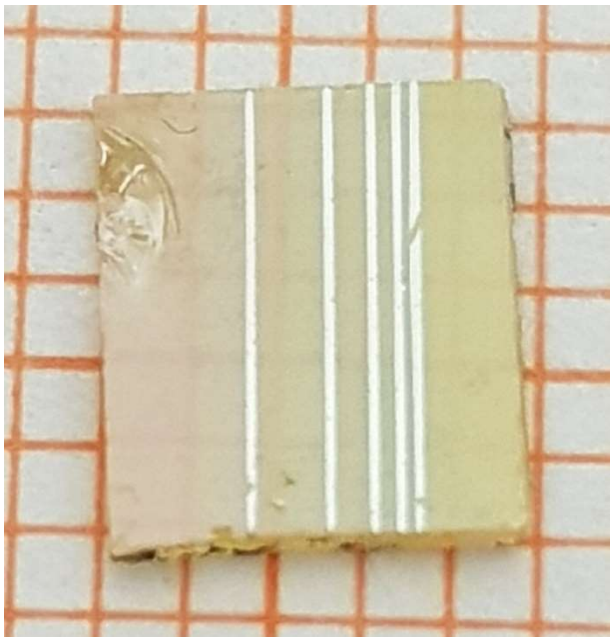

*Figure 4.18 Au-electrodes evaporated on the thin film with different distances.*

For this, Au electrodes were deposited on the film surface through evaporation with different distances as seen in Figure 4.18. I-V curves were recorded with and without illumination by a white light source in the range of -10 and +10 V. The results plotted in Figure 4.19 show a clear increase in the current when the layer is illuminated. This means that charge carriers are generated by the photons entering the layer or even only are generates on the surface .

For a distance between the electrodes of 800 µm, the conductivity increases from 23 S/µm to 32 S/µm under illumination. To prove that this increase is light related, the light was turned once on while sweeping the voltage, as shown in Figure 4.20. The sample shows a clear response by increasing the current at the moment the light is turned on.

It has to be mentioned, that the value of the current under illumination decreases with a bigger distance between the electrodes. The general consideration is that in order to contribute to the measure current, the photogenerated carriers, must reach the sample electrodes. However, a part of them will be scattered and/or trapped by defects. The probability of the scattering on defects increases for longer distances, therefore the total photocurrent decreases.

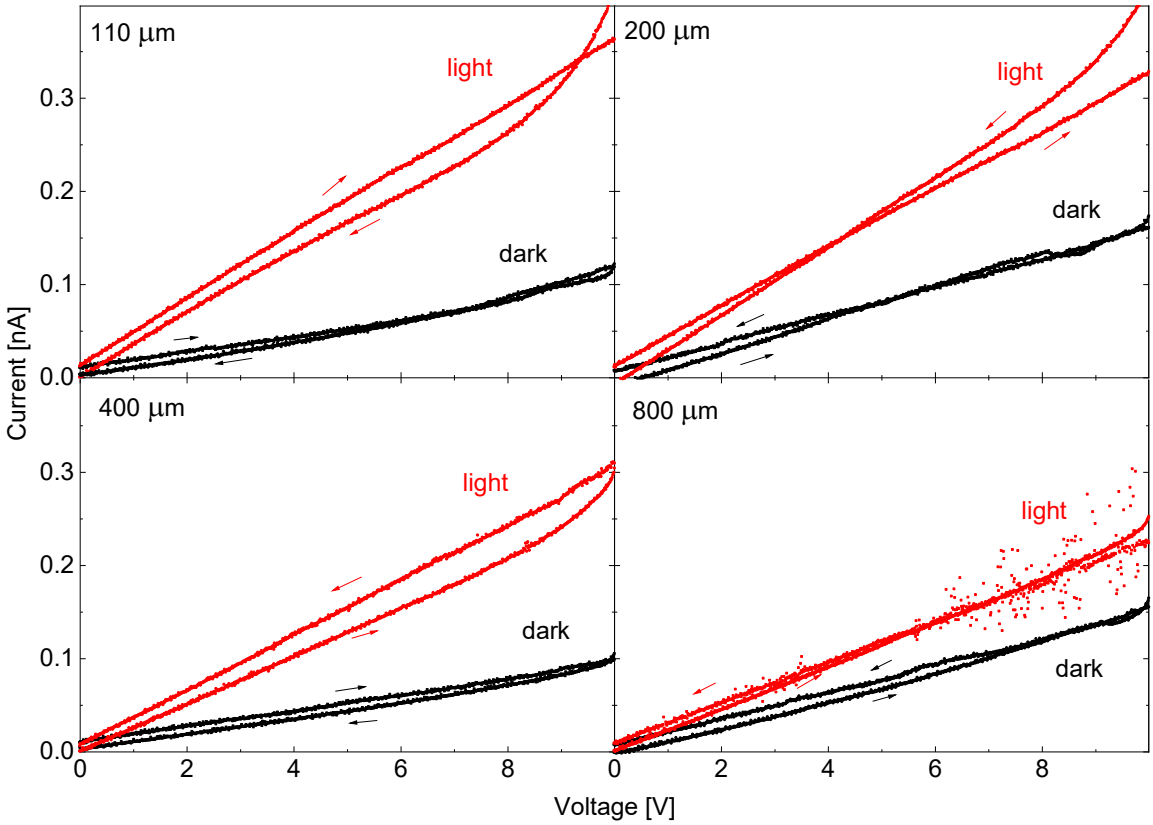


*Figure 4.19 Transition line measurement response of a PFN film sample in the dark (black lines) and under illumination (red lines) for different distances between electrodes.*

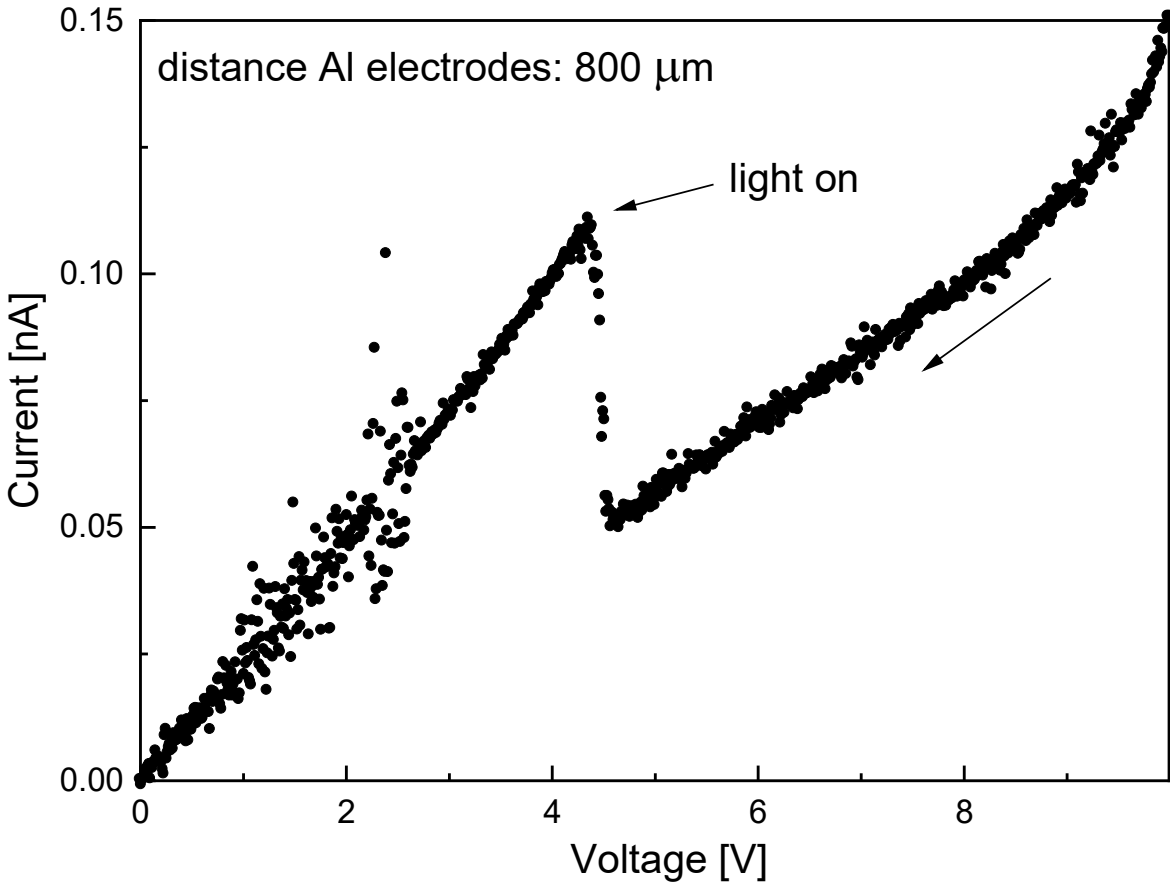


*Figure 4.20 Transition line measurement response for a lateral electrode distance of 800 µm. The sample was illuminated while sweeping and shows a response in increasing current.*

The life time of the charge carriers was measured and calculated by A. Schmitz by time resolved photoluminescence. The green emission shows a long, non-exponential decay with a long effective life time of ~ 400 ns in Figure 4.21. Such lifetimes are often observed in lead-containing semiconductors [176]. This means that charge carriers are generated in the total area, but most of them recombine before they reach the electrode and cannot be extracted.

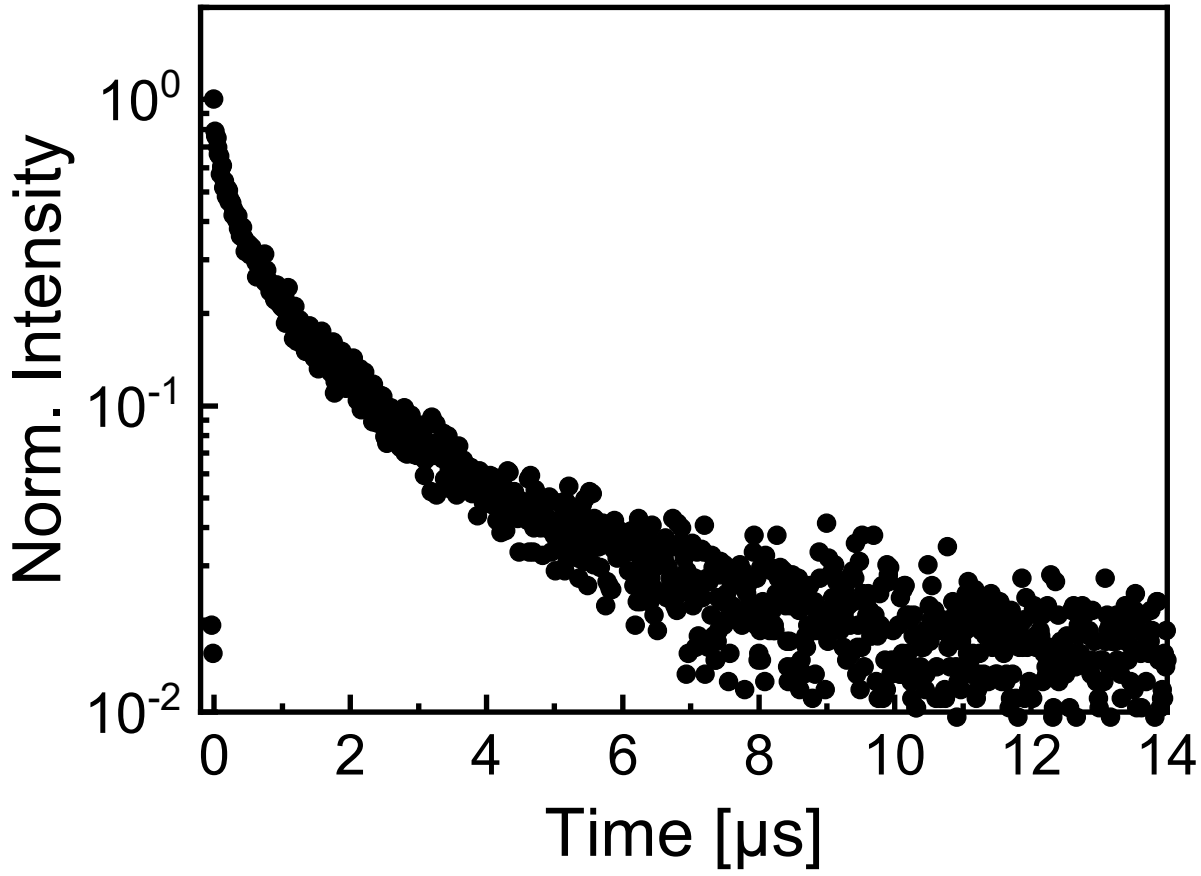


*Figure 4.21 Transient photoluminescence decay of the PFN film.*

## 4.3. Spin Coating

Spin coating is a popular, relatively cheap, and readily available method for producing homogeneous thick or thin films of good quality. While depositing, the substrate is sucked onto a rotator with vacuum. After the material to be coated is dripped onto the substrate in a solution or dispersion (Figure 4.22 a), the rotator begins to turn. The centrifugal forces push the liquid outwards and a homogeneous layer thickness can be created (Figure 4.22 b). There are a few things to consider when spin coating: the viscosity of the applied material, the rotation speed, and the rotation time adjust the layer thickness. As soon as the rotator stops, the liquid at the

edge may flow back to the center of the sample due to surface tension (Figure 4.22 c). Normally, an annealing step follows the coating in order to evaporate the solvent and form the film.

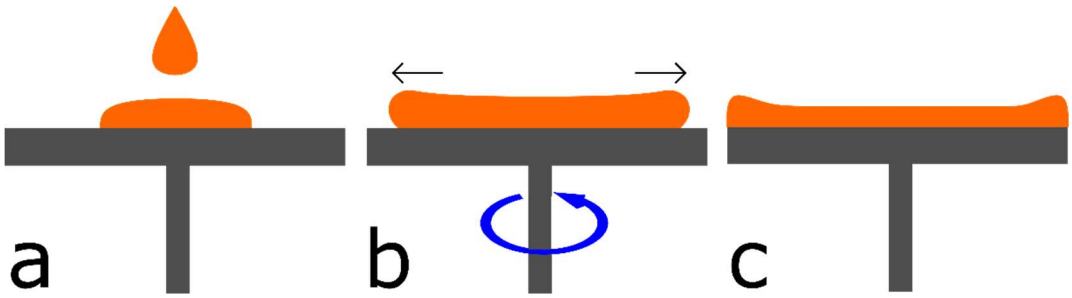


*Figure 4.22 Spin coating principles: a) the solution is dripped onto the substrate, b) the rotator is turned on and the solution is forced to the outer edges of the substrate, c) when the rotator stops, the film edges remain thicker.*

## 4.4. Thin films by sol-gel

### 4.4.1. Preparation

0.44 mol (+10 % lead excess) of lead (II) acetate trihydrate (≥ 99.99 %, Sigma Aldrich) and 0.4 mol of iron (II) acetate (95 %, Sigma Aldrich) were mixed separately in 10 and 5 ml glacial acetic acid (99. %, VWR), respectively. After both powders were fully dissolved, they were mixed. 0.4 mol niobium n-propoxide (99 %, Alfa Aesar) was dissolved in 1 ml of 2-methoxyethanol and added to the lead-iron solution. For better solubility 10 ml glacial acetic acid was added again [89]. The result was a clear brownish solution which can be stored in a glove box.

*Figure 4.23 Sol gel solution after mixing precursors together.*

The deposition was carried out in a glove box as well to protect the substrate from contamination. The solution was filtered through a 0.4 µm membrane filter and spin coated onto a STO substrate at 2000 rpm for 60 s. After depositing, the sample was annealed at 300 °C for 5 min. The procedure was repeated until the desired thickness was achieved.

Figure 4.24 shows the $\theta$-$2\theta$ XRD measurement of the annealed sample before sintering. Compared to the STO pattern (Figure 4.2) only a small amorphous hump from around 25 to 35 ° appears. The crystalline perovskite phase does not form due to the low heating temperature of 300 °C.

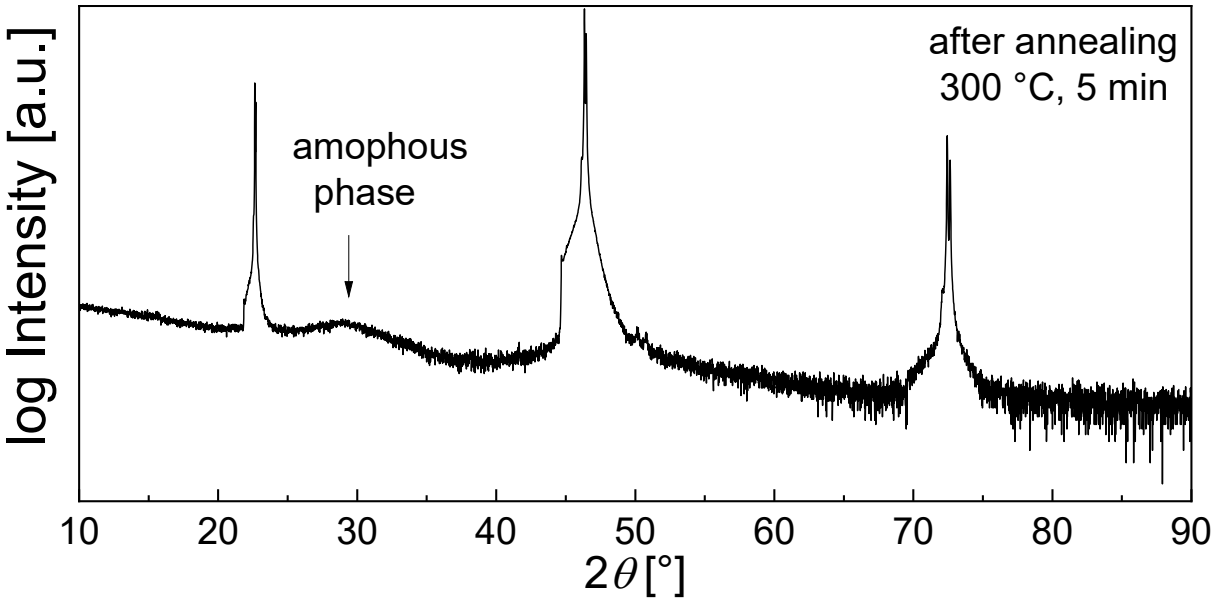


*Figure 4.24 XRD θ-2θ measurement of a sol-gel deposited PFN film after annealing at 300 °C.*

Figure 4.26 shows optical images of the deposited layer before and after annealing. It can be seen that the layer is thicker at the edges of the substrate due to the accumulation of the solution and the subsequent reflux after spinning. These differences in layer thickness are even clearer visible after sintering. A colour change before and after sintering indicates densification of the layer.

### 4.4.2. Parameter Variation

During the preparation of a new material batch a parameter study needs to be conducted to find the optimum parameters. Sintering temperature (1000, 1100 or 1200 °C) and sintering time (3h or 5h) were varied to minimize the amount of excess lead by minimizing lead loss. Both $\theta$-$2\theta$ and grazing incidence XRD measurements were performed to estimate the phase content and crystalline structure of the films.

On the basis of the grazing incidence measurements in Figure 4.25 the amount of PFN, pyrochlore, and other phases could be calculated through the Rietveld refinement. At a sintering temperature of 1000 °C, more than 30 % of PbO were left in the sample. To get rid of this, a higher sintering temperature or longer sintering time are needed. By increasing the sintering temperature to 1100 °C, PbO vanished and the relative amount of the pyrochlore phase was reduced from 21.4 to 6.7 %. A further increase of the sintering temperature led to a higher lead loss and the formation of niobium oxide and magnetite due to the decomposition of PFN. 1100 °C turned out to be the best sintering temperature, and the corresponding sintering time was tuned. With a sintering time of 3 h a single phase polycrystalline sample was achieved.

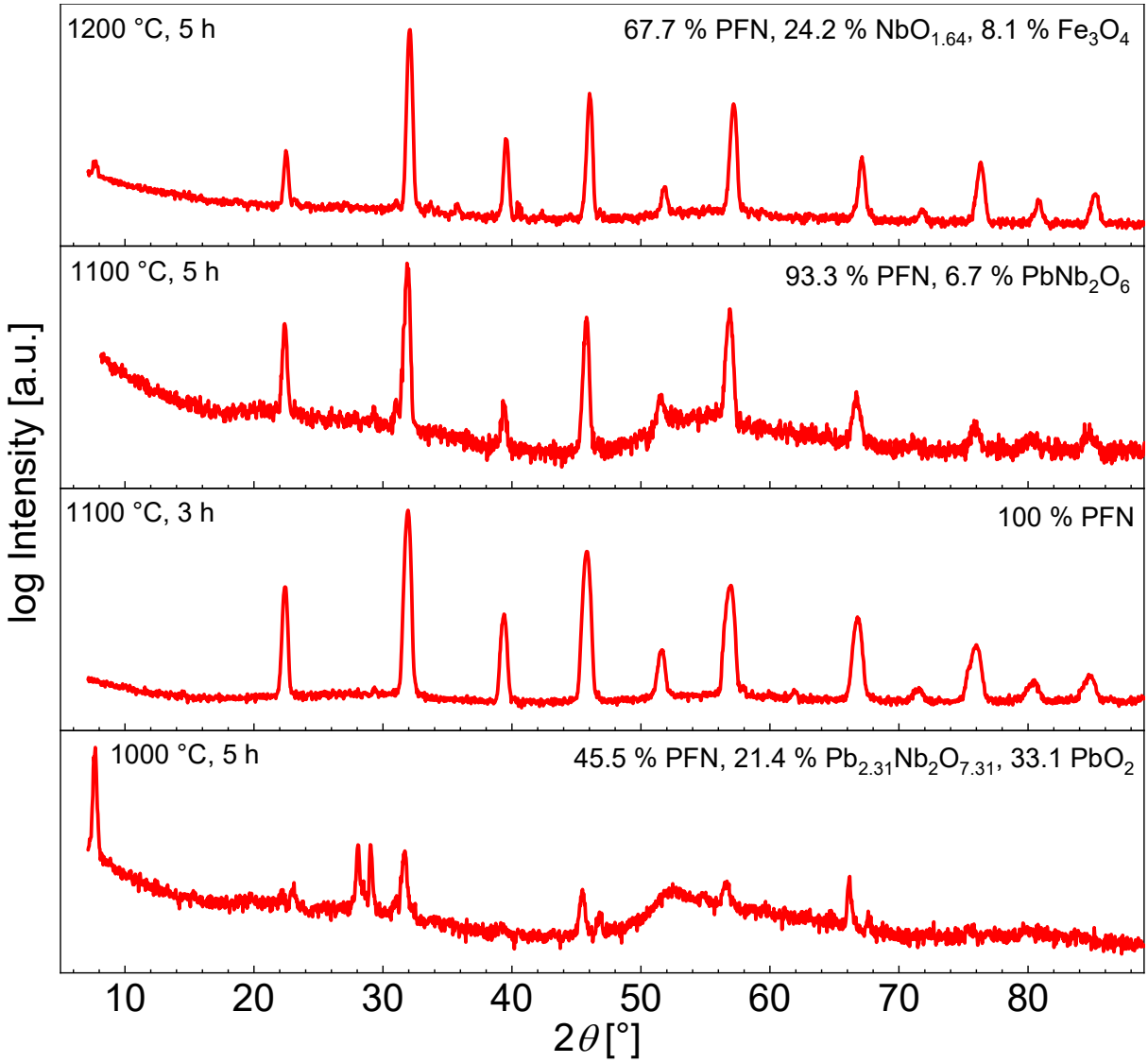


*Figure 4.25 Grazing incidence measurement of sol-gel deposited PFN films for different sintering temperatures and time.*

Since the prepared batch was a small trial to find the best sintering conditions, a bigger batch for further investigations needed to be mixed. In this case, the sintering time had to be adapted. In all following measurements the sintering time was 5 h to achieve a pure perovskite phase.

To check whether the purity of the phase changes with other layer thicknesses, samples with 3, 5, and 7 layers were prepared. It is observable that the thickness inhomogeneities for the 3-layer sample are more developed, due to the recoil of the solution after rotating. The more layers deposited, the more balanced the thickness will be, because the difference in surface tension of the solution and the underlying layer is changing when deposited onto the same material.

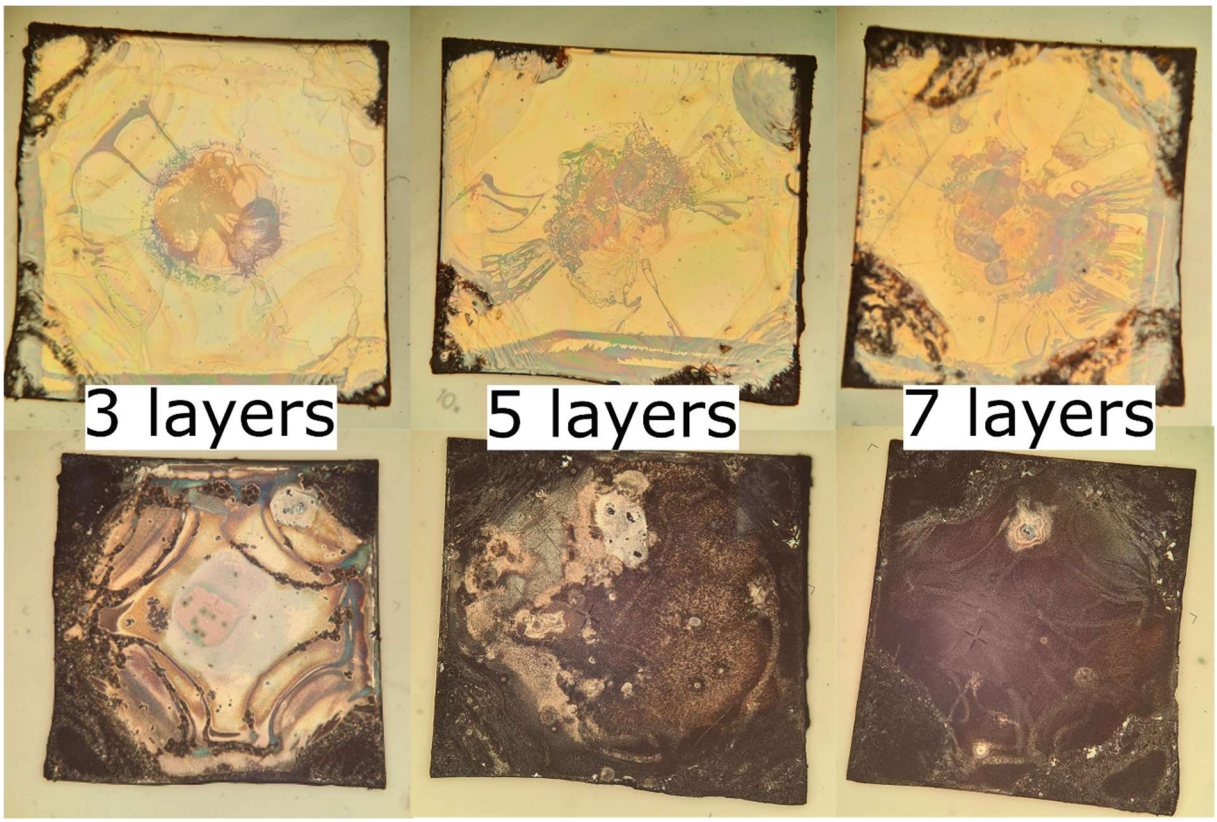


*Figure 4.26 Optical microscope images for the as annealed substrates (top) and the sintered substrates (bottom) for different deposition numbers.*

This thickness inhomogeneity makes it difficult to correctly estimate the layer thickness through SEM images on layer cross sections, since only a small area is visible and even there the thickness range is quite big. The thickness of the films after deposition of three layers is around 100 - 300 nm, while it is around 1000 nm and 1800 nm for the films with 5 and 7 layers, respectively, as shown in Figure 4.27.

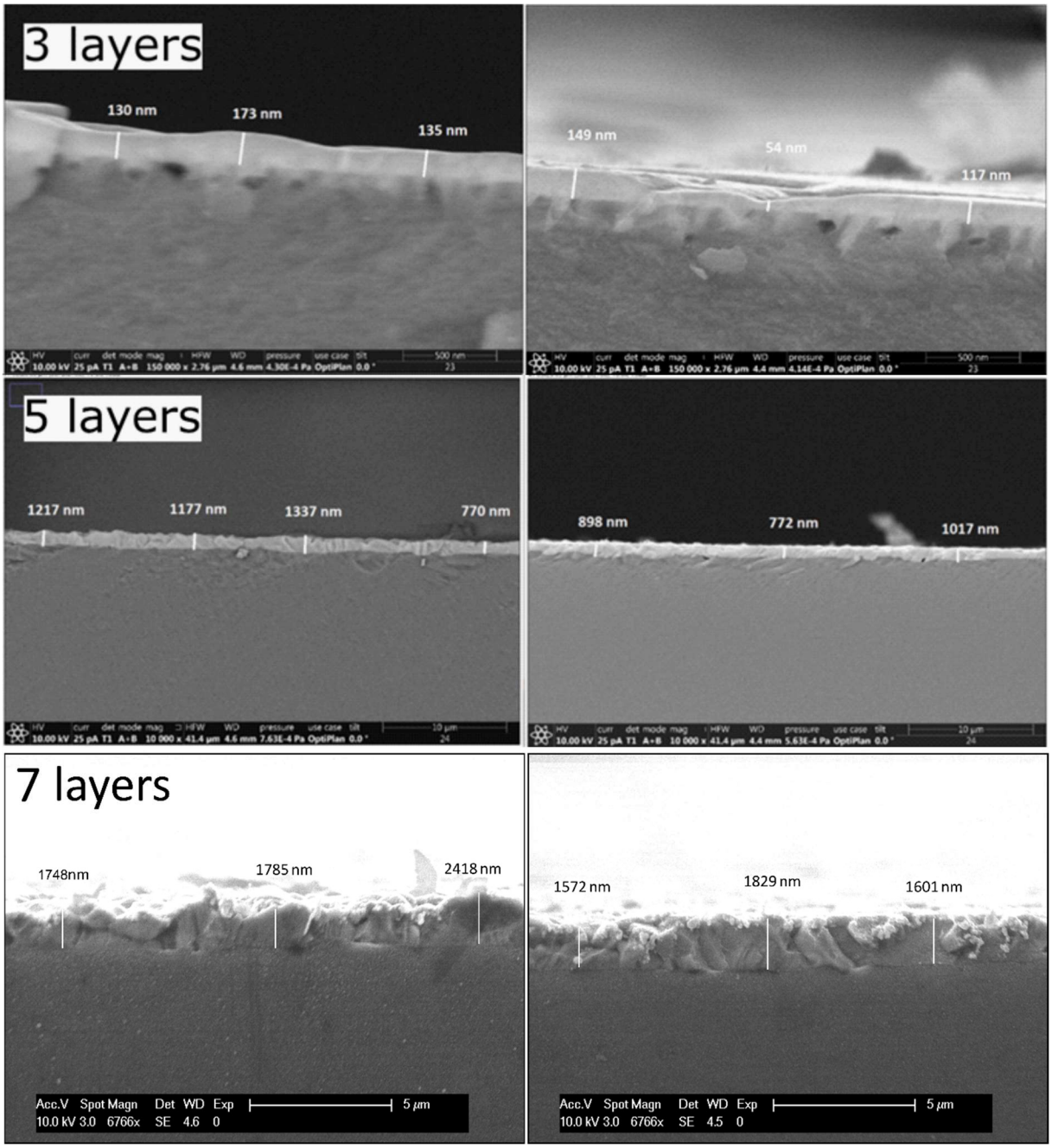


*Figure 4.27 Cross-section SEM images of the sol-gel PFN films with three, five and seven deposited layers.*

A closer look on the structure of the grains is revealed in Figure 4.28. The sample of the five layers shows a columnar growth of grains across the film from the surface to the substrate. However, for the seven layers there are several grains across the sample thickness. The film with the seven layers, appears uneven and not uniform.

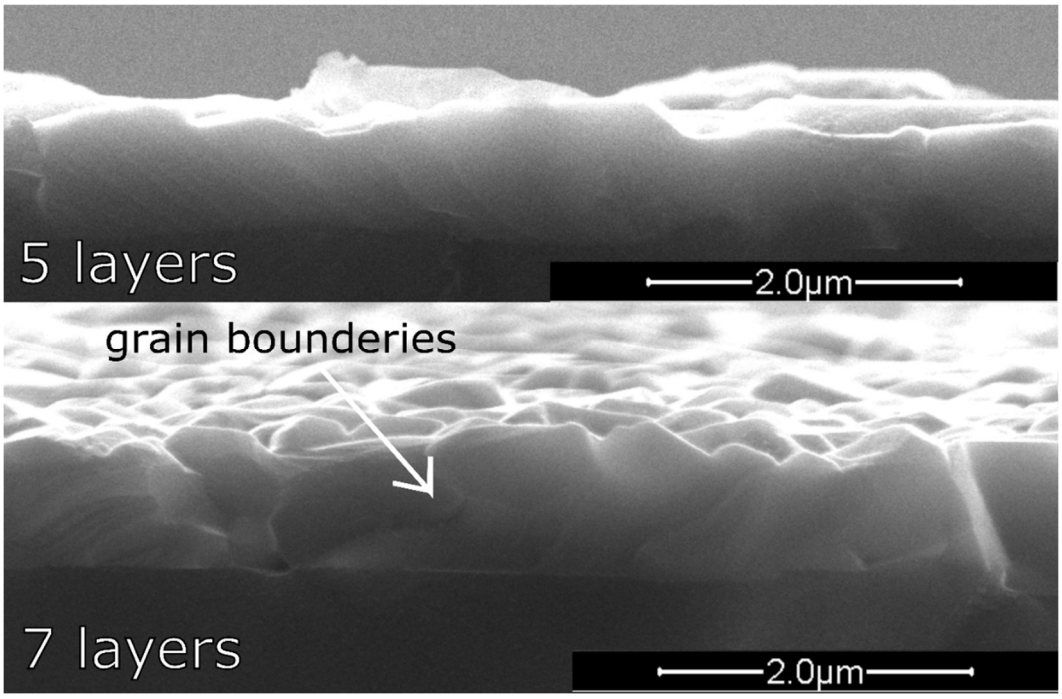


*Figure 4.28 Close up of crosssection SEM images of the layers deposited five and seven times.*

The GIXRD pattern in Figure 4.29 reveals that the pure perovskite phase was formed for all three film thicknesses. The only difference lies in the X-ray diffraction peaks at 57 and 76 ° (for a closer look see in Appendix Figure 6.8): The peaks seem to have shoulders (marked by arrows), which might originate from impurities.

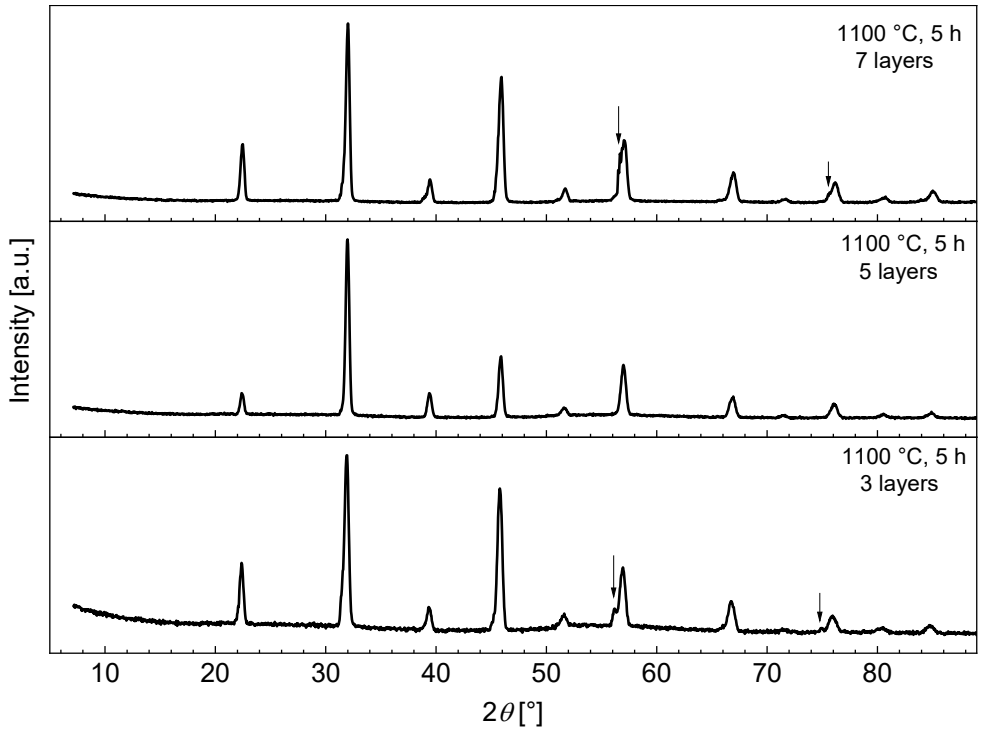


*Figure 4.29 GIXRD patterns for the sol-gel deposited PFN films with the different thicknesses.*

Based on these results, the number of layers was chosen to 5 layers in the following.

### 4.4.3. Optical properties

The light absorption by the PFN films deposited via spin coating was further investigated through reflectance measurements. The band gap width was evaluated using the Tauc plots method (Figure 4.30 a). For the direct band gap, it yields a clear value for $E_{G,fund}$ of 2.69 eV. The defect related transition is around 2.3 eV in accordance with the measurements of the PLD layers. In the indirect band gap plot, the defect related transition can be seen more clearly at 2.28 eV. From the PLD layer measurements the fundamental band gap is 2.64 and is slightly lower than the value obtained by UV-vis.

The values of $E_{G,fund}$ for the sol-gel prepared PFN thin films match the values previously described. They are just a bit smaller than the values obtained for the films deposited by PLD.

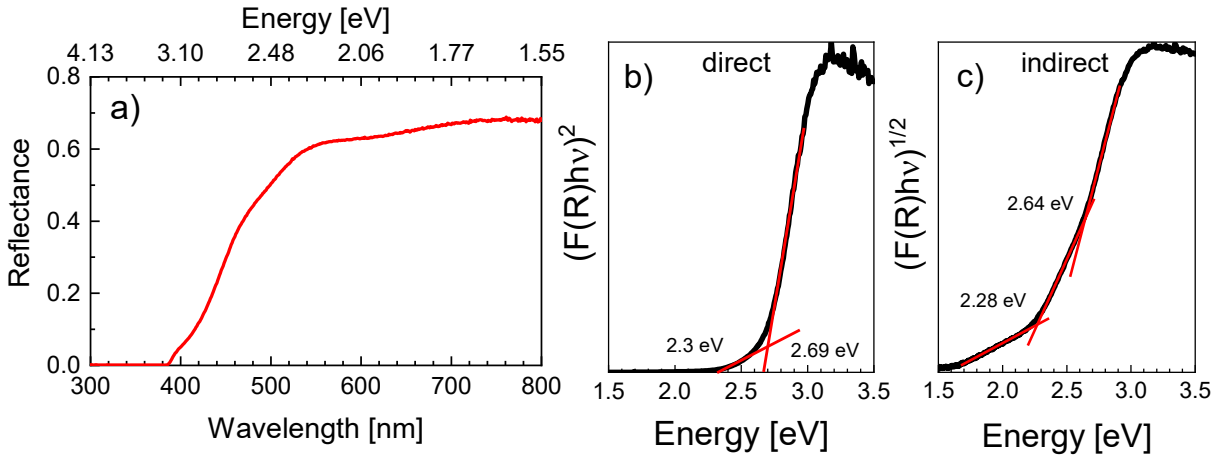


*Figure 4.30 Reflectance spectra for the sol-gel PFN film from UV-Vis reflectance measurements (a). Tauc plots for direct (b) and indirect (c) band gap.*

## 4.5. Band structure of PFN

No major differences in the bandgap values were found between the films prepared by PLD and sol_gel, although the microstructure and thicknesses differed greatly. However, the literature discusses the band gap values of other ferroelectric films such as PZT and PLZT, which differ at different thicknesses [177–179], but, no clear trend in one direction can be seen. To obtain further evidence of the film thickness independence, additional UV-vis measurements were performed on a crushed single crystal. The single crystal was provided by Prof. Antony Kania from the university of Silesia in Katowice. Since no single crystals could be measured at a piece, the crystal therefore had to be crushed before the measurement. It turns out that the bulk PFN value of the band gap is also around ~2.67 eV for both the direct (Figure 4.31 a) and the indirect (Figure 4.31 b) band gap. This value is roughly in agreement with that of the film reported before, so that size effects could be excluded.

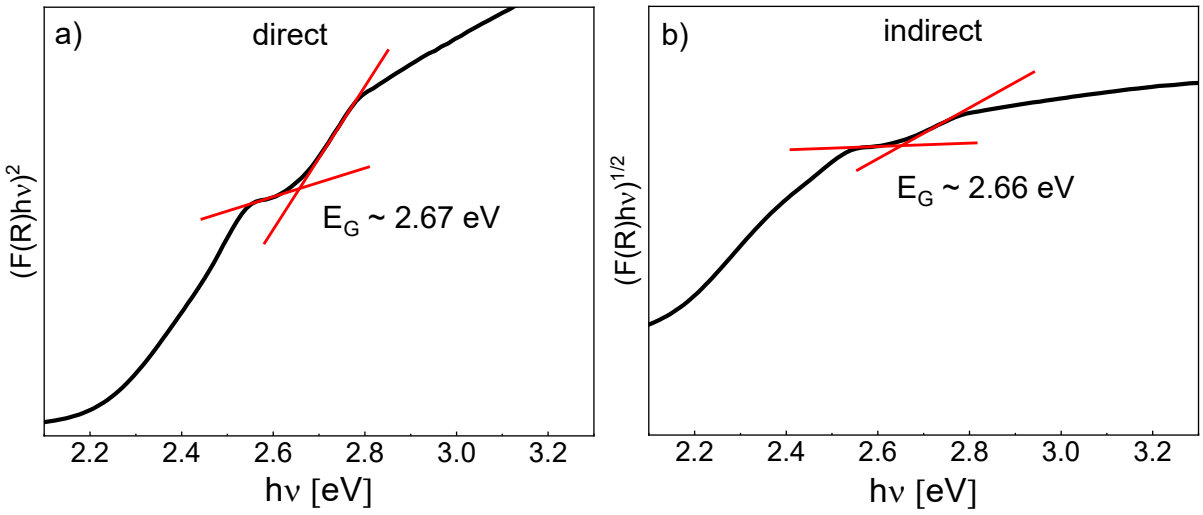


*Figure 4.31 Tauc plot from reference measurements done by UV-Vis spectroscopy on a crushed PFN single crystal for the direct (a) and indirect (b) band gap.*

The band gap transitions in PFN have been described and explained in detail, however, the question of the type of band gap remains unanswered so far. Although, the values for the defect related transitions and fundamental band gap do not differ significantly in the case of a direct or an indirect transition, it is nevertheless of great interest to answer this question. In the literature [18,130,180] the band gaps of perovskite ferroelectrics, like lead-based PZT and PLZT, or BFO, are considered to be direct band gaps. PFN belongs to the same group of materials, so the allegation that it also has a direct band gap seems to be plausible, especially as the DFT calculations predict the same [22]. Nevertheless, this assumption needs to be proven. A hypothesis to confirm the direct bandgap could be done by the absorption coefficient. The plot of the absorption coefficient $\alpha$ of different semiconductors is shown by Stillman *et. al* [181]. It changes in orders of magnitude near the band edge energy. Comparing the direct to the indirect semiconductors the direct change is “harder” while it appears smooth for the indirect ones. Figure 4.32 shows the absorption coefficient for a crushed PFN crystal and films deposited by PLD and by spin coating. All of them appear different, however, they are similar in their characteristics as the crushed crystal (Figure 4.32 a) has a more developed Urbach tail. Due to the higher surface area of the powder more states can be located in the band gap. As already discussed before, the strong increase in the slope is shifted to smaller energies due to the trap states within the band gap. Nevertheless, a steep rise in $\alpha$ is recognizably beneath the fundamental band gap at around 2.75 eV measured before and a major change in the slope is apparent. In the samples deposited by PLD (Figure 4.32 b) and by spin coating (Figure 4.32 c) the same trend is observable, however, the Urbach tail is not so pronounced.

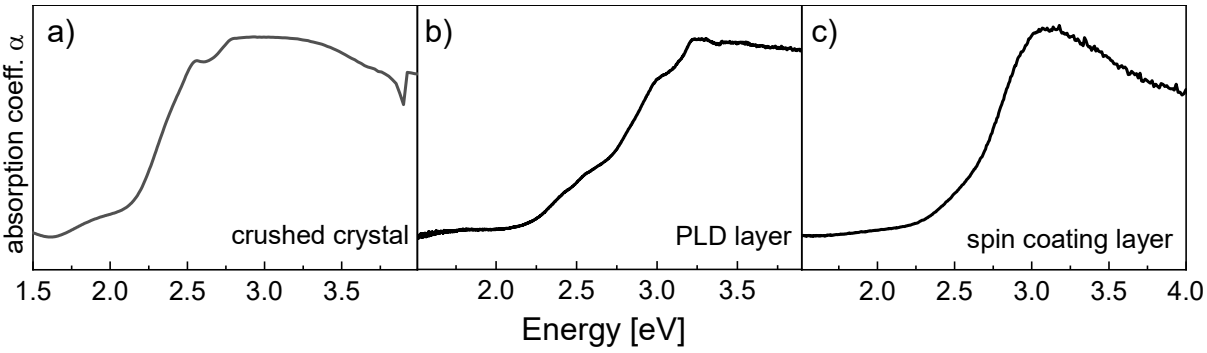


*Figure 4.32 Absorption coefficient for the crushed crystal (a), the layer deposited by PLD (b), and spin coating (c).*

Plotting the logarithmic absorption coefficient for all three samples and fitting the Urbach region, the Urbach energy $E_U$ can be calculated from the slope as visualized in Figure 4.33. As mentioned in Chapter 1.5.1.2 a small $E_U$ indicates a high structural quality. The results for the calculated $E_U$ confirm this as the sample prepared by PLD has the smallest $E_U$-value of 0.24 eV and the crushed single crystal the highest $E_U$-value of 0.313 eV.

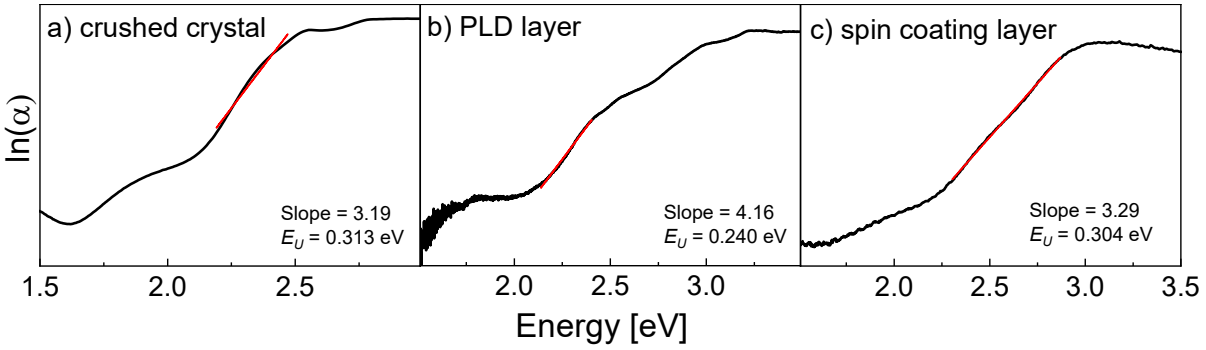


*Figure 4.33 Logarithmic plot of the absorption coefficient versus photon energy showing the Urbach energy fit and its values for the crushed crystal (a), the layer deposited by PLD (b) and spin coating (c).*

Another postulation can be made through the temperature dependent measurement of the crushed single crystal bulk PFN by UV-Vis spectroscopy as seen in Figure 4.34 for the direct and indirect Tauc plot. To excite an electron to the conduction band via an indirect band gap the phonons are an important factor to keep the photon energy needed low. That suggests that, if phonons are involved, the temperature dependency of the indirect band gap in the phonon absorption part should be recognizable [182]. However, as Figure 4.34 b reveals, the temperature dependency in this part is quite low and can be attributed to the normal band gap change with temperature as discussed in the literature many times [107–109] and shown in Figure 4.34. With increasing temperature, the band gap is decreasing due to thermal expansion and the electron phonon interaction. However, the part, which is markable changing with temperature is the Urbach tail, as this is seen in the literature [109] as well.

These arguments might not replace DFT calculations or investigative measurements, nevertheless, they strengthen the allegation of a direct band gap, which will be concluded in this work for PFN.

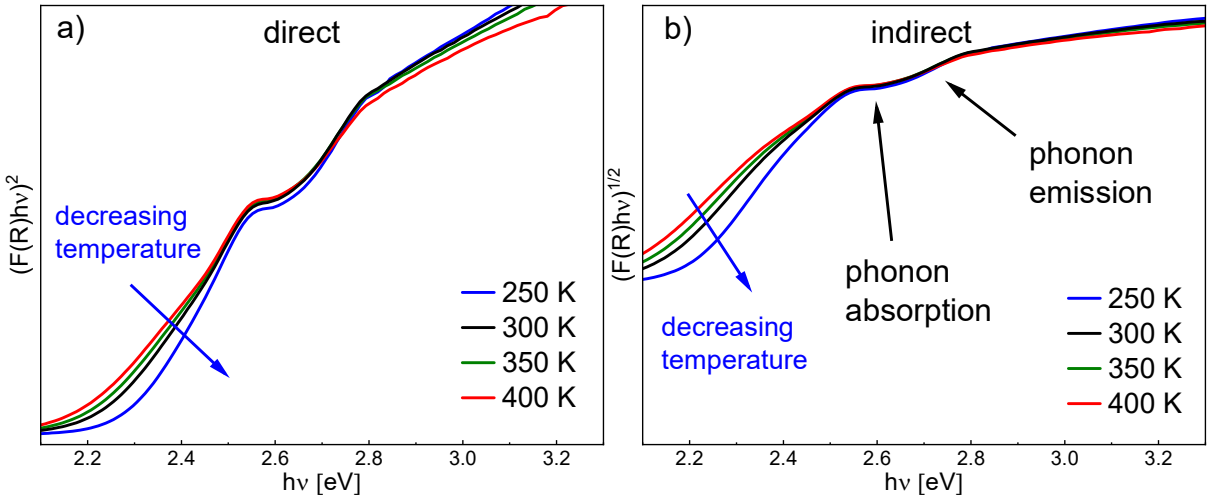


*Figure 4.34 Tauc plots from reflectivity measurements on a crushed PFN single crystal in dependency of the temperature for a direct (a) and indirect (b)band gap.*

## 4.6. Summary

PFN films with a pure perovskite phase were successfully deposited on a STO(001) substrate by PLD and spin coating. The optimal substrate deposition temperature for the PLD was found out to be 700 °C which results in a pure phase, epitaxial growth, high crystallinity, and a smooth surface. The PFN phase is more likely tetragonal by adapting to the cubic substrate. The film thickness was calculated to be 100 nm and no occurrence of a size effect was seen. The grain size is 75 ± 15 nm. With a higher layer thickness, the surface becomes rougher, and the grains grow which could influence the properties of the material.

The band gap was measured with UV-Vis spectroscopy and UPS/IPES. The results show that the fundamental band gap of the PFN layer deposited by PLD is around 2.75 eV and a defect related transition is found at around 2.3 eV. The Tauc plots for direct and indirect band gap representation look similar and their fits provide approximately the same values of the band gap. Photoluminescence measurements confirm, that the defect related transition is due to intermediate electronic states within the band gap mostly originating from oxygen and lead vacancies. Initial measurements towards photovoltaic properties were done by TLM. During illuminating the measured conductivity increased from 23 S/µm to 32 S/µm with an electrode distance of 800 µm.

PFN Thin Films

The PFN films prepared by spin coating on a STO(001) are polycrystalline and the grains growth columnar with thinner layers and start growing across the sample with thicker layers. The sintering temperature needs to be 1100 °C with a sintering time of at least 3 h depending on the batch. The layer thickness is irregular and lies around 1000 nm after 5 depositions. The band gap was obtained from UV-Vis spectroscopy with a value of around 2.64 - 2.69 eV. The defect related transition could only be indicated for the direct plot, however, in the indirect plot is around 2.28 eV.

The band gap values from the layers deposited with PLD and spin coating are in good agreement with each other. Another band gap was measured at 2.67 eV for a crushed single crystal sample. Due to the agreement with the other measurements the size effect for the band gap value can be excluded. The question for the band gap nature if direct or indirect could not be answered in investigative way, however, an estimation with the plot of the absorption coefficient and the temperature dependent UV-Vis spectroscopy measurements could be made. These do not show a change in the emission part of the indirect band gap resulting that no phonon interaction is necessary to excite an electron from the upper edge of the valence band to the lower edge from the conduction band.

# 5. Conclusion and Outlook

The optimal conditions to synthesize dense PFN ceramics which are usable for target preparation for PLD deposition were established. The best synthesis method includes the mechanochemical activation in a first step, however, the solid-state method was more convincing due to the leeway in the obtainable properties. By changing the calcination and sintering temperatures, a ceramic that showed the best ferroelectric and magnetic properties could be produced.

It was found that the sintering and calcination temperatures affect the distribution of the cations in the PFN ceramics. The higher sintering temperature makes PFN more ordered which results in a less diffuse ferroelectric phase transition and slightly decreases the Neél temperature, however, probably only spatial ordering can be achieved.

The band gap of PFN was experimentally determined to be 2.7 eV. Nevertheless, another band gap of about 2.3 eV was also found, which is due to transitions between defect levels and the conduction/valence bands. In addition, the nature of the band gap was discussed at length and the decision was made that PFN has a direct band gap. Furthermore, the first evidence for the photoelectric effect in this material was provided.

Because of the smaller band gap compared to other lead-containing materials that have already been considered for an absorber layer, these studies are concluded with the statement that PFN could be suitable as absorber layers in solar cells.

This field offers numerous possibilities for subsequent research, which is mainly concerned with the production of solar cells. Experiments can be started in which top and bottom electrodes are applied to the layers and thus the photovoltaic efficiency can be determined. By changing the cell structure, it may be possible to improve the efficiency afterwards.

In addition, the question of the direct band gap for PFN can be confirmed with theoretical calculations. The defect-related band gap can also be examined more closely in an extendes theoretical study.

# 6. Appendix

## 6.1. List of figures

Appendix

Appendix

Appendix

Appendix

Appendix

Appendix

## 6.2. List of tables

## 6.3. ISCD

### 6.3.1. ISCD 98-006-8242 Lead oxide (Litharge)

**Chemical formula**: $O_1Pb_1$

**Crystalographic data:**

Crystal system: Tetragonal

Space group: P 4/n m m

Space group number: 129

**Lattice constantss** $a$ [Å]: 3.9740 $\alpha$ [°]: 90.0000

$b$ [Å]: 3.9740 $\beta$ [°]: 90.0000

$c$ [Å]: 5.0220 $\gamma$ [°]: 90.0000

Calculated density [g/cm$^3$]: 9.34

Measured density [g/cm$^3$]: 9.30

Cell volume [$10^6$ pm$^3$]: 79.31

**List of reflectios**

| No. | h | k | l | d [Å] | 2θ [°] | I [%] |
|---|---|---|---|---|---|---|
| 1 | 0 | 0 | 1 | 5.02200 | 17.646 | 4.0 |
| 2 | 0 | 1 | 1 | 3.11633 | 28.622 | 100.0 |
| 3 | 1 | 1 | 0 | 2.81004 | 31.820 | 28.4 |
| 4 | 0 | 0 | 2 | 2.51100 | 35.729 | 8.6 |
| 5 | 1 | 1 | 1 | 2.45225 | 36.615 | 0.0 |
| 6 | 0 | 1 | 2 | 2.12276 | 42.554 | 0.7 |
| 7 | 0 | 2 | 0 | 1.98700 | 45.619 | 7.9 |
| 8 | 1 | 1 | 2 | 1.87238 | 48.586 | 10.9 |
| 9 | 0 | 2 | 1 | 1.84764 | 49.279 | 0.3 |
| 10 | 1 | 2 | 1 | 1.67541 | 54.744 | 9.5 |
| 11 | 0 | 0 | 3 | 1.67400 | 54.794 | 0.1 |
| 12 | 0 | 2 | 2 | 1.55816 | 59.256 | 2.4 |
| 13 | 0 | 1 | 3 | 1.54272 | 59.909 | 2.5 |
| 14 | 1 | 2 | 2 | 1.45064 | 64.147 | 0.1 |
| 15 | 1 | 1 | 3 | 1.43815 | 64.772 | 0.2 |
| 16 | 2 | 2 | 0 | 1.40502 | 66.494 | 0.7 |
| 17 | 2 | 2 | 1 | 1.35306 | 69.403 | 0.0 |
| 18 | 0 | 3 | 1 | 1.28086 | 73.940 | 0.6 |
| 19 | 0 | 2 | 3 | 1.28023 | 73.982 | 0.0 |
| 20 | 1 | 3 | 0 | 1.25669 | 75.608 | 0.4 |
| 21 | 0 | 0 | 4 | 1.25550 | 75.692 | 0.1 |
| 22 | 2 | 2 | 2 | 1.22613 | 77.840 | 0.3 |
| 23 | 1 | 3 | 1 | 1.21910 | 78.375 | 0.0 |
| 24 | 1 | 2 | 3 | 1.21856 | 78.416 | 0.6 |
| 25 | 0 | 1 | 4 | 1.19718 | 80.096 | 0.0 |
| 26 | 0 | 3 | 2 | 1.17163 | 82.213 | 0.0 |
| 27 | 1 | 1 | 4 | 1.14629 | 84.442 | 0.1 |
| 28 | 1 | 3 | 2 | 1.12380 | 86.540 | 0.3 |

**Line pattern**

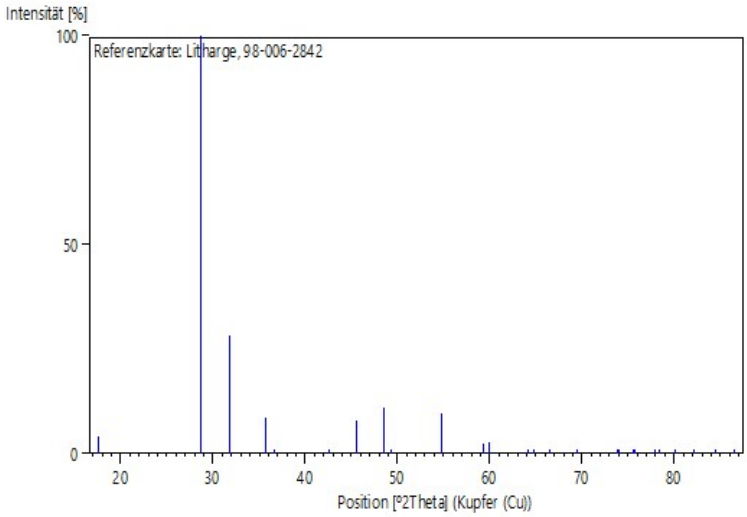


### 6.3.2. ISCD 98-008-8358 PFN (monoclinic)

**Chemical formula**: $PbFe_{0.5}Nb_{0.5}O_3$

**Crystalographic data:**

Crystal system: Monoclinic

Space group: C 1 m 1

Space group number: 8

| | | | | |
|---|---|---|---|---|
| **Lattice constantss** | $a$ [Å]: | 5.6760 | $\alpha$ [°]: | 90.0000 |
| | $b$ [Å]: | 5.6680 | $\beta$ [°]: | 90.1600 |
| | $c$ [Å]: | 4.0150 | $\gamma$ [°]: | 90.0000 |

Calculated density [$g/cm^3$]: 8.47

Cell volume [$10^6$ $pm^3$]: 129.17

Appendix

## List of reflectios

| No. | h | k | l | d [Å] | 2θ [°] | I [%] |
|---|---|---|---|---|---|---|
| 1 | 0 | 0 | 1 | 4.01498 | 22.122 | 18.7 |
| 2 | 1 | 1 | 0 | 4.01070 | 22.146 | 34.9 |
| 3 | 1 | 1 | -1 | 2.84031 | 31.472 | 91.5 |
| 4 | 2 | 0 | 0 | 2.83799 | 31.498 | 49.0 |
| 5 | 1 | 1 | 1 | 2.83471 | 31.535 | 100.0 |
| 6 | 0 | 2 | 0 | 2.83400 | 31.544 | 47.2 |
| 7 | 2 | 0 | -1 | 2.32055 | 38.774 | 8.2 |
| 8 | 0 | 2 | -1 | 2.31532 | 38.865 | 9.8 |
| 9 | 2 | 0 | 1 | 2.31445 | 38.880 | 11.8 |
| 10 | 0 | 0 | 2 | 2.00749 | 45.128 | 24.0 |
| 11 | 2 | 2 | 0 | 2.00535 | 45.178 | 49.0 |
| 12 | 1 | 1 | -2 | 1.79659 | 50.777 | 3.3 |
| 13 | 2 | 2 | -1 | 1.79544 | 50.812 | 3.5 |
| 14 | 3 | 1 | 0 | 1.79465 | 50.836 | 3.8 |
| 15 | 1 | 1 | 2 | 1.79376 | 50.863 | 3.2 |
| 16 | 2 | 2 | 1 | 1.79261 | 50.898 | 3.0 |
| 17 | 2 | 0 | -2 | 1.64107 | 55.989 | 6.7 |
| 18 | 3 | 1 | -1 | 1.64004 | 56.027 | 13.4 |
| 19 | 0 | 2 | -2 | 1.63814 | 56.098 | 7.4 |
| 20 | 1 | 3 | -1 | 1.63742 | 56.125 | 13.7 |
| 21 | 3 | 1 | 1 | 1.63681 | 56.148 | 17.3 |
| 22 | 1 | 3 | 1 | 1.63635 | 56.165 | 14.7 |
| 23 | 2 | 2 | -2 | 1.42016 | 65.695 | 9.2 |
| 24 | 4 | 0 | 0 | 1.41899 | 65.756 | 5.7 |
| 25 | 2 | 2 | 2 | 1.41736 | 65.841 | 13.9 |
| 26 | 0 | 4 | 0 | 1.41700 | 65.860 | 5.8 |
| 27 | 3 | 1 | -2 | 1.33972 | 70.195 | 1.1 |
| 28 | 4 | 0 | -1 | 1.33907 | 70.234 | 0.7 |
| 29 | 0 | 0 | 3 | 1.33833 | 70.279 | 0.7 |
| 30 | 1 | 3 | -2 | 1.33770 | 70.317 | 0.7 |
| 31 | 3 | 3 | 0 | 1.33690 | 70.365 | 0.9 |
| 32 | 4 | 0 | 1 | 1.33672 | 70.376 | 0.7 |
| 33 | 1 | 3 | 2 | 1.33653 | 70.387 | 0.7 |
| 34 | 3 | 1 | 2 | 1.33620 | 70.408 | 1.2 |
| 35 | 1 | 1 | -3 | 1.27027 | 74.660 | 4.1 |
| 36 | 3 | 3 | -1 | 1.26918 | 74.735 | 4.2 |
| 37 | 1 | 1 | 3 | 1.26876 | 74.764 | 5.4 |
| 38 | 2 | 4 | 0 | 1.26776 | 74.833 | 4.7 |
| 39 | 3 | 3 | 1 | 1.26768 | 74.839 | 5.5 |
| 40 | 2 | 0 | -3 | 1.21179 | 78.940 | 0.3 |
| 41 | 4 | 2 | -1 | 1.21072 | 79.023 | 0.7 |
| 42 | 0 | 2 | -3 | 1.21017 | 79.066 | 0.4 |
| 43 | 2 | 4 | -1 | 1.20936 | 79.129 | 0.7 |
| 44 | 2 | 0 | 3 | 1.20918 | 79.143 | 0.8 |
| 45 | 4 | 2 | 1 | 1.20899 | 79.158 | 1.4 |
| 46 | 2 | 4 | 1 | 1.20849 | 79.197 | 1.0 |
| 47 | 4 | 0 | -2 | 1.16027 | 83.195 | 1.5 |
| 48 | 0 | 4 | -2 | 1.15766 | 83.425 | 2.3 |
| 49 | 4 | 0 | 2 | 1.15722 | 83.464 | 3.3 |
| 50 | 2 | 2 | -3 | 1.11421 | 87.473 | 0.6 |
| 51 | 3 | 3 | -2 | 1.11375 | 87.518 | 0.5 |
| 52 | 5 | 1 | 0 | 1.11309 | 87.583 | 0.7 |
| 53 | 2 | 2 | 3 | 1.11218 | 87.673 | 0.5 |
| 54 | 3 | 3 | 2 | 1.11172 | 87.718 | 0.4 |
| 55 | 1 | 5 | 0 | 1.11165 | 87.726 | 0.1 |

**Line pattern**

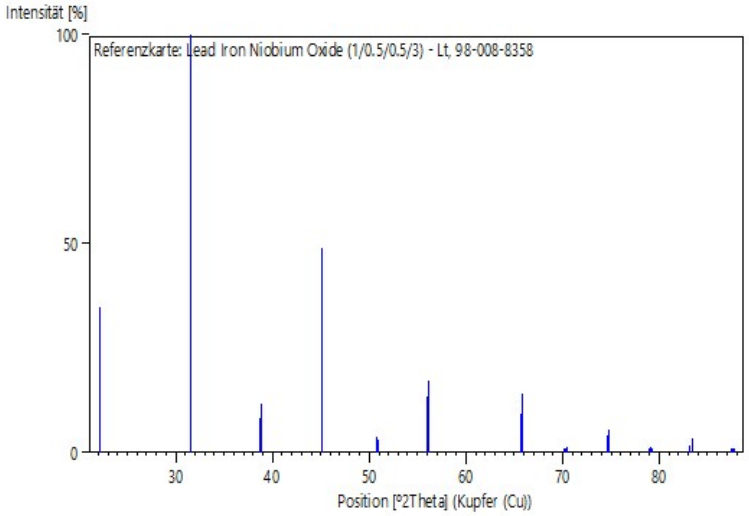


### 6.3.1. ISCD 98-009-0491 PFN (hexagonal)

**Chemical formula**: $PbFe_{0.5}Nb_{0.5}O_3$

**Crystalographic data:**

Crystal system: Hexagonal

Space group: R 3 m

Space group number: 160

| | | | | |
|---|---|---|---|---|
| **Lattice constantss** | $a$ [Å]: | 5.665 | $\alpha$ [°]: | 90.0000 |
| | $b$ [Å]: | 5.665 | $\beta$ [°]: | 90.0000 |
| | $c$ [Å]: | 6.9589 | $\gamma$ [°]: | 120.0000 |

Calculated density [$g/cm^3$]: 8.48

Cell volume [$10^6$ $pm^3$]: 193.44

Appendix

## List of reflectios

| No. | h | k | l | d [Å] | 2θ [°] | I [%] |
|---|---|---|---|---|---|---|
| 1 | 1 | 0 | 1 | 4.00997 | 22.150 | 35.7 |
| 2 | 0 | 1 | 2 | 2.83822 | 31.495 | 100.0 |
| 3 | 1 | 1 | 0 | 2.83275 | 31.558 | 99.8 |
| 4 | 0 | 0 | 3 | 2.31963 | 38.790 | 5.8 |
| 5 | 0 | 2 | 1 | 2.31367 | 38.894 | 19.8 |
| 6 | 2 | 0 | 2 | 2.00499 | 45.187 | 50.4 |
| 7 | 1 | 1 | 3 | 1.79470 | 50.835 | 6.7 |
| 8 | 2 | 1 | 1 | 1.79193 | 50.919 | 4.3 |
| 9 | 1 | 0 | 4 | 1.63970 | 56.040 | 15.5 |
| 10 | 1 | 2 | 2 | 1.63654 | 56.158 | 30.9 |
| 11 | 3 | 0 | 0 | 1.63549 | 56.197 | 7.6 |
| 12 | 0 | 2 | 4 | 1.41911 | 65.750 | 10.9 |
| 13 | 2 | 2 | 0 | 1.41637 | 65.893 | 12.6 |
| 14 | 0 | 1 | 5 | 1.33895 | 70.241 | 1.3 |
| 15 | 3 | 0 | 3 | 1.33666 | 70.380 | 0.8 |
| 16 | 1 | 3 | 1 | 1.33551 | 70.449 | 0.9 |
| 17 | 2 | 1 | 4 | 1.26880 | 74.762 | 9.9 |
| 18 | 3 | 1 | 2 | 1.26733 | 74.863 | 10.1 |
| 19 | 2 | 0 | 5 | 1.21054 | 79.037 | 0.6 |
| 20 | 2 | 2 | 3 | 1.20884 | 79.170 | 1.3 |
| 21 | 4 | 0 | 1 | 1.20799 | 79.236 | 0.8 |
| 22 | 0 | 0 | 6 | 1.15982 | 83.235 | 1.2 |
| 23 | 0 | 4 | 2 | 1.15684 | 83.498 | 5.0 |
| 24 | 1 | 2 | 5 | 1.11316 | 87.577 | 1.0 |
| 25 | 3 | 2 | 1 | 1.11118 | 87.772 | 0.2 |

## Line pattern

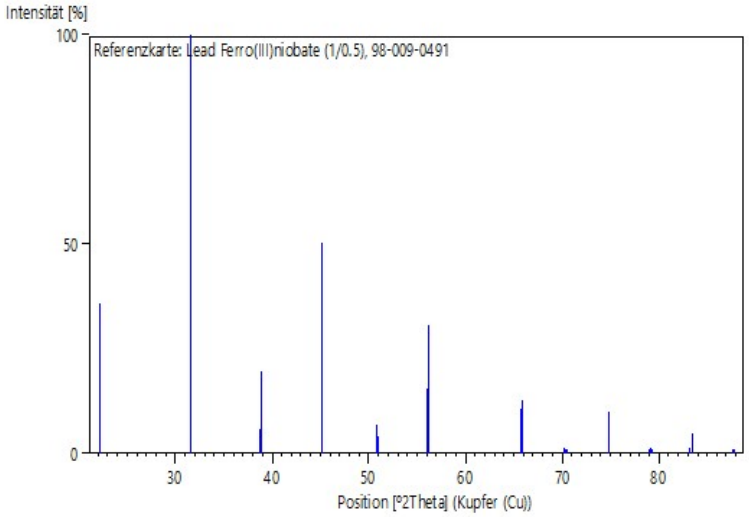

## 6.4. Chapter 4

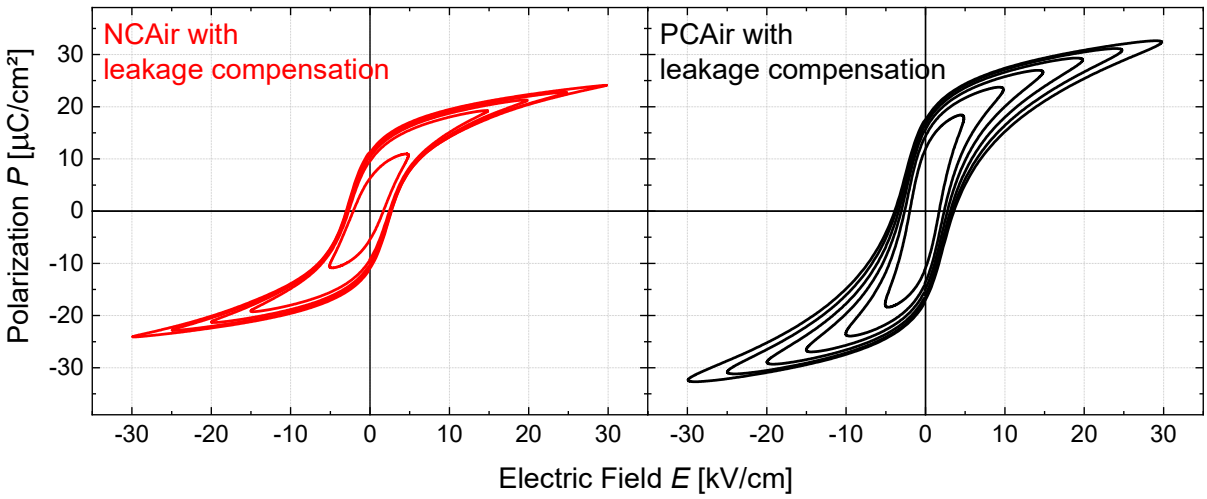


*Figure 6.1 Polarization hysteresis loops for NCAir and PCAir at 1 Hz with leakage compensation*

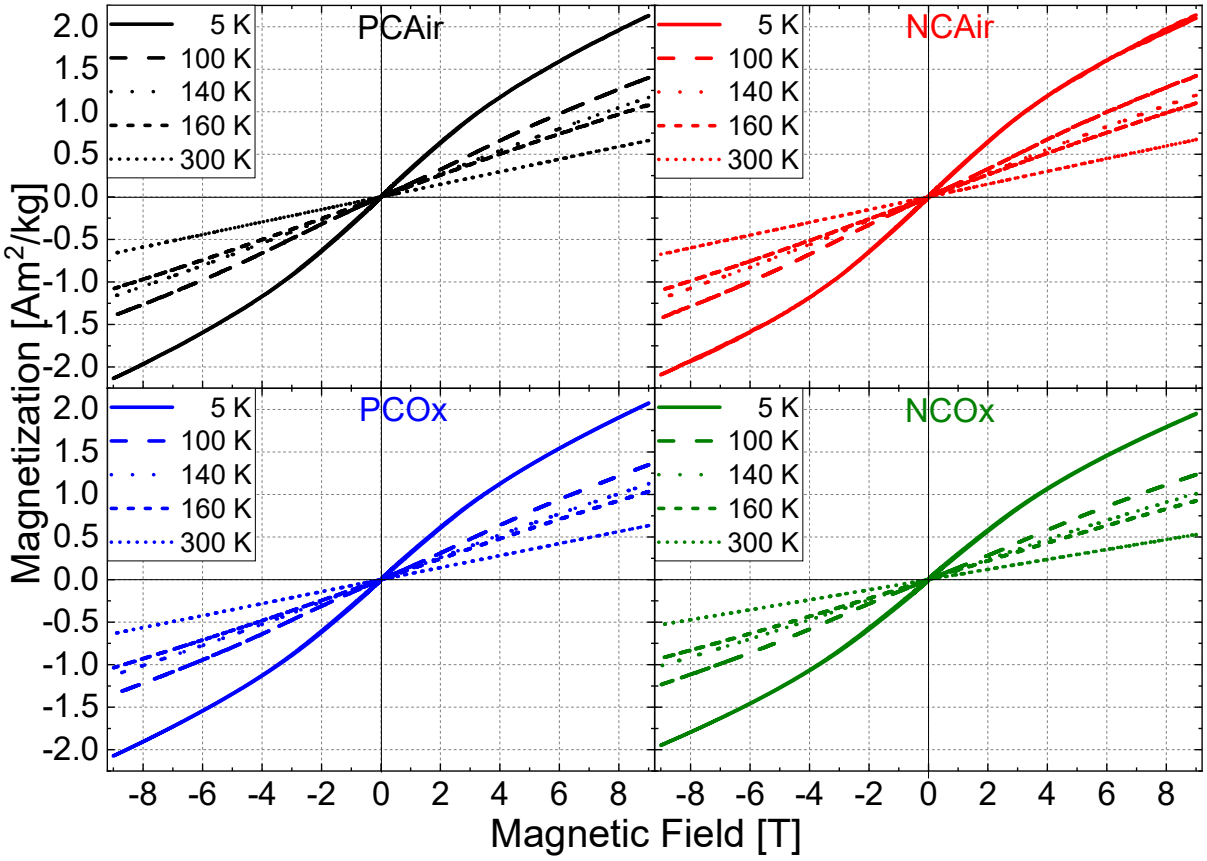


*Figure 6.2 Magnetic hysteresis loops for hte temperatures 5, 100, 140, 160 and 300 K.*

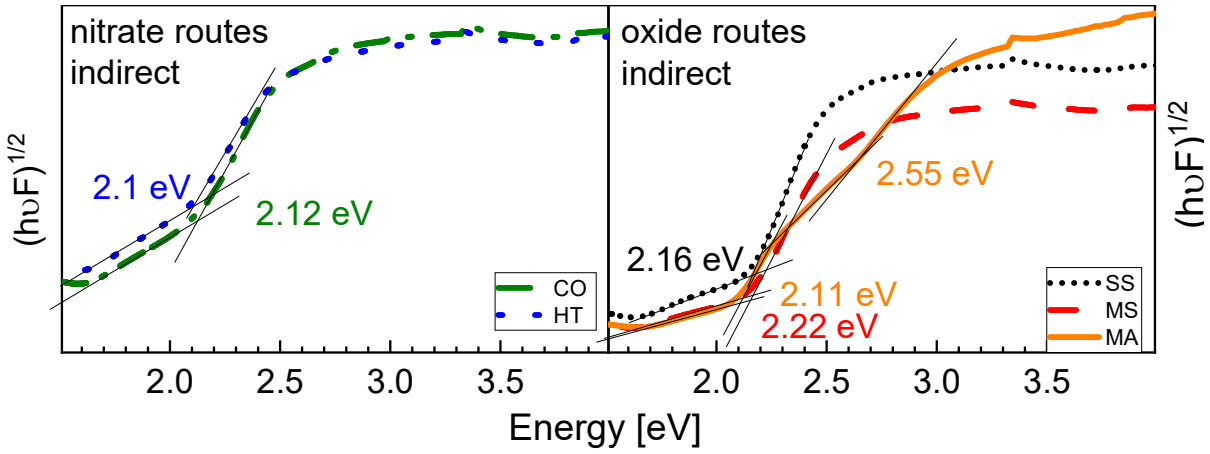


*Figure 6.3 Tauc plot of reflectivity graphs for PFN powders prepared by different synthesis routes for indirect band gap.*

## 6.5. Chapter 5

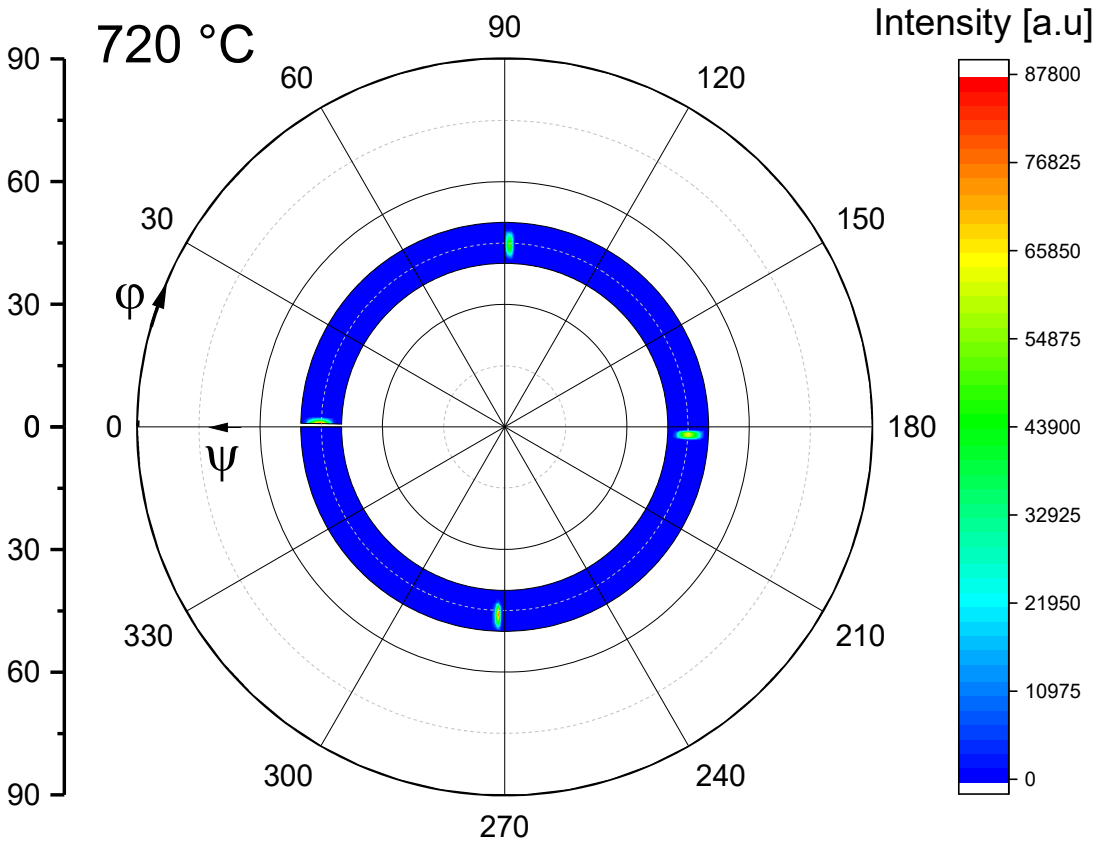


*Figure 6.4 Pole figure measurement of the PFN layer deposited at 720 °C in the ψ range of 40 to 50 °.*

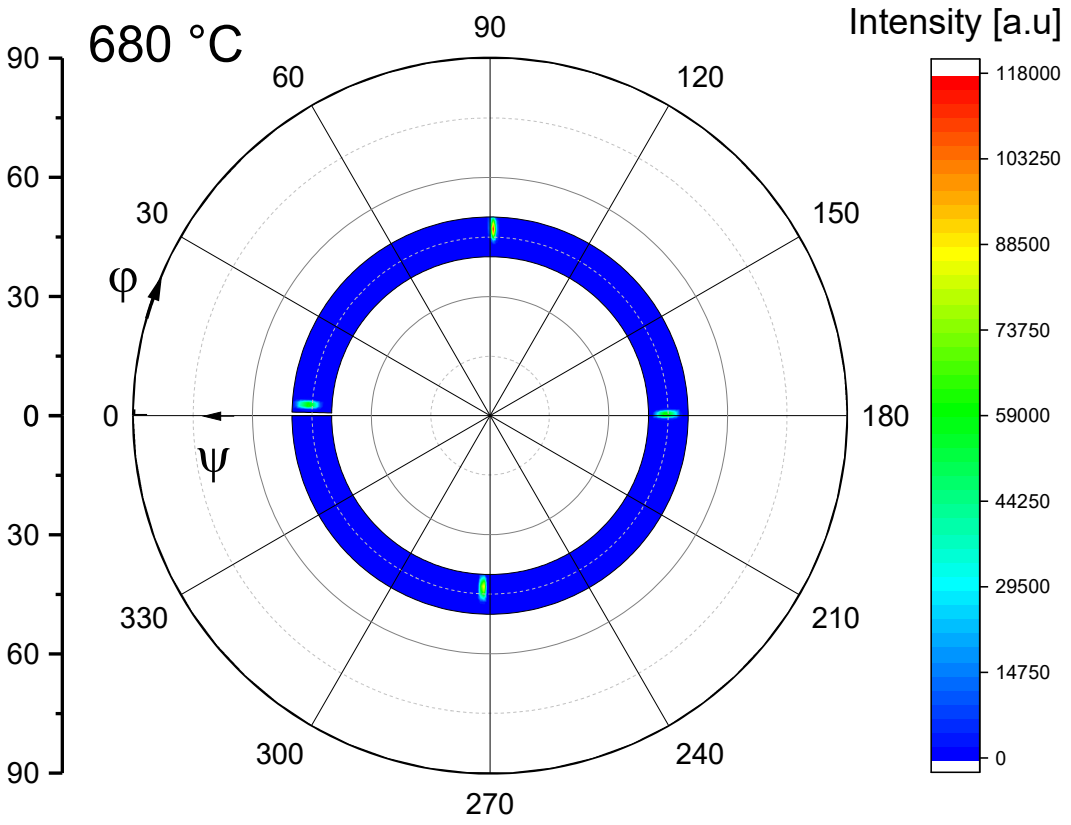


*Figure 6.5 Pole figure measurement of the PFN layer deposited at 680 °C in the ψ range of 40 to 50 °.*

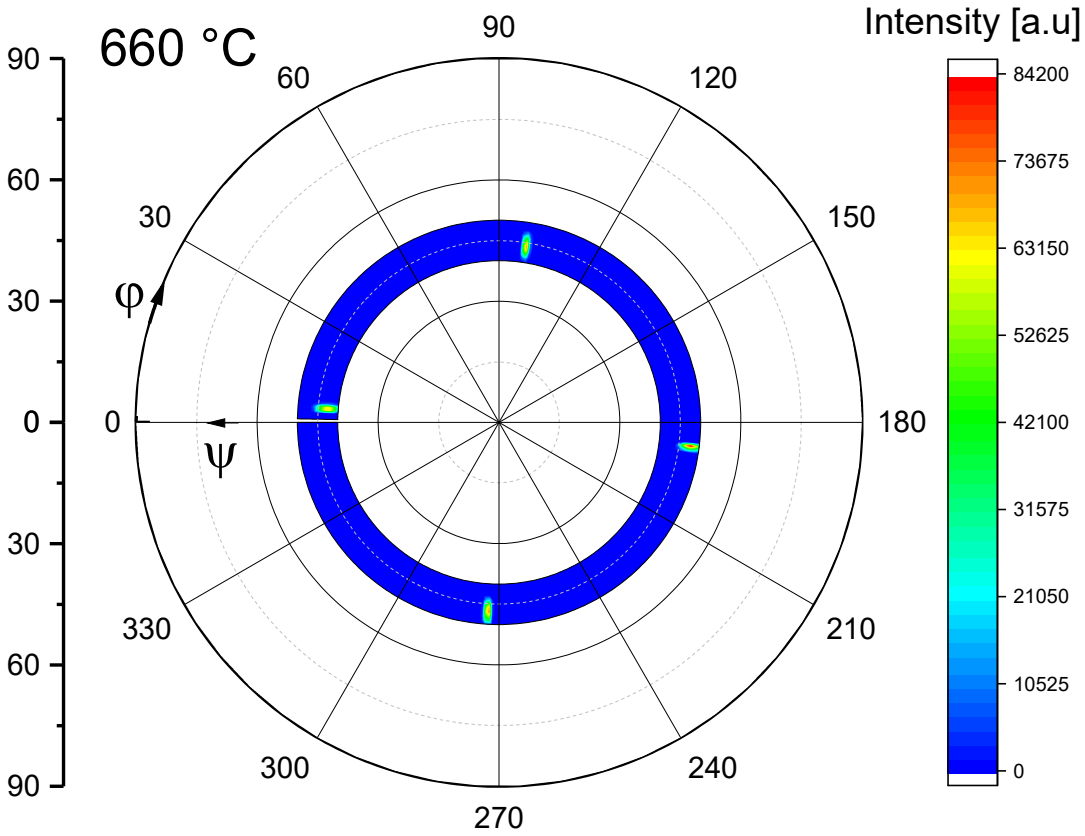


*Figure 6.6 Pole figure measurement of the PFN layer deposited at 660 °C in the ψ range of 40 to 50 °.*

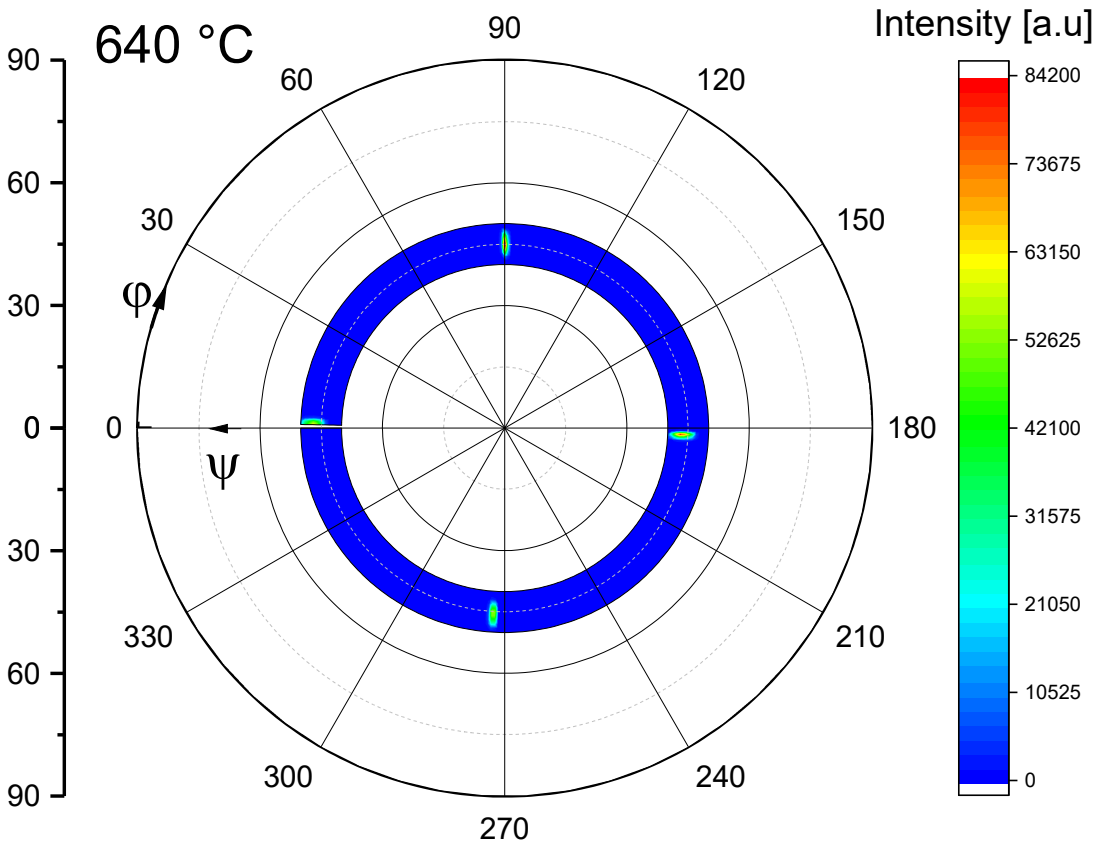


*Figure 6.7 Pole figure measurement of the PFN layer deposited at 640 °C in the ψ range of 40 to 50 °.*

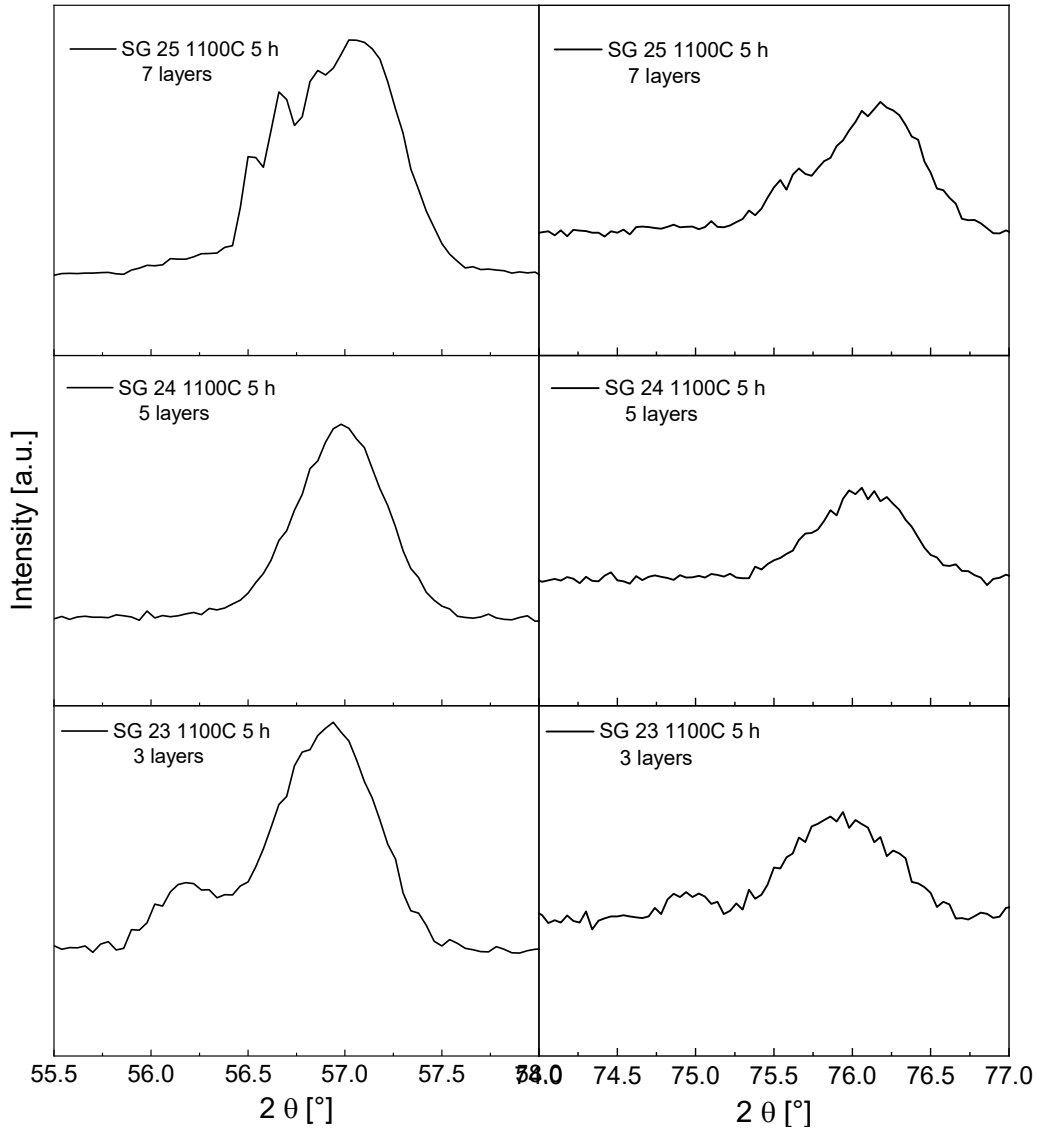


*Figure 6.8 Zoom of the GIXRD patterns for the sol-gel deposited PFN films with the different thicknesses.*

# 7. Bibliography

## Publications

**N. Bartek, V. V. Shvartsman, H. Bouyanfif, A. Schmitz, G. Bacher, S. Olthof, S. Sirotinskaya, N. Benson, and D. C. Lupascu**

*Band gap of $Pb(Fe_{0.5}Nb_{0.5})O_3$ thin films prepared by pulsed laser deposition* Materials 14, 6841 (2021) https://doi.org/10.3390/ma14226841

**Nicole Bartek, Vladimir V. Shvartsman, Soma Salamon, Heiko Wende, Doru C. Lupascu**

*Influence of calcination and sintering temperatures on dielectric and magnetic properties of $Pb(Fe_{0.5}Nb_{0.5})O_3$ ceramics synthesized by the solid state method* Ceram. Intern. 47, 23396-23403 (2021) https://doi.org/10.1016/j.ceramint.2021.05.055

**N. Bartek, V. V. Shvartsman, D. C. Lupascu, U. Prah and H. Uršič**

*Influence of synthesis route on the properties of lead iron niobate* 2019 IEEE International Symposium on Applications of Ferroelectrics (ISAF), Lausanne, Switzerland, 2019, pp. 1-4. 10.1109/ISAF43169.2019.9034943

## Conference contributions

01/2020 **Electronic Materials and Applikations (EMA, Orlando)**

N.Bartek, V. V. Shvartsman, and . C. Lupascu

*Influence of calcination and sintering temperatures on properties of lead iron niobate multiferroic ceramics*

11/2019 **Cenide Jahresfeier (Duisburg)**

N. Bartek, T. Akbari-Hamed, V. V. Shvartsman, and D. C. Lupascu

*Effect of calcination temperature on dielectric and ferroelectric properties of lead iron niobite*

07/2019 **IEEE International Symposium on Applications of Ferroelectric (ISAF, Lausanne)**

N. Bartek, U. Prah, V. V. Shvartsman, H. Ursic and D. C. Lupascu

*Influence of synthesis route on the properties of lead iron niobate*

03/2019 **Deutsche Physikalische Gesellschaft e. V. (DPG, Regensburg)**

N. Bartek, V.Shvartsman, and D. Lupascu

*Effect of synthesis method on properties of multiferroic lead iron niobat*

# 8. References

[1] Statista. Neuzulassungen E-Autos Welt. Available from: <https://www.solarserver.de/2021/03/09/neuzulassungen-von-elektrofahrzeugen-2020-weltweit-stark-gestiegen/>.

[2] Statista. Prognose Energieverbrauch. Available from: <https://de.statista.com/statistik/daten/studie/28941/umfrage/prognose-zum-energieverbrauch-weltweit-betrachtet-von-1980-bis-2030/>.

[3] European Commision. Energy Roadmap 2050. Available from: <https://ec.europa.eu/energy/sites/ener/files/documents/2012_energy_roadmap_2050_en_0.pdf>.

[4] Fraunhofer ISE. Anteil erneuerbarer Energien. Available from: <https://www.ise.fraunhofer.de/de/presse-und-medien/news/2021/nettostromerzeugung-im-1-quartal-2021-anteil-der-erneuerbaren-energien-im-jahresvergleich-gesunken.html>.

[5] DISA Energy. Windkraftanlagen Anforderungen. Available from: <https://www.disa-energy.de/?page=1,1,2,Standortfaktoren+f%FCr+Windanlagen>.

[6] Park N-G. Perovskite solar cells: an emerging photovoltaic technology. Mater. 2015;18(2):65–72. doi:10.1016/j.mattod.2014.07.007.

[7] Paillard C, Bai X, Infante IC, Guennou M, Geneste G, Alexe M et al. Photovoltaics with Ferroelectrics: Current Status and Beyond. Adv. Mater. 2016;28(26):5153–68. doi:10.1002/adma.201505215.

[8] Nechache R, Harnagea C, Li S, Cardenas L, Huang W, Chakrabartty J et al. Bandgap tuning of multiferroic oxide solar cells. Nature Photon 2015;9(1):61–7. doi:10.1038/nphoton.2014.255.

[9] Li H, Zhu J, Wu Q, Zhuang J, Guo H, Ma Z et al. Enhanced photovoltaic properties of PbTiO3-based ferroelectric thin films prepared by a sol-gel process. Ceram 2017;43(16):13063–8. doi:10.1016/j.ceramint.2017.06.151.

References

[10] Zheng F, Xin Y, Huang W, Zhang J, Wang X, Shen M et al. Above 1% efficiency of a ferroelectric solar cell based on the Pb(Zr,Ti)O 3 film. J. Mater. Chem. A 2014;2(5):1363–8. doi:10.1039/C3TA13724D.

[11] Qin M, Yao K, Liang YC. High efficient photovoltaics in nanoscaled ferroelectric thin films. Appl. Phys. Lett. 2008;93:122904. doi:10.1063/1.2990754.

[12] Badapanda T, Rout SK, Cavalcante LS, Sczancoski JC, Panigrahi S, Longo E et al. Optical and dielectric relaxor behaviour of $Ba(Zr_{0.25}Ti_{0.75})O$ ceramic explained by means of distorted clusters. J. Phys. D: Appl. Phys. 2009;42(17):175414. doi:10.1088/0022-3727/42/17/175414.

[13] Sun E, Zhang R, Wang Z, Xu D, Li L, C. W. Optical interband transitions in relaxor-based ferroelectric $0.93Pb(Zn_{1/3}Nb_{2/3})O_3$-$0.07PbTiO_3$ single crystal. J. Appl. Phys. 2010;107(11):113532. doi:10.1063/1.3446293.

[14] Bennett JW, Grinberg I, Rappe AM. New highly polar semiconductor ferroelectrics through d8 cation-O vacancy substitution into PbTiO3: a theoretical study. J. Am. Chem. Soc. 2008;130(51):17409–12. doi:10.1021/ja8052249.

[15] Bao D, Yao, X. Shinozaki, K., Mizutani N. Crystallization and optical properties of sol–gel derived $PbTiO_3$ thin films. J. Phys. D 2003;36:2141–5.

[16] Oanh LM, Do DB, Phu ND, Mai TN, Minh NV. Influence of Mn Doping on the Structure, Optical,and Magnetic Properties of $PbTiO_3$ Material. IEEE Trans. Magn. 2014;50(6):1–4. doi:10.1109/TMAG.2013.2297516.

[17] Thakoor S, Maserjian J. Photoresponse probe of the space charge distribution in ferroelectric lead zirconate titanate thin film memory capacitors. J. Vac. Sci. Technol. 1994;12(2):295–9. doi:10.1116/1.578871.

[18] Yang YS, Kim JP, Lee SH, Joo HJ, Jang MS. Space charge effects in the photocurrent spectrum of ferroelectric $Pb(Zr,Ti)O_3$ thin films. J Korean Phys Soc 1999;35:1168–71.

[19] Warren WL, Tuttle BA, McWhorter PJ, Rong FC, Poindexter EH. Identification of paramagnetic $Pb^{+3}$ defects in lead zirconate titanate ceramics. Appl. Phys. Lett. 1993;62(5):482–4. doi:10.1063/1.108940.

References

[20] Seager CH, Land CE. Optical absorption in ion-implanted lead lanthanum zirconate titanate ceramics. Appl. Phys. Lett. 1984;45(4):395–7. doi:10.1063/1.95233.

[21] Panda B, Ray SK, Dhar A, Sarkar A, Bhattacharya D, Chopra KL. Electron beam deposited lead-lanthanum-zirconate-titanate thin films for silicon based device applications. J. Appl. Phys. 1996;79(2):1008. doi:10.1063/1.360887.

[22] Bharti C, Dutta A, Shannigrahi S, Choudhary SN, Thapa RK, Sinha TP. Impedance spectroscopy, electronic structure and X-ray photoelectron spectroscopy studies of $Pb(Fe_{1/2}Nb_{1/2})O_3$. J Electron Spectros Relat Phenomena 2009;169:80–5. doi:10.1016/j.elspec.2008.12.001.

[23] Burfoot JC. Ferroelectrics: An Introduction to the Physical Principles. London: Butler & Tanner Ltd; 1967.

[24] Scott JF (ed.). Ferroelectric Memories: Springer.

[25] Smolenskii GA, Bokov VA, Isupov VA, Krainik NN, Pas (eds.). Ferroelectrics and related Materials. Amsterdam: OPA Ltd. for Gordon an Breach Science Publishers; 1984.

[26] Cross LE. Relaxor ferroelectrics. Ferroelectrics 1987;76(1):241–67. doi:10.1080/00150198708016945.

[27] Cowley RA, Gvasaliya SN, Lushnikov SG, Roessli B, Rotaru GM. Relaxing with relaxors: a review of relaxor ferroelectrics. Adv. Phys. 2011;60(2):229–327. doi:10.1080/00018732.2011.555385.

[28] Li F, Zhang S, Damjanovic D, Chen L-Q, Shrout TR. Local Structural Heterogeneity and Electromechanical Responses of Ferroelectrics: Learning from Relaxor Ferroelectrics. Adv. Funct. Mater. 2018;28(37):1801504. doi:10.1002/adfm.201801504.

[29] Krause B, Cowley JM, Wheatley J. Short-range ordering in $PbMg_{1/3}Nb_{2/3}O_3$. Acta Cryst. 1979(A35):1015–7. doi:10.1107/S0567739479002230.

[30] Takenaka H, Grinberg I, Liu S, Rappe AM. Slush-like polar structures in single-crystal relaxors. Nature 2017;546(7658):391–5. doi:10.1038/nature22068. Available from: <https://www.nature.com/articles/nature22068#citeas>.

References

[31] Clarke R, Burfoot JC. The diffuse phase transition in potassium strontium niobate. Ferroelectrics 1974;8(1):505–6. doi:10.1080/00150197408234141.

[32] Yasuda N, Ueda. Y. Temperature and pressure dependence of dielectric properties of $Pb(Fe_{1/2}Nb_{1/2})O_3$ with the diffuse phase transition. J. Phys.: Condens. Matter 1989;1:5179–85.

[33] Raymond O, Font R, Suárez-Almodovar N, Portelles J, Siqueiros JM. Frequency-temperature response of ferroelectromagnetic $Pb(Fe_{1/2}Nb_{1/2})O_3$ceramics obtained by different precursors. Part II. Impedance spectroscopy characterization. J. Appl. Phys. 2005;97:84107. doi:10.1063/1.1870100.

[34] Shvartsman VV, Lupascu DC. Lead-Free Relaxor Ferroelectrics. J. Am. Ceram. Soc. 2012;95:1–26. doi:10.1111/j.1551-2916.2011.04952.x.

[35] Orihara H, Hashimoto S, Ishibashi Y. A Theory of D-E Hysteresis Loop Based on the Avrami Model. J. Phys. Soc. Japan 1994;63(3):1031–5. doi:10.1143/JPSJ.63.1031.

[36] Rao M, Krishnamurthy HR, Pandit R. Magnetic hysteresis in two model spin systems. Phys. Rev. B 1990;42(1):856–84. doi:10.1103/PhysRevB.42.856.

[37] Lo WS, Pelcovits RA. Ising model in a time-dependent magnetic field. Phys. Rev. A 1990;42(12):7471–4. doi:10.1103/PhysRevA.42.7471.

[38] Omura M, Adachi H, Ishibashi Y. Simulations of Ferroelectric Characteristics Using a One-Dimensional Lattice Model. Jpn. J. Appl. Phys. 1991;30(Part 1, No. 9B):2384–7. doi:10.1143/JJAP.30.2384.

[39] Sengupta S, Marathe Y, Puri S. Cell-dynamical simulation of magnetic hysteresis in the two-dimensional Ising system. Phys. Rev. B 1992;45(14):7828–31. doi:10.1103/PhysRevB.45.7828.

[40] Avrami M. Kinetics of Phase Change. I General Theory. J. Chem. Phys. 1939;7(12):1103–12. doi:10.1063/1.1750380.

[41] Avrami M. Kinetics of Phase Change. II Transformation-Time Relations for Random Distribution of Nuclei. J. Chem. Phys. 1940;8(2):212–24. doi:10.1063/1.1750631.

References

[42] Avrami M. Granulation, Phase Change, and Microstructure Kinetics of Phase Change. III. J. Chem. Phys. 1941;9(2):177–84. doi:10.1063/1.1750872.

[43] Hashimoto S, Orihara H, Ishibashi Y. Study on D-E Hysteresis Loop of TGS Based on the Avrami-Type Model. J. Phys. Soc. Japan 1994;63(63):1601–10. doi:10.1143/JPSJ.63.1601.

[44] Valasek J. Piezo-Electric and Allied Phenomena in Rochelle Salt. Phys. Rev. 1921;17:475–81. doi:10.1103/PhysRev.17.475.

[45] Wul B. Barium Titanate: a New Ferro-Electric. Nature 1946;157:808.

[46] Hippel A von, Breckenridge RG, Chesley FG, Tisza L. High dielectric constant ceramics. Ind. Eng. Chem. Res. 1946;38(11):1098.

[47] Cano AQ, Meier D, Trassin M. Multiferroics: Fundamentals and Applications. Berlin/Boston: De Gruyter; 2021.

[48] Ishihara T (ed.). Perovskite Oxide for Solid Oxide Fuel Cells. Dordrecht Heidelberg London New York: Springer; 2009.

[49] Vopson MM. Fundamentals of Multiferroic Materials and Their Possible Applications. Crit. Rev. Solid State Mater. Sci. 2015;40(4):223–50. doi:10.1080/10408436.2014.992584.

[50] Khomskii D. Classifying multiferroics: Mechanisms and effects. Physics 2009;2:20. doi:10.1103/Physics.2.20.

[51] Roth S, Stahl A. Elektrizität und Magnetismus. Berlin, Heidelberg: Springer Berlin Heidelberg; 2018.

[52] Helme L. Neutron Scattering Studies of Correlated Electron Systems; 2006.

[53] Wang F, Dong BJ, Zhang YQ, Liu W, Zhang HR, Bai Y et al. Single orthorhombic b axis orientation and antiferromagnetic ordering type in multiferroic $CaMnO_3$ thin film with $La_{0.67}Ca_{0.33}MnO_3$ buffer layer. Appl. Phys. Lett. 2017;111(12):122902. doi:10.1063/1.5003815.

References

[54] Smolenskii GA, Agranovskaia AI, Popov SN, Isupov VA. New Ferroelectrics of Complex Composition II. Sov. Phys. - Tech. Phys. 1959;10:1981–2.

[55] Bokov VA, Myl'nikova IE, and Smolenskii GA. Ferroelectrics antiferromagnetics. J. Exptl. Theoret. Phys. (U.S.S.R.) 1962;42:643–6.

[56] Gao XS, Chen XY, Yin J, Wu J, Liu ZG. Ferroelectric and dielectric properties of ferroelectromagnet $Pb(Fe_{1/2}Nb_{1/2})O_3$ ceramics and thin films. J. Mater. Sci. 2000;35:5421–5. doi:10.1023/A:1004815416774.

[57] Ivanov SA, Tellgren R, Rundlof H, Thomas NW, Anata S. Investigation of the structure of the relaxor ferroelectric $Pb(Fe_{1/2}Nb_{1/2})O_3$ by neutron powder diffraction. J. Phys.: Condens. Matter 2000;12:2393–400.

[58] Bochenek D, Guzdek P. Ferroelectric and magnetic properties of ferroelectromagnetic $Pb(Fe_{1/2}Nb_{1/2})O_3$ type ceramics. J. Magn. Magn. Mat. 2011;323:369–74. doi:10.1016/j.jmmm.2010.09.046.

[59] Lampis N, Sciau P, Lehmann AG. Rietveld refinements of the paraelectric and ferroelectric structures of $PbFe_{0.5}Nb_{0.5}O_3$. J. Phys.: Condens. Matter 1999;11:3489–500. doi:10.1088/0953-8984/11/17/307.

[60] Mishra RK, Choudhary RNP, Banerjee A. Bulk permittivity, low frequency relaxation and the magnetic properties of $Pb(Fe_{1/2}Nb_{1/2})O_3$ ceramics. J. Phys.: Condens. Matter 2010;22:25901–9. doi:10.1088/0953-8984/22/2/025901.

[61] Bochenek D, Niemiec P, Guzdek P, Wzorek M. Magnetoelectric and electric measurements of the $(1-x)BiFeO_3$ –$(x)Pb(Fe_{1/2}Nb_{1/2})O_3$ solid solutions. Mater. Chem. Phys. 2017;195:199–206. doi:10.1016/j.matchemphys.2017.04.022.

[62] Matteppanavar S, Rayaprol S, Singh S, Reddy VR, Angadi B. Evidence for magneto-electric and spin–lattice coupling in $PbFe_{0.5}Nb_{0.5}O_3$ through structural and magneto-electric studies. J. Mater. Sci. 2015;50:4980–93. doi:10.1007/s10853-015-9046-5.

[63] Quek HM, Yan MF. Sol-gel preparation and dielectric properties of lead iron niobate thin films. Ferroelectrics 1987;74:95–108. doi:10.1080/00150198708014499.

References

[64] Benkhaled N, Djermouni M, Zaoui A, Kondakova I, Kuzian R, Hayn R. Magnetic properties of the multiferroic double perovskite lead iron niobate: Role of disorder. J. Magn. Magn. Mat. 2020;515:167309. doi:10.1016/j.jmmm.2020.167309.

[65] Zagorodniy YO, Kuzian RO, Kondakova IV, Maryško M, Chlan V, Štěpánková H et al. Chemical disorder and $^{207}$Pb hyperfine fields in the magnetoelectric multiferroic $Pb(Fe_{1/2}Sb_{1/2})O_3$ and its solid solution with $Pb(Fe_{1/2}Nb_{1/2})O_3$. Phys. Rev. Materials 2018;2:14401. doi:10.1103/PhysRevMaterials.2.014401.

[66] Raevski IP, Kubrin SP, Raevskaya SI, Titov VV, Prosandeev SA, Sarychev DA et al. Studies of Ferroelectric and Magnetic Phase Transitions in $Pb_{1-x}A_xFe_{1/2}Nb_{1/2}O_3$ (A-Ca, Ba) Solid Solutions. Ferroelectrics 2010;398:16–25. doi:10.1080/00150193.2010.489807.

[67] Kimura K, Yokochi K, Kondo R, Urushihara D, Yamamoto Y, Ang AK et al. Local structural analysis of $Pb(Fe_{1/2}Nb_{1/2})O_3$ multiferroic material using X-ray fluorescence holography. Jpn. J. Appl. Phys. 2019;58:100601. doi:10.7567/1347-4065/ab4681.

[68] Pietrzak J, Maryanowska A, leciejewicz J. Magnetic Ordering in $Pb(Fe_{0.5}Nb_{0.5})O_3$ at 4.2 K. Phys. Stat. Sol. 1981;65:K79-82.

[69] Rotaru GM, Roessli B, Amato A, Gvasaliya SN, Mudry C, Lushnikov SG et al. Spin-glass state and long-range magnetic order in $Pb(Fe_{1/2}Nb_{1/2})O_3$ seen via neutron scattering and muon spin rotation. Phys. Rev. B 2010;105:257202. doi:10.1103/PhysRevB.79.184430.

[70] Kleemann W, Shvartsman VV, Borisov P, Kania A. Coexistence of antiferromagnetic and spin cluster glass order in the magnetoelectric relaxor multiferroic $PbFe_{0.5}Nb_{0.5}O_3$. PRL 2010;105:257202. doi:10.1103/PhysRevLett.105.257202.

[71] Chillal S, Thede M, Litterst FJ, Gvasaliya SN, Shaplygina TA, Lushnikov SG et al. Microscopic coexistence of antiferromagnetic and spin-glass states. Phys. Rev. B 2013;87:220403(R). doi:10.1103/PhysRevB.87.220403.

[72] Vannimenus J, Toulouse G. Theory of the frustration effect. II. Ising spins on a square lattice. J. Phys. C: Solid State Phys. 1977;10(18):L537-L542. doi:10.1088/0022-3719/10/18/008.

References

[73] Kleemann W, Shvartsman VV, Borisov P, Kania A. Coexistence of antiferromagnetic and spin cluster glass order in the magnetoelectric relaxor multiferroic PbFe 0.5 Nb 0.5 O3. Phys. Rev. Lett. 2010;105(25):257202. doi:10.1103/PhysRevLett.105.257202.

[74] Laguta VV, Morozovska AN, Eliseev EA, Raevski IP, Raevskaya SI, Sitalo EI et al. Room-temperature paramagnetoelectric effect in magnetoelectric multiferroics $Pb(Fe_{1/2}Nb_{1/2})O_3$ and its solid solution with $PbTiO_3$. J Mater Sci 2016;51:5330–42. doi:10.1007/s10853-016-9836-4.

[75] Brunskill IH, Schmid H, Tissot P. The characterrization of high temperature solution-grown crystals of $Pb(Fe_{1/2}Nb_{1/2})O_3$. Ferroelectrics 1981;37(1):547–50. doi:10.1080/00150198108223482.

[76] Bartek N, Shvartsman VV, Lupascu DC, Prah U, Ursic H. Influence of synthesis route on the properties of lead iron niobate. IEEE International Symposium on Applications of Ferroelectrics (ISAF), Lausanne, Switzerland 2019:1–4. doi:10.1109/ISAF43169.2019.9034943.

[77] Zieleniec K, Milata, M., and Wojcik, K. Electric conductivity of lead iron niobate. Ferroelectrics 2003;289:107–20. doi:10.1080/00150190390221331.

[78] Jenhi M, el Ghadraoui EH, Balli H, el Aatmani M, Rafiq M. Synthesis and Characterization of $Pb(Fe_{0.5}Nb_{0.5})O_3$ by Sol-Gel and Solid-State Method. Ann. Chim. Sci. Mat 1998;23:151–4. doi:10.1016/S0151-9107(98)80044-5.

[79] Font R, Raymond O, Martinez E, Portelles J, Siqueiros JM. Ferroelectric hysteresis and aging effect analysis in multiferroic $Pb(Fe_{0.5}Nb_{0.5})O_3$ ceramics. J. Appl. Phys. 2009;105:114110 1. doi:10.1063/1.3142420.

[80] Turik AV, Pavlenko AV, Andryushin KP, Shevtsova SI, Reznichenko LA, Chernobabov AI. Magnetoelectricity in the $Pb(Fe_{1/2}Nb_{1/2})O_3$ Ceramics. Phys. Solid State 2012;54:947–50. doi:10.1134/S1063783412050447.

[81] Prah U, Wencka M, Kutnjak Z, Vrabelj M, Drnovsek S, Malič B et al. Multicaloric effect in polycrystalline $Pb(Fe_{0.5}Nb_{0.5})O_3$. Microelectron. J. 2017;47:165–70.

References

[82] Blinc R, Cevc P, Zorko A, Holc J, Kosec M, Trontelj Z et al. Electron paramagnetic resonance of magnetoelectric $Pb(Fe_{1/2}Nb_{1/2})O_3$. J. Appl. Phys. 2007;101:33901. doi:10.1063/1.2432309.

[83] Kmjec T, Adamec M, Kubaniova D, Plocek J, Dopita M, Cesnek M et al. $^{57}$Fe-enriched perovskites $M(Fe_{0.5}Nb_{0.5})O_3$ (M – Pb, Ba) studied by Mössbauer spectroscopy, NMR and XRD in the wide temperature range 4.2–533 K. J. Magn. Magn. Mat. 2019;475:334–44. doi:10.1016/j.jmmm.2018.11.087.

[84] Anata S, Thomas NW. Relationships between sintering Conditions, Microstructure and Dielectric Properties of Lead Iron niobate. J. Euro. Ceram. Soc. 1999;19:1873–81. doi:10.1016/S0955-2219(98)00290-8.

[85] Gruszka I, Kania A, Talik E, Szubka M, Miga S, Klimontko J et al. Characterization of multiferroic $PbFe_{0.5}Nb_{0.5}O_3$ and $PbFe_{0.5}Ta_{0.5}O_3$ ceramics derived from citrate polymeric precursors. J. Am. Ceram. Soc. 2019;102:1296–308. doi:10.1111/jace.15998.

[86] Bochenek D, Niemiec P. Dielectric properties of the PFN ceramics obtained different chemical-wet technology and sintering by hot pressing method. MATEC Web Conf. 2018;242:1002. doi:10.1051/matecconf/201824201002.

[87] Bartek N, Shvartsman VV, Salamon S, Wende H, Lupascu DC. Influence of calcination and sintering temperatures on dielectric and magnetic properties of $Pb(Fe_{0.5}Nb_{0.5})O_3$ ceramics synthesized by the solid state method. Ceram. Int. 2021;47(16):23396–403. doi:10.1016/j.ceramint.2021.05.055.

[88] Raevski IP, Kubrin SP, Kovrigina SA, Raevskaya SI, Titov VV, Emelyanov AS et al. The Effect of PbO-Nonstoichiometry on Dielectric and Semiconducting Properties of $PbFe_{0.5}Nb_{0.5}O_3$-Based Ceramics. Ferroelectrics 2010;397:96–101. doi:10.1080/00150193.2010.484738.

[89] Liu Q, Yi GH, Barber DJ. Oriented nano-structured $Pb(Fe_{0.5}Nb_{0.5})O_3$ thin films on $SrTiO_3$ (100) substrates by sol-gel technique. Mater. Lett. (Materials Letters) 1999;38:239–44.

References

[90] Sedlar M, Sayer M. Study of electrical properties of rapid thermally processed lead iron niobate films synthesized by a sol gel method. J. Appl. Phys. 1996;80(1):372–5. doi:10.1063/1.362791.

[91] Kang J, Yoko T, sdakka S. Preparation of Lead-Based Perovskite Films by Sol-Gel Method and Their Properties. Jpn. J. Appl. Phys. 1991;30:2182.

[92] Raymond O, Ostos C, Font R, Curiel M, Bueno-Baques D, Machorro R et al. Multiferroic properties and magnetoelectric coupling in highly textured $Pb(Fe_{0.5}Nb_{0.5})O_3$ thin films obtained by RF sputtering. Acta Mater. 2014;66:184–91. doi:10.1016/j.actamat.2013.11.073.

[93] Yan L, Li J, Suchicital C, Viehland D. Multiferroic epitaxial $Pb(Fe_{1/2}Nb_{1/2})O_3$ thin films: A relaxor ferroelectric/weak ferromagnet with a variable structure. Appl. Phys. Lett. 2006;89:132913. doi:10.1063/1.2357926.

[94] Yan L, Li J, Viehland D. Structure of (001)-, (110)-, and (111)-oriented $Pb(Fe_{1/2}Nb_{1/2})O_3$ epitaxial thin films on $SrRuO_3$-buffered $SrTiO_3$ substrates. J. Mater. Res. 2008;23:663–70. doi:10.1557/JMR.2008.0081.

[95] Yan L, Zhao X, Li J, Viehland D. Enhancement of multiferroic properties of $Pb(Fe_{1/2}Nb_{1/2})O_3$ thin films on $SrRuO_3$ buffered SrTiO3 substrates. Appl. Phys. Lett. 2009;94:192903. doi:10.1063/1.3138162.

[96] Correa M, Kumar A, Katiyar RS, Rinaldi C. Observation of magnetoelectric coupling in glassy epitaxial $Pb(Fe_{0.5}Nb_{0.5})O_3$ thin films. Appl. Phys. Lett. 2008;93:192907. doi:10.1063/1.3021394.

[97] Peng W, Lemée N, Karkut M, Dkhil B, Shvartsman VV, Borisov P et al. Spin-lattice coupling in multiferroic $Pb(Fe_{1/2}Nb_{1/2})O_3$ thin films. Appl. Phys. Lett. 2009;94:12509. doi:10.1063/1.3067872.

[98] Peng W, Lemée N, Holc J, Kosec M, Blinc R, Karkut MG. Epitaxial growth and structural characterization of $Pb(Fe_{1/2}Nb_{1/2})O_3$ thin films. Journal of Magnetism and Magnetic Materials 2009;321(11):1754–7. doi:10.1016/j.jmmm.2009.02.021.

References

[99] Correa M, Kumar A, Priya S, Katiyar RS, Scott JF. Phonon anomalies and phonon-spin coupling in oriented $PbFe_{0.5}Nb_{0.5}O_3$ thin films. Phys. Rev. B 2011;83:14302. doi:10.1103/PhysRevB.83.014302.

[100] Sobiestianskas R, Peng W, Lemée N, Karkut M, Banys J, Holc J et al. Microwave dielectric dispersion in a multiferroic $Pb(Fe_{1/2}Nb_{1/2})O_3$ thin film. Appl. Phys. Lett. 2012;100:122904. doi:10.1063/1.3696043.

[101] Yuzyuk YI, Raevski IP, Raevskaya SI, Lemée N, Karkut MG, Peng W et al. Misfit strain-induced changes in the Fe-sublattice of multiferroic $Pb(Fe_{1/2}Nb_{1/2})O_3$ epitaxial nanofilm seen via Raman spectroscopy. Journal of Alloys and Compounds 2017;695:1821–5. doi:10.1016/j.jallcom.2016.11.015.

[102] Yan L, Li J, Viehland D. Deposition conditions and electrical properties of relaxor ferroelectric $Pb(Fe_{1/2}Nb_{1/2})O_3$ thin films prepared by pulsed laser deposition. J. Appl. Phys. 2007;101:104107. doi:10.1063/1.2724592.

[103] Makuła P, Pacia M, Macyk W. How To Correctly Determine the Band Gap Energy of Modified Semiconductor Photocatalysts Based on UV-Vis Spectra. J. Phys. Chem. Lett. 2018;9(23):6814–7. doi:10.1021/acs.jpclett.8b02892.

[104] Amin R, Mishra P, Khatun N, Ayaz S, Srivastava T, Sen S. Effect of titanium on the structural and optical property of NiO nano powders. In: AIP Conf. Proc, p. 30129.

[105] Urbach F. The Long-Wavelength Edge of Photographic Sensitivity and of the Electronic Absorption of Solids. Phys. Rev;92:1324. doi:10.1103/physrev.92.1324.

[106] Ikhmayies SJ, Ahmad-Bitar RN. A study of the optical bandgap energy and Urbach tail of spray-deposited CdS:In thin films. J. Mater. Res. Technol. 2013;2(3):221–7. doi:10.1016/j.jmrt.2013.02.012.

[107] Ledinsky M, Schönfeldová T, Holovský J, Aydin E, Hájková Z, Landová L et al. Temperature Dependence of the Urbach Energy in Lead Iodide Perovskites. J. Phys. Chem. Lett. 2019;10(6):1368–73. doi:10.1021/acs.jpclett.9b00138.

[108] Wu J, Walukiewicz W, Shan W, Yu KM, Ager JW, Li SX et al. Temperature dependence of the fundamental band gap of InN. J. Appl. Phys. 2003;94(7):4457–60. doi:10.1063/1.1605815.

References

[109] Rakhshani AE. Study of Urbach tail, bandgap energy and grainboundary characteristics in CdS by modulated photocurrent spectroscopy. J. Phys.: Condens. Matter 2000(12):4391–400.

[110] Becquerel E. Mémoire sur les effets électriques produits sous l'influence des rayons solaires. Compt. rend. 1839;9:561.

[111] Gelmetti I, Cabau L, Montcada NF, Palomares E. Selective Organic Contacts for Methyl Ammonium Lead Iodide (MAPI) Perovskite Solar Cells: Influence of Layer Thickness on Carriers Extraction and Carriers Lifetime. ACS applied materials & interfaces 2017;9(26):21599–605. doi:10.1021/acsami.7b06638.

[112] Gordillo G, Torres OG, Abella MC, Peña JC, Virguez O. Improving the stability of $MAPbI_3$ films by using a new synthesis route. J. Mater. Res. Technol. 2020;9(6):13759–69. doi:10.1016/j.jmrt.2020.09.095.

[113] Huang X, Zhao Z, Cao L, Chen Y, Zhu E, Lin Z et al. High-performance transition metal-doped $Pt_3Ni$ octahedra for oxygen reduction reaction. Science 2015;348:123–1234. doi:10.1126/science.aaa8765.

[114] Shockley W, Queisser HJ. Detailed Balance Limit of Efficiency of p-n Junction Solar Cells. J. Appl. Phys. 1961;32(3):510–9. doi:10.1063/1.1736034.

[115] Ichiki M, Maeda R, Morikawa Y, Mabune Y, Nakada T, Nonaka K. Photovoltaic effect of lead lanthanum zirconate titanate in a layered film structure design. Appl. Phys. Lett. 2004;84(3):395–7. doi:10.1063/1.1641528.

[116] Brody PS. Large polarization-dependent photovoltages in ceramic $BaTiO_3$ + 5 wt.% $CaTiO_3$. Sol. State Comm.:679.

[117] Glass AM, Linde D von der, Negran TJ. High-voltage bulk photovoltaic effect and the photorefractive process in $LiNbO_3$. Appl. Phys. Lett. 1974;25(4):233–5. doi:10.1063/1.1655453.

[118] Chynoweth AG. Surface Space-Charge Layers in Barium Titanate. Phys. Rev. 1956;102(3):705–14.

References

[119] Fridkin VM. Bulk photovoltaic effect in noncentrosymmetric crystals. Crystallogr. Rep. 2001;46(4):654–8.

[120] Butler KT, Frost JM, Walsh A. Ferroelectric materials for solar energy conversion: photoferroics revisited. Energy Environ. Sci. 2015;8(3):838–48. doi:10.1039/C4EE03523B.

[121] Belinicher VI, Sturman BI. The photogalvanic effect in media lacking a center of symmetry. Sov. Phys. Usp. 1980;23(3):199–223. doi:10.1070/PU1980v023n03ABEH004703.

[122] Han X, Ji Y, Yang Y. Ferroelectric Photovoltaic Materials and Devices. Adv. Funct. Mater. 2021:2109625. doi:10.1002/adfm.202109625.

[123] Zhao X, Song K, Huang H, Han W, Yang Y. Ferroelectric Materials for Solar Energy Scavenging and Photodetectors. Adv. Opt. Mater. 2021;10(2):2101741. doi:10.1002/adom.202101741.

[124] Dresselhaus G. Spin-Orbit Coupling Effects in Zinc Blende Structures. Phys. Rev. 1955;100(2). doi:10.1103/PhysRev.100.580.

[125] Yang SY, Seidel J, Byrnes SJ, Shafer P, Yang C-H, Rossell MD et al. Above-bandgap voltages from ferroelectric photovoltaic devices. Nat. Nanotechnol 2010;5(2):143–7. doi:10.1038/nnano.2009.451.

[126] Qin M, Yao K, Liang YC, Shannigrahi S. Thickness effects on photoinduced current in ferroelectric $(Pb_{0.97}La_{0.03})(Zr_{0.52}Ti_{0.48})O_3$ thin films. J. Appl. Phys. 2007;101(1):14104. doi:10.1063/1.2405732.

[127] Berenov A, Petrov P, Moffat B, Phair J, Allers L, Whatmore RW. Pyroelectric and photovoltaic properties of Nb-doped PZT thin films. APL Mater. 2021;9:41108. doi:10.1063/5.0039593.

[128] Chen B, Zuo Z, Liu Y, Zhan Q-F, Xie Y, Yang H et al. Tunable photovoltaic effects in transparent $Pb(Zr_{0.53},Ti_{0.47})O_3$ capacitors. Appl. Phys. Lett. 2012;100(17):173903. doi:10.1063/1.4709406.

References

[129] Paik YH, Kojori HS, Yun J-H, Kim SJ. Improved efficiency of ferroelectric Pb(Zr, Ti)$O_3$ (PZT) based photovoltaic device with colloidal quantum dots. Mater. Lett. (Materials Letters) 2016;185:247–51. doi:10.1016/j.matlet.2016.08.082.

[130] Yang SY, Martin LW, Byrnes SJ, Conry TE, Basu SR, Paran D et al. Photovoltaic effects in $BiFeO_3$. Appl. Phys. Lett. 2009;95(6):62909. doi:10.1063/1.3204695.

[131] Basu SR, Martin LW, Chu YH, Gajek M, Ramesh R, Rai RC et al. Photoconductivity in $BiFeO_3$ thin films. Appl. Phys. Lett. 2008;92(9):91905. doi:10.1063/1.2887908.

[132] Ihlefeld JF, Podraza NJ, Liu ZK, Rai RC, Xu X, Heeg T et al. Optical band gap of BiFeO3 grown by molecular-beam epitaxy. Appl. Phys. Lett. 2008;92(14):142908. doi:10.1063/1.2901160.

[133] Chen G, Chen J, Pei W, Lu Y, Zhang Q, He Y. Bismuth ferrite materials for solar cells: Current status and prospects. Mater. Res. Bull. 2019;110:39–49. doi:10.1016/j.materresbull.2018.10.011.

[134] Gao X, Xue J, Wang J. Sequential Combination of Constituent Oxides in the Synthesis of $Pb(Fe_{1/2}Nb_{1/2})O_3$ by Mechanical Activation. J Am Ceram Soc 2002;85:565–72. doi:10.1111/j.1151-2916.2002.tb00133.x.

[135] Birkholz M. Thin Film Analysis by X-Ray Scattering. Weinheim: Wiley-VCH; 2006.

[136] Derriche N, Godin S, Greenwood R, Mercado A, Warner AN. Reflection High-Energy Electron Diffraction 2019. Available from: <https://phas.ubc.ca/~berciu/TEACHING/PHYS502/PROJECTS/RHEED.pdf>.

[137] Kalinin SV, Bonnell DA. Imaging mechanism of piezoresponse force microscopy of ferroelectric surfaces. Phys. Rev. B 2002;65(12):125408. doi:10.1103/PhysRevB.65.125408.

[138] Piezoelectric characterization. Available from: <http://mentors.tanms-erc.org/mentor-responsibilities/piezoelectric-characterization>.

[139] Waser R (ed.). Polar oxides: Properties, characterization, and imaging. Weinheim: Wiley-VCH; 2005.

[140] aixACCT. Manual: aixPlorer Software. Version 3.0.46.0 M1.

References

[141] Shimadzu. Light path. Available from: <https://www.shimadzu.de/uv-2600i-uv-2700i>.

[142] Bredas J-L. Mind the gap! Mater. Horiz. 2014;1:17–9. doi:10.1039/C3MH00098B.

[143] Terashima M, Miyayama T, Shirao T, Mo HW, Hatae Y, Fujimoto H et al. The electronic band structure analysis of OLED device by means of in situ LEIPS and UPS combined with GCIB. Surf. Interface Anal. 2020;52(12):948–52. doi:10.1002/sia.6777.

[144] Sekar MMA, Halliyal A. Low-Temperature Synthesis, Characterization, and Properties of Lead-Based Ferroelectric Niobates. J. Am. Ceram. Soc. (Journal of the American Ceramic Society) 1998;81:380–8.

[145] Chiu CC, Li CC, Desu SB. Molten Salt Synthesis of a Complex Perovskite, $Pb(Fe_{0.5}Nb_{0.5})O_3$. J. Am. Ceram. Soc. (Journal of the American Ceramic Society) 1991;74:38–41.

[146] Stojanovic BD, Simoes AZ, Paiva-Santos CO, Jovalekic C, Mitic VV, Varela JA. Mechanochemical synthesis of barium titanate. J. Euro. Ceram. Soc. 2005;25(12):1985–9. doi:10.1016/j.jeurceramsoc.2005.03.003.

[147] Rahaman MN. Sintering of Ceramics. Boca Raton, FL: CRC Press, Taylor & Francis Group; 2011.

[148] Anata S, Thomas NW. Relationships between Sintering Conditions, Microstructure and Dielectric Properties of Lead Iron Niobate. J. Euro. Ceram. Soc. 1999;19:1873–81.

[149] Gusev AA, Raevski IP, Avvakumov EG, Isupov VP, Kubrin SP, Chen H et al. The Effect of Mechanical Activation on the Synthesis and Properties of Multiferroic Lead Iron Niobate. In: Chang, Parinov et al. – Advanced Materials, p. 15–26.

[150] Gusev A. A., Raevski IP, Avvakumov EG, Isupov VP. Phase formation on the surface of lead ferroniobate depending on the conditions of mechanochemical synthesis and sintering. Sci Sintering 2016;48:283–92. doi:10.2298/SOS1603283G.

[151] Chiu CC, Desu SB. Microstructure and properties of lead ferroniobate ceramics $P(Fe_{0.5}Nb_{0.5})O_3$. mater. Sci. Eng. B21 1993:26–35. doi:10.1016/0921-5107(93)90261-K.

References

[152] Kozlenko DP, Kichanov SE, Lukin EV, Dang NT, Dubrovinsky LS, Liermann H-P et al. Pressure-induced polar phases in relaxor multiferroic $PbFe_{0.5}Nb_{0.5}O_3$. Phys. Rev. B 2014;89(17). doi:10.1103/PhysRevB.89.174107.

[153] García-Flores AF, Tenne DA, Choi YJ, Ren WJ, Xi XX, Cheong SW. Temperature-dependent Raman scattering of multiferroic $Pb(Fe_{1/2}Nb_{1/2})O_3$. J. Phys. Condens 2011;23(1):15401. doi:10.1088/0953-8984/23/1/015401.

[154] Laguta VV, Glinchuk MD, Maryško M, Kuzian RO, Prosandeev SA, Raevskaya SI et al. Effect of Ba and Ti doping on magnetic properties of multiferroic Pb(Fe 1/2 Nb 1/2 )O 3. Phys. Rev. B 2013;87(6). doi:10.1103/PhysRevB.87.064403.

[155] Matteppanavar S, Angadi B, Rayaprol S. Low temperature magnetic studies on $PbFe_{0.5}Nb_{0.5}O_3$ multiferroic. Physica B: Condensed Matter 2014;448:229–32. doi:10.1016/j.physb.2014.04.024.

[156] Havlicek R, Vejpravova JP, Bochenek D. Structure and magnetic properties of perovskite-like multiferroic $PbFe_{0.5}Nb_{0.5}O_3$. J. Phys.: Conf. Ser. 2010;200:012058 1-4. doi:10.1088/1742-6596/200/1/012058.

[157] Prah U, Rojac T, Wencka M, Dragomir M, Bradeško A, Benčan A et al. Improving the multicaloric properties of $Pb(Fe_{0.5}Nb_{0.5})O_3$ by controlling the sintering conditions and doping with manganese. J. Eur. Ceram. 2019;39:4122–30. doi:10.1016/j.jeurceramsoc.2019.05.062.

[158] Singh SP, Pandey D, Yoon S, Baik S, Shin N. Evidence for monoclinic crystal structure and negative thermal expansion below magnetic transition temperature in $Pb(Fe_{1/2}Nb_{1/2})O_3$. Appl. Phys. Lett. 2007;90:242915-4. doi:10.1063/1.2748856.

[159] Majumder SB, Bhattacharyya S, Katiyar RS, Manivannan A, Dutta P, Seehra MS. Dielectric and magnetic properties of sol-gel-derived lead iron niobate ceramics. J. Appl. Phys. 2006;99:24108. doi:10.1063/1.2158131.

[160] Bochenek D, Surowiak Z, Krok-Kowalski J, Poltierova-Vejpravova J. Influence of the sintering conditions on the physical proprieties of the ceramic PFN multiferroics. J. Electrocerams (Journal of Electroceramics) 2010;25:122–9. doi:10.1007/s10832-010-9599-2.

References

[161] Kirillov VV, Isupov VA. Relaxation polarization of $PbMg_{1/3}Nb_{1/3}O_3$(PMN)-A ferroelectric with a diffused phase transition. Ferroelectrics 1973;5:3–9. doi:10.1080/00150197308235773.

[162] Smolenskii GA, Yudin VM. Weak ferromagnetism of some BFO-PFN compounds perovskites. Phys. Solid State 1965;6:2936–42.

[163] Goodenough JB, Wickham DG, Croft WJ. Some Magnetic and Crystallographic Properties of the System $Li_x^{++}Ni_{1-2x}^{++}Ni_x^{+++}O^*$. J. Phys. Chem. Solids 1958;5:107–16. doi:10.1016/0022-3697(58)90136-7.

[164] Gilleo MA. Superexchange interaction in ferrimagnetic garnets and spinels which contain randomly incomplete linkages. J. Phys. Chem. Solids 1960;13:33–9. doi:10.1016/0022-3697(60)90124-4.

[165] Raevskaya SI, Kubrin SP, Raevski IP, Chou CC, Chen H, Titov VV et al. The effect of quenching on semiconductive properties and magnetic phase transition temperature of multiferroic $Pb(Fe_{1/2}Nb_{1/2})O_3$ ceramics. Ferroelectrics 2017;509:64–73. doi:10.1080/00150193.2017.1293452.

[166] Guzdek P. The magnetostrictive and magnetoelectric characterization of $Ni_{0.3}Zn_{0.62}Cu_{0.08}Fe_2O_4$–$Pb(FeNb)_{0.5}O_3$ laminated composite. J. Magn. Magn. Mat. 2014;349:219–23. doi:10.1016/j.jmmm.2013.08.064.

[167] Matteppanavar S, Rayaprol S, Angadi B. Low-temperature neutron diffraction and magnetic studies on the magnetoelectric multiferroic $Pb(Fe_{0.534}Nb_{0.4}W_{0.066})O_3$. J. Mater. Sci. 2017;52:10709–17. doi:10.1007/s10853-017-1256-6.

[168] Chrisey. D. B. Pulsed laser deposition of thin film: Wiley; 1994.

[169] Pinna N, Knez M. Atomic Layer Deposition of Nanostructured Materials: Wiley-VCH; 2012.

[170] Bartek N, Shvartsman VV, Bouyanfif H, Schmitz A, Bacher G, Olthof S et al. Band Gap of Pb(Fe0.5Nb0.5)O3 Thin Films Prepared by Pulsed Laser Deposition. Materials 2021;14(22):6841. doi:10.3390/ma14226841.

References

[171] Teixeira GF, Gasparotto G, Paris EC, Zaghete MA, Longo E, Varela JA. Photoluminescence properties of PZT 52/48 synthesized by microwave hydrothermal method using PVA with template. J. Lumin. 2012;132(1):46–50. doi:10.1016/j.jlumin.2011.06.041.

[172] Sczancoski JC, Cavalcante LS, Joya MR, Espinosa JWM, Pizani PS, Varela JA et al. Synthesis, growth process and photoluminescence properties of SrWO4 powders. J. Colloid Interface Sci 2009;330(1):227–36. doi:10.1016/j.jcis.2008.10.034.

[173] Longo E, Figueiredo AT de, Silva MS, Longo VM, Mastelaro VR, Vieira ND et al. Influence of structural disorder on the photoluminescence emission of PZT powders. J. Phys. Chem. A 2008;112(38):8953–7. doi:10.1021/jp801607m.

[174] Yu JG, Zhao XF, Liu SW, Li M, Mann S, Ng D. Poly(methacrylic acid)-mediated morphosynthesis of PbWO4 micro-crystals. Appl. Phys. A 2007;87(1):113–20. doi:10.1007/s00339-006-3850-3.

[175] Hu Y, Gu H, Sun X, You J, Wang J. Photoluminescence and Raman scattering studies on $PbTiO_3$ nanowires fabricated by hydrothermal method at low temperature. Appl. Phys. Lett. 2006;88(19):193120. doi:10.1063/1.2203736.

[176] Maurya JC, Dixit AV, Manorama V, Bhoraskar SV. Effect of reduction of PLZT on carrier lifetime determined by EBIC. Sol. State Comm. 1987;64(9):1235–40. doi:10.1016/0038-1098(87)90739-3.

[177] Chen G, Zou K, Yu Y, Zhang Y, Zhang Q, Lu Y et al. Effects of the film thickness and poling electric field on photovoltaic performances of $(Pb,La)(Zr,Ti)O_3$ ferroelectric thin film-based devices. Ceram. Int. 2020;46(4):4148–53. doi:10.1016/j.ceramint.2019.10.131.

[178] He J, Li F, Chen X, Qian S, Gilleo MA, Bi K et al. Thickness Dependence of Ferroelectric and Optical Properties in $Pb(Zr0.53Ti0.47)O_3$ Thin Films. Sensors 2019;19. doi:10.3390/s19194073.

[179] He XY, Ding AL, Zhang Y, Cao ZP, Qiu PS. Influence of Film Thickness on Optical Properties of PLZT Thin Films Derived from MOD Method. KEM 2007;280-283:231–4. doi:10.4028/www.scientific.net/KEM.280-283.231.

References

[180] Peng CH, Chang JF, Desu SB. Optical properties of PZT, PLZT and PNZT thin film. Mat. Res. Soc. Symp. Proc. 1991;243:21–6.

[181] Stillman GE, Robbins VM, Tabatabaie N. III-V compound semiconductor devices: Optical detectors. IEEE Trans. Electron Devices 1984;31(11):1643–55. doi:10.1109/T-ED.1984.21765.

[182] Nelson J. The Physics of Solar Cells. Singapore: Imperial Collage Press.